UNIVERSITY OF BIRMINGHAM

SYNTHESIS, STRUCTURE AND PROPERTIES OF BIFUNCTIONAL CARBOXYPHOSPHONATE METAL–ORGANIC FRAMEWORKS

by

Joseph A Barker

A thesis submitted to the University of Birmingham for the degree of

Doctor of Philosophy

School of Chemistry
College of Engineering and Physical Sciences
The University of Birmingham

April 2022

Abstract

Metal–organic frameworks (MOFs) are porous materials made of metal ions or nodes connected by organic linker molecules to form 3-dimensional frameworks with potential voids. Since the late 1990's they have been the subject of intense scientific interest for a wide range of applications including gas storage, proton conductivity, waste remediation and catalysis to name but a few. The most common type of linker molecules are those based on carboxylate functional groups, usually containing 2, 3 or 4 of these groups per linker molecule. However, the area of carboxylate MOFs has been extremely widely researched and the variety of coordination motifs is relatively limited. There is a significant amount of research interest in phosphonate MOFs, as these have a wider variety of coordination motifs and thus should be able to form a wider variety of structures. Additionally, phosphonate groups, like carboxylates, form strong coordination bonds leading to structures with significant thermal and chemical stability. However, phosphonate linkers are not without their issues. With a tendency to form dense layered structures and undergo rapid nucleation, the synthesis of large single crystals of a phosphonate MOF is difficult. This work focused on the use of bifunctional carboxyphosphonate linker molecules in order to balance the positive and negative properties of each functional group. Starting with a study of the synthesis of the ion-exchangeable carboxyphosphonate MOF, BIRM-1 $(NH_4)_2[Zn_2(O_3PCH_2CH_2COO)_2 \cdot 5H_2O$ and two of its forms with alkali metal cations in place of ammonium cations. Properties and structural behaviours of the material were also examined with brief studies on the material's potential for applications such as proton conductivity and ammonia storage. The focus of the work then shifts towards the synthesis and characterisation of novel carboxyphosphonate materials. Firstly, using magnesium as the metal in attempts to produce a lightweight framework and then moving onto using a different linker. The linker that was chosen was 4-phosphonobenzoic acid. A total of 5 novel phases were produced in this work with one of them showing significant surface area (813 $m^2 g^{-1}$) and meeting the definition of a MOF. This material has been denoted BIRM-10 and possesses the formula $Zn_{1.1}(O_3PC_7H_4COO)(OH)_{0.1}(NH_4)_{0.9} \cdot 0.33H_2O$. A further 3 unsolved phases, 2 based on magnesium and 1 on cadmium, were synthesised with at least one of these also displaying significant surface area.

Acknowledgements

First and foremost, I would like to thank my supervisor Professor Paul Anderson for the guidance, help and teaching he has provided throughout my studies, originally as an MSci student and then during my PhD.

I'd also like to thank Dr Louise Male for all the help and training with single crystal diffraction, both the data collection and analysis.

I also tremendously appreciate the help and Dr Phil Chater from Diamond Lightsource in collecting, processing and helping me analyse the PDF work contained within this thesis.

Other people I'd like to thank for their contributions to this work include Matt James for taking conductivity measurements on BIRM-1 for me. Dr Karen Robertson for providing the equipment and knowledge for setting up the flow synthesis experiments for BIRM-1. Dr Josh Makepeace and Dr Manoj Ravi for the help and equipment in conducting an ammonia uptake measurement. David Burgess for collecting AFM images.

Thanks also go to the School of Chemistry for granting me a scholarship, allowing me to undertake this PhD degree.

On a more personal note, I'd like to thank all of Floor 5 for the good times had and valuable friendships made. I'd especially like to thank Harry, Luke and Rob who have made my time at Birmingham particularly enjoyable.

Finally, my partner George, whose love and companionship I have immensely enjoyed for 5 years now and without which I would be lost. Through the good times and the bad you have been by my side, always there for me.

Dedication

I'd like to dedicate this thesis to my paternal Grandfather, Thomas Barker, and my maternal Grandmother, Margaret Hurst, who both sadly passed away during the time I was doing this PhD. My Grandad was a former chemist himself, whose stories of his time in the lab are part of what led me to pursue a career in science. And I will always remember the constant love and support provided to me by my Nan.

Rest in peace

Table of Abbreviations

AFM	Atomic force microscopy
BET	Brunauer-Emmett-Teller
BIRM-1	MOF with formula $(NH_4)_2[Zn_2(O_3P(CH_2)_2COO)_2]\cdot 5H_2O$
BIRM-10	MOF with formula $Zn_{1.1}(O_3PC_7H_4COO)(OH)_{0.1}(NH_4)_{0.9}\cdot 0.33H_2O$
BIRM-2	Layered framework with formula $Zn(O_3P(CH_2)_2COOH)\cdot H_2O$
BIRM-3	Dense framework with formula $(NH_4)[Zn_2(O_3P(CH_2)_2COO)]$
BIRM-4	Dense framework with formula $(NH_4)[Zn_2(O_3P(CH_2)_2COO)]$
BIRM-6	Coordination polymer with formula $Mg(O_3PCH_2CH_2CO_2H)\cdot 4H_2O$
BIRM-7	Pillared–layered framework with formula $Mg_3(O_3PCH_2CH_2CO_2)_2$
BIRM-8	Layered framework with formula $Zn(O_3PC_6H_4COOH)\cdot H_2O$
BIRM-9	Layered framework with formula $Zn_4(O_3PC_7H_4COO)_2(OH)_2\cdot 2H_2O$
DTA	Differential thermal analysis
EDX	Energy dispersive X-ray
FTIR	Fourier transform infrared
HT-BIRM-1	BIRM-1 synthesised *via* a hydrothermal method
M^+-BIRM-1	BIRM-1 with a different cation (M^+) in place of ammonium
MOFs	Metal–organic frameworks
MS	Mass spectrometry
PDF	Pair distribution function
PXRD	Powder X-ray diffraction
RT-BIRM-1	BIRM-1 synthesised *via* a room temperature method
SEM	Scanning electron microscopy
TGA	Thermogravimetric analysis
XRD	X-ray diffraction

Table of Contents

1 Introduction

1.1 Metal–Organic Frameworks

Metal–organic frameworks (MOFs) are a class of inorganic-organic hybrid materials. They are constructed of metal ions or clusters linked together by coordinated organic linker molecules in order to form an extended 3-dimensional framework with potential voids.[1] MOF-5 is often referred to as the archetypal MOF and is shown in Figure 1.1.[2] For MOF synthesis transition metals are most commonly used. However, many MOFs made using s-, p- and f-block elements have also been published. A potential void is a volume within the material that is typically filled with solvent after synthesis and may be possible to evacuate, a process known as activating. These voids may take the form of long channels along one or more dimension or large cavities such as those in MOF-5. It is these potential voids that give rise to the significant scientific interest in MOFs. The internal surface area that these voids provide can be exploited for applications such as gas storage or catalysis.[3] The pores may also be filled with proton carriers allowing for proton conductivity or the pores may only be accessible through certain sized apertures allowing for gas separation.

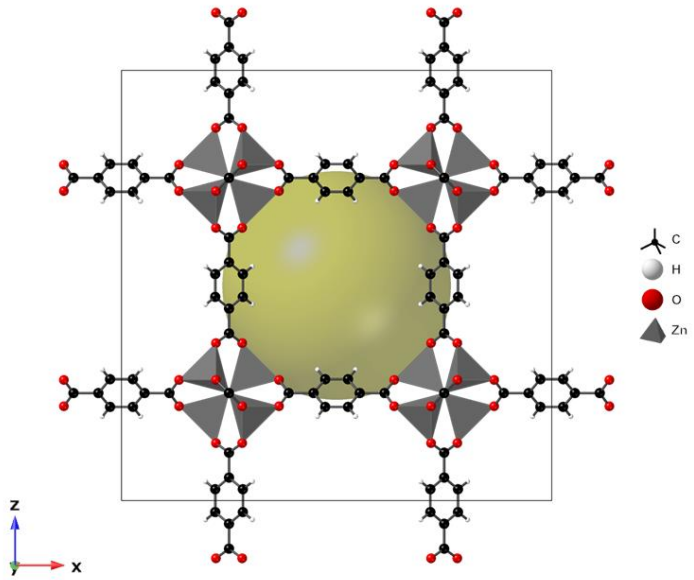

Figure 1.1) Crystal structure of MOF-5, the volume of the internal cavity is represented by the yellow sphere and the unit cell by the black square.[2]

The term metal–organic framework was coined in the 1990's by Yaghi et al.[1] however, the development of these materials has a longer history. Materials that would fit the definition of a metal–organic framework have been synthesised since at least 1959.[4] However, such materials were first examined for their porosity in the late 1980's by Hoskins and Robson.[5] In their work they describe the design, synthesis and structure of a new class of porous materials, explaining why and how they believe the material's cavities will lead to their use in a range of applications. The new material they synthesised was $Cu^{I}[C(C_6H_4CN)_4]$, which is shown in Figure 1.2. The structure can be described as like a diamond net which is elongated due to the long $C(C_6H_4CN)_4$ linker units, allowing for cavities within the structure. The framework is positively charged and is balanced by BF_4^- anions within the cavities which are not shown.[5] The same researchers also published another porous material a year later; made up of zinc and copper with cyanide linkers containing tetramethylammonium cations in the pores.[6]

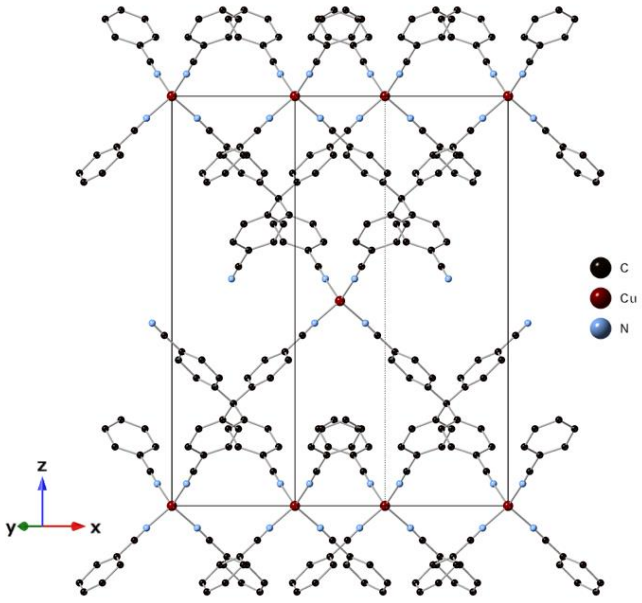

Figure 1.2) Crystal structure of $Cu^{I}[C(C_6H_4CN)_4]$, hydrogen atoms and solvent is not shown. The unit cell is represented by the black outline[5]

Following on from this work, interest in this new class of materials grew greatly. The end of the 1990's saw Yaghi et al. publish the first metal–organic framework which exhibits permanent porosity, MOF-5. This meaning it was the first such material which could have the cavities evacuated of solvent and other

molecules in order for the internal surface area and pore volume to be exploited. MOF-5 has already been shown in Figure 1.1. It is made up of clusters of 4 zinc oxide tetrahedra connected by benzene-1,4-dicarboxylic acid (BDC). The discovery of MOF-5 was followed by the development of the concept of reticular synthesis by Eddaoudi et al.[7,8] Reticular synthesis is the idea that the linker molecules used in the formation of a MOF may be changed or functionalised in a way that does not affect the formation chemistry of the material. This can then be used to make a large series of materials where small changes to the linker are made in order to tailor the properties to certain applications. Eddaoudi et al. made a number of changes to the BDC linker used in the synthesis of MOF-5 and developed a series of 16 isoreticular MOFs which are shown in Figure 1.3.[7] Changes made to the BDC linker include lengthening by using a linker with one or two more benzene rings in the chain. Functionalisation of the BDC linker was also used such as the introduction of an amine group onto the aromatic ring which would then effectively functionalise the walls of the cavities.

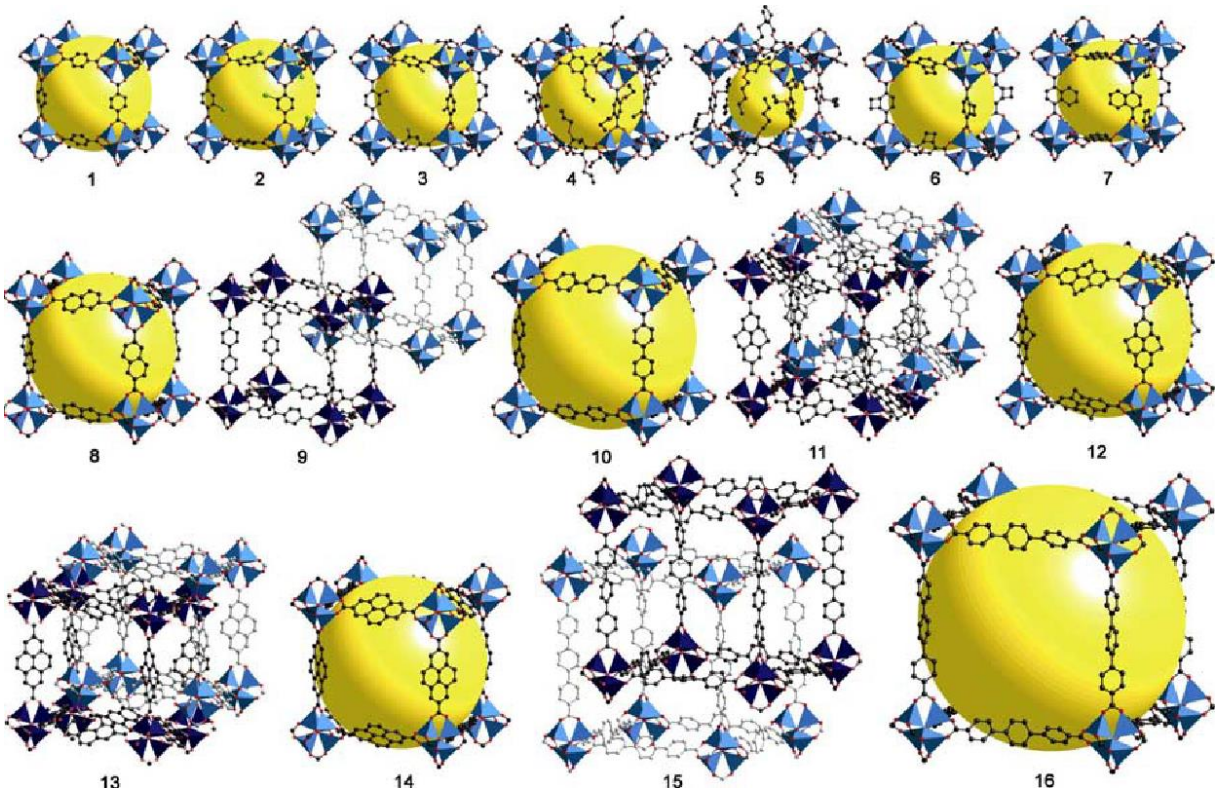

Figure 1.3) The isoreticular series of MOFs published by Eddaoudi et al. Figure reproduced from Rowsell and Yaghi.[9] *Zinc tetrahedra shown in blue, carbon atoms in black, oxygen in red and cavity volume represented by yellow spheres. Structures 9, 11,13 and 15 are catenated.*

1.1.1 Coordinating Groups

1.1.1.1 Carboxylate

Carboxylate coordinating groups are the most commonly used in linkers for MOF synthesis. This is due to their cheapness, predictable chemistry and their formation of strong coordination bonds leading to frameworks with good thermal stability. Many early MOFs used neutrally charged nitrogen-based linkers, such as in the work of Hoskins and Robson, and found problems with low thermal stability. Additionally, the negative charge of carboxylates counters the positive charge of metal ions, unlike many nitrogen-based linkers. This leads to a neutral framework and no need for balancing counter-ions within the internal pores which, depending on the application, may be undesirable. Figure 1.4 shows a few examples of carboxylate-based linker molecules. Note that linker molecules will usually have rigid carbon chains based on aromatic, alkene or alkyne groups. This is because more flexible aliphatic chains will lead to frameworks which are not likely to provide permanent porosity. However many MOF materials are still made with flexible linkers as permanent porosity is not always necessary for certain applications.[10]

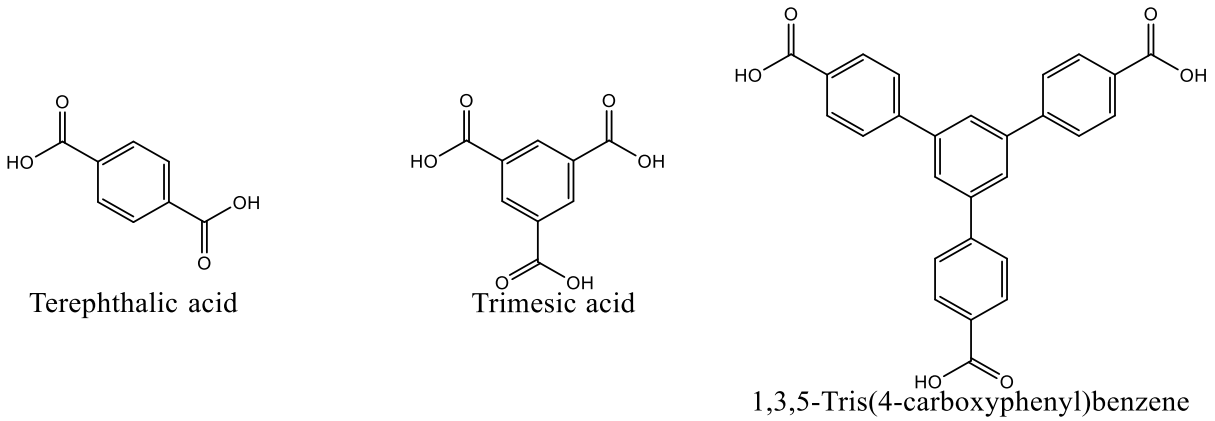

Figure 1.4) Some examples of carboxylate-based linker molecules

1.1.1.2 Phosphonate

Phosphonate-based linkers are somewhat less commonly used than carboxylate for several reasons. They tend to be less widely commercially available and are more expensive due to being more complicated to synthesise. Their coordination chemistry is also somewhat less predictable as they have

3 oxygen atoms capable of forming coordination bonds as opposed to two on a carboxylate. Whilst this does add unpredictability it also opens the possibility of new frameworks *via* coordination motifs which are not accessible using carboxylates. Similar to carboxylates, phosphonates also form strong coordination bonds. This allows for good thermal stability which would be required for many applications. Another drawback of phosphonate-based linkers is that phosphonate compounds have a tendency to crystallise rapidly as layered phases.[11] Whilst their tendency to form layered materials I obviously problematic if the aim of the work is to produce porous MOFs, the rapid crystallisation also makes the growth of single crystals and subsequent structure solutions difficult.[11–13]

The history of phosphonate MOFs extends back to the 1990's when widespread interest in MOFs began to develop. Le Bideau et al. developed the first phosphonate-based open framework in 1994, made up of tetragonal pyramids of Cu^{II} ions and simple monotopic methylphosphonate linkers.[14] The structure of this material is shown in Figure 1.5. Although there are potential voids, they are in fact too small (3 Å) to incorporate guest molecules. This material also does not really fit the definition of a MOF as the framework is constructed of phosphorous and copper polyhedra with the methyl group furnishing the sides of the channels rather than forming part of the structure. Regardless, it was the publication of this material that led to significant interest in phosphonate based open frameworks and MOFs. Similar materials to the $Cu(O_3PCH_3)$ but based on aluminium were produced the same year by Maeda et al.[13,15] In later years, related materials based on scandium[16] and iron[17] were also produced.

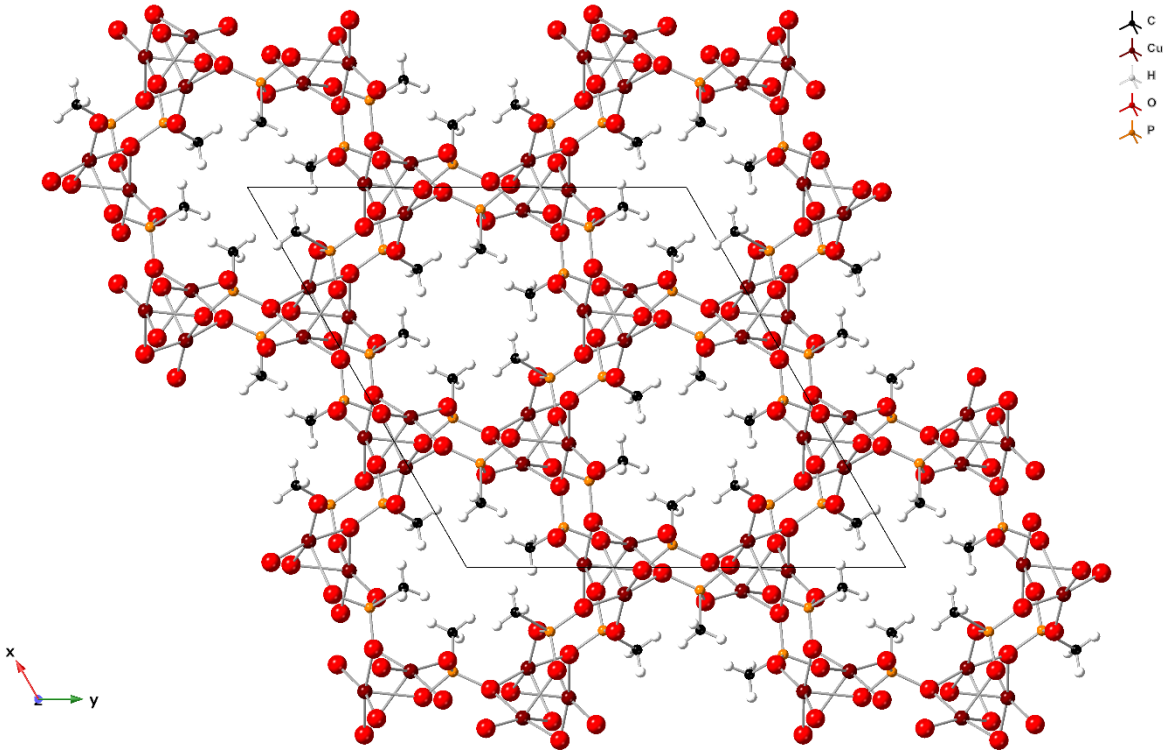

Figure 1.5) Crystal structure of Cu(O_3PCH_3). The unit cell is indicated by the black outline[14]

Three years after the development of Cu(O_3PCH_3), Sevov and Lohse developed a cobalt-based MOF using alkylbisphosphonate linkers.[18] The structure, which is shown in Figure 1.6, is a porous neutral framework with water molecules located within the pores. Cobalt(II) ions are present in both octahedral and tetrahedral geometries. Isostructural materials based on zinc[19] and nickel[20] were also developed in later years. The notable aspect of this material is that the use of a carbon chain opened the possibility for chain extension and thus the expansion of pores. What followed was multiple attempts by researchers to produce MOFs using $O_3P(CH_2)_nPO_3$ linkers molecules.

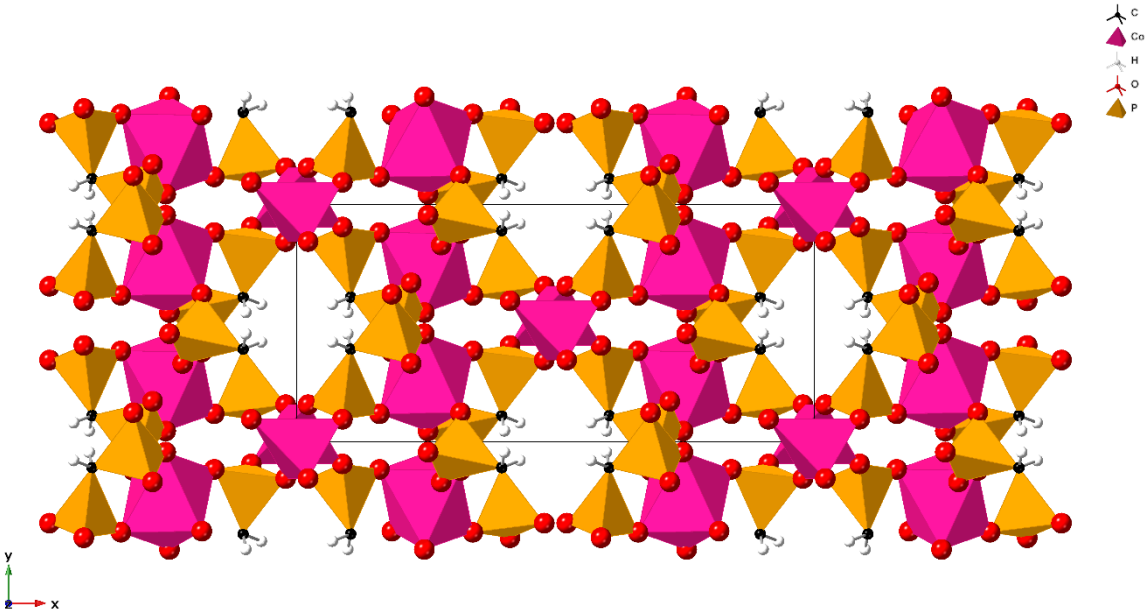

Figure 1.6) Crystal structure of $Co_2(O_3PCH_2PO_3)\cdot H_2O$. Water molecules are omitted to highlight the porous structure. The unit cell is indicated by the black outline[18]

Most researchers failed in making porous materials and instead produced dense pillared–layered structures.[21–26] These structures would be composed of 2-dimensional inorganic sheets of metal oxide and CPO_3 tetrahedra which would then be linked together by the carbon chains. An example from the work of Tuikka et al. is shown in Figure 1.7.[26]

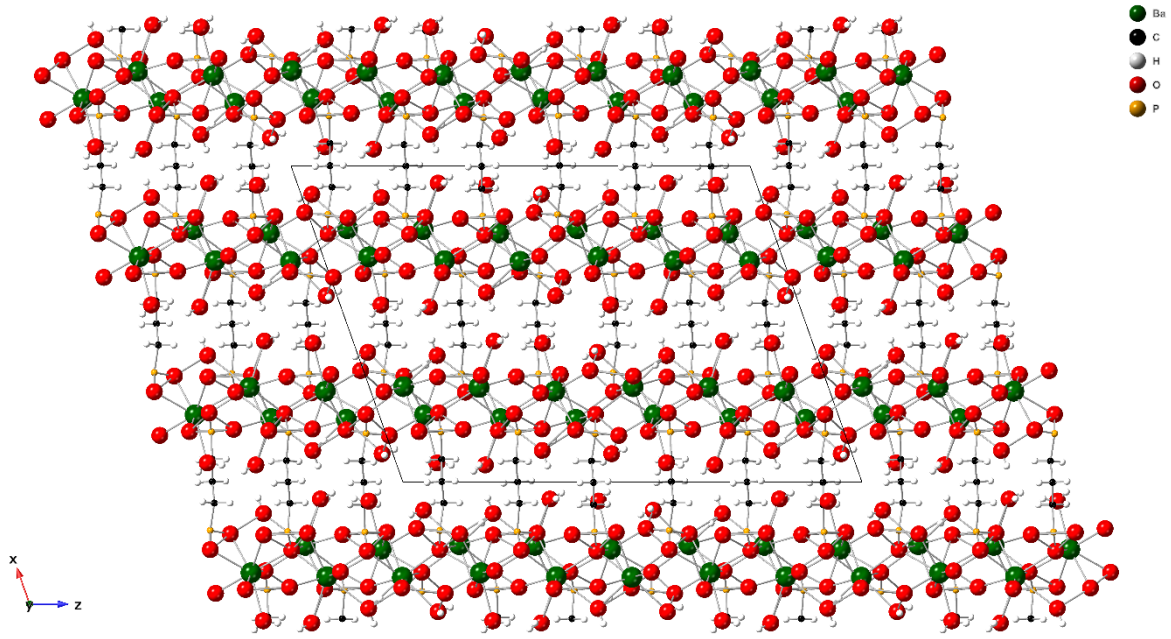

Figure 1.7) Crystal structure of $Ba_2(O_3P(CH_2)_3PO_3)\cdot 3H_2O$. The unit cell is indicated by the black outline.[26]

However, some of these pillared–layered frameworks were structured in such a way to allow for porosity. As early as 1997, Clearfield et al. had success in forming a copper-based pillared–layered framework using ethylenebisphosphonic acid which possessed one-dimensional channels. This was synthesised alongside a non-porous copper-based pillared–layered framework as well as two such zinc-based materials.[27] The structure of the copper-based open framework is shown in Figure 1.8.

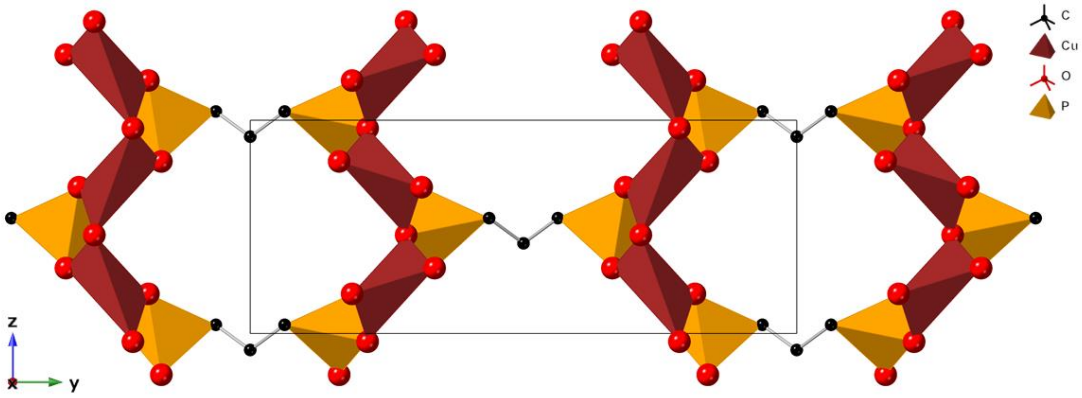

Figure 1.8) Crystal structure of $Cu_2(O_3P(CH_2)_3PO_3)_2\cdot 3H_2O$. Water molecules located within the channels have been omitted for clarity. The position of hydrogen atoms was not included in the crystal structure. The unit cell is indicated by the black square.[27]

The Clearfield group later produced more copper-based pillared–layered open frameworks using C_4 and C_5 alyklbisphosphonate linkers.[28] This is another example of producing isoreticular MOF materials. In 2014 this work on isoreticular expansion of the alkyl chains was built upon with the publication of nine new compounds.[29] Only two of these new compounds contained potential voids in the form of small one-dimensional channels. This work highlighted the difficulties in synthesising porous frameworks from bisphosphonate linker molecules.

Following this work, several attempts using aromatic bisphosphonates as the linker molecules were made by various groups. However, these attempts also largely resulted in dense pillared–layered materials rather than open frameworks.[30–35] An example based on sodium is shown in Figure 1.9. One attempt by Taylor et al. using 1,2,4,5-tetrakis(phosphonomethyl)benzene led to a 3-dimensional framework with channels capable of allowing the conduction of protons along them. The authors named this material PCMOF-5.[36] The structure of this material is shown in Figure 1.10.

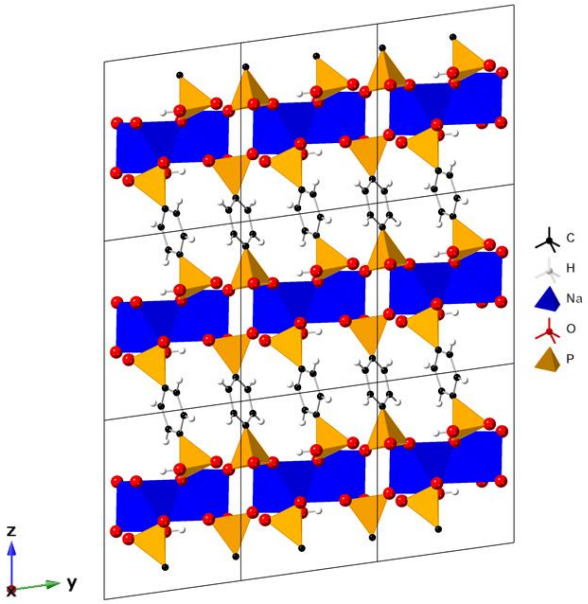

Figure 1.9) Crystal structure of Na(H_3bdp), H_3bdp is the singularly deprotonated form of 1,4-benzenediphosphonic acid. The location of one of the hydrogens could not be deduced by the authors.[35] *The unit cells are indicated by the black outline.*

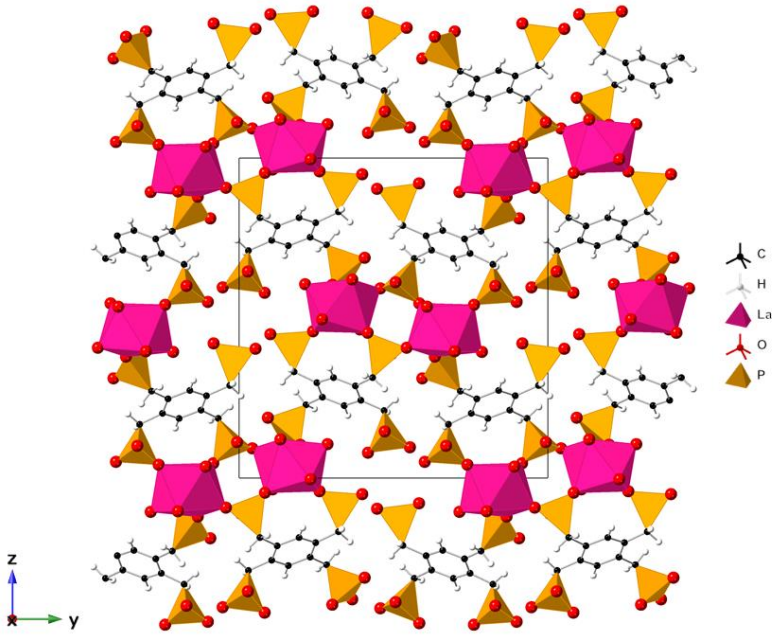

Figure 1.10) Crystal structure of PCMOF-5. Water located within the narrow channels has been omitted for clarity.[36]

Attention largely turned to introducing additional functionality to the linker or crystallising frameworks with a co-linker present, the hypothesis being that the additional functionality and coordinating groups would disrupt the formation of the preferred layered forms and instead possibly lead to the crystallisation of open frameworks.

The use of *N*,*N*′-piperazinebis(methylenephosphonic acid) as a linker led to significant developments in the field with the publication of STA-12 (STA = St. Andrews) and MIL-91 (MIL = Material Institute Lavoisier) in 2006.[37,38] STA-12 was synthesised as nickel(II) cobalt(II) and iron(II) forms. Whereas MIL-91 was synthesised as titanium(IV) and aluminium(III) forms, the metal ions are present as $[TiO]^{2+}$ and $[AlOH]^{2+}$. These materials represent the first large pore phosphonate-based frameworks published. STA-12 possesses pores with a diameter of approximately 10 Å which are filled with extra-framework water molecules. The cobalt and nickel forms have been shown to possess permanent porosity upon reversible removal of the water.[37] Likewise, both forms of the MIL-91 MOF can undergo reversible dehydration with the internal surface area of the materials becoming accessible. However, the pores of MIL-91 are significantly smaller with openings of 3.5 × 4 Å. The structure of MIL-19 is shown in Figure 1.11.[35]

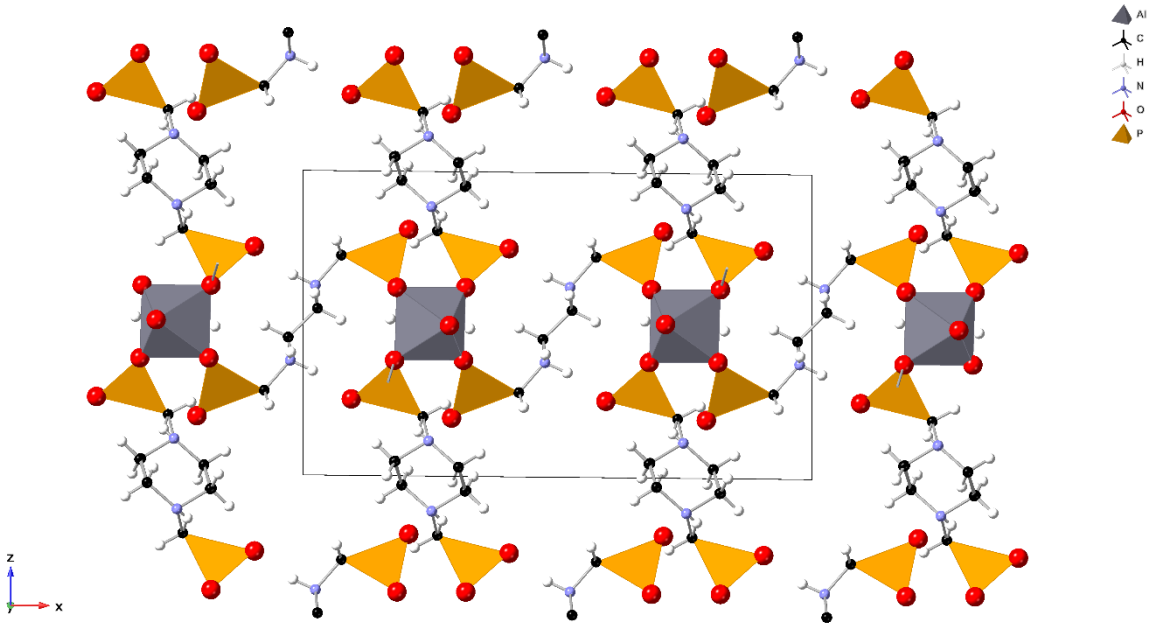

Figure 1.11) Crystal structure of MIL-91(Al). Water molecules have been omitted for clarity. Unit cell is indicated by the black outline.[38]

In 2011, a subsequent study showed that it was possible to further expand the pores of STA-12 by synthesising related materials in an isoreticular fashion.[39] Use of *N*,*N*′-4,4′-bipiperidinebis(methylenephosphonic acid) in place of the *N*,*N*′-piperazinebis(methylenephosphonic acid) used previously led to a new framework termed STA-16. A comparison of the two linker molecules is shown in Figure 1.12. STA-16 is structurally very closed related to STA-12, the most significant difference being the presence of an elongated linker. The channels which run through the structure have a diameter of approximately 18 Å, which are, as expected, much larger than those in STA-12.[39] The structures of both materials are shown in Figure 1.13.

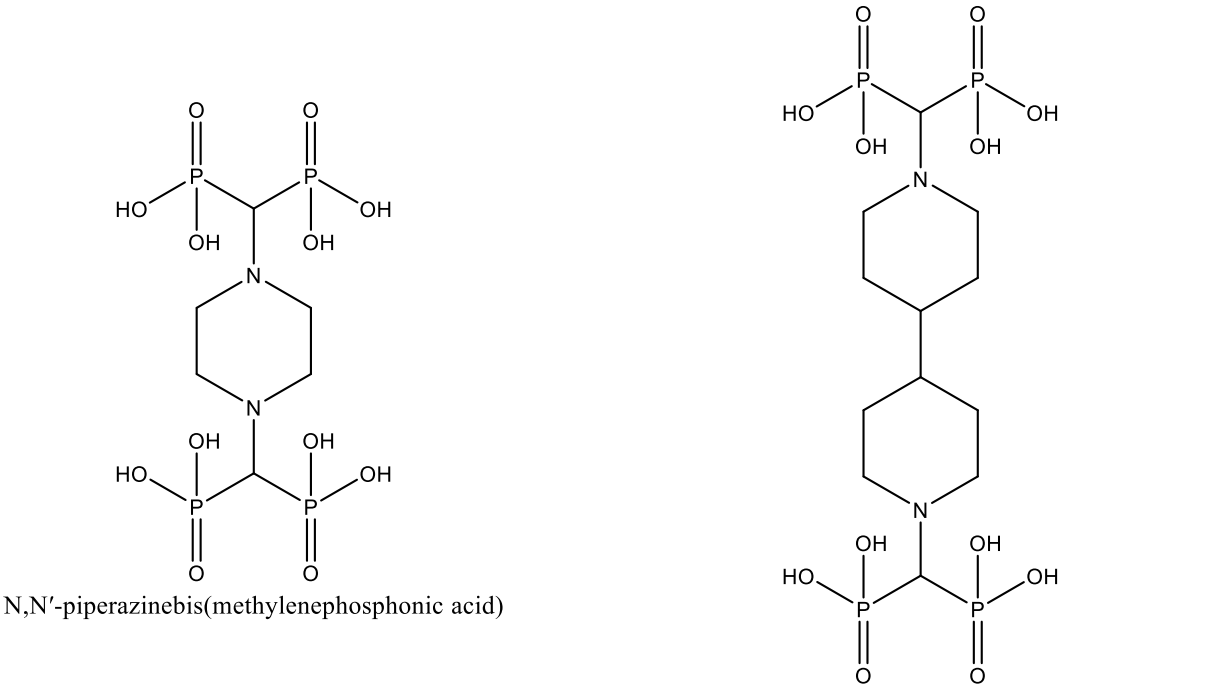

Figure 1.12) Comparison of the linker molecules used in STA-12 (left) and STA-16 (right)[39]

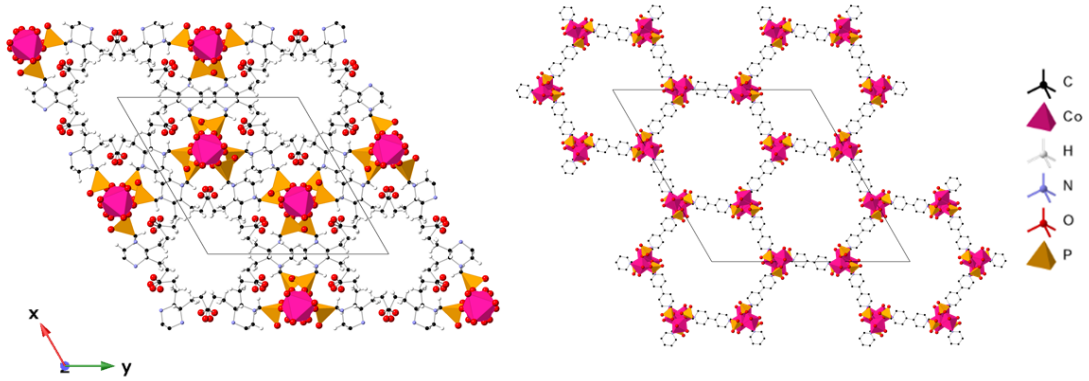

Figure 1.13) Crystal Structure of STA-12(Co) (left) and STA-16(Co) (right). Structures are not drawn to scale. Water molecules and structural disorder have been omitted for clarity. Hydrogen positions for STA-16 were not included in the crystallographic information. Unit cells are indicated by the black outlines.[37,39]

More recently, use of non-linear, tri- and tetra-topic phosphonate linkers has seen success in producing MOFs with permanent porosity.[40–42] A notable series of frameworks is the CAU (Christian-Albrechts-Universität) family of MOFs.[43,44] CAU-29 and CAU-30 are porphyrin-based tetratopic phosphonate MOFs. Significantly, CAU-30 is one of the most porous metal phosphonates published to date with specific surface areas of 910 or 970 $m^2 g^{-1}$ for the zirconium or hafnium form respectively.[44,45] In addition

to this, CAU-30 exhibits excellent stability with respect to both temperature and pH. The material is stable up to 420 °C in air and in a pH range of 0-12 in HCl/NaOH.[44] The crystal structure of CAU-30 is displayed in Figure 1.14.

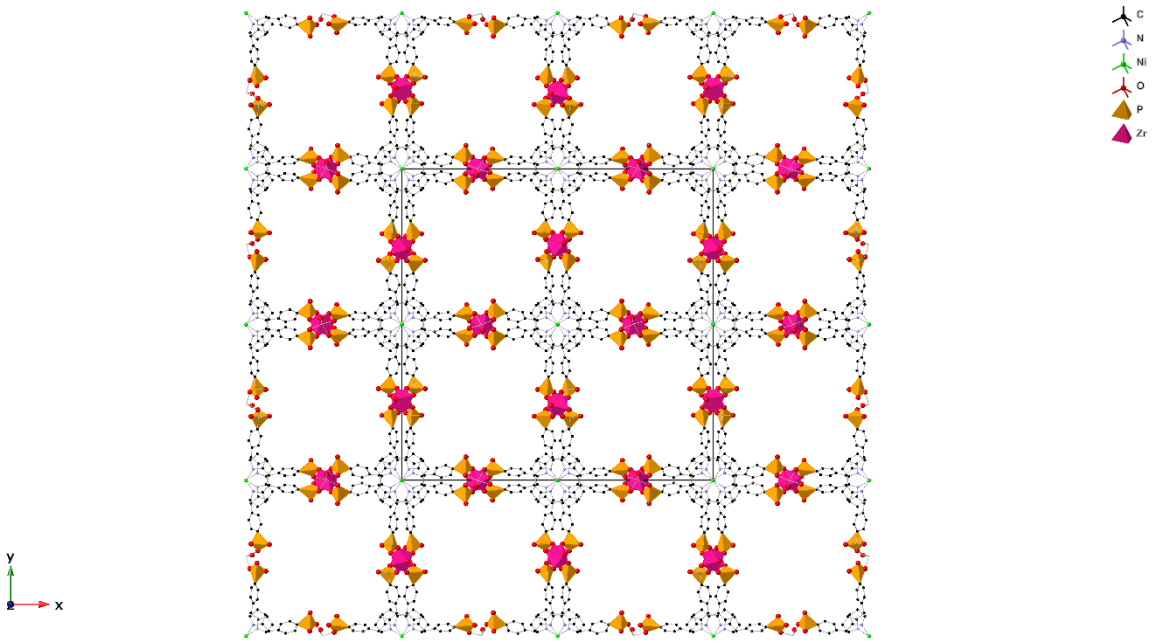

Figure 1.14) Crystal structure of CAU-30(Zr). Water molecules have been omitted for clarity. Hydrogen atoms were not included in the published structure. The unit cell is indicated by the black outline.[44]

1.1.1.3 Carboxyphosphonate

A different approach taken by some researchers was to use a bifunctional linker. Doing this may balance the benefits and drawbacks of each functional group, for example, the varied geometry and possibility for new structures of phosphonates whilst avoiding the tendency of producing layered materials.[12] As with much of the field, work on trying to produce open frameworks using carboxyphosphonates dates back to at least the mid 1990's.[46] Early attempts were largely focused on short carboxyalkylphosphonates, similar to the early work on disphosphonates discussed previously.[46–55] Carboxyethylphosphonate was a particularly popular choice of linker molecule.[46,47,50–53,55] The majority of the published materials, however, are either layered or dense pillared frameworks. Some success in producing open frameworks was found with three narrow-pore zinc-based frameworks being

published.[56–58] One of these frameworks is shown in Figure 1.15. Additionally, many years later, in 2019, BIRM-1 (BIRM = University of Birmingham) was published. BIRM-1 is a zinc carboxyethylphosphonate MOF which can undergo ion-exchange and reversible amorphization upon dehydration.[59] The material will be covered in greater depth in a later section.

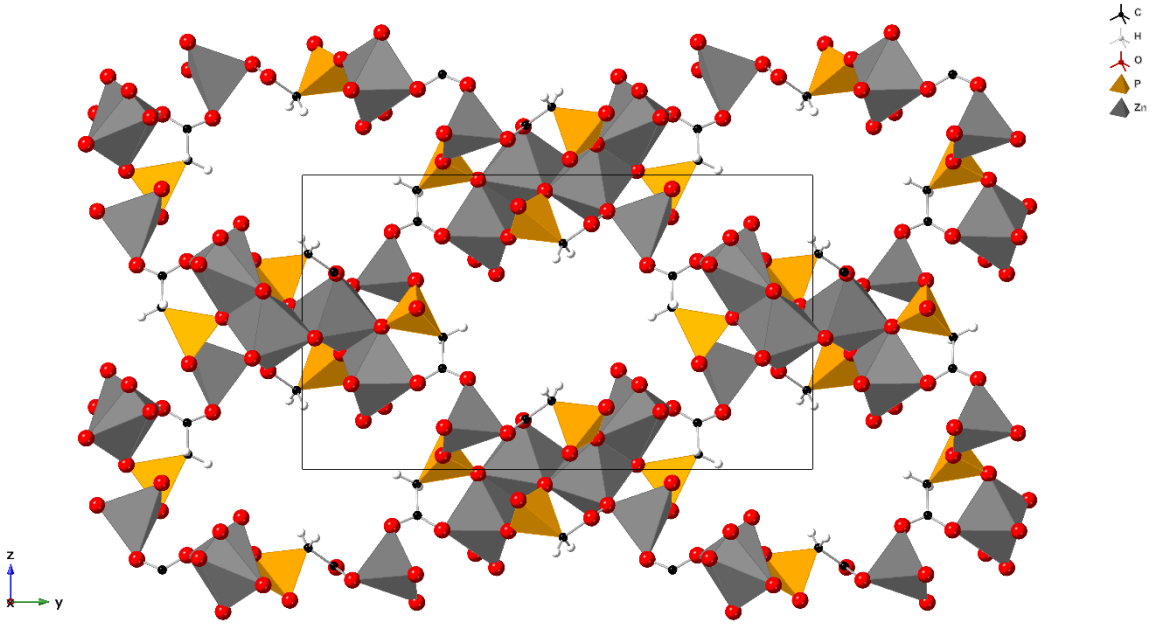

Figure 1.15) Crystal structure of a porous zinc carboxyethylphosphonate synthesised by Hix et al.[56] *Water molecules are removed for clarity. The unit cell is indicated by the black outline.*

Strategies for producing porous carboxyphosphonate MOFs developed much like those utilising purely phosphonates linkers. Introduction of additional functionality on the linker proved to be successful in the work of Colodrero et al. who published a large range of lanthanide MOFs using 2-hydroxyphosphonoacetate as the linker.[60] Aryl carboxyphosphonates also became a popular choice leading to a significant number of framework materials. Mixed success was had using these linkers and many of the resulting structures were dense layered or pillared structures.[50,61–65] However, amongst these denser structures, some open frameworks were produced as well.[63,66] While this was done without necessarily having to resort to large non-linear and tritopic or tetratopic linkers, as was needed for the breakthrough in phosphonate frameworks, such structures have been published in recent years.[67–70]

From the work on aryl carboxyphosphonates, several frameworks based on the 4-phosphonobenzoic acid linker have been published.[63–66,71] Chen et al. published 6 frameworks, of which 3 are zeolitic open frameworks, synthesised under mixed-solvothermal conditions with the use of amine based templating agents. The other 3 frameworks are pillared–layered type structures. There is no adsorption data published alongside the structures.[63] Most of the structures retain the templating agents either in the pores or actually coordinated to metals within the framework. TGA data is included in the publication that indicates the templating agents are not removed until collapse of the framework occurs. This means that for those structures activating the frameworks to make use of their internal surface area is likely to be impossible.[63] One of the reported frameworks from Chen et al. with a zeolitic topology is shown in Figure 1.16. Despite a high calculated pore volume ratio of 46.1%, the presence of the templating agent likely means most of the internal volume will not be accessible upon dehydration. TGA does show a loss of 2.57% below 150 °C, suggesting some water is removed and some internal volume may be accessible. However, no adsorption data or post-dehydration x-ray diffraction are provided.[63]

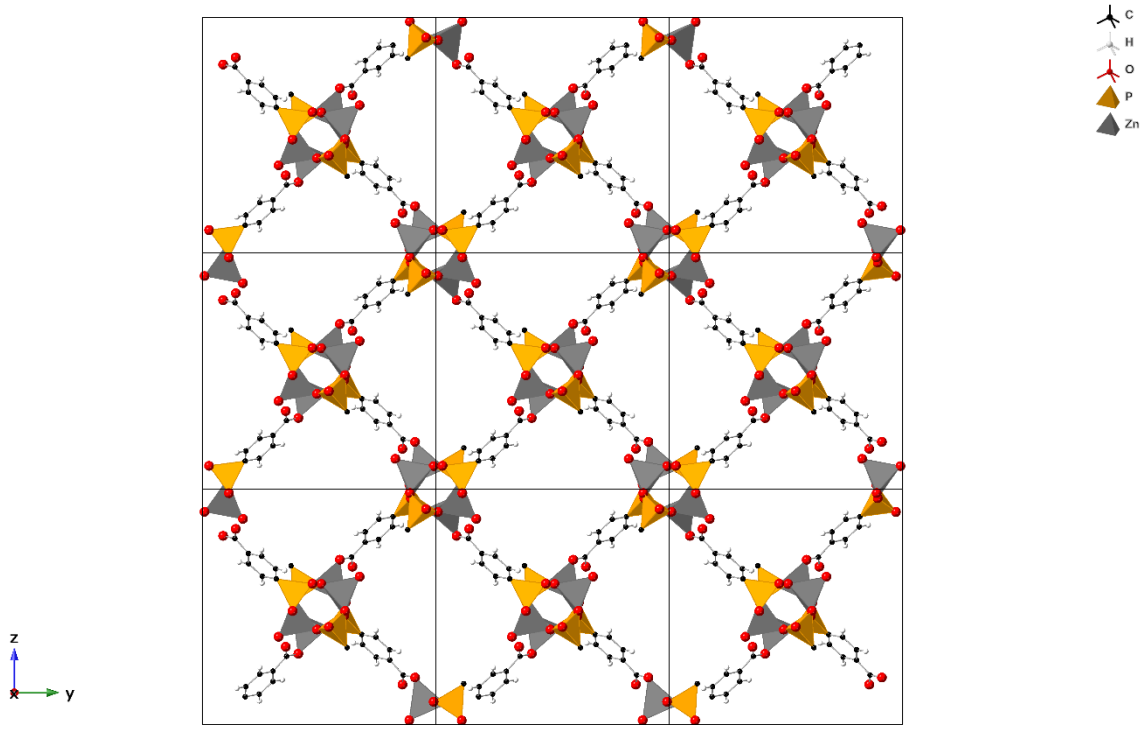

Figure 1.16) Crystal structure of a carboxyphosphonate MOF from the work of Chen et al.[63] Water and templating agents have been omitted for clarity. Unit cells are indicated by the black outline.

It seems there is still research to do on MOFs based on the simple 4-phosphonobenzoic acid linker as the framework materials published thus far are either dense materials or do not seem to have significant accessible internal surface area.

Overall, the area of carboxyphosphonate frameworks remains relatively unexplored. Especially compared to phosphonate and, even more so, carboxylate frameworks. Progress appears to have slowed in recent years with relatively few new structures having been published since 2015.[59,72–76] This is despite the potential for novel structures arising from the many coordinating modes that phosphonate groups can take and the ability for the carboxylate group to control for some of the drawbacks of using phosphonates.[11]

1.1.1.4 Imidazolate

Though not directly relevant to the work set out in this thesis, it would be appropriate to mention the third common type of coordinating group used in MOF synthesis. Imidazolate and related derivatives are commonly used to form a subclass of MOF known as a zeolitic imidazolate framework (ZIF). The zeolitic term comes from the fact that they share zeolite topologies. They owe their zeolitic structures to the equivalence of the Si-O-Si bond angle to that of the metal-imidazolate-metal bond angle at 145°. ZIFs are noted for their high porosity as well as excellent chemical and thermal stability. They are subject to a significant amount of research interest. One of the most highly studied ZIFs is ZIF-8 which adopts a sodalite structure and is shown in Figure 1.17.[77]

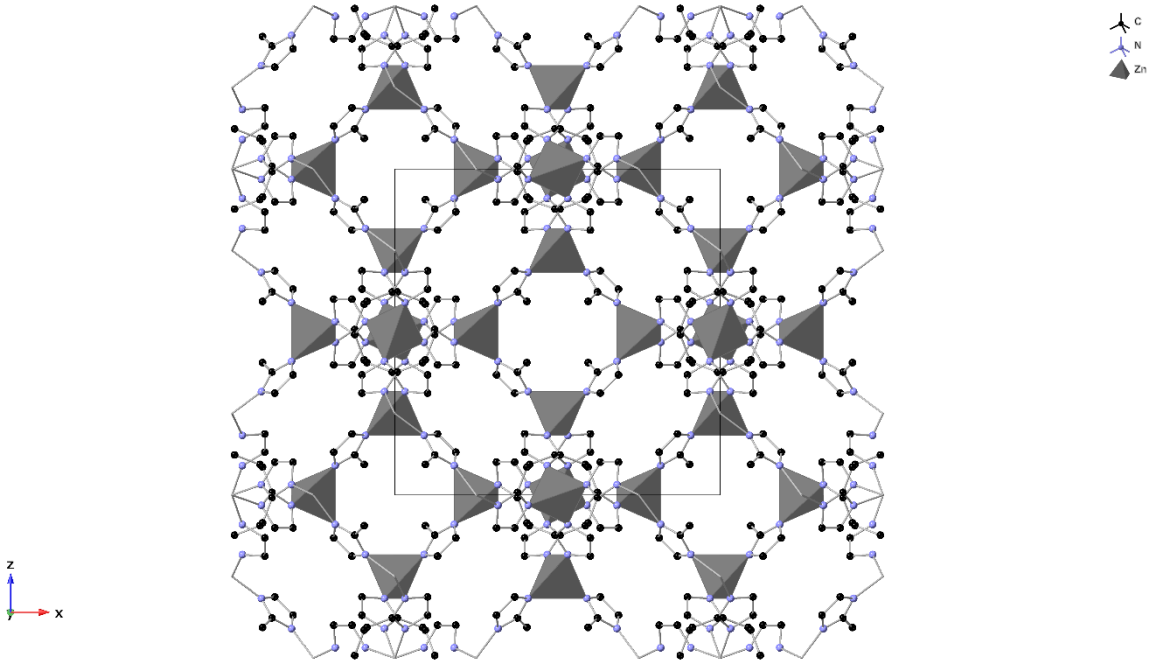

Figure 1.17) Crystal structure of ZIF-8. Solvent molecules and hydrogen atoms omitted for clarity.[77]

1.1.2 Synthesis

Most MOFs in recent years are synthesised via solvothermal methods whereby the reagents in solvent are sealed in a vessel and heated above the boiling point of the solvent in order to generate autogenous pressure.[78] However, much of the early work such as that by Hoskins and Robson employed much milder conditions as the target structures were much simpler.[5,6] Typically these early materials used techniques such as evaporative crystallisation or diffusion crystallisation techniques. These techniques were often successful at obtaining large single crystals for structure solution from diffraction.[78] Some more modern and complex MOF materials have had room-temperature synthesis methods developed for them.[79–81] Often this results in nanocrystals being obtained, so a high-temperature route that develops large crystals for single crystal diffraction would be needed in most cases for structure solution. Nanocrystals can be beneficial for many applications, for example smaller crystals would limit the effect of gas diffusion kinetics for adsorption.[3] Additionally, chemical and thermal stability of at least some of the materials synthesised in this way remains good.[78,81] Despite this, MOF synthesis remains a complex matter and multiple studies have shown that, in many cases, precise control of variables such as temperature or time is critical to obtaining the desired phases.[82,83]

Alternative synthetic procedures of MOFs do exist, and can be used in order to obtain new frameworks which are not otherwise accessible.[78] One example is heating synthesis solutions using microwaves. Use of microwaves for heating can lead to energy efficiency, rapid heating rates and homogenous thermal conditions throughout the synthesis solution. Microwave synthesis also tends to provide nanocrystalline products.[78] A significant drawback is that these syntheses are not always easy to replicate on different microwave synthesis instruments by different manufacturers.[78,84]

A number of MOFs have also been synthesised using mechanochemistry routes.[78,85] The main motivation for MOF synthesis by mechanochemistry is environmental friendliness. Little or no solvent is required, and reactions are carried out at room temperature meaning little energy input. Additionally, by the nature of this synthesis technique small particles are obtained which, as mentioned previously, can be beneficial for certain applications.[78,85]

Other, less commonly used, synthesis techniques include sonochemical and electrochemical synthesis. In the case of sonochemical synthesis the aim is usually to achieve high yield in short reaction times. Electrochemical synthesis was developed from a requirement to eliminate counter ions contained within metal salts such as nitrates as these can be particularly hazardous when used on an industrial scale.[78]

1.1.3 Applications

MOFs are of interest for a wide range of applications, owing to their designability, stability, potential porosity, tunability and more. Some of the applications that are of most interest to MOF researchers are covered briefly here.

1.1.3.1 Gas Storage and Separation

The ability to either store or purify useful gases for fuel sources and be able to separate out harmful gases from waste streams is very important for the development of a green economy. MOFs, with their potential for ultrahigh porosity and the possibility of producing structures with pore apertures of well-defined shape and size, are ideal candidates for gas storage and separation applications. This has been a highly active area of research since the first publications on methane storage within a MOF in 2000[86]

and hydrogen storage in 2003.[2] Most early work in this area focused on increasing the porosity of frameworks in order to improve gravimetric capacity at low temperature and high pressure. This is exemplified by the ultrahigh porosity frameworks NU-100 and MOF-210.[87,88] Whilst increasing pore volume and surface area increased gravimetric capacity, it did not help much to increase volumetric capacity. To achieve this, increases to adsorption enthalpy of hydrogen are necessary. One route is to introduce open metal sites to the framework.[3] Introduction of alkali metal cations into MOFs failed to achieve significant improvement in adsorption enthalpy or hydrogen uptake.[87,88] However, introduction of transition metal open sites has improved volumetric capacity and adsorption enthalpy, Including record high hydrogen capacity in the MOF Ni_2(m-dobdc) (m-dobdc = 4,6-dioxido-1,3-benzenedicarboxylate).[89–91] This framework was shown to have a usable volumetric capacity of 11 g dm^{-3} at 25 °C when cycled between 5 and 100 bar and 23 g dm^{-3} when a temperature swing of -75 to 25 °C is used.[91] The crystal structure of the isostructural cobalt form is shown in Figure 1.18 with hydrogen adsorption sites as determined by in-situ neutron scattering shown.

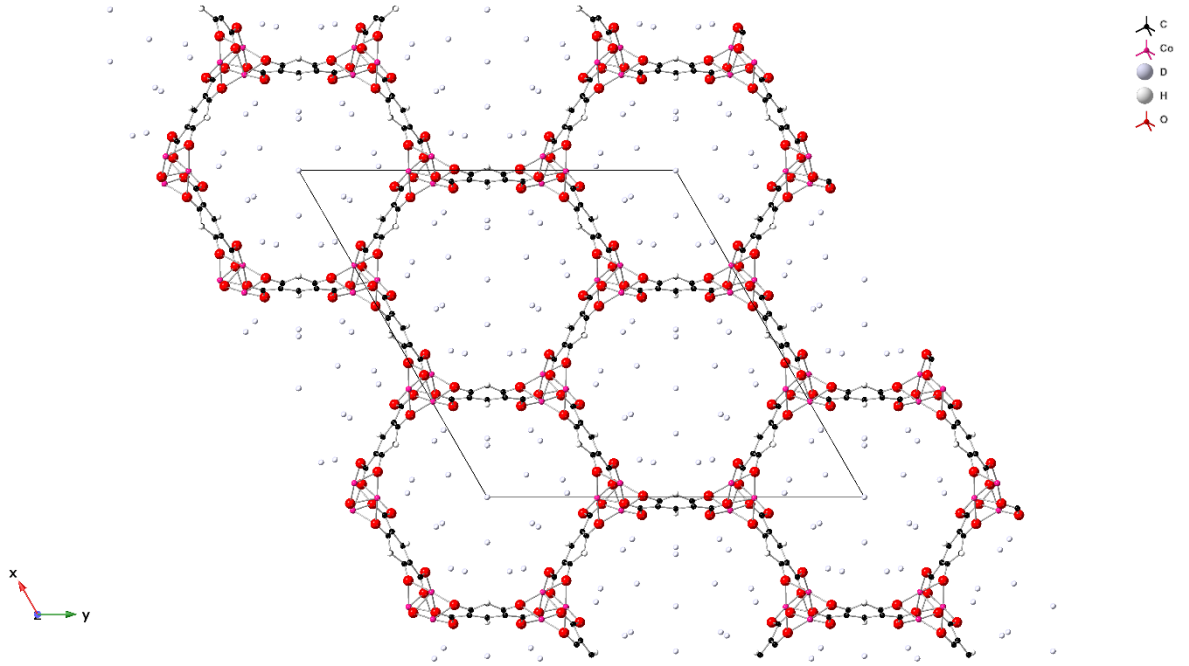

Figure 1.18) Crystal structure of Co_2(Co-dobdc) within hydrogen adsorption sites shown by deuterium atoms (D).[91]

Hydrogen storage within MOFs has in fact progressed to the point where car manufacturer Mercedes-Benz has previously produced a prototype model of a hydrogen powered car which uses MOF hydrogen storage technology.[92]

MOFs are also studied for storage of other fuels such as methane.[3] The first MOF material studied for methane storage was $[CuSiF_6(4,4'\text{-bipyridine})_2]_n$. The material was shown to be capable of methane uptake of 104 mg g^{-1} at a very high 36 atm of pressure at 298 K.[86] Similar to hydrogen storage, studies have generally found that gravimetric capacity increases with pore volume. As such, an optimal strategy may again be the incorporation of unsaturated metal cations.[3] Recent work by Chen et al. found impressive volumetric and gravimetric capacities in the MOF MFU-4l-Li, shown in Figure 1.19. The structure is functionalised with lithium cations which possess an open site upon activation.[93] This material has a usable gravimetric capacity of 0.38 g g^{-1} and volumetric capacity of 251 cm^3 cm^{-3} under a temperature/pressure swing from 77 K and 100 bar to 160 K and 5 bar.[93]

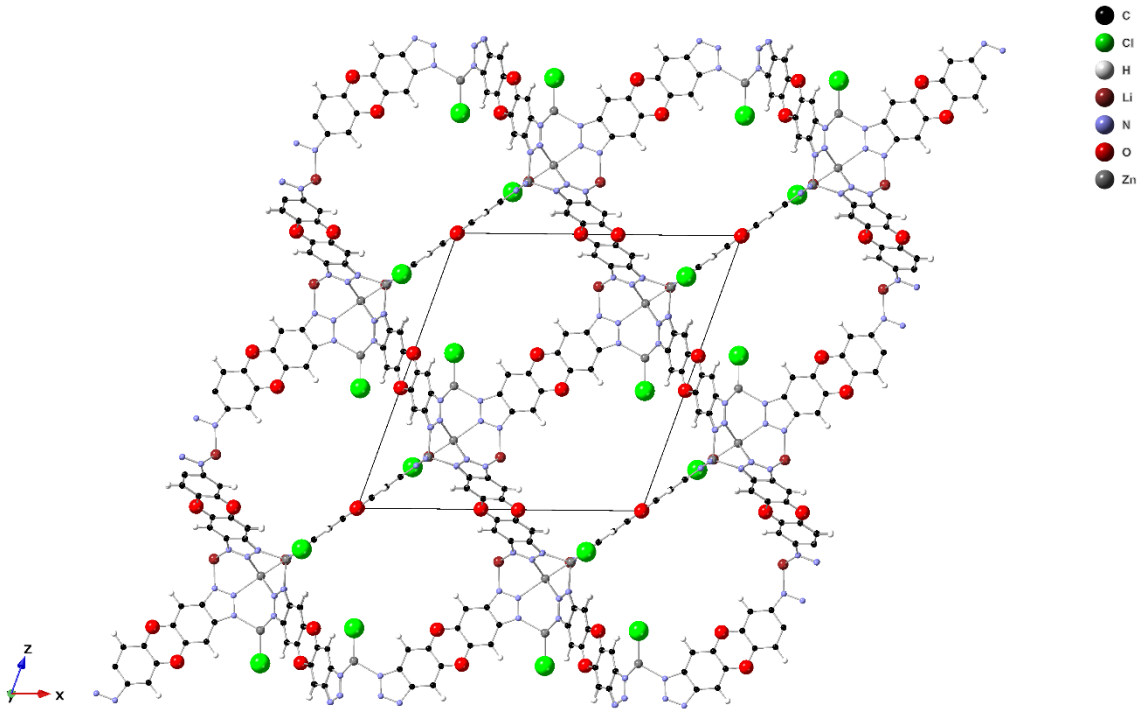

Figure 1.19) Crystal structure of MFU-4l-Li. Unit cell is indicated by the black outline.[93]

Another important factor for methane storage is that of selectively. Some sources of methane, such as coal bed methane only possesses a 30% concentration of the gas. As such, the ability to easily separate and store the gas with as little energy input as possible is important. Wang et al. found that the nickel MOF $Ni(ina)_2$ (ina = isonicotinic acid) can adsorb methane from nitrogen/methane mixes with 99% selectivity. As well as having a uptake capacity of 40.8 $cm^3\ g^{-1}$ under ambient conditions.[94] Efforts to commercialise MOFs for methane storage have been taken by BASF.[95]

Ammonia is another gas of interest for storage applications of MOFs. Interest in ammonia storage stems both from removal of the toxic gas sources such as waste stream and as a source of hydrogen fuel. As ammonia is highly basic and reactive, framework materials need to have very good chemical stability in order to successfully adsorb the gas. The current best gravimetric capacity for ammonia adsorption in a MOF was achieved using Cu_2Cl_2BBTA (BBTA = 1H,5H-benzo(1,2-d),(4,5-d′)bistriazole).[3,96] With this material an ammonia uptake of 19.79 mmol g^{-1} at 1 bar and 298 K was obtained.[96] Research by Godfrey et al. on MFM-300(Al) achieved a gravimetric capacity for ammonia of 15.7 mmol g^{-1} but importantly found a packing density of 0.7 g cm^{-3} which is higher than liquid ammonia at 240 K (0.681 g cm^{-3}).[97] This could lead to a significant decrease in the energy input required for storage and transportation of ammonia.

1.1.3.2 Proton Conductivity

MOFs, especially those with phosphonate coordination groups, are commonly studied for proton conductivity behaviour. Phosphonates are particularly well suited for this application as if a MOF can be formed where only one of the acidic protons are removed in the synthesis process, then the result is a framework with acidic protons already present.[98] Other routes to achieve proton conductivity in MOFs can include functionalisation of the linker with acidic groups that furnish the interior of pores or the inclusion of acidic cations such as ammonium within the structure.[3,98] Proton conductivity is an important property necessary for materials used in fuel cells which will become more important as the transition to a green economy progresses. Well defined conduction pathways in the form of channels

and pores within MOFs, as well as their designability and tunability, make them attractive materials for this application.

The first MOF studied for proton conductivity was *N*,*N*'-bis-(2-hydroxyethyl)dithiooxamidatocopper(II) ($Cu[HOC_2H_4\text{-}DTOA]_2$) in 2002. Although the reported conductivity was low (2.2×10^{-6} S cm^{-1}) it showed that MOFs could be used for proton conductivity but more work had to be done on identifying how to improve the materials for this application.[99] To this end, later work focused on the introduction of acidic groups to the MOF structure, such as the functionalisation of MIL-53 by Shigematsu et al.[100] Their work looked at functionalising the 1,4-benzenedicarboxylic acid linkers with various proton containing groups and found the addition of further carboxylic acid groups to give the largest improvement.[100] Although this work established that proton conductivity could be increased by the introduction of acidic groups, the materials reported in the study still only show low conductivity values with the highest achieved conductivity being 7×10^{-6} S cm^{-1}. However, using the same principles, PCMOF-5 was developed exhibiting much higher proton conductivity of 4×10^{-3} S cm^{-1}.[36] PCMOF-5 has already been discussed in this literature review when discussing the development of phosphonate MOFs. The structure is shown in Figure 1.10 and is based on a tetrakis phosphonate linker with one of the phosphonate groups remaining uncoordinated and providing an acidic environment within the pores.[36]

As mentioned, another way to introduce an acidic environment for proton conduction is the incorporation of acidic cations within the pores of a material. One common way of doing this is the inclusion of ammonium cations. One such material, $(NH_4)_2(adp)[Zn_2(ox)_3]\cdot nH_2O$ (adp = adipic acid, ox = oxalate), was synthesised and characterised by Sadakiyo et al.[101] The structure is shown in Figure 1.20. The authors report a proton conductivity value of 8×10^{-3} S cm^{-1} which is approaching that of the industry standard of Nafion.[101,102] There are now a number of MOF materials that exhibit conductivities in this range and research continues with attempts to reach higher conductivies.[3,98]

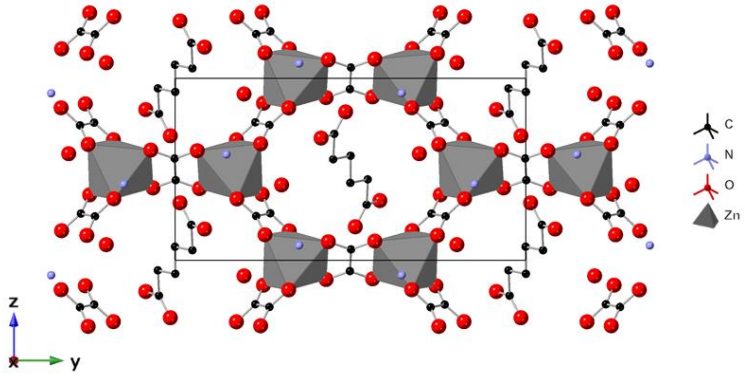

Figure 1.20) Crystal structure of $(NH_4)_2(adp)[Zn_2(ox)_3]\cdot nH_2O$. Unit cell is indicated by the black outline. Hydrogen positions were not included in the published structure.[101]

1.1.3.3 Other Applications

The list of potential applications of MOF materials is extensive and it would not be particularly beneficial to cover all of them in depth here. However, other applications for which MOFs are studied include waste remediation,[103–105] water harvesting,[106] sensing,[107–109] catalysis[110–112] and even batteries.[113,114]

1.2 BIRM-1

BIRM-1 is a zinc-based carboxyethylphosphonate MOF first synthesised at the University of Birmingham by Chao Zhao.[59,115] It will be the focus of the first two results chapters of this thesis. The material is made by a one pot hydrothermal method using zinc nitrate, 3-phosphonopropionic acid, urea and tetraethylammonium bromide. The role of tetraethylammonium bromide is believed to be that of either a templating agent, mineraliser, or both. Meanwhile, urea acts as a pH modulator, breaking down in-situ to ammonium carbonate to deprotonate the linker slowly and lead to slow crystal growth. The reaction occurs at 87 °C over 24 hours. With the synthesis temperature at 87 °C it is not a 'true' hydrothermal synthesis as it is conducted below the boiling point of water. The original preparation was actually conducted under reflux conditions however it was later found that temperature control was much easier with a hydrothermal bomb heated within an oven.[115]

1.2.1 Structure

The structure of BIRM-1 (Figure 1.21) consists of CPO_3 and ZnO_4 tetrahedra forming double chains which extend along the z-axis forming a helix. These double chains wrap around small pores of approximately 4 Å diameter, the pores are not fully enclosed as can be seen more clearly in Figure 1.22 and Figure 1.23. The double chains are linked together by the carboxyethylphosphonate linker which is fully deprotonated. This leaves a larger pore of approximately 7.6 Å diameter between the 4 helical double chains. The phosphonate group forms the CPO_3 tetrahedra which in turn forms the double chains by corner sharing coordination with three ZnO_4 tetrahedra. The carboxylate group has one oxygen coordinated to a ZnO_4 tetrahedra whilst the other oxygen lines the interior of the larger pore, likely coordinating to any cations present within. Structural formula and basic crystallographic details of BIRM-1 are given in Table 1.1.

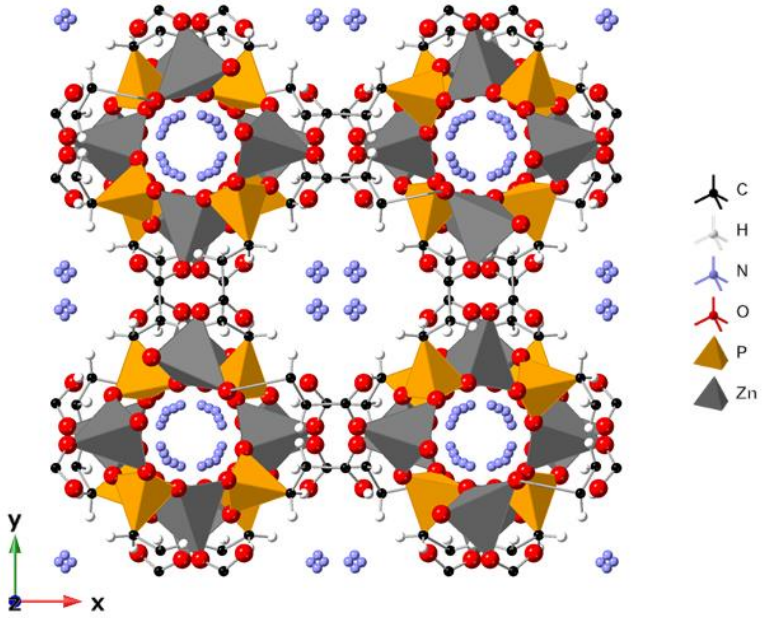

Figure 1.21) Crystal structure of BIRM-1 looking along the z-axis. Oxygen atoms from solvent water have been removed for clarity. Nitrogen atoms are from extra-framework ammonium cations. Location of hydrogen atoms from ammonium cations could not be determined in Zhao's work[59]

Table 1.1) Basic structural and crystallographic details of BIRM-1[59]

Formula	$(NH_4)_2[Zn_2(O_3P(CH_2)_2COO)_2]\cdot 5H_2O$
Space group	$I4_1/acd$
a (Å)	22.3019(2)
c (Å)	17.7384(1)
Volume (Å^3)	8822.6(11)

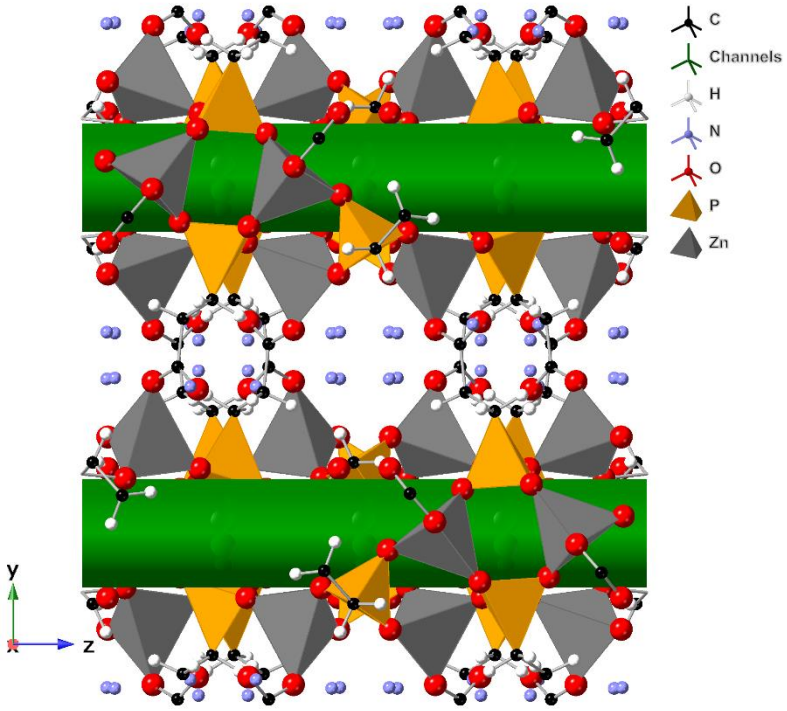

Figure 1.22) Crystal structure of BIRM-1 along the x-axis with the small channels within the double chains indicated by green rods.

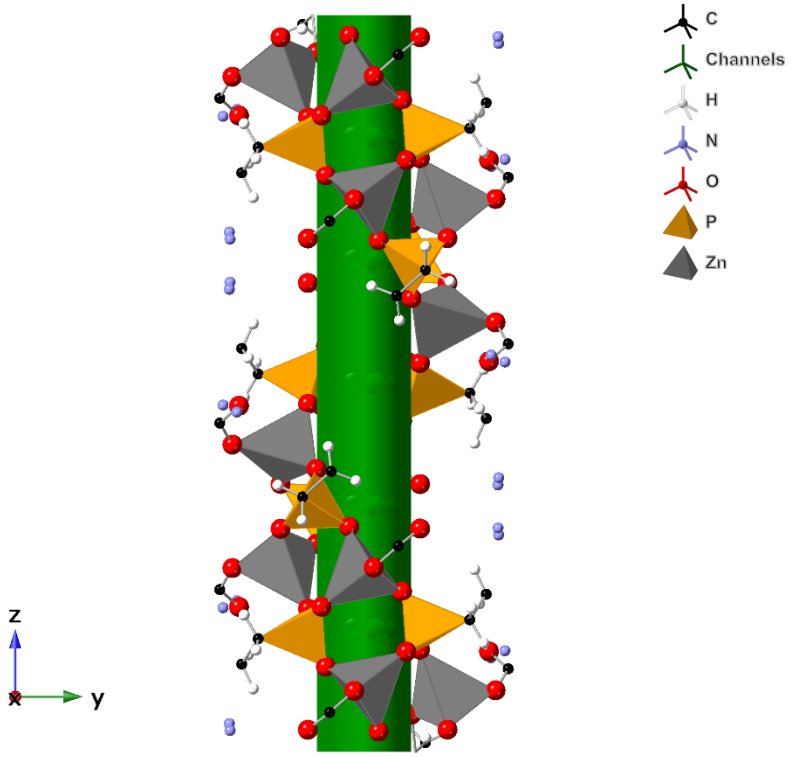

Figure 1.23) The structure of the helix of double chains as viewed along the x-axis.

The choice of a bifunctional linker stems from arguments discussed in section 1.1.1.3. The use of a phosphonate coordinating group can lead to a greater variety of new and interesting structural motifs whilst combining it with a carboxylate group can help alleviate some of the difficulties involved in making phosphonate materials, namely their propensity towards dense layered structures and fast nucleation.[12]

1.2.2 Properties

Zhao worked on studying the properties of BIRM-1 with a focus on ion-exchange behaviour as well as some work on assessing the material's porosity and dehydration behaviour.[59] Zhao found that the as-synthesised ammonium form BIRM-1 was able to undergo ion-exchange with a range of cations including alkali, alkaline earth and even some transition metals.[59,115] Some of these ion-exchanged variants are isostructural to BIRM-1 with a proportion of ammonium cations exchanged for the new cations. One example of this is the potassium exchanged form of BIRM-1 (K^+-BIRM-1), shown in Figure 1.24, which exchanges to roughly 80%.[59] For some other variants, peak splitting is observed

suggesting a change in symmetry in the crystal structure which has been confirmed by indexing of powder diffraction patterns.[115]

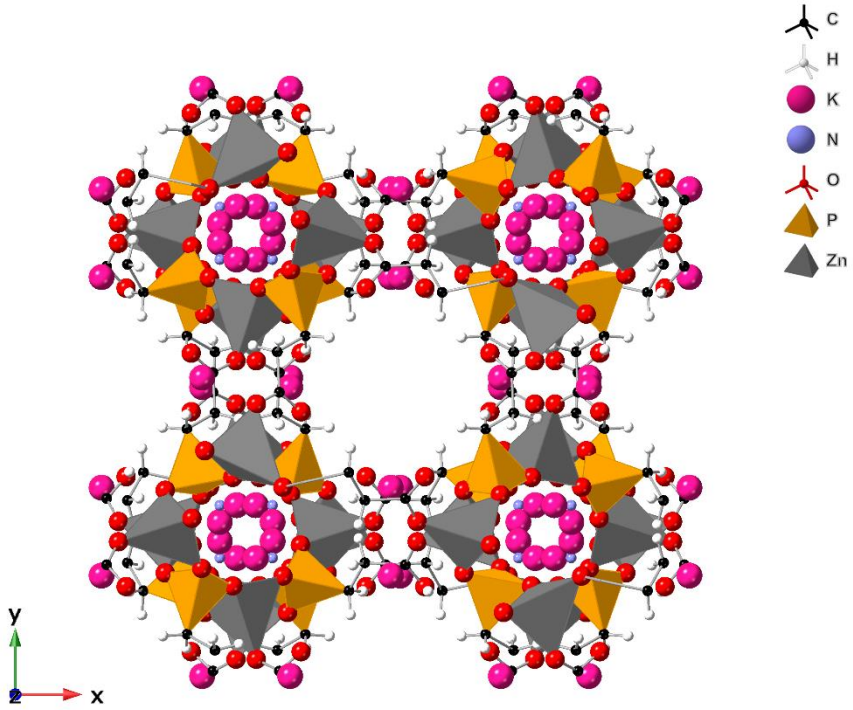

Figure 1.24) Crystal structure of K^+-BIRM-1 looking along the z-axis. Oxygen atoms from solvent water have been removed for clarity. Location of hydrogen atoms from residual ammonium cations could not be determined in Zhao's work[59]

The ability to undergo ion-exchange is a significant feature of BIRM-1. Only a small subset of all MOFs can successfully undergo ion-exchange of extra framework ions, this proportion is reduce further when considering cation exchange.[116] Ion-exchange opens up both new possible applications as well as the possibility of enhancing the properties of BIRM-1 for other applications. For example, Williams studied the possibility of exchanging caesium and strontium into BIRM-1 and heating the material up to form dense stable phosphate phases.[117] Caesium and strontium are waste products of nuclear fission, so there could be a potential application in nuclear waste remediation. The exchange of transition metals could provide open metal sites on which gases could be more strongly adsorbed or they could even act as catalytic sites.

Zhao made multiple attempts at hydrogen uptake experiments but found that the capacity of BIRM-1 is negligible. Upon investigation it was found that the material turns amorphous after dehydration and it is

likely that the structural changes involved include collapse of the pores within. Various attempts at dehydration using different combinations of temperature, vacuum and solvent exchange were unsuccessful. It was, however, discovered that BIRM-1 is able to undergo solvent exchange with a range of solvents whilst the framework remains intact. Additionally, BIRM-1 shows reversible dehydration behaviour. After dehydration, if the material is left in humid air the crystallinity returns suggesting that the framework is not breaking down but just deforming in a non-uniform way that removes crystallinity and porosity.[59]

1.2.3 Existing Issues

This lack of porosity on dehydration is not ideal as many of the applications of MOFs stem from the use of the internal surface area the pores and channels can provide. Therefore, a MOF without permanent porosity is likely to have a relatively limited range of potential applications. Additionally, work by Zhao and later by several others found the synthesis of BIRM-1 to be particularly temperature sensitive.[117–119] The sensitivity of the synthesis can lead to difficulties in producing sufficient quantities of the material reliably. This can make study of the material's properties and of the exchanged variants structures more time consuming and expensive. In addition, any attempt at scaling up the synthesis of the material would likely meet significant issues due to this sensitivity.

1.2.3.1 Competing Phases

The temperature sensitivity in the synthesis of BIRM-1 comes from 3 related competing phases. One of which is a layered phase, shown in Figure 1.25, where the carboxylic acid group of the linker is not deprotonated. The structural formula and basic crystallographic details are given in Table 1.2. This phase typically forms at lower temperatures.[115] The layers are formed of CPO_3 tetrahedra and ZnO_6 octahedra. The layers are held together *via* hydrogen bonding between carboxylic acid groups. The organic linkers or disordered over two locations. Each zinc is edge sharing with one and corner sharing with three CPO_3 tetrahedra. The remaining coordinating oxygen is from a water molecule. The layers do not have any pores or channels in them through which a molecule could enter. This layered phase has been termed

'BIRM-2' by our research group. An isostructural form of this material with Mn(II) in place of Zn(II) is known.[120]

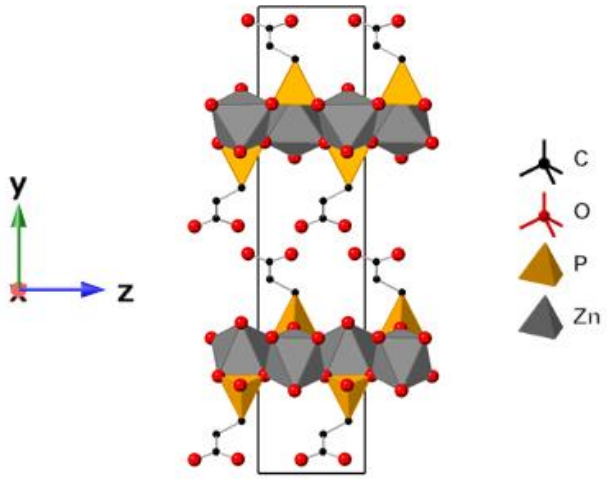

Figure 1.25) Crystal structure of the layered phase, BIRM-2. Hydrogen atoms omitted. Disorder in the organic linker has been removed for clarity. The unit cell is indicated by the black outline.[115]

Table 1.2) Basic structural and crystallographic details of BIRM-2[115]

Formula	$Zn(O_3P(CH_2)_2COOH)\cdot H_2O$
Space group	$Pbn2_1$
a (Å)	4.8021(6)
b (Å)	24.6753(27)
c (Å)	5.6528(6)
Volume ($Å^3$)	669.82(13)

When the synthesis solution is heated for prolonged periods of time or at elevated temperatures, there are two phases which may form. The first of which is a pillared–layered structure which has been termed 'BIRM-3', the structure of which is shown in Figure 1.26. It consists of two-dimensional layers of corner sharing ZnO_4 and CPO_3 tetrahedra which are joined by the linker molecule which is coordinated at both ends. There are small channels which run through the 2-dimensional layers and contain ammonium cations. The channel structure within the 2-dimensional layer is similar to that of the zeolite gismondite which has known phosphonate analogues.[63,121] The structural formula and basic crystallographic details for BIRM-3 are given in Table 1.3

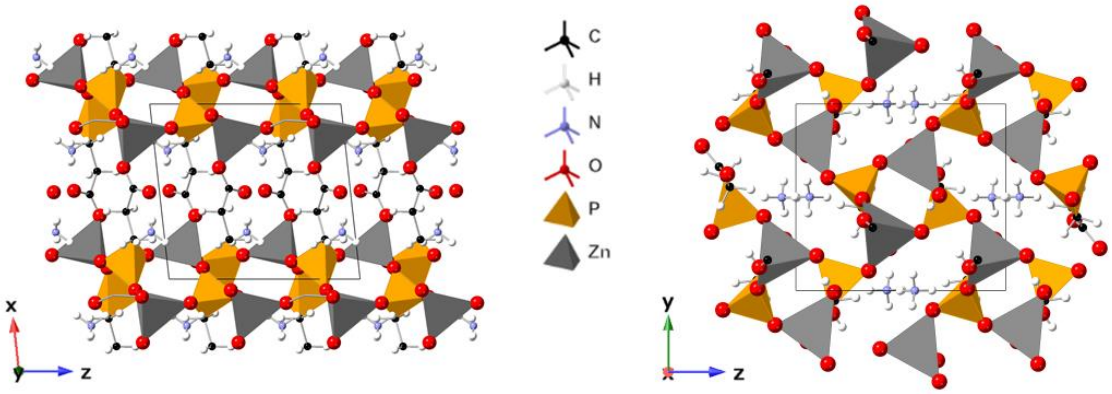

Figure 1.26) Crystal structure of the pillared–layered phase BIRM-3. Unit cells are indicated by the black outline.[115]

Table 1.3) Basic structural and crystallographic details of BIRM-3

Formula	$(NH_4)[Zn_2(O_3P(CH_2)_2COO)]$
Space group	$P2_1/c$
a (Å)	8.9458(1)
b (Å)	8.5427(1)
c (Å)	9.7352(1)
β (°)	96.3234(5)
Volume (Å^3)	739.45(2)

The other phase which can form at elevated temperature or after prolonged heating times is termed BIRM-4 and shown in Figure 1.27, with structural formula and basic crystallographic details in Table 1.4. This phase consists of ZnO_4 and CPO_3 tetrahedra forming double chains which run along the x-axis. Though these chains do not form helices as in BIRM-1. The double chains are connected *via* the organic linker which is coordinated at both ends. Collapsed pores containing ammonium ions are present between the double chains.

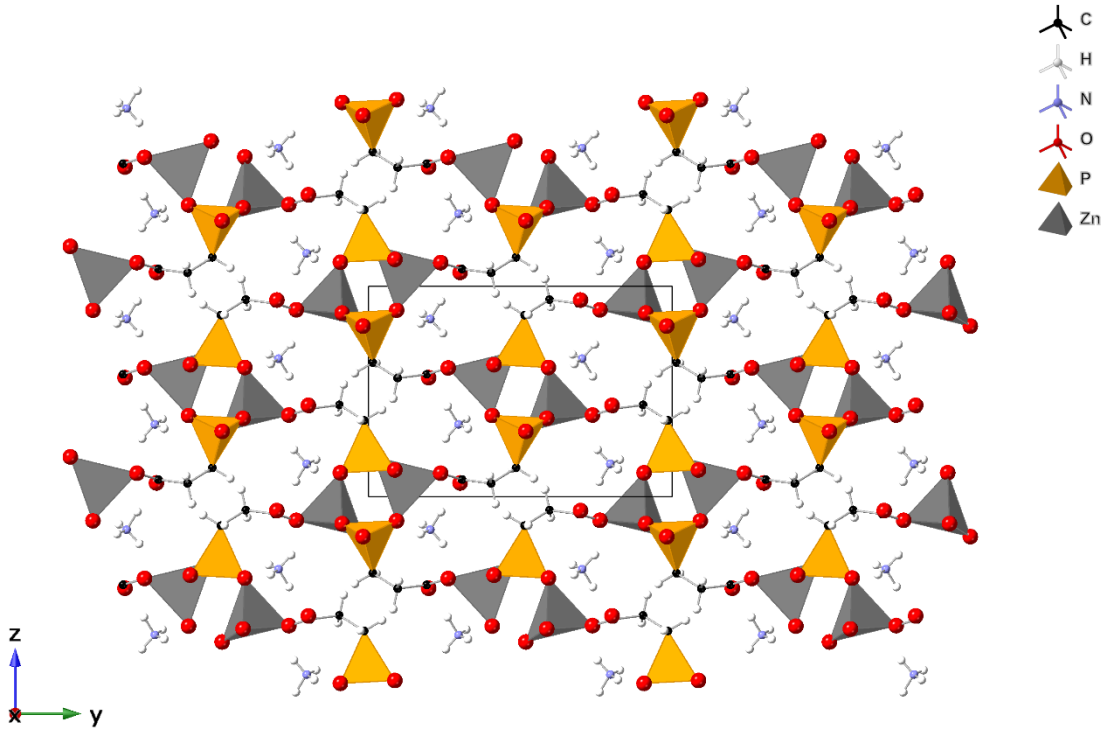

Figure 1.27) Crystal structure of the pillared–layered phase BIRM-4. Unit cell is indicated by the black outline.[115]

Table 1.4) Basic structural and crystallographic details of BIRM-4

Formula	$(NH_4)[Zn_2(O_3P(CH_2)_2COO)]$
Space group	$P2_1/c$
a (Å)	5.1807(2)
b (Å)	14.0010(7)
c (Å)	9.6965(4)
β (°)	91.13(3)
Volume (Å^3)	703.2(7)

Zhao hypothesised a synthesis-phase relationship between the four competing phases. In this phase sequence he places the layered phase first, followed by BIRM-1 and then the two denser phases.[115] No attempt was made in his work to rationalise the reasons for each phase forming but a suggestion was made that it was a complicated relationship between synthesis temperature, time and pH among other more difficult to control variables.[115] Later work expanded on this by producing the four different phases at a range of synthesis temperatures between 75 and 90 °C with all 4 of the competing phases being

observed between 80 and 90 °C.[118] It was concluded that the sensitivity is likely due, at least in part, to the in-situ breakdown of urea to ammonium carbonate which then deprotonates the linker. If the temperature was too low, it in turn would lead to a pH that was too low, and the carboxylic acid would not be deprotonated leading to the formation of the layered phase. The dense phases could either be thermodynamic products that are favoured at higher temperatures or phases which are formed at higher pH ranges.

1.3 Summary

To summarise the current literature in this area, phosphonate MOFs are relatively much less common than their carboxylate-based counterparts, due to issues such as expense and tendency to crystallise rapidly as powders. However, they are of interest as they can form a higher variety of coordination motifs compared to carboxylates thanks to the high number of coordinating atoms. Additionally, phosphonate MOFs have shown promise for a variety of applications, especially proton conductivity.

Further, the previously published BIRM-1 MOF has been detailed, highlighting the interesting properties such as extra-framework cations and reversible dehydration that the material possesses. Existing issues with the synthesis of BIRM-1, ie. the high temperature sensitivity, were also explained.

Overall, there are gaps identified in the literature as well as further work from previous studies on BIRM-1 being highlighted.

1.4 Project Aims

The first aim of this work is a study into an alternative synthesis route to BIRM-1, one which avoids the fine temperature control necessary of the hydrothermal preparation. As part of this aim, data must be collected and analysed to establish that the product of any successful alternative synthetic route is indeed the same structure as BIRM-1. This is not necessarily straight forward as a simple indexing of PXRD patterns would only confirm the unit cell, not the contents. Therefore this is an important step in achieving that aim. An assessment will then have to be made of what impact, if any, the synthesis routes have on properties of the material. This will be tied into an additional aim, that of the second chapter of

this thesis which is to explore and expand the understanding of the properties of BIRM-1. This will be conducted with a focus on potential applications such as proton conductivity and ammonia storage. Additionally, an examination using total scattering data collected at a synchrotron of the dehydration of BIRM-1. This will allow better understanding of the structural changes involved, potentially informing the design of related materials to enable the synthesis of frameworks with permanent porosity. Aims of the work presented in the second half of this thesis turn towards attempts to make novel carboxyphosphonate MOFs based on different metals and different linkers. This will be done with a focus on obtaining lightweight, rigid and robust frameworks as these will be most likely to show promise for applications. The use of a rigid linker should enable a framework to exhibit permanent porosity, usually crucial for any gas storage or separation applications.

2 Experimental

2.1 Synthesis Techniques

Most the syntheses in this work were done either *via* a hydrothermal route or by a direct precipitation by deprotonation of acidic linker molecules followed by coordination to metal ions. There were also some experiments which were conducted by employing slow crystallisation methods such as vapour diffusion, layered diffusion and evaporative crystallisation.

2.1.1 Hydrothermal Synthesis

The hydrothermal syntheses in this work were conducted in 23 ml Teflon lined stainless steel autoclaves purchased from Parr Instrument Company. Precursor solutions were prepared, typically consisting of a metal salt, linker and some form of base with the optional addition of templating agents and/or modulators. The solutions were then loaded into the autoclaves which were then sealed and placed into ovens for heating. After a defined period of time (typically 24 hours) the autoclaves were removed from the ovens and allowed to cool. Once cool the product was recovered *via* vacuum filtration and washed with an appropriate solvent, usually the solvent the product was synthesised in. The product is then left to dry in air for a day before characterisation by powder x-ray diffraction and other techniques.

2.1.2 Slow Crystallisations

During attempts to make larger crystals of particular products for use in single crystal diffraction experiments, some different synthesis attempts were tried. These included a classic evaporative crystallisation where a precursor solution of metal salt and linker was made, adjusted to an appropriate pH and then left for the solvent to evaporate, leaving the product behind.

2.1.2.1 Layered Diffusion

The layered diffusion crystallisation technique involves preparing your precursor solution in one solvent, in which the product is soluble, and then layering it with another solvent in which your product is insoluble. This second solvent is known as the “antisolvent”. At the interface of the two solvents

product should slowly crystallise as the two solvents slowly mix, the product can then be recovered. Figure 2.1 shows a graphical representation of layered diffusion crystallisation.

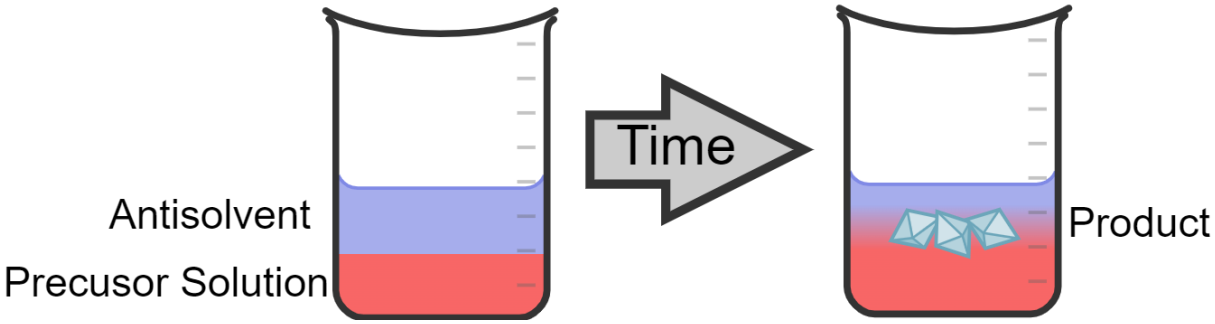

Figure 2.1) Graphical representation of layered diffusion crystallisation. The two solvents shown by red and blue.

2.1.2.2 Vapour Diffusion

For vapour diffusion crystallisation a precursor solution was prepared, as before, in a solvent within which the product is soluble. This solution is placed in a container which in turn is placed in a larger container filled with an antisolvent. The larger container is sealed and the antisolvent evaporates, then condenses and mixes with the precursor solution. As the proportion of antisolvent in the precursor solution slowly rises, product crystallises out and can be recovered. A graphical representation of this process is displayed in Figure 2.2, below.

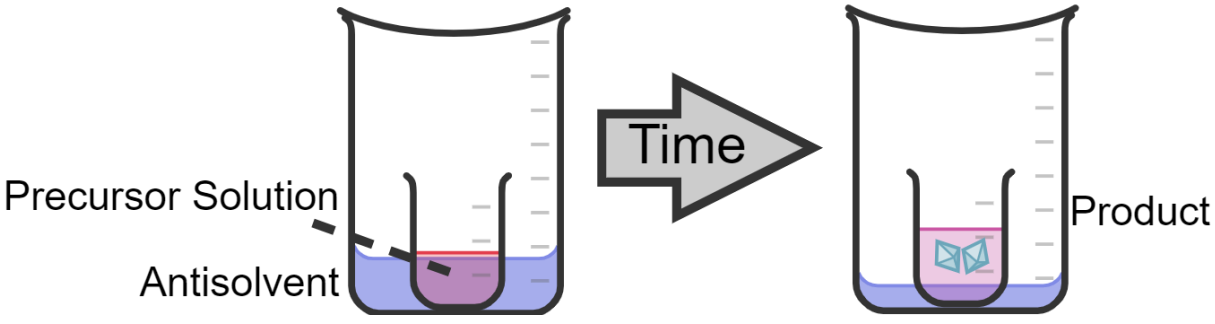

Figure 2.2) Graphical representation of vapour diffusion crystallisation

2.2 X-Ray Diffraction Techniques

Diffraction techniques and especially x-ray diffraction techniques are the most common method of characterisation for crystalline materials. Being used for checking the purity of a material, structure solution, crystallite size analysis and more. It is an extremely useful and important technique within the field of materials chemistry.

2.2.1 Fundamentals

A crystalline material is made up of an extended lattice of points simply known as lattice points, these are locations where atoms (or groups of atoms) may be placed. For a crystalline material the lattice extends effectively to infinity, in all directions, this is called long-range order. Figure 2.3, below, depicts a basic representation of a lattice. In certain materials lattice points may be occupied by vaccancies.

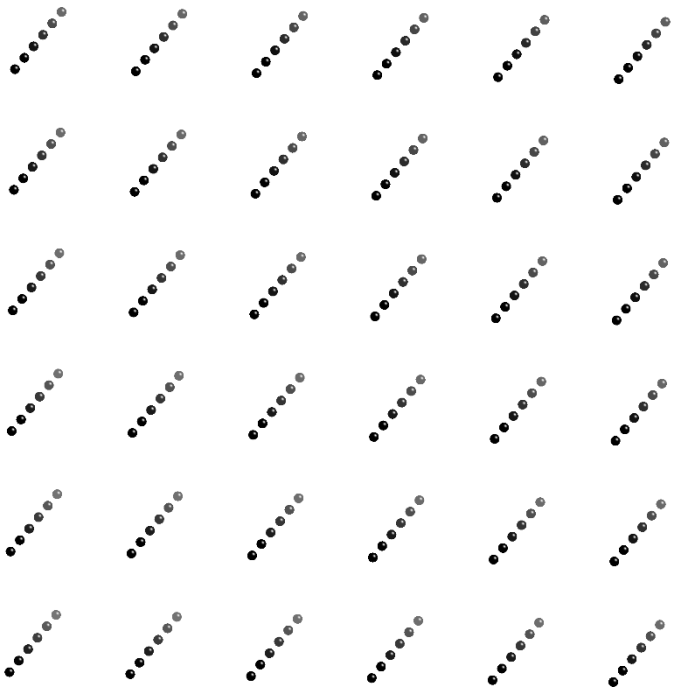

Figure 2.3) A basic representation of a 3-dimensional lattice with lattice points represented by black spheres

The smallest repeating unit that describes the full structure of a particular lattice is known as the unit cell. A unit cell contains all structural information of the material, needing only to duplicate this cell across 3-dimensions in order to have an accurate representation of said material. This is different to the

asymmetric unit which is the smallest possible representation of a material and requires information about symmetry operations to describe how it then forms a unit cell. The shape of a unit cell determines which crystal system describes it, with there being 7 in total, these are listed in Table 2.1. The lattice parameters define the axes of a unit cell (a, b and c) as well as the angles between them (α, β and γ).

Table 2.1) A summary of the 7 crystal systems along with the axes and angle relationships that define them

Crystal System	Axes Relationship	Angle Relationship
Cubic	$a = b = c$	$\alpha = \beta = \gamma = 90°$
Tetragonal	$a = b \neq c$	$\alpha = \beta = \gamma = 90°$
Orthorhombic	$a \neq b \neq c$	$\alpha = \beta = \gamma = 90°$
Monoclinic	$a \neq b \neq c$	$\alpha = \gamma = 90°, \beta \neq 90°$
Triclinic	$a \neq b \neq c$	$\alpha \neq \beta \neq \gamma \neq 90°$
Hexagonal	$a = b \neq c$	$\alpha = \beta = 90°, \gamma = 120°$
Rhombohedral	$a = b = c$	$\alpha = \beta = \gamma \neq 90°$

When a crystal system is further described by the centring of lattice points, of which there are 4 possibilities, a Bravais lattice is obtained. Primitive centring (often represented as P) is when the unit cell only has points in the corners. A body centred (represented by I) has the same 4 points as a P unit cell with an additional lattice point in the middle of the cell. Facial centring (represented with F) has lattice points in every corner as well as in the middle of each face of the unit cell. Base centring (represented with C) is similar to face centring but only 2 of the 6 faces contain a lattice point. In total there are 14 possible Bravais lattices possible and which one a material crystallises into has significant impact on what the resulting diffraction pattern looks like.[122] The 14 possible Bravais lattices are represented in Figure 2.4.

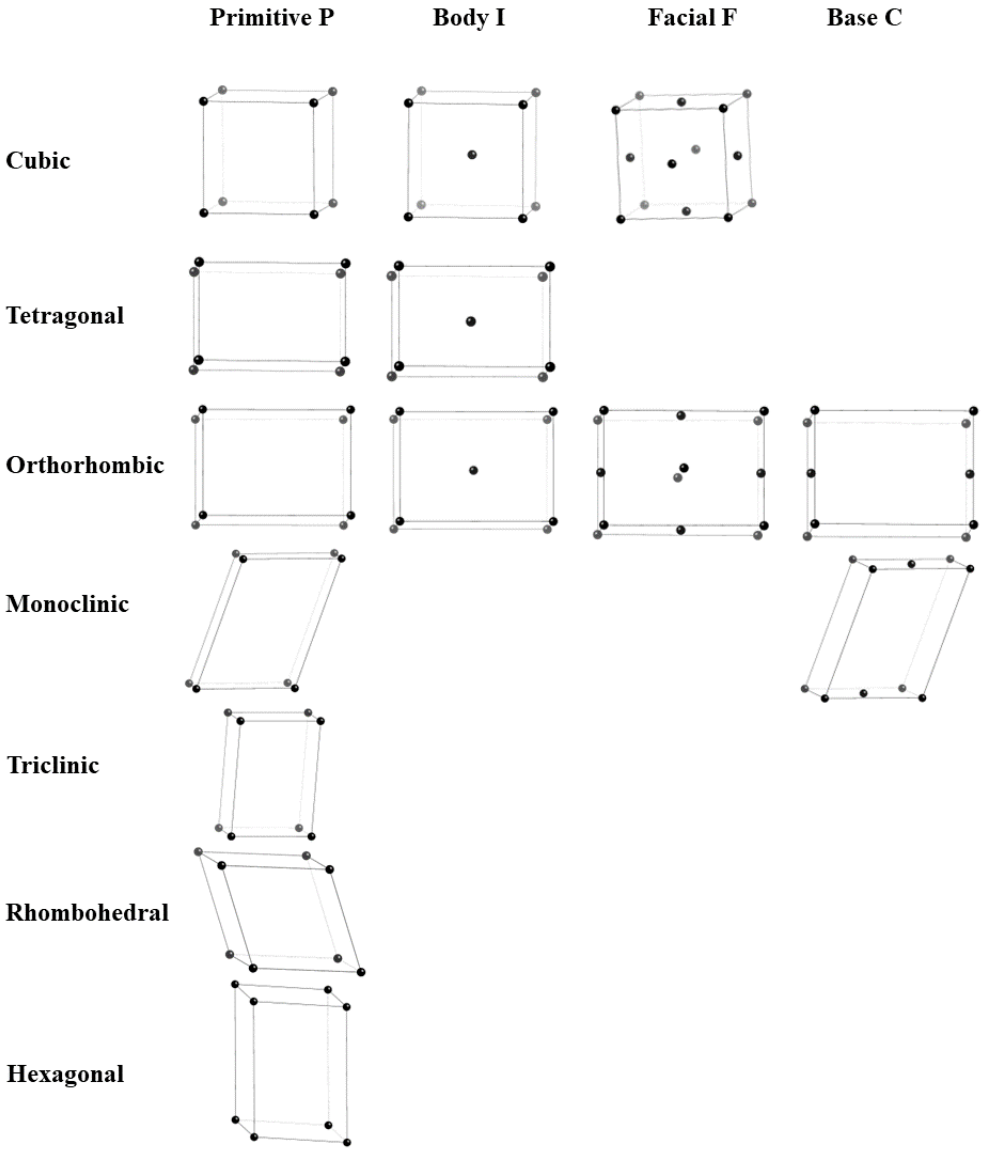

Figure 2.4) Graphical representation of the possible Bravais lattices

Miller indices are used for describing lattice planes, regularly spaced planes consisting of lattice points that exist in crystalline materials. These lattice planes act as diffraction gratings for x-rays and give rise to diffraction peaks. Miller indices are given in the form (hkl) where each letter is given as an integer representing the inverse fraction of where the plane intersects that edge of the unit cell. For example, if a lattice plane intersects the unit cell halfway along the a-axis, the miller index h will be given as 2 as it is the reciprocal of $\frac{1}{2}$, the same is done for k representing the b-axis and l for the c-axis. Note that depending on the crystal system many lattice planes are equivalent, such as for tetragonal where $a = b \neq c$ this means that (100) and (010) are equivalent but (001) is unique.[122] Some examples of lattice

planes are represented in Figure 2.5. The distance between lattice planes is given as d_{hkl}, sometimes d-spacing or simply d.

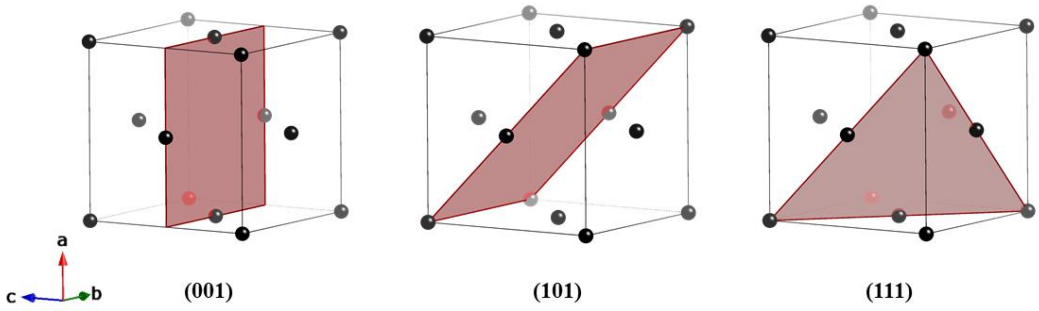

Figure 2.5) Graphical representation of lattice planes on an F-centred cubic Bravais lattice

Diffraction is a well-known phenomenon, it occurs when a wave passes through an opening similar in size to its wavelength, the outcome is the bending of the wave, effectively the gap it has passed through acts as a new, secondary, source of the wave, propagating the wave outwards. Diffraction can happen with any sort of waves, from ocean waves and sound waves to the x-rays used in characterising crystalline materials, electron and neutron diffraction are also commonly used in materials science.

In the case of x-ray diffraction, the opening through which the x-rays are diffracted is the space between the lattice planes, the d-spacing. The larger the distance between the lattice planes, the less the x-rays are diffracted. After diffraction the x-rays propagate outwards, the presence of more than one lattice plane (many millions in a typical crystal) gives rise to constructive and destructive interference. A graphical representation of this is given in Figure 2.6. Constructive interference occurs when the waves are in-phase with each other and destructive interference when they are not, diffraction spots appear where there is constructive interference occurring. The outcome of this is a representation of the reciprocal lattice of the material.

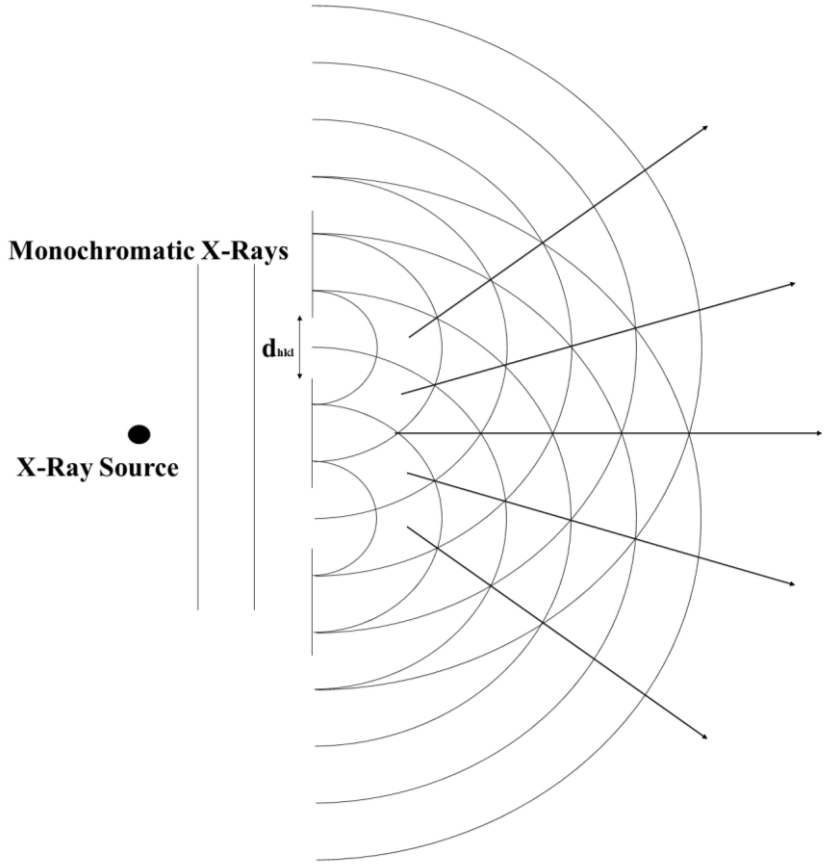

Figure 2.6) A representation of diffraction through two slits, in x-ray diffraction the 'slits' are the spacing between lattice planes. In this figure arrows indicate where constructive interference is occurring and thus where diffraction spots would be expected to appear.

All the background of diffraction discussed so far can combine for the derivation of Bragg's law. Bragg's law determines the location of diffraction spots and relates them to lattice plane spacings (d_{hkl}). Figure 2.7 is a graphical representation of the derivation.

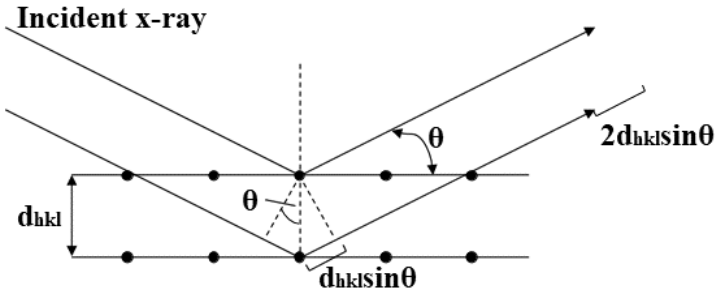

Figure 2.7) A graphical representation of the derivation of Braggs law.

For two x-rays to be in phase after diffraction and thus produce a diffraction spot the path difference must be an integer multiple of the incident wavelength. The path difference is effectively the difference in location of the two outgoing x-rays caused by their scattering at different lattice planes. From Figure 2.7 it can be calculated that the path difference is as given in Equation 1.

$Path\ Length\ Difference = 2d_{hkl}sin\theta\#(1)$ As just discussed, in order for the outgoing x-rays to be in phase, interfere constructively and produce diffraction spots the path length difference must be equal to an integer multiple of the wavelength of the x-rays. Applying this condition gives Equation 2 which is known as Bragg's law. Where λ is the wavelength of the x-rays used.

$n\lambda = 2d_{hkl}sin\theta\#(2)$ This equation can be applied in practice using a diffractometer. There are multiple different experimental setups used but the most common for powder diffraction is known as the Bragg-Brentano geometry, a representation of this is shown in Figure 2.8.

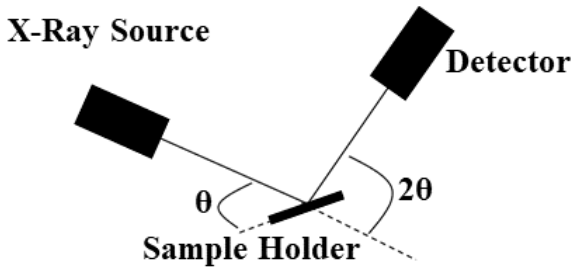

Figure 2.8) A simplified representation of a Bragg-Brentano θ/2θ geometry diffractometer. Note that in reality there are additional features such as filters, divergence slits and often monochromators.

The particular geometry shown above is the θ/2θ setup, in this case the source is held stationary whilst the sample and detector are moved around by θ and 2θ degrees respectively. Also common are θ/θ setups where the sample is held stationary, usually in the horizontal position, whilst the source and detector are both moved by θ degrees, this is particularly useful for liquid samples.[122] The diffractometer used in the vast majority of work done in this thesis was setup with Bragg-Brentano θ/2θ geometry. However, some diffraction experiments were run on a Debye-Scherrer diffractometer (represented in Figure 2.9) fitted with a cryostream to enable data collection at 120 K, which experiments were run like this and why will be made clear in the relevant results section.

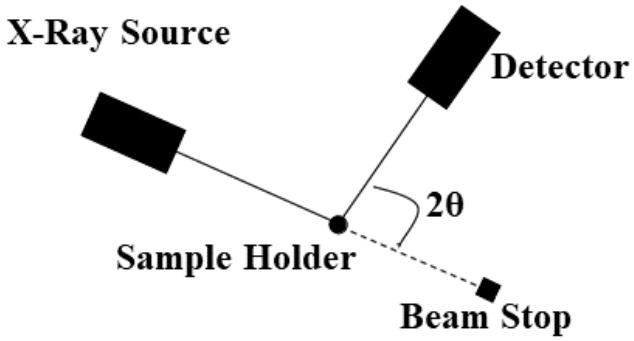

Figure 2.9) A simplified representation of a Debye-Scherrer diffractometer. Note that in reality there are many additional features such as filters, divergence slits and often monochromators

Single crystal diffractometers use a somewhat different setup. The single crystal is mounted on a goniometer which can be rotated through various axes depending on the geometry the instrument is set up with. The work done in this thesis was conducted using an instrument that uses a four-circle 'kappa' geometry. The crystal mounted on the goniometer can be rotated around 3 different circles with the fourth circle being the movement of the detector around the crystal. The four circles are labelled ω, κ, φ and θ. Just like for the powder diffraction setups, θ is the angle between the x-ray source and detector, it is manipulated through movement of the detector whilst the source is stationary. ω is coaxial with θ, both sitting on the horizontal plane. κ is titled by 50° to this horizontal plane, φ is then titled at 50° to the κ-axis. This geometry allows a cooling instrument to be mounted above the goniometer, enabling data collection at low temperatures. Another important difference in single crystal experiment setups compared to powder is the use of area detectors which allow the collection of many diffraction spots consecutively. The most common form of these detectors is called a charged coupled device (CCD).[123]

2.2.2 Diffraction Experiments

The diffractometer routinely used in this work is a Bruker D8 Advance diffractometer in Bragg-Brentano θ/2θ geometry and a copper anode x-ray source. It was fitted with a nickel filter to remove contribution from Cu Kβ to the x-rays but did not have a monochromator fitted meaning both Cu $K\alpha_1$ and $K\alpha_2$ were present in the incident x-rays, the result of this is broadening of low angle peaks and splitting of high angle peaks. A solid-state position sensitive detector with a 3° window was used. The samples were

spun at 15 rpm during data collection which lasted for 30 minutes and angles 5-50° were collected routinely. Samples were dried in air, then ground to a powder before data collection.

For data collection at 120 K a Siemens D5000 diffractometer in Debye-Scherrer geometry and fitted with an Oxford Cryosystems cryostream is used. This instrument was also fitted with a nickel filter and a silicon monochromator, as well as using a copper source. A position sensitive detector was also fitted to this instrument. Samples were dried and ground, then packed into a 1 mm inner diameter borosilicate glass capillary and cooled to 120 K, the capillaries were spun at 15 rpm during data collection.

For single crystal diffraction work an Aglient SuperNova was used. This diffractometer was setup with the kappa geometry and a CCD detector. Both copper and molybdenum anode sources were available on the instrument; the copper source was used as the longer wavelength is more appropriate for low angle peaks, common for large unit cells that MOFs tend to have. The instrument was also fitted with an Oxford Cryosystems cryostream and data collection was performed at 100 K. For some structures reported in this work, data was collected by the National Crystallographic Service based at the University of Southampton, where this is the case it has been made clear in the relevant sections.

2.2.3 Powder Diffraction Data Analysis

2.2.3.1 Indexing

Often when making an unknown crystalline material the first step after collecting diffraction data is to calculate the unit cell parameters, this process is known as 'indexing'. Indexing is particularly problematic in powder diffraction compared to single crystal diffraction as a powder diffraction pattern is effectively a one-dimensional projection of a three-dimensional lattice. However, by exploiting the fact each diffraction spot (or peak in powder diffraction) represents a plane in the reciprocal lattice, that may or may not be of equal length to each other, the following, Equation 3 can be formed.[124]

$$d^*_{hkl} = ha^* + kb^* + lc^* \#(3)$$

Taking the inverse of this and squaring the values gives the following Equation 4,

$$\frac{1}{d_{hkl}^2} = \frac{h^2}{a^2} + \frac{k^2}{b^2} + \frac{l^2}{c^2} \#(4)$$

the values are all squared as now real space is being considered, the d-spacing of (100) and ($\underline{1}$00) are the same but a negative value wouldn't make any physical sense, therefore the equation is squared to ensure a positive value. Bragg's law can be used to obtain d_{hkl} allowing the use of Equation 4 to calculate the unit cell.

The above equations only hold true for lattice cells with 90° angles. When lower symmetry unit cells are involved automatic indexing algorithms must be used. In modern times, virtually all indexing is done by computer algorithms and very rarely would manual indexing of an unknown material be attempted.

The software used for indexing of this work was GSAS-II, the indexing algorithms written into this software are based on methodology developed by Coehlo.[125,126]

2.2.3.2 Pawley Fitting

Pawley fitting is a form of whole powder pattern structureless fitting, that is to say the aim of the method is to fit the whole powder pattern to a unit cell without knowing the complete structure, i.e. atomic positions. It is a common technique used to confirm the product of a synthesis has unit cell parameters that match what was expected, such as if it is the synthesis of a known phase or to confirm results from indexing. It can also be used to track changes in the size of a unit cell upon some sort of external input such as heat or pressure.[122,127]

The software TOPAS academic v6 was used in this work to carry out Pawley fitting.[128]

2.2.3.3 Rietveld Refinement

Rietveld refinement, as opposed to Pawley fitting, takes into account the whole structure, meaning that variables such as atom positions and occupancies are vitally important and can be refined. Due to this, it is now crucial to consider not just the position of peaks, but also their intensity. The intensity of a peak

is a function of the electron density within the relevant lattice plane. Individual atoms have atomic scattering factors f_n which is proportional to the number of electrons of that atom and decreases with increasing diffraction angle, θ. The scattering factors of individual atoms combine in the following relationship shown in Equation 5

$$F_{hkl} = \sum_{n=0}^{n=N} f_n \, exp \, exp \, [2\pi i(hx_n + ky_n + lz_n)] \, \#(5)$$

where F_{hkl} is the structure factor of a given hkl plane. $2\pi(hx_n+ky_n+lz_n)$ is equal to the phase angle of a particular atom n of fractional coordinates ($x_n \, y_n \, z_n$). Using the structure factor, the intensity of a peak I_{hkl} can then be calculated using Equation 6

$$I_{hkl} = K \times p_{hkl} \times L_\theta \times P_\theta \times A_\theta \times T_{hkl} \times E_{hkl} \times |F_{hkl}|^2 \, \#(6)$$

The scale factor K is used to normalise experimental intensities to calculated intensities. p_{hkl} is the multiplicity of the diffraction peak, it accounts for reflections which are equivalent via symmetry such as (100) (010) and (001) in a cubic lattice. L_θ accounts for contributions arising from geometrical factors. P_θ is the polarisation factor which factors in the polarisation of x-rays after scattering. A_θ is a multiplier related to absorption effects. T_{hkl} is the preferred orientation factor, powder samples theoretically contain a vast number of randomly orientated crystals however crystal shapes such as plates and rods typically adopt certain orientations more favourably. E_{hkl} is the extinction multiplier, it is usually disregarded for powder samples as its effects are negligible. The extinction multiplier accounts for x-rays which are reflected back into the crystalline sample and are often out of phase with other scattering.[122,129]

Rietveld refinement is a least-squares minimisation process whereby the difference R between the observed intensities Y_o and the calculated intensities Y_c are reduced as much as possible by adjusting parameters such as the lattice cell parameters, atomic positions and occupancies. This minimisation is given by Equation 7

$$R = \sum \; w(Y_o - Y_c)^2 \, \#(7)$$

The value *w* is a weighting that is assigned to each step, inversely proportional to the observed intensity. The result is a system by which structural changes in a material can be quantified from powder data, without the need for single crystals.[122,124,129,130]

The quality of the results from Rietveld refinement can be assessed in several ways. The most important check of quality is that the structural model which is produced makes chemical sense, for example it is fully charge balanced and that bond numbers, lengths and angles are appropriate. The second is that of the 'visual fit'. The Rietveld process produces three patterns, the observed (the raw data), the calculated and the difference between them. The difference line should be as flat as reasonably possible, there is always likely to be a few artifacts especially where large peaks are present as it can be difficult to accurately model their shapes. There should not, however, be peaks that remain in the difference, i.e. they are not accounted for in the model. Finally, there are a number of equations that assess the quality of the fit which are important to Rietveld refinement. The most straight forward of these is the weighted R-factor R_{wp}, the calculated of which is given by Equation 8

$$R_{wp}{}^2 = \frac{\sum \quad w(Y_o - Y_c)^2}{\sum \quad w(Y_o)^2} \#(8)$$

R_{wp} commonly given as the squared value as calculated above or the square root of that. The best theoretical value of R_{wp} is given as R_{exp}, it is dependent on the number of data points *N* and is calculated as shown in Equation 9

$$R_{exp}{}^2 = \frac{N}{\sum \quad w(Y_o)^2} \#(9)$$

The final measure of fit that is commonly used in Rietveld is that of χ^2 which is simply a comparison of the weight R-factor R_{wp} to the minimal possible value R_{exp}, as shown in Equation 10

$$\chi^2 = \left(\frac{R_{wp}}{R_{exp}}\right)^2 \#(10)$$

Whilst these calculated values are often a useful measure of the quality of a Rietveld refinement, they should not be taken as an absolute measure. Much more important is that the model makes chemical sense and the visual fit is good. The R_{wp} and χ^2 can often be misleading, for example, a set of data with significantly high background will always give a low value for R_{wp} as most of the observed counts can be factored in to fitting the background. Likewise, data collected over a long time period with many points will paradoxically provide an inflated value of χ^2 even though the data will be of higher quality than if it were collected quickly.[131]

The Rietveld refinements produced in this work were done using TOPAS academic software.[128]

2.2.4 Single Crystal Data Analysis

After data collection is completed, data reduction must be performed. In this work, this task was performed by Dr Louise Male. Data reduction can consist of several steps, Lorentz-polarisation must be factored in. Adsorption corrections are also performed, as x-rays travel through a crystal sample the beam is weakened by scattering and ionisation occurring within the material. These factors increase relative to the scattering factor of an atom, as such it is much more of an issue for materials containing heavier elements.

Following this, structure solution work was conducted using the software Olex2. The initial structure solution was done using the SHELXT intrinsic phasing technique.[132,133] Further refinement of the model used a least squares method as part of the SHELXL program, applied within the Olex2 software.[133,134] This least squares refinement works in a similar way to the Rietveld refinement used for powder data. Structures were then refined anisotropically where data quality allowed. Hydrogen atoms were added to appropriate atoms as fixed riding models with thermal parameters linked to the parent atom.

Some structures reported in this work were solved either by Dr Louise Male from the School of Chemistry, University of Birmingham or the National Crystallographic Service based at the University of Southampton. Where this is the case, it has been made clear in the relevant sections.

2.2.5 Total Scattering and Pair Distribution Function

Whilst in the study of crystalline materials the background noise underneath the Bragg peaks is usually discarded and of little interest, it actually contains a wealth of structural information. The background contains, amongst other things, contributions from diffuse scattering by the sample. Diffuse scattering comes from x-rays interacting with any atoms in the structure whether they have periodical ordering or not. Therefore, it is possible to characterise non-crystalline materials by measuring the total scattering and transforming it into a pair distribution function (PDF). A PDF gives the probability of finding a pair of atoms at a distance, *r*, apart. The data is collected much like any other powder diffraction data; however, a synchrotron source is usually used for its high intensity radiation. High intensity radiation (high flux) is required for satisfactory real space resolution in the PDF. The first step in the data processing is to subtract any contributions from other sources of scattering. This means taking blank measurements of the sample holder in order to subtract scattering contributions from the holder and the air. Additionally, contributions from factors such as Compton scattering and fluorescence are removed. The data is then normalised to the incoming flux. After this data reduction what is left is known as the coherent scatter intensity *I(Q)*, a function of *Q* which is given in Equation 11.[122]

$$Q = \frac{4\pi \; sin \; sin \; \theta}{\lambda} \#(11)$$

The total scattering structure function *S(Q)* is then calculated by dividing *I(Q)* by the average scattering per atom and the total number of scatterers *N*. *S(Q)* is still essentially a normal powder X-ray diffraction pattern which has had the previous subtractions and normalisations applied. A Fourier transform can then be applied to the total scattering function to give the PDF, as shown in Equation 12.

$$g(r) = \frac{2}{\pi}\int_0^\infty \quad Q[S(Q) - 1] \; sin \; sin \; (Qr) \; dQ \#(12)$$

The term *g(r)* is the probability of finding an atom pair at distance *r*. This means a PDF is made up of peaks out to high *r* for a crystalline material with long range order. For a material which is amorphous there will only be peaks representing short range order at low *r*. There are more normalisations of a PDF

than *g(r)* available with slightly different definitions. However, they all fundamentally show the same thing which is the probability of finding an atom pair at a distance *r*.[122,135] The normalisation used in this work is known as the differential correlation function *d(r)*. The differential correlation function *d(r)* is linked to *g(r)* by the relation shown in Equation 13, where ρ_0 is the average atomic density of the material in units of atoms $Å^{-3}$.[135]

$$d(r) = 4\pi r \rho_0 g(r) \#(13)$$

2.3 Thermogravimetric Analysis

Thermogravimetric analysis (TGA) is a common technique used to study the stability and decomposition of MOFs as well as many other materials. The technique involves heating a small amount of sample in a crucible at a controlled rate in a controlled atmosphere. Many different gases are used including oxygen, hydrogen, nitrogen, argon and air. TGA is commonly coupled with other techniques such as mass spectrometry (MS) or infrared spectroscopy in order to study the decomposition products of the material as it breaks down. Another technique often combined with TGA is differential thermal analysis (DTA), this involves heating a second crucible which is either empty or containing an inert reference material, the two crucibles are heated together in identical conditions and the difference in temperature change is measured. The difference in temperature change can reveal physical and chemical changes the sample is going through such as dehydration or phase changes. These changes must be either exothermic or endothermic in nature to be revealed by DTA.

In this work TGA was coupled with DTA and MS to characterise the decomposition profile of the materials made. The instrument used was a Netzsch STA 449 F3 Jupiter TGA-DTA-MS. The decomposition profile was measured between 40 – 700 °C and conducted in a 50:50 mixture of oxygen and nitrogen to ensure any organic components are properly burnt off and avoid any coking of the interior of the instrument. For the MS, mass-to-charge ratios (*m/z*) of 16, 17 and 18 were measured to record water and ammonia being released, *m/z* of 44 was also recorded to account for carbon dioxide.

2.4 Scanning Electron Microscopy

Scanning electron microscopy (SEM) is a common technique for imaging materials on a micrometre and nanometre scale. The surface is scanned with a focused electron beam, the electrons are then scattered both inelastically (secondary electrons, SE) and elastically (back scattered electrons, BSE) and measured with a detector. SE are commonly used to measure surface morphology whilst BSE can give information on phase purity as heavier atoms scatter the electrons more strongly, appearing as brighter spots on an SEM image.

SEM is commonly coupled with a technique called energy dispersive x-ray (EDX) spectroscopy which is used for elemental analysis of the sample. This is done through ejection of a core electron with an incoming electron, similar techniques such as x-ray fluorescence use x-rays to eject the electron. When a core electron is ejected, it leaves behind what is called an electron hole. An electron from an outer orbital, higher in energy, will fill the hole and in the process a photon with energy equal to the difference in the orbitals is released. The energy, and thus wavelength, of the ejected photon is characteristic of the element it is released from, enabling the elemental composition to be analysed. Figure 2.10 is a graphical representation of this process. There are many factors that influence the accuracy of EDX that are difficult to control, for this reason EDX is commonly used as an estimation of chemical composition rather than a highly accurate measure.

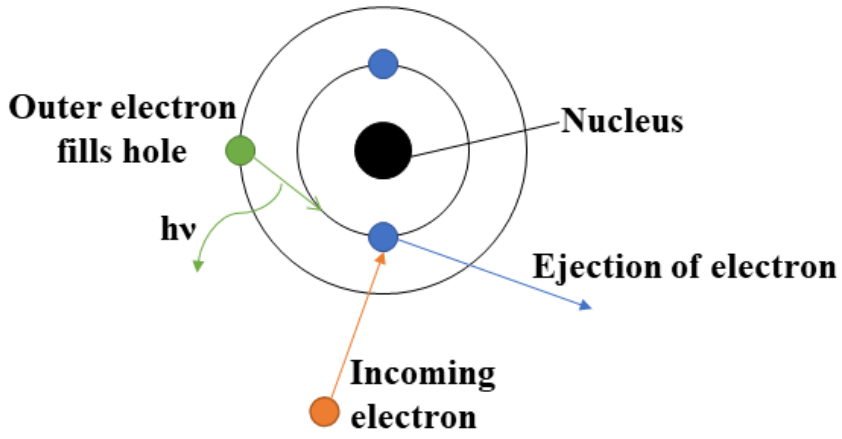

Figure 2.10) A representation of how EDX works through the ejection of a core electron followed by an outer electron filling the hole left, ejecting a photon with a wavelength characteristic of the element

The SEM-EDX used in this work is a benchtop Hitachi TM4000 Plus SEM coupled with an Oxford Instruments AztecOne EDX detector. When images were taken of samples without the need for EDX they were typically coated in carbon to increase conductivity and give better quality images, when EDX was required, coating is not used as it can affect the results. In this work the BSE detector was typically used in order to confirm phase purity; as the overall morphology of the crystals can still be obtained, use of the SE detector was not necessary. The electron source was used on the 15 kV setting (the highest available for the instrument) in order to give the best resolution possible. As the instrument used was a benchtop device, the resolution is limited and nanofeatures typically cannot be resolved.

2.5 Fourier Transformed Infrared Spectroscopy

Fourier transformed infrared spectroscopy (FTIR) is a common laboratory technique used to detect functional groups within a material or molecule. Infrared radiation is passed through the material (typically wavenumbers from ca. 400-4000 cm^{-1} are used) and then detected on the other side. The amount of transmitted infrared radiation is measured, sometimes the inverse of this is taken and it is displayed as the absorbance. Absorbance at particular wavenumbers, corresponding to a particular energy, is characteristic of different functional groups allowing the analyst to determine which groups are present. This process occurs due to vibrations within the molecule. When a photon with a particular energy passes through a molecule, if the energy is equal to a vibrational energy level within the molecule, it will be absorbed and cause the molecule to vibrate. This process only occurs if it results in a change to the permanent dipole of the molecule, this means that homoatomic diatomic molecules such as N_2 or O_2 cannot be detected through FTIR.

For liquid and gas samples the infrared radiation can simply be passed through the sample and detected on the other side, however for most solid samples this would result in the total blocking of the radiation leading to a different experimental setup being required. Attenuated total reflectance (ATR) is the technique used to solve this issue. It exploits total internal reflectance through a crystal upon which the sample is pressed down to ensure good contact. An evanescent wave occurs where the infrared beam is internally reflected, this wave reaches a small distance into the sample. An evanescent wave is an

unusual phenomena that occurs with no net energy flow, therefore any infrared radiation absorbed from the evanescent wave affects the beam as a whole. The process of ATR is represented in Figure 2.11.

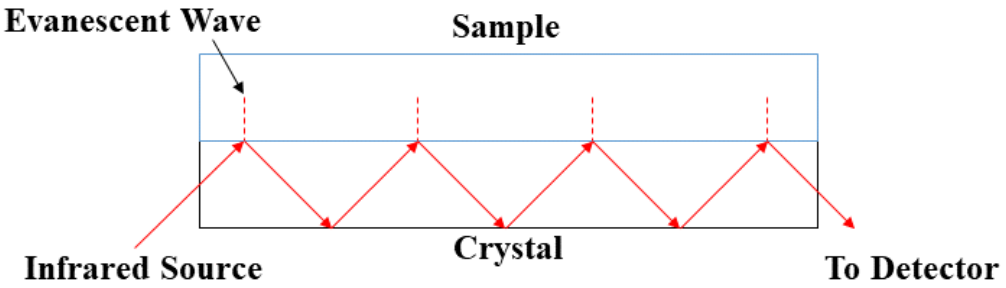

Figure 2.11) Graphical representation of attenuated total reflectance in FTIR

The instrument used in this work was a Bruker Alpha II FTIR spectrometer with an ATR attachment which uses a diamond crystal.

2.6 Surface Area Measurements

The most common technique for measuring the surface area of porous materials is the application of the Brunauer-Emmett-Teller (BET) theory to the adsorption of molecules to solid surfaces. The BET theory is applicable to the adsorption of inert gas molecules that undergo multilayer adsorption on a solid surface. The most common probe molecule used is nitrogen, however carbon dioxide and argon are also frequently used. In theory, any gas molecule that will not react with the adsorbent being studied may be used to probe surface area using the BET method. In order to apply the BET method an adsorption isotherm first needs to be measured. An adsorption isotherm is a measurement, at constant temperature, of the amount of the adsorbent which has adsorbed at a range of relative pressures up to the saturation point p_0. The relative pressure is typically given as p/p_0. The BET equation is applied in its linear form given as Equation 14.[136]

$$\frac{p/p_0}{n(1-p/p_0)} = \frac{1}{n_m C} + \frac{C-1}{n_m C}(p/p_0) \#(14)$$

In this equation, n is the amount adsorbed at the given relative pressure and n_m is the capacity of a monolayer. C is known as the BET constant and relates to the energy of monolayer formation. A very low value for C (ca. <2) indicates weak interactions between adsorbent and probe molecule, the BET

theory is not applicable in these cases. A very high value for C (ca. >150) is either indicative of very strong adsorbent-adsorbate interactions or the filling of micropores.[136]

From Equation 14 we can see there is a linear relationship between $(p/p_0)/n(1-p/p_0)$ and p/p_0, therefore a linear plot known as a 'BET plot' can be made. The plot is only linear over a limited range, usually at low relative pressure. Taking the gradient of this region n_m can be calculated and applied to Equation 15 to give a_s, the specific BET surface area of the material,

$$a_s = \frac{n_m N \sigma_m}{m} \#(15)$$

where N is the Avogadro constant, σ_m is the cross-sectional area of the adsorbent molecule and m is the mass of adsorbent.[136]

A significant concern is that the BET theory does not hold up particularly well for microporous materials such as those studied in this work, this is due to the difficulty in separating the effect of multilayer adsorption and micropore filling to the isotherm. There are three conditions which must be met in order to maintain confidence in a measurement. The BET constant C should be positive as a negative value would indicate adsorption being energetically unfavourable. The BET equation should only be applied in the region where $n(1-p/p_0)$ increases continuously with p/p_0. Finally, the value of p/p_0 that corresponds to n_m, i.e. complete monolayer coverage, should be within the BET range. These conditions were set out by Roqueroul et al.[137] Even with these conditions, BET surface area measured on microporous materials should not be treated as an absolute measure of the adsorbent's monolayer capacity. Treating results measured this way as representing an estimate or the apparent surface area is more appropriate.

The surface area measurements done in this work were conducted using a Quantachrome NOVA 1000e surface area and pore size analyser. Nitrogen was used as the probe molecule and the isotherms were recorded at 77 K. Samples were vacuum dried at 120 °C for 16 hours prior to measurement.

3 Synthesis of BIRM-1

3.1 Introduction

This chapter looks at the synthesis of the ion-exchangeable carboxyphosphonate MOF 'BIRM-1' which was previously developed and refined by Chao Zhao.[115,59] Zhao studied the syntheses and structures of BIRM-1 and ion-exchanged variants of the material. In addition, Zhao also synthesised and characterised three other carboxyphosphonate phases that resulted from the same reagents under different conditions.[115] Despite the previous work done on BIRM-1, the synthesis remains difficult to conduct as excellent thermal control is necessary in order to obtain a phase pure product.[118] The work in this chapter explores new methods to synthesise the BIRM-1 MOF, the sodium and potassium extra-framework cation variants of BIRM-1, as well as a related layered material.

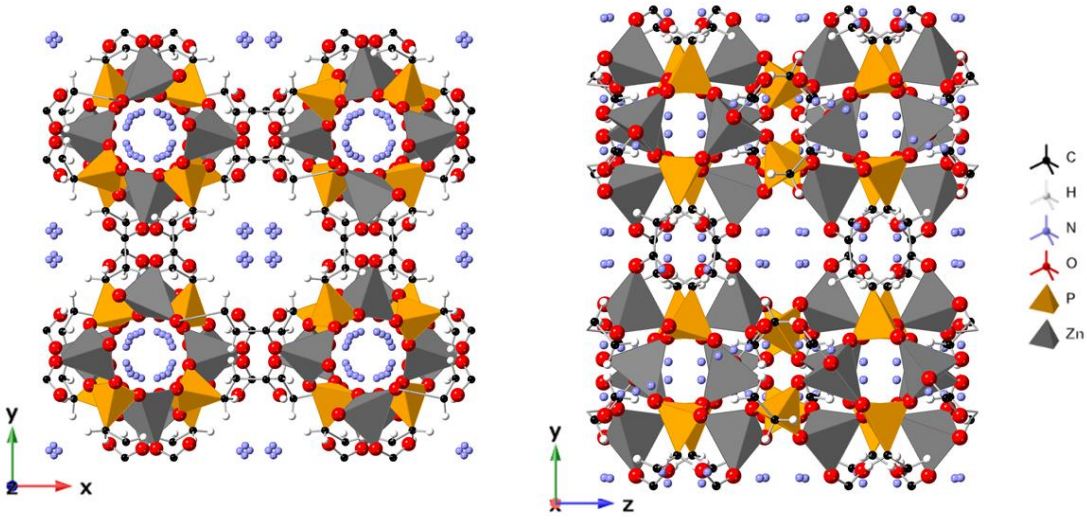

Figure 3.1) Crystal structure of BIRM-1 looking along the z-axis (left) and x-axis (right). Solvent water molecules are omitted for clarity. Hydrogen atoms from ammonium cations are not shown.[59]

3.2 Experimental

3.2.1 Hydrothermal Synthesis of BIRM-1

The hydrothermal synthesis of BIRM-1 in this work was carried out *via* the methodology developed and published by Zhao.[59,115] This involves preparing an aqueous solution of zinc nitrate hexahydrate, 3-phosphonopropionic acid, tetraethylammonium bromide and urea in the molar ratio 1:1.75:1.3:9 in 11.25 ml of deionised water. Table 3.1 gives the masses used for synthesis in this work. All reagents

were sourced from Sigma Aldrich and were of the following purities: zinc nitrate hexahydrate 98%, 3-phosphonopropionic acid 94%, urea 99% and tetraethylammonium bromide 98%.

Table 3.1) Quantities of reagents used in the hydrothermal synthesis of BIRM-1 according to Zhao's method[59,115]

	Zinc nitrate hexahydrate	3-phosphonopropionic acid	Tetraethylammonium bromide	Urea
Molar Ratio	1	1.75	1.3	9
Mass (g)	1.6695	1.5098	1.5342	3.0631

The aqueous solution was then loaded into a 23 ml stainless steel autoclave and heated to 87°C for 24 hours.[118] Product was recovered by vacuum filtration, washed with deionised water, then left to dry in air for a day before characterisation by PXRD.

3.2.2 Room-Temperature Synthesis of BIRM-1 and Associated Layered Phase

The room-temperature synthesis of BIRM-1 was initially carried out using the same quantities of reagents as the hydrothermal synthesis, as listed in Table 3.1, but without the addition of urea. After preparation of the precursor solution of zinc nitrate, 3-phosphonopropionic acid and tetraethylammonium bromide ammonia hydroxide solution (ca. 28% w/w) was added dropwise whilst stirring until the pH reaches ca. 6. Further work discovered that the pH range appropriate for formation of BIRM-1 was around 6-8; at lower pH the layered phase is obtained. Additional further work found that the addition of tetraethylammonium bromide is not necessary. For direct synthesis of the forms of BIRM-1 with alkali metals (Na, K) as the extra-framework ions, 2 M solutions of the corresponding hydroxide were added dropwise in place of ammonia solution. Product was recovered by vacuum filtration, washed with deionised water, then left to dry in air for a day before characterisation by PXRD. For recording the titration curve during the synthesis of RT-K-BIRM-1, the precursor solution was prepared as standard and then 2 M potassium hydroxide was added in 500 μL steps using a micropipette.

3.3 Hydrothermal Synthesis

As discussed previously, the hydrothermal synthesis procedure of BIRM-1 is particularly temperature sensitive. A relatively small temperature difference can result in the synthesis of four distinct phases.

Therefore, the first step in any new project working on BIRM-1 is to successfully synthesise the material *via* the hydrothermal route. The procedure established by Zhao was used in this work.[59] A synthesis was set up and a white sample composed of needle-like crystals was obtained. This matched the description given by Zhao.[59] A Pawley fit was carried out in order to confirm the same phase was obtained, the results of this is shown in Figure 3.2 with the lattice parameters given in Table 3.2.

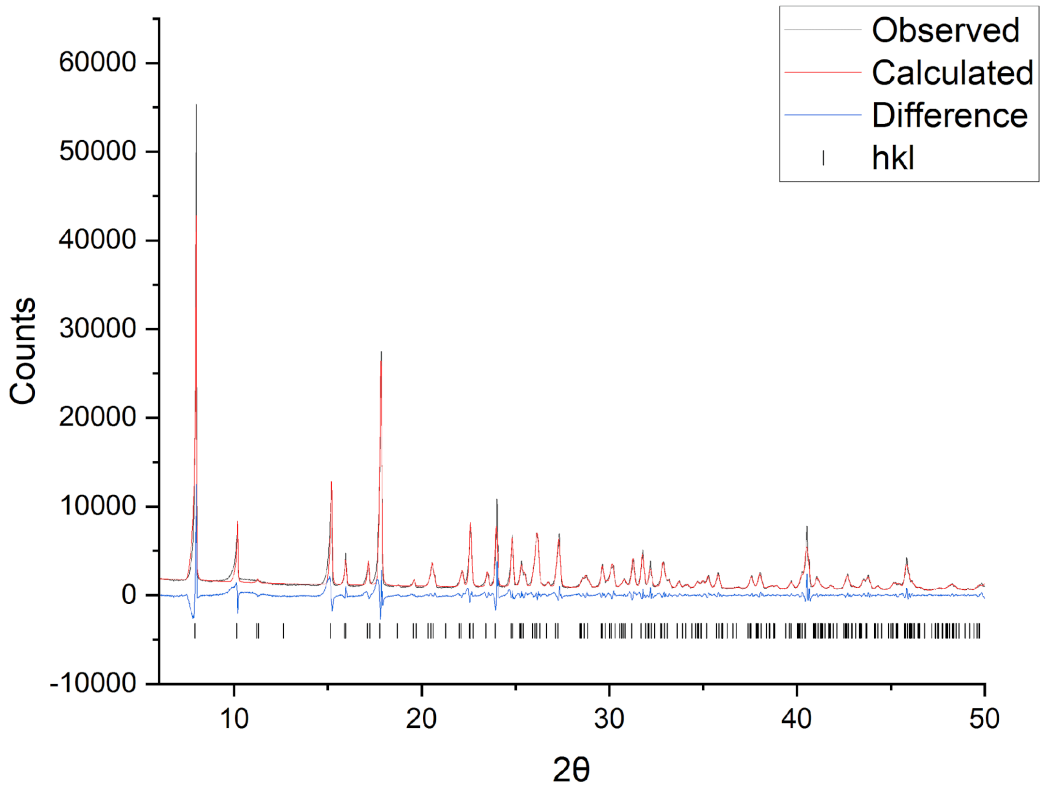

Figure 3.2) Pawley fit of hydrothermally synthesised BIRM-1 from data collected at room temperature

Table 3.2) A comparison of cell parameters from this work to those reported by Zhao[59]

BIRM-1	Refined Parameters	Parameters Reported by Zhao[59]
a (Å)	22.3057(14)	22.3019(2)
c (Å)	18.0005(29)	17.7384(1)
Volume (Å^3)	8956(2)	8822(1)

The Pawley fit gave unit cell parameters which are similar but not quite the same as those given by Zhao, especially for the *c* lattice parameter. A few reasons could be given for this. Zhao reported on the flexibility of the framework and how it can be reversibly dehydrated. It is plausible therefore that a differing level of hydration in the material could lead to a slight difference in lattice parameters.

However, this material has not been subjected to heat or place in a drying oven at any point nor had the samples in Zhao's work. So, there is not much opportunity for a significant difference in hydration level to arise. Instead, the likely cause of this discrepancy is the temperature at which the data for fitting was collected. The unit cell given by Zhao was determined by single crystal diffraction data collected at 120 K whereas the data in this work was collected at room temperature (ca. 295 K). This large difference in temperature likely caused thermal expansion within the material. To confirm this further data were collected at 120 K and Pawley fitted as shown in Figure 3.3 with the lattice parameters given in Table 3.3. Note that the relative intensities are rather different. This is due to a different diffractometer being used due to the requirement for a cryostream. The diffractometer used to collect the data at 120 K is the D5000 instrument which uses a transmission geometry and a capillary sample holder. These differences in experimental setup greatly lessen the preferred crystal orientation effect compared to data collected on the D8. This is also beneficial for conducting Rietveld refinement. Data were collected over a 2θ range of 5-50 °C over 32 hours. Only data above 7° 2θ were included in the Rietveld refinement due to presence of an unusual feature in the background.

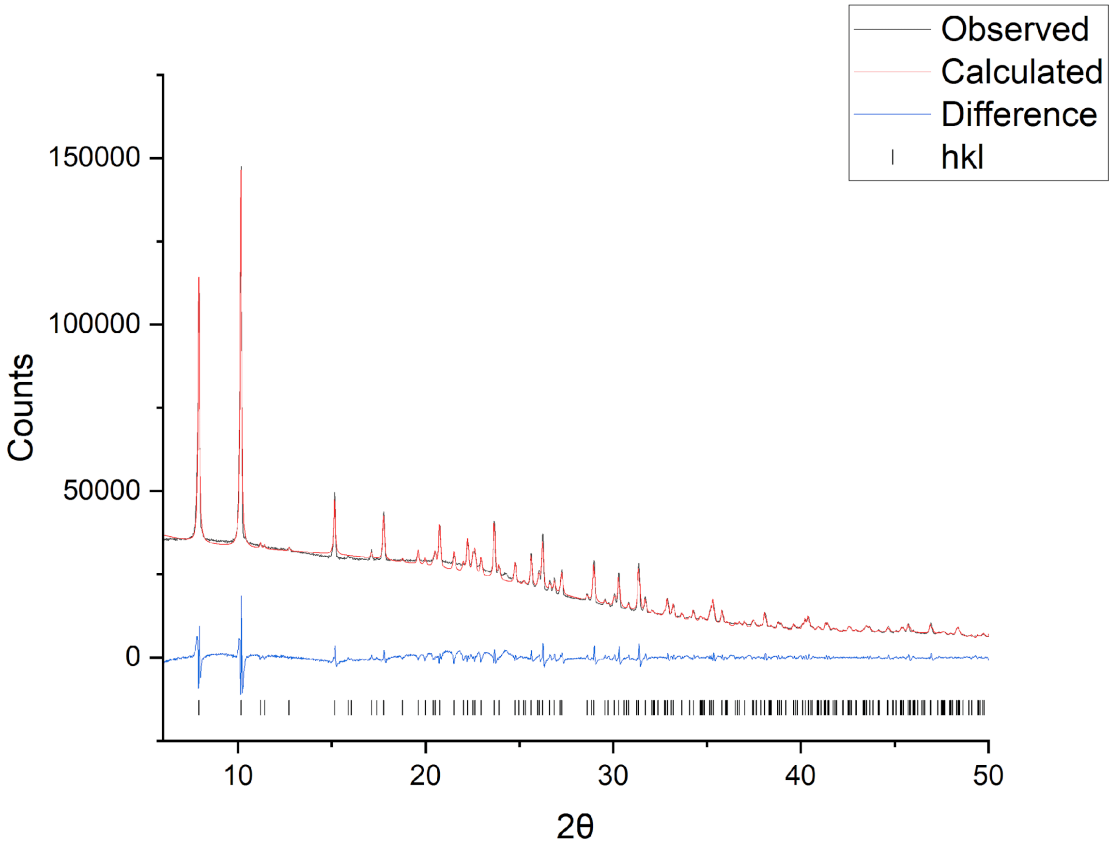

Figure 3.3) Pawley fit of hydrothermally synthesised BIRM-1 from data collected at 120 K

Table 3.3) A comparison of cell parameters determined from the data collected in this work to those reported by Zhao[59]

BIRM-1	Refined Parameters	Parameters Reported by Zhao[59]
a (Å)	22.3087(10)	22.3019(2)
c (Å)	17.7618(10)	17.7384(1)
Volume (Å^3)	8839(1)	8822(1)

The unit cell determined from data collected at 120 K shows much better agreement with that reported by Zhao. Interestingly the *a* parameter appears to extend slightly on cooling down but the change is negligible and only just outside of error. The *c*-axis, though much closer is still slightly different to that found by Zhao. This could be due to this data being collected from powder and being a better average of unit cells from many crystallites compared to Zhao's value which is from a single crystal. Additionally, this is a much more reasonable discrepancy to be explained by small differences in hydration. The data do seem to confirm both that BIRM-1 has been successfully synthesised in this

work and that there is a noticeable thermal expansion effect. A Rietveld refinement was conducted on the data collected at 120 K to confirm that the structure is indeed the same as reported by Zhao.

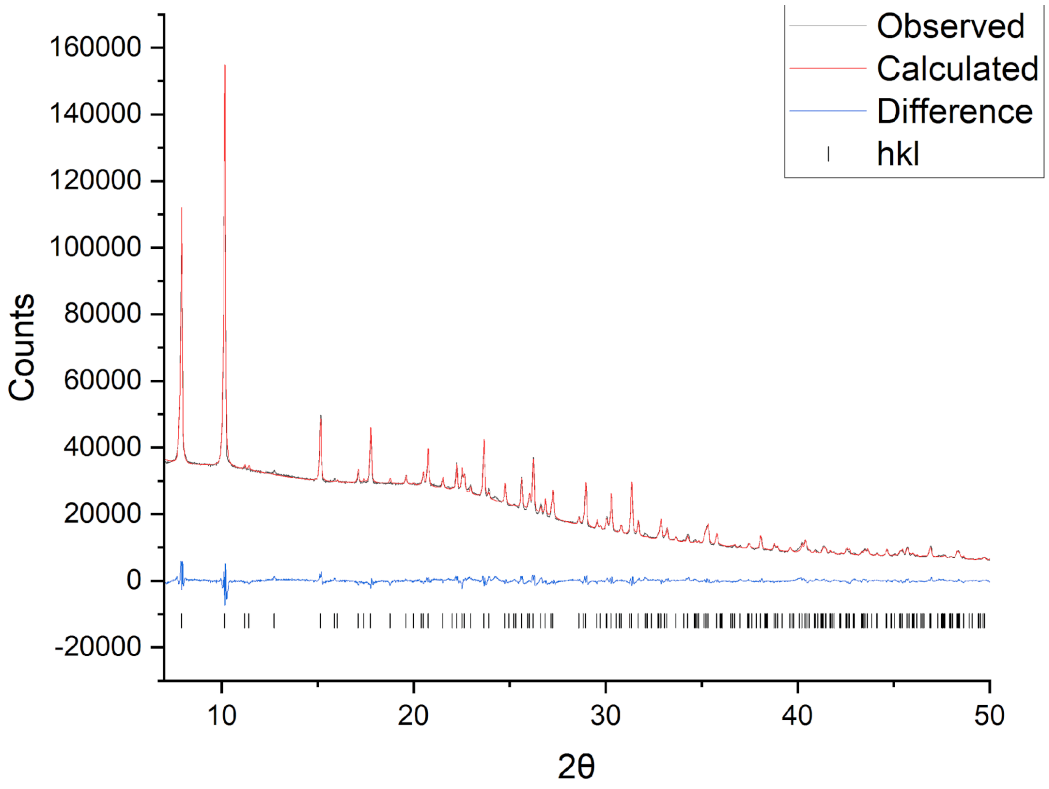

Figure 3.4) Rietveld refinement of hydrothermally synthesised BIRM-1 from data collected at 120 K

The data collected for Rietveld refinement has an unusual background profile. probably due to the use of a borosilicate capillary to hold the sample. The background was refined using a Chebyshev polynomial with 12 variables. The refinement produced prior to any refinement of atom positions was a good match between structure and model. However, these variables were allowed to refine to see if the fit could be further improved. Soft restraints on bond angles for the carbon chain (109.5°) and carboxylate group (120°) were required. After those soft restraints were applied, the framework settled and is virtually identical to that determined by Zhao both from single crystal diffraction.[59] However, there were some differences found when the pore contents were allowed to refine. One of the ammonium cations within the large pore consistently moved to overlap with the other cation on its site. This suggests that the occupancy of that site is greater than it is actually assigned. To remedy this, the nitrogen atom that refined away from its initial location was removed and its occupancy added to the cation site with

which it kept overlapping. This was not enough to fully satisfy the refinement as when the next refinement step occurred an oxygen atom representing a water molecule moved to overlap with the cation site. Several other oxygen atoms also moved to overlap with each other. Oxygen atoms were removed until no overlapping was occurring and then the occupancies of all remaining pore contents atoms was allowed to refine. The occupancy of the nitrogen atom in the large pore refined to 0.96. This was then fixed to 1 whilst the nitrogen atom located within the small channels of BIRM-1 was changed to an oxygen in order to preserve charge balance. It is worth noting that with the uncoordinated carboxylate oxygen being present within the large pore, this provides a centre of negative charge and thus the most likely site within the structure for an extra-framework cation to be located. The extra-framework contents within the channels could likely be water. The outcome of the removal and reassignment of the pore contents is more water on fewer but higher occupancy sites. The refined structure has 4.43 water molecules compared to 2.5 in the original structure. Something else important to note is that when refining the pore contents, it is water and ammonium molecules which are weak scatterers with very similar electron density and also a significant amount of disorder associated with them. It would be possible to find thousands of different distributions of these sites within the pores which give a satisfactory fit. Therefore, this is not an assessment that Zhao's assignment is wrong but rather a different interpretation of the data. Thermal parameters kept refining to negative values and were grouped together by element type. This did not help for the thermal parameters of carbon atoms which kept refining to nonsensical values. They were therefore fixed to the original values determined by Zhao. At the end of the refinement hydrogen atoms were placed geometrically onto the carbon atoms. The final R_{wp} of the fit was 2.31% with a GoF of 3.35. The GoF is likely as high owing to the large amount of data collected for the refinement which can cause an inflated value.[131] Atom positions of the refined structure are given in Table 3.4 with a graphical depiction in Figure 3.5. Further crystallographic information is provided in the appendix.

Table 3.4) List of atom positions, occupancies and thermal parameters for the refined structure of BIRM-1

Atom	x	y	z	Occupancy	B_{eq}
C1	0.3103	0.2360	0.1716	1	2.132
C2	0.3101	0.2956	0.1699	1	2.495
H2A	0.3146	0.3143	0.1196	1	3.000
H2B	0.2698	0.3065	0.1891	1	3.000
C3	0.3484	0.3213	0.2320	1	2.321
H3A	0.9885	0.3180	0.2085	1	2.763
H3B	0.3490	0.2986	0.2799	1	2.763
O1	0.3987	0.4306	0.2929	1	0.745(532)
O2	0.3203	0.4532	0.1665	1	0.745(532)
O3	0.2700	0.2107	0.1315	1	0.745(532)
O4	0.2812	0.4108	0.2936	1	0.745(532)
O5	0.3583	0.2015	0.2012	1	0.745(532)
P1	0.3356	0.4054	0.2436	1	1.394(539)
Zn1	0.2482	0.1311	0.1153	1	0.813(269)
N101	0.4747	0.2090	0.1995	1	5.425(1543)
O201	0.2775	0.9401	0.0940	0.470	5.321(758)
O202	0.2610	0.9335	0.0394	0.452	5.321(758)
O203	0.3314	0.8816	-0.0251	0.321	5.321(758)
O301	0.5141	0.4158	0.2775	0.641	5.321(758)
O302	0.4827	0.3299	0.3088	0.801	5.321(758)
O401	0.3416	0.8697	0.0436	0.454	5.321(758)
O402	0.4095	0.8446	0.1560	0.260	5.321(758)
O403	0.4457	0.9324	0.1776	0.125	5.321(758)
O501	0.4375	0.1961	0.3653	0.207	5.321(758)
O502	0.2939	0.1962	0.3468	0.243	5.321(758)
O601	0.2131	0.2963	-0.0024	0.458	5.321(758)

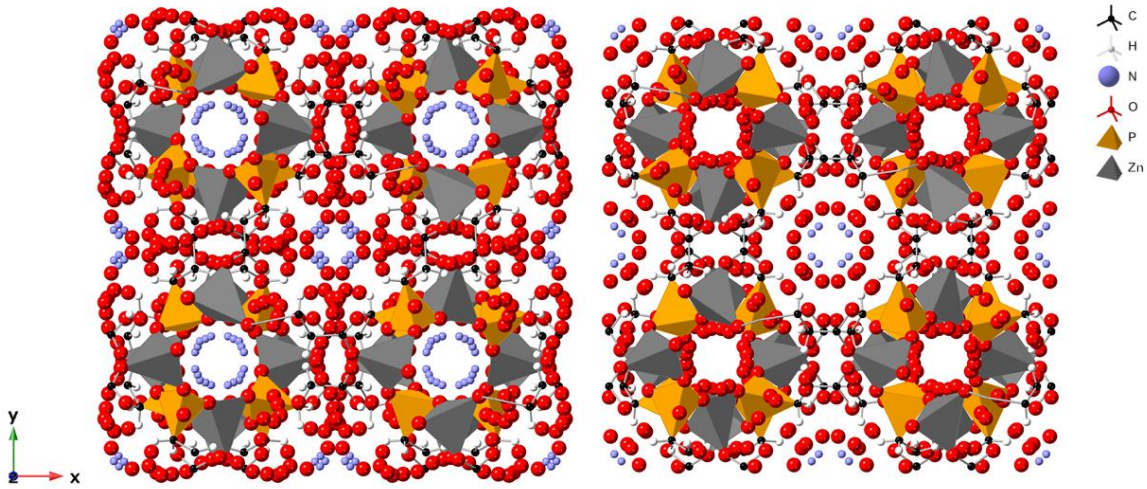

Figure 3.5) Crystal structure of BIRM-1 as determined by Zhao (left) and as refined in this work (right).

3.4 Facile Room Temperature Synthesis of BIRM-1

The unreliable synthesis of BIRM-1 *via* a hydrothermal route is a significant problem when trying to study the material. A lot of time and resources are wasted in attempting to get a phase pure product. As such, refining the synthesis or developing an alternative synthetic route would be an important development in this work.

As the sensitivity to temperature in the hydrothermal synthesis is believed to come from the *in-situ* decomposition of urea, it was hypothesised that using a simple base may be able to lead to the formation of BIRM-1. A precursor solution of zinc nitrate and 3-phosphonopropionic acid was prepared using the same quantities used in the hydrothermal synthesis, shown in Table 3.1. Note that TEAB was not used in this synthesis. To this solution ammonium hydroxide was added dropwise until a pH of ca. 6 was reached. A white precipitate formed, was filtered and left to dry in air. The product was a white powder with indistinct morphology.

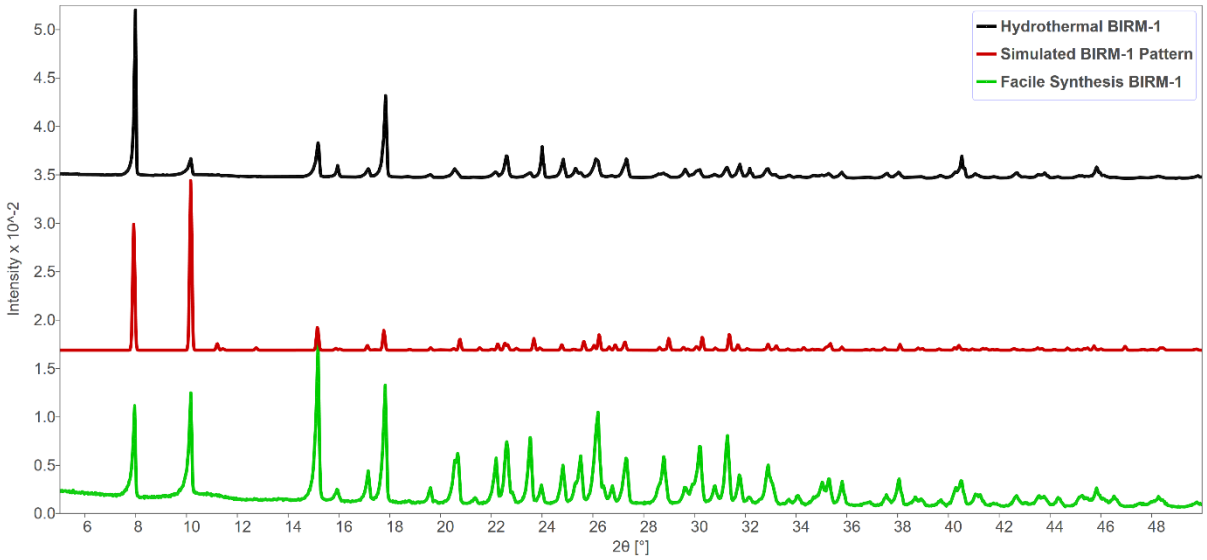

Figure 3.6) Powder diffraction pattern of hydrothermal BIRM-1 (black), a simulated diffraction pattern of BIRM-1 based on the crystal structure published by Zhao[59] (red) and the powder diffraction pattern from the product of the room-temperature synthesis (green).

The powder diffraction pattern of this product is shown by the green trace in Figure 3.6, above. Though there are significant differences in the relative intensities of peaks, the peak positions are the same as those from the hydrothermally synthesised BIRM-1, indicating the same unit cell. The differences in relative intensities could be due to a preferred crystal orientation effect due to the hydrothermal BIRM-1's large needle-shaped crystals compared to the powder obtained from the room-temperature synthesis. The difference in crystallite size can be seen clearly in Figure 3.7, below. Additionally, there could be differences in hydration level or cation content within the channels of the material, such as the presence of the TEA^+ cation in the hydrothermally synthesised product. Henceforth the product made *via* the hydrothermal route will be denoted as HT-BIRM-1 and the product of the room temperature synthesis RT-BIRM-1.

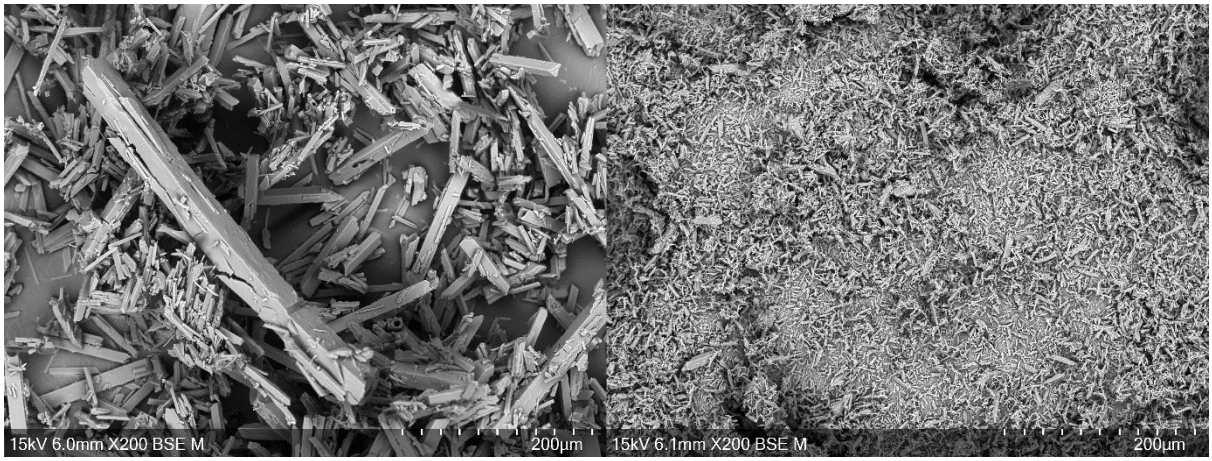

Figure 3.7) SEM images of HT-BIRM-1 (left) and RT-BIRM-1 (right) at 200× magnification

3.4.1 Structure

Rietveld refinement of powder x-ray diffraction data of RT-BIRM-1 using the structural model of HT-BIRM-1 was performed and the fit is shown in Figure 3.8. This was done to ensure there are no significant differences in structure between the products of the two synthesis methods. Data for refinement were collected at 120 K on a Siemens D5000 diffractometer in transmission geometry. Data were collected between 5 and 50° 2θ over 32 hours. However, only data starting from 7° were included in the refinement.

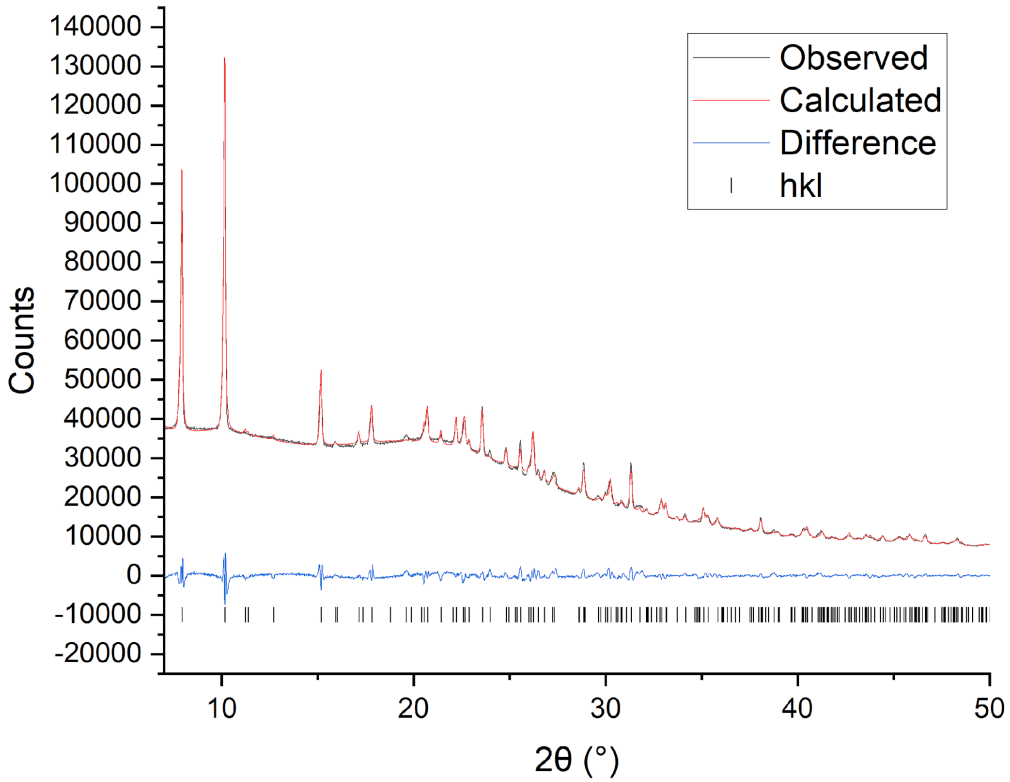

Figure 3.8) Rietveld refinement of BIRM-1 synthesised at room temperature. Data collected at 120 K

This data set shares the unusual background profile seen for in the data collected on the hydrothermally synthesised material, supporting the idea that it is due to the experimental setup. The background was refined using a Chebyshev polynomial with 12 variables. Soft restraints on bond angles for the carbon chain (109.5°) and carboxylate group (120°) were required. After restraints were applied, refinement of the framework was trivial. Atoms were allowed to refine but movement was minimal, showing good agreement between the data and the structural model determined by Zhao.[59] Following this, the atom positions of pore contents were allowed to refine. This led to many atoms 'overlapping' and occupying the same positions, as was the case for the refinement of HT-BIRM-1. This suggests that the occupancies in the model are not accurate. The site which caused most issue in this sense was that of N101, the same site as with HT-BIRM-1, within the large pore. Oxygens from intrapore water kept refining to that position, as well as N102 corresponding to the other cation in the pore. Therefore, the occupancies of both N101 and N102 were allowed to refine in their original positions. N101 refined to an occupancy of 1 whilst N102 refined to a very low value and the decision was made to remove it from the refinement.

If the occupancy of N101 is indeed 1 then due to charge balance it must be the only cation within the structure. As pointed out previously, it is notable that this site is located close to the uncoordinated oxygen from the carboxylate group which would be a source of relative negative charge. Therefore, it would be the most likely location for a cation to be located within the structure. In response to this, the nitrogen atoms located within the small pore were changed to oxygen atoms as they likely represent intrapore water molecules. Allowing the pore contents to refine again, many of the oxygen atoms corresponding to intrapore water continued to overlap. Where this occurred, one of the oxygens would be deleted and the atoms allowed to refine again until no oxygen atoms overlapped. The occupancies of these oxygen atoms were then allowed to refine. The outcome was fewer water oxygen sites than in the starting structure, as well as them being in slightly different locations. However, the occupancy of these sites was typically higher. Overall, the refined structure has ca. 3.4 water molecules per zinc compared to 2.5 in the starting structure. Finally, thermal parameters were allowed to refine. As some were refining to nonsensical values, thermal parameters were grouped together by element. For oxygen, framework components and water oxygens were grouped separately. Thermal parameters of hydrogen atoms were fixed to values 1.2× the value for carbon atoms. The refined crystal structure for RT-BIRM-1 is shown in Figure 3.9 compared to the structural model for HT-BIRM-1. The final refinement had a R_{wp} of 2.25% and GoF of 3.47. Whilst the GoF value was relatively high, this is likely an artifact due to how it is calculated and the large quantity of datapoints collected.[131] A list of atom positions and their details is given in Table 3.5 whilst further crystallographic detail is given in the appendix. Whilst the thermal parameters for framework oxygen, phosphorus and zinc are unreasonably low, it is important to note that they have extremely large errors associated with them.

Table 3.5) List of atom positions, occupancies and thermal parameters for RT-BIRM-1.

Atom	x	y	z	Occupancy	B_{eq}
C1	0.3073	0.2344	0.1705	1	1.025(1875)
C2	0.3025	0.302	0.1784	1	1.025(1875)
H2A	0.3076	0.3205	0.1285	1	1.230
H2B	0.2628	0.3127	0.198	1	1.230
C3	0.3524	0.331	0.2337	1	1.025(1875)
H3A	0.3896	0.3252	0.2073	1	1.230
H3B	0.3501	0.3058	0.2787	1	1.230
O1	0.3918	0.4222	0.2944	1	0.024(908)
O2	0.3232	0.4479	0.1753	1	0.024(908)
O3	0.2703	0.2171	0.1323	1	0.024(908)
O4	0.2725	0.4145	0.2899	1	0.024(908)
O5	0.3545	0.1933	0.2136	1	0.024(908)
P1	0.3327	0.4057	0.2452	1	0.0007(9776)
Zn1	0.2519	0.1328	0.1158	1	0.0007(4744)
N101	0.4777	0.2116	0.2086	1	1.001(2174)
O201	0.2662	0.9359	0.0909	0.838	6.749(1423)
O202	0.2547	0.8553	0.0486	0.255	6.749(1423)
O301	0.5047	0.3701	0.3118	0.711	6.749(1423)
O401	0.3762	0.8526	0.0676	0.515	6.749(1423)
O402	0.4182	0.836	0.1299	0.380	6.749(1423)
O601	0.1784	0.2722	0.03	0.672	6.749(1423)

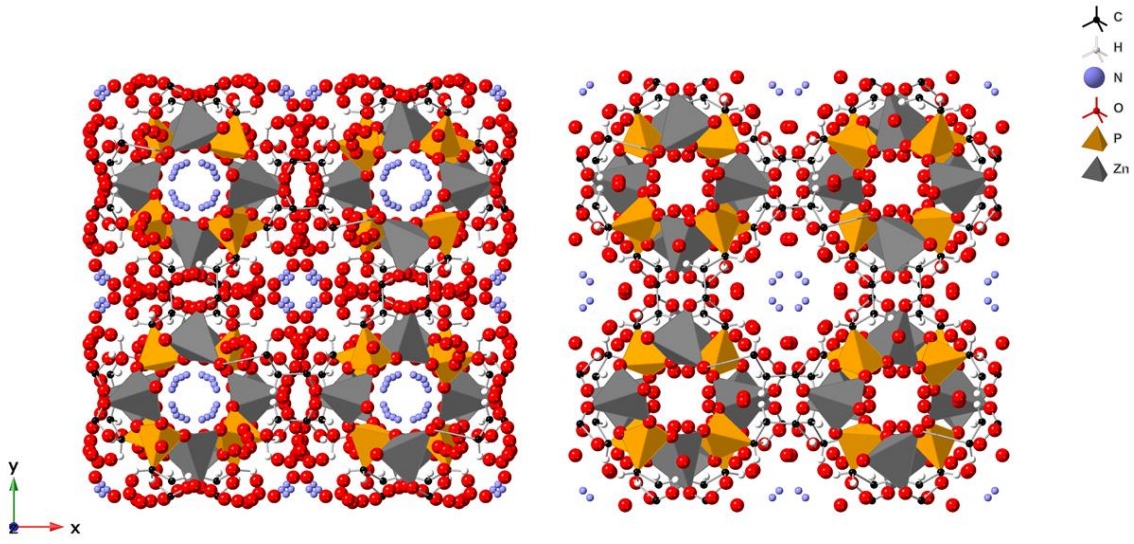

Figure 3.9) Crystal structure of HT-BIRM-1 as determined by Zhao (left) and RT-BIRM-1 (right)

3.4.2 FTIR

Figure 3.10, below, displays the FTIR spectra of BIRM-1 when synthesised *via* the two different routes. There were no significant differences between the two samples, indicating that the same functional groups and connectivity are present in both materials. HT-BIRM-1 did have lower intensity across the broad peak relating to O–H and N–H stretching vibrations. This likely indicates a lower level of hydration or ammonium within the material, despite the fact that the refined crystal structure suggests a higher level of hydration than RT-BIRM-1.

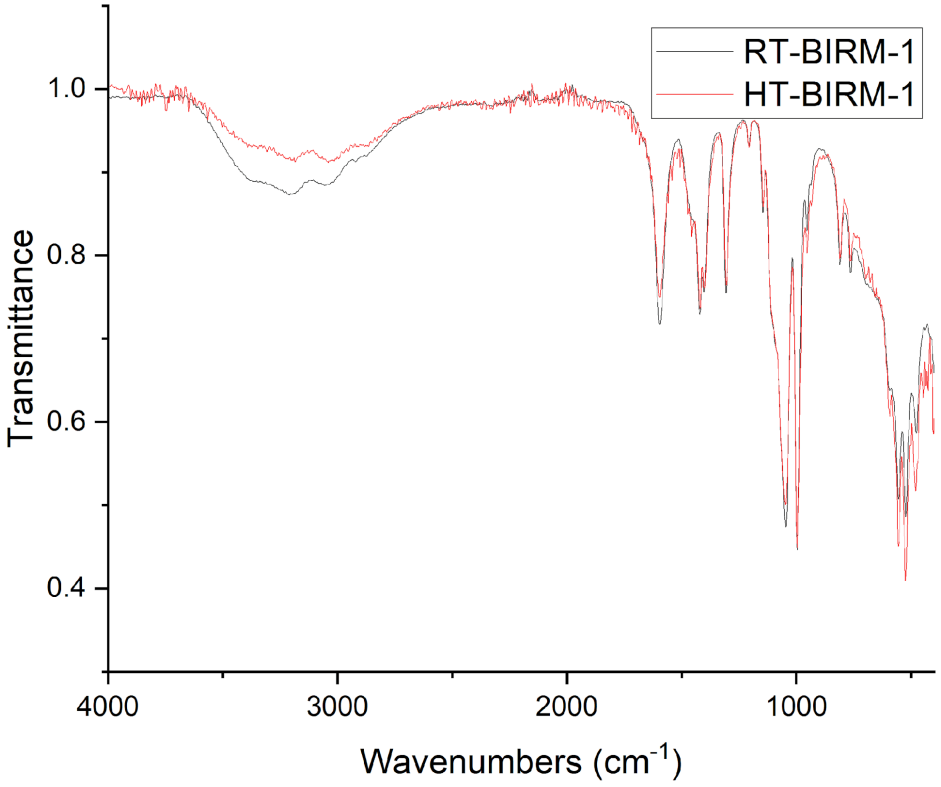

Figure 3.10) ATR-FTIR spectra of HT-BIRM-1 (black) and RT-BIRM-1 (red).

Table 3.6) Observed FTIR peaks and their assignments

Peak (cm^{-1})	Assignment
3400, broad, weak	Water (O–H), Ammonium (N–H)
1596, medium	Carboxylate (COO^-)
1305, sharp, medium	Carboxylate (C–O)
1397, sharp, medium	Carboxylate (COO^-)
1421, sharp, medium	Phosphonate (P–C)
996, sharp, strong	Phosphonate (P–O)

3.4.3 TGA-MS

A comparative thermogravimetric analysis of the two products is shown in Figure 3.11 and Figure 3.12. The TGA shows that there are notable differences in the decomposition profile of each material. The most significant difference is the water content of each and how this water is removed from the material.

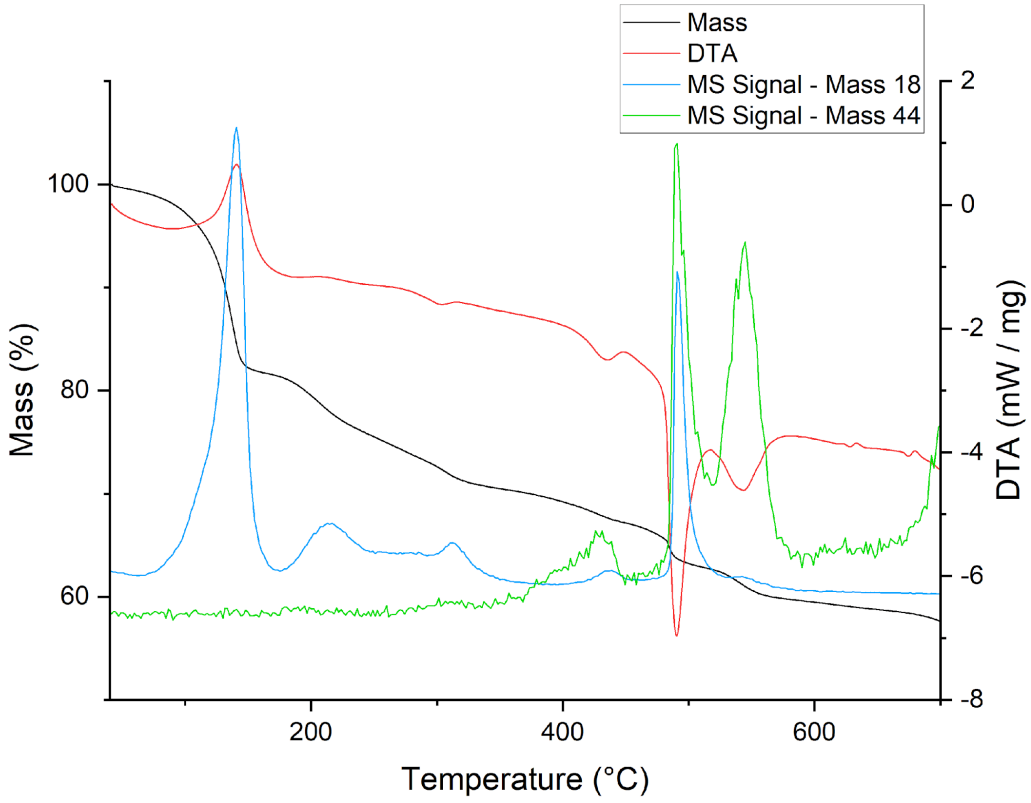

Figure 3.11) Thermogravimetric analysis of HT-BIRM-1

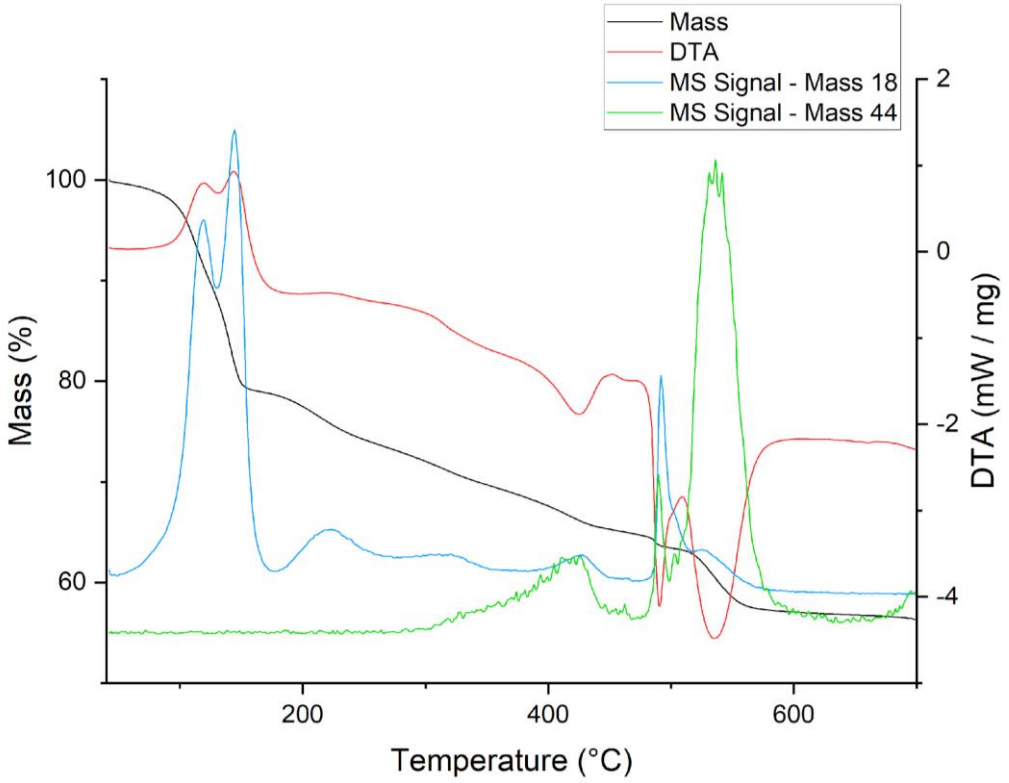

Figure 3.12) Thermogravimetric analysis of RT-BIRM-1

Whilst the water in HT-BIRM-1 is removed in one step, the water from RT-BIRM-1 is removed in two distinct stages. It should be noted that the major dehydration step from HT-BIRM-1 shared a similar starting temperature to that of RT-BIRM-1. This indicates that there are also two dehydration stages for HT-BIRM-1 but that the first stage involves a much smaller amount relative to the second, a slight shoulder to the first dehydration peak can in fact be seen in the MS signal peak for HT-BIRM-1 The two dehydration peaks could be due to water in different chemical environments being removed at different temperatures. The refined structure of RT-BIRM-1 has water and cations in different locations and occupancies compared to HT-BIRM-1. The different quantities of water being removed is in good agreement of the refined crystal structures. Whilst HT-BIRM-1 loses 18.3% of its mass in the 40 – 160 °C range, the calculated amount for total dehydration is 16.12% based on the structure reported by Zhao.[59] For RT-BIRM-1 the agreement is better with a 21.02% loss in mass compared to 21.87% calculated. Additionally, the possible presence of TEAB could occupy much of the pore space in HT-BIRM-1 leading to less water contained within. It appears that the structure reported by Zhao for HT-BIRM-1 gives a more accurate representation of the pore water than the structure refined in this work.

However, the refined structure of RT-BIRM-1 does seem to be a good representation of that material as supported by both TGA and FTIR data.

The other difference in decomposition profile between the two materials is the breakdown of the framework between 490°C and 580°C, where there are two exothermic emissions of carbon dioxide and water. Whilst there is no difference in the temperature at which structural breakdown occurs between the two materials, the first peak is much more prominent for HT-BIRM-1. This could be from the presence of TEAB adding additional organic material in the pores which is burnt off at this point. Alternatively, it could be that the second peak is larger than the first for RT-BIRM-1 due to decomposition of amorphous organic material. It can be observed in Figure 3.6 that the PXRD pattern of RT-BIRM-1 has a higher background indicating non-crystalline material could be present. There is also a peak in the mass spectrometry data in this region for *m/z* = 44, correlating to carbon dioxide given off as the structure breaks down and linker oxidises. This is present for both materials, as would be expected.

Other than the stages of the decomposition profile already discussed, both materials also have three peaks in the mass spectrometry data for *m/z* = 17 and 18 at intermediate temperatures. The peaks are in similar positions for each material but there are slight differences such as relative area under the peaks for each material. This is combined with a consistent loss in mass throughout this temperature range for both materials. Most likely this mass loss and corresponding *m/z* signals are due to release of ammonia.

3.4.4 Synthesis of Layered Phase

Zhao in his PhD work established a connection between 4 different zinc carboxyethylphosphonate phases which can be obtained *via* hydrothermal treatment of the precursor solution used in the synthesis of BIRM-1.[115] These included a layered phase (BIRM-2), the BIRM-1 phase and two denser phases (BIRM-3 and BIRM-4). Zhao put forward the idea that these phases may be related to the degree of decomposition of urea which occurs *in situ* during the synthesis. Work in a later master's project established a relationship between temperature and phase outcome.[118] It was found that at lower temperatures the layered phase would form, followed by BIRM-1 and then the denser phases at higher

temperatures. With this knowledge and the new room-temperature synthesis route to BIRM-1, an experiment was planned to see if these phases could be obtained *via* the room-temperature route. A hypothesis was developed that the layered phase may be obtainable by the same technique as BIRM-1 but by adjusting the pH of the precursor solution to a lower pH, and the denser phases when the solution is adjusted to a higher pH than for forming BIRM-1. The synthesis protocol used in this experiment is given in section 3.2.2. The method used was very similar to that for obtaining BIRM-1 at room temperature, base is added to a precursor solution of zinc nitrate and 3-phosphonopropionic acid. However, to obtain the layered phase the pH was adjusted to ca. 5 compared to ca. 6 for BIRM-1.

Figure 3.13 and Table 3.7, show the results of the synthesis of the layered phase *via* a room-temperature method. The Pawley fit and the resulting lattice parameters show good agreement with the unit cell reported by Zhao in his PhD work.[115]

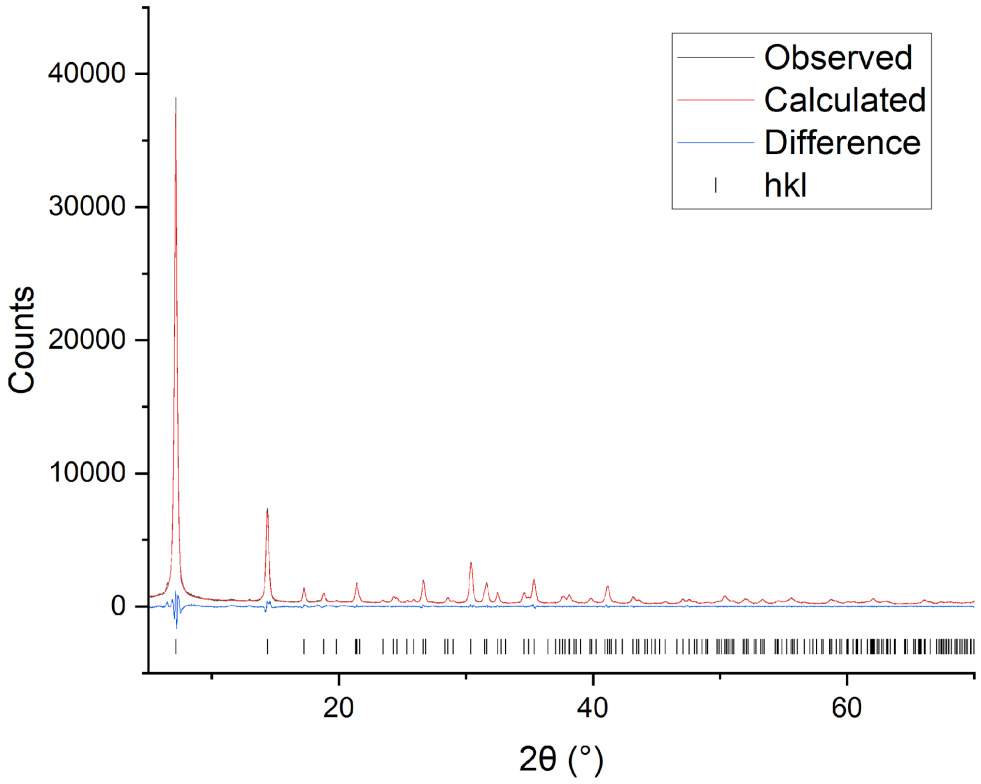

Figure 3.13) Pawley fit of the layered phase successfully synthesised at room temperature using ammonia solution. Calculated pattern in red, observed in blue with the difference in grey. Blue ticks at the bottom represent positions of calculated peaks.

Table 3.7) Unit cell parameters obtained from this work compared to those reported by Zhao[115]

Layered Material	Refined Parameters	Parameters Reported by Zhao[115]
a (Å)	4.8068(4)	4.8021(6)
b (Å)	24.6343(13)	24.6753(27)
c (Å)	5.6525(4)	5.6528(6)
Volume (Å^3)	669.32(7)	669.82(13)

It was found that when the pH was increased to above ca. 8, rather than a transition to the dense phases obtained in previous work, the precipitate would instead redissolve. At very high pH, precipitate would once again form but this was identified *via* powder XRD as zinc hydroxide rather than a phase containing the carboxyphosphonate linker.

3.4.5 Implications for Cation Forms

A major implication of the new room temperature synthesis is the possibility of accessing ion forms of BIRM-1 previously inaccessible due to incomplete ion-exchange. For example, Zhao reported K^+-BIRM-1 with an ionic content of ca. 80% potassium. This new synthesis route might allow access to a 100% potassium cation form.

3.4.5.1 Direct Synthesis of K^+-BIRM-1

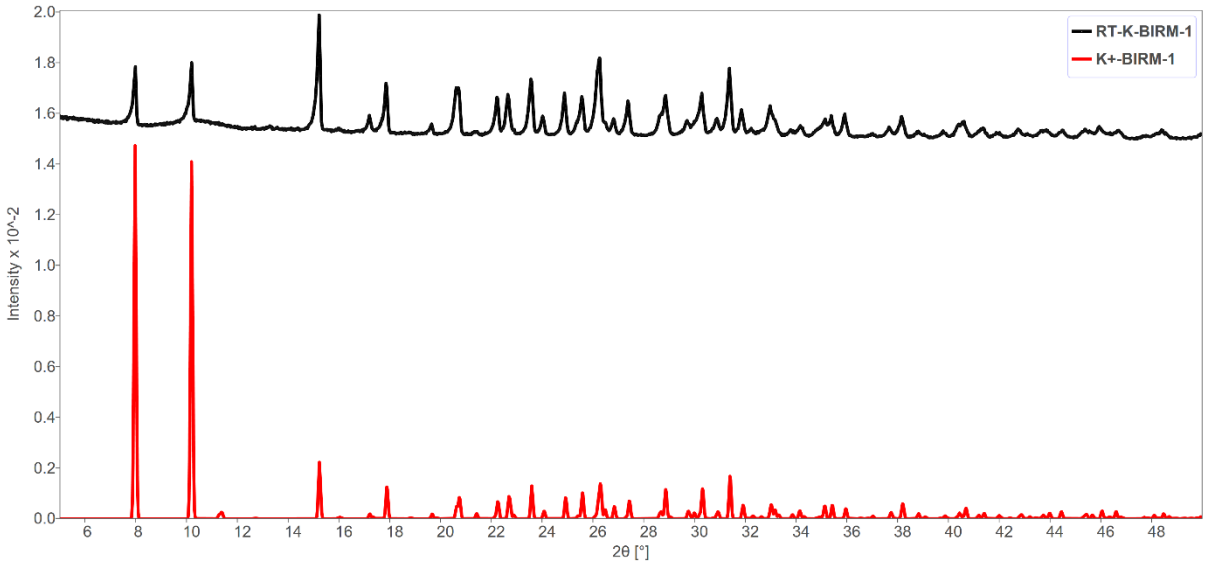

Figure 3.14) The powder diffraction pattern of RT-K-BIRM-1 (black) compared to a simulated pattern generated from the structure published by Zhao[59]

The room temperature synthesis technique was repeated using potassium hydroxide in place of ammonium hydroxide. Figure 3.14, above, shows the PXRD pattern of this product compared to one simulated using the structure published by Zhao from his ion-exchanged single crystals.[59] The powder diffraction pattern shows a good match in terms of peak position indicating the same unit cell but the peak intensities differ significantly. This is not unexpected. The cause is most likely that the product of the ion-exchange had a cation content of ca. 80% potassium with the rest being residual ammonium cations, which would not be present in the direct synthesis. This would cause a significant difference in peak intensities due to the difference in electron density within the structure. Another major contributor to the difference could be the preferred crystal orientation effect. Additionally, any difference in hydration levels would also contribute. As with the room temperature synthesis of the ammonium form of BIRM-1, RT-K^+-BIRM-1 is obtained as a fine powder, making single crystal diffraction an impossibility. Therefore the 80% potassium-exchanged cif file is the best model we have available at present. An attempt at data collection on the D5000 diffractometer at 120 K was undertaken with the aim for producing a Rietveld refinement for the RT-K-BIRM-1 sample. This is shown in Figure 3.15 with lattice parameters given in Table 3.8.

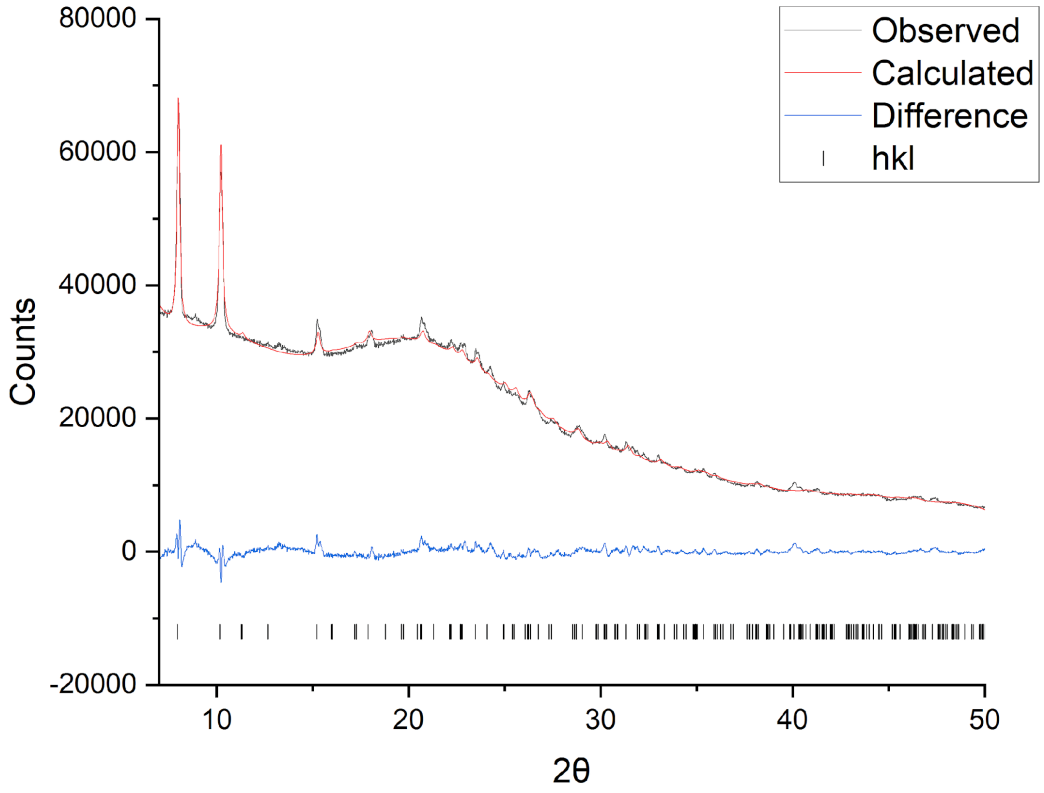

Figure 3.15) Rietveld refinement of RT-K^+BIRM-. Data collected at 120 K

Table 3.8) A comparison of cell parameters determined from the data collected in this work to those reported by Zhao[59]

BIRM-1	Refined Parameters	Parameters Reported by Zhao[59]
a (Å)	22.1581(93)	22.1937(2)
c (Å)	17.9904(141)	17.8525(1)
Volume (Å^3)	8833(11)	8793(1)

The data collected for the Rietveld refinement was of low quality. The reason for this is likely the relatively high absorbance of X-rays by potassium compared to ammonium. The transmission geometry of the D5000 diffractometer used in this work leaves data particularly susceptible to absorption effects. However, the reflection geometry of the D8 leaves the data vulnerable to preferred orientation effects. Better data could be obtained through use of a smaller capillary or from a synchrotron radiation source. Use of a small capillary may hamper attempts to refine the positions of lighter atoms. Due to the poor data quality, a proper refinement of the structure was not possible. Rather, only the background, peak shape, lattice parameters and sample displacement were allowed to refine. The lattice parameters (Table 3.8) are close to those reported by Zhao.[59] The differences can likely be accounted for by the difference

in potassium content and hydration levels. This sample was also made without TEAB present; the TEA cation might occupy the pores and distort the overall structure. The R_{wp} value of the refinement was 2.52% with a GoF of 3.63. It does appear that RT-K-BIRM-1 has been obtained, with some impurities as there are small peaks at ca. 9° and 13° 2θ which are not accounted for from the structure.

The difference in crystallite size of each product is clearly visible in Figure 3.16, below. The effect of synthesis method on crystallite size was the same as that for the ammonium form of BIRM-1.

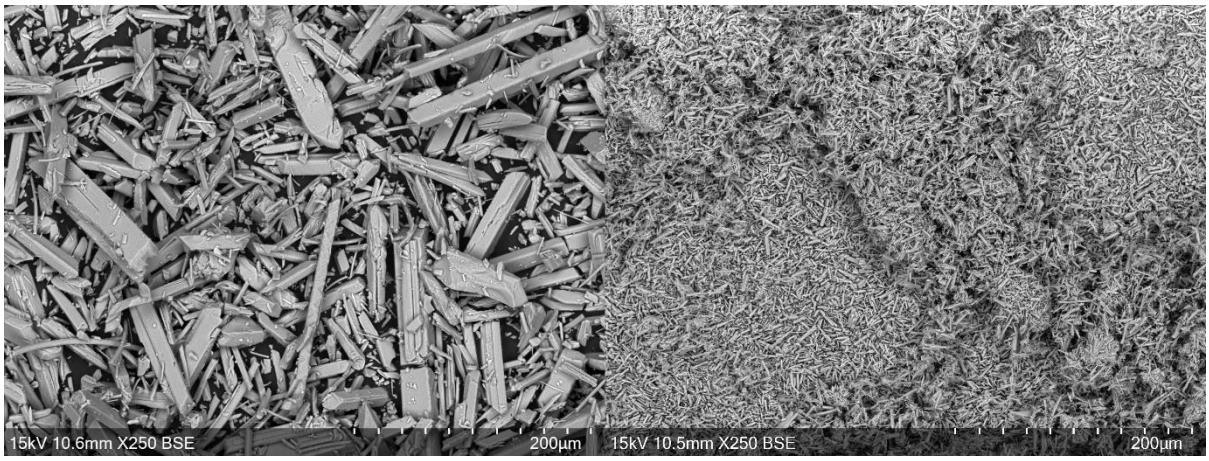

Figure 3.16) SEM images of HT-K-BIRM-1 (left) obtained via *ion-exchange of HT-BIRM-1 and RT-K-BIRM-1 (right) synthesised* via *a direct room temperature method. Images were taken at 250× magnification*

Table 3.9) EDX analysis of K^+-BIRM-1 synthesised in three different ways. Ratios are normalised to the phosphorus content; standard deviation is given as error.

Sample	Zn:P Molar Ratio	K:P Molar Ratio
Potassium Exchanged HT-BIRM-1	1.23 ± 0.03	0.76 ± 0.04
Potassium Exchanged RT-BIRM-1	1.36 ± 0.03	0.60 ± 0.02
Directly Synthesised Potassium RT-BIRM-1	1.09 ± 0.03	0.87 ± 0.02
Theoretical Potassium BIRM-1	1	1

Table 3.9, above, shows the ratios of zinc and potassium to phosphorus within K^+-BIRM-1 synthesised *via* three different routes. There is a clear difference in potassium content. The highest potassium content of 0.87 for every phosphorus is obtained when K^+-BIRM-1 is synthesised directly at room temperature by addition of potassium hydroxide to a precursor solution. The lowest potassium content of 0.6 for every phosphorus atom is for the ion-exchanged RT-BIRM-1. It would be expected that RT-BIRM-1,

with the much smaller crystallite size, would exchange to a greater extent than HT-BIRM-1 as the pores would be much more accessible. It is not clear why it performed relatively poorly at ion-exchange. One explanation could be due to lower crystallinity and the presence of non-crystalline material that does not undergo ion-exchange. The presence of higher background in the powder XRD pattern of RT-BIRM-1 supports this. The differences in zinc content are unexpected. Whilst EDX is, at best, an estimation of elemental composition, the measured zinc levels are far enough apart that it is a real difference being observed. It could be that some zinc has occupied extra-framework cation sites within the pores for some of the samples.

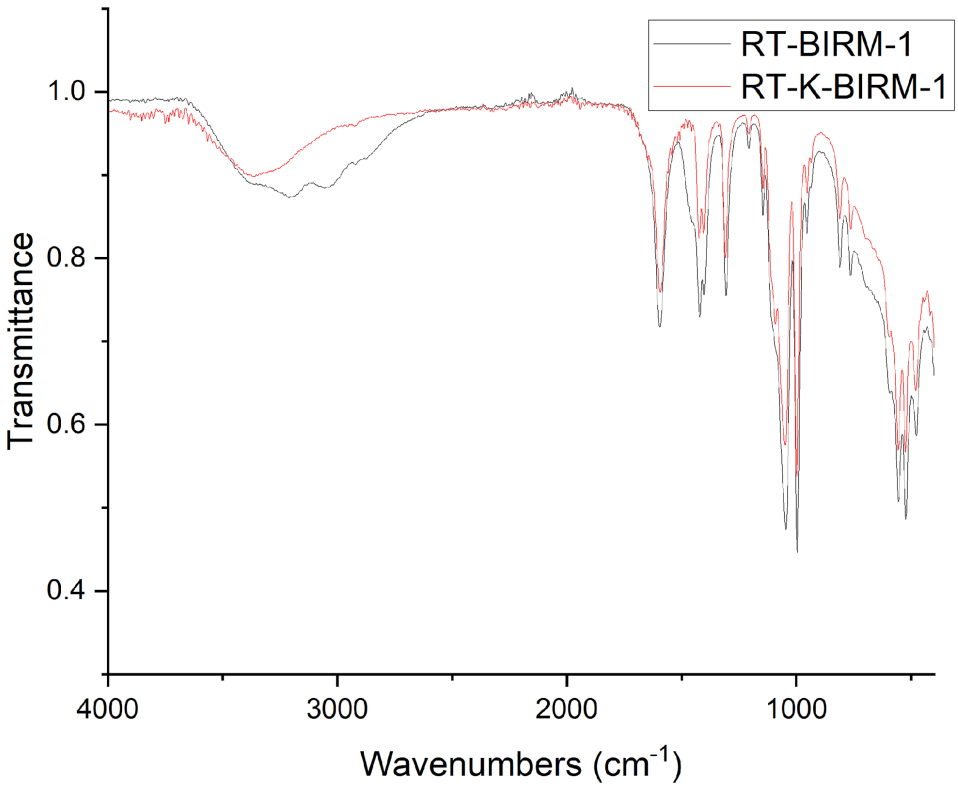

Figure 3.17) ATR-FTIR spectra of RT-BIRM-1 (black) and RT-K-BIRM-1 (red)

Figure 3.17 shows FTIR spectra of both the ammonium-containing RT-BIRM-1 and the potassium RT-K^+-BIRM-1. The spectra are very similar with the exception of the broad peak found at high wavenumbers which relates to both O-H and N-H stretching vibrations. As can be expected, the broad peak for RT-K-BIRM-1 is much smaller as the contribution from N-H centred around 3000 cm^{-1} is not

there due to ammonium not being present. The only other discrepancy between the two spectra is a peak that presents as a shoulder due to overlap, located at about 1450 cm^{-1} in the RT-BIRM-1 FTIR spectra. This peak originates from the N-H bending vibration and is further evidence of the presence of ammonium cations. The rest of the spectra being very similar is a good indication that the connectivity of the frameworks in the two materials is identical, in other words, the only difference between RT-BIRM-1 and RT-K-BIRM-1 is the cationic content of the pores.

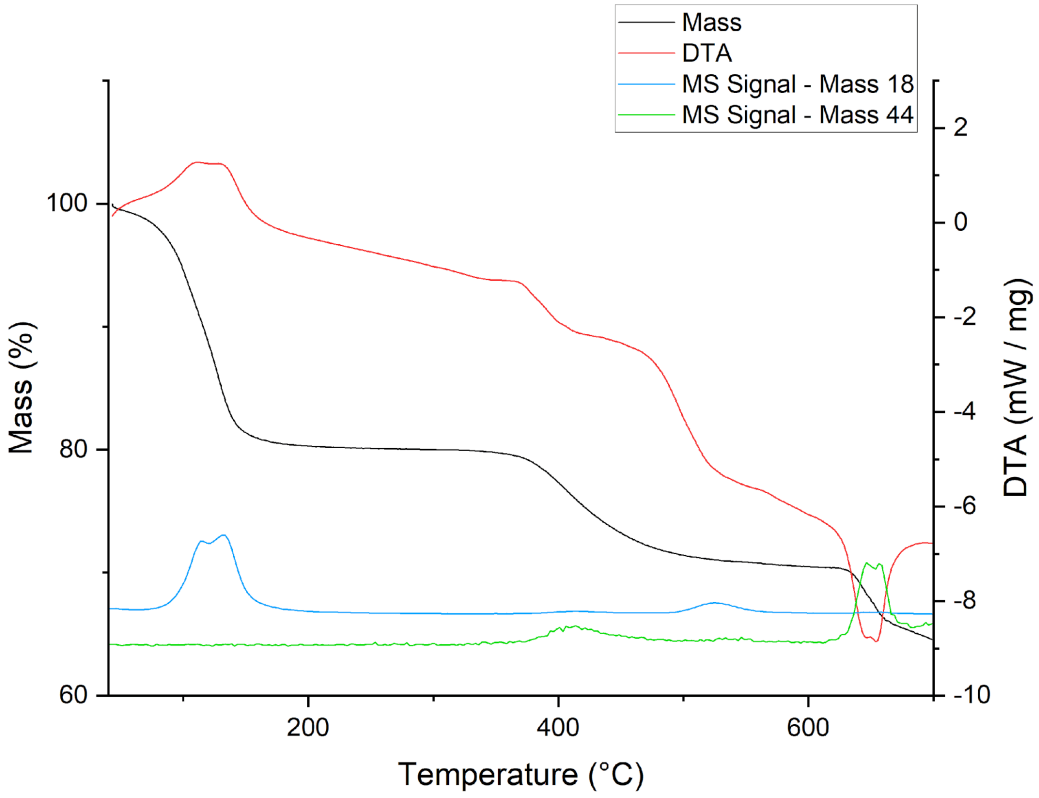

Figure 3.18) Thermogravimetric analysis of RT-K-BIRM-1

Figure 3.18, above, shows a TGA-MS plot of RT-K-BIRM-1. It shares some similarities with the TGA-MS plot for RT-BIRM-1, i.e. the ammonium form of BIRM-1, shown in Figure 3.12. These similarities include the two mass 18 peaks just above 100°C and associated 20% mass loss, and a mass 44 emission around 400°C. The dehydration step showing a 20% mass loss is consistent with the material containing 3.33 molecules of water per zinc atom. There are also many differences in the decomposition profile of the two materials. For instance, the ammonium form of BIRM-1 undergoes a continuous loss of mass between 200°C and 500°C whereas the potassium form shown here has a stable plateau in most of this

region. This difference can be attributed to loss of ammonia and is supported by the mass 18 emission line in Figure 3.12. The mass loss from the potassium form at 400°C appears to be from a partial collapse of the framework as evidenced by the slight emission of mass 44, correlating to carbon dioxide. As this sample was made without the TEAB salt present, this mass 44 emission must be from partial pyrolysis of the organic linker, likely a decarboxylation. Total decarboxylation of the material would lead to a mass loss of 18%. The mass loss observed in this step is only 10%. This could either be due to a partial decarboxylation or formation of carbonates. The last step in the decomposition profile at ca. 650°C with accompanying *m/z* 44 and exothermic DTA peaks occurring at a higher temperature for the potassium form of BIRM-1 compared to ammonium form where this step occurred in two stages at around 490°C and 540°C. Figure 3.19 shows a Pawley fit of the products obtained after TGA of RT-K-BIRM-1. The same products were obtained as were identified by Zhao, those being potassium zinc phosphate and potassium tetrazinc phosphate.[115] The presence of the latter phase suggests an excess of zinc compared to potassium in the structure, which is also indicated by the EDX results earlier in this section. This could be due to some zinc being present in place of potassium in the pores of the material. As suggested by Zhao, there could also be amorphous potassium phases present after TGA.[115] Alternatively, potassium oxides are known to be volatile at relatively low temperatures and this may explain the deficiency of potassium in the product phases.[138]

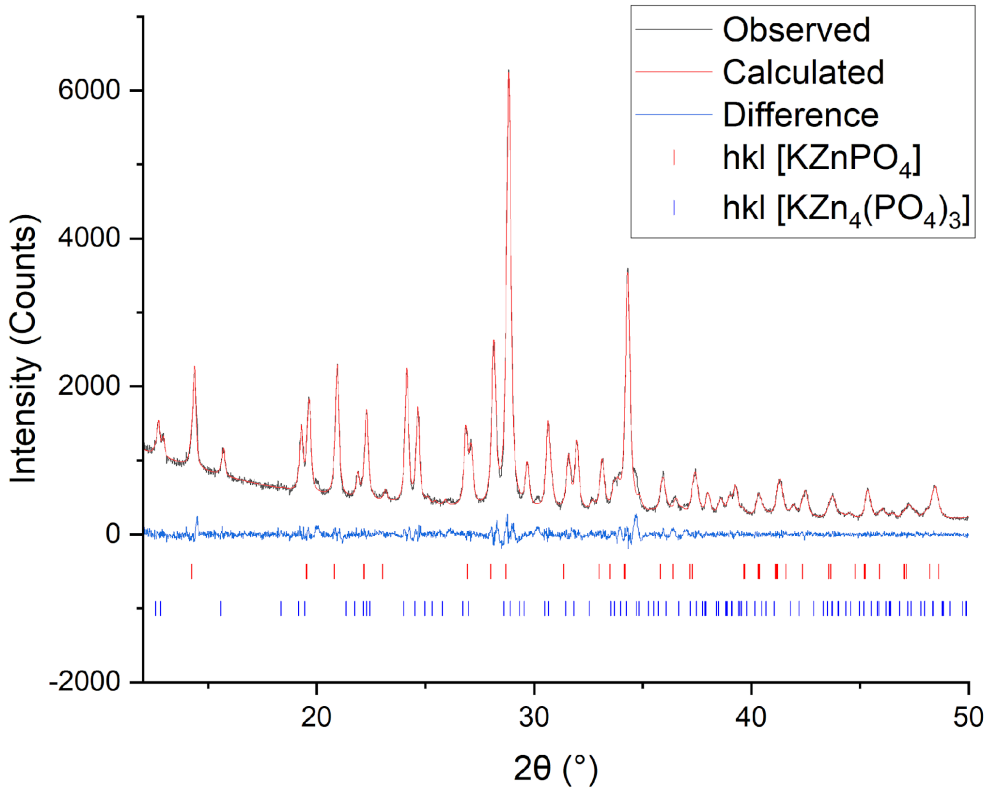

Figure 3.19) Pawley fit of the decomposition products formed during TGA of RT-K-BIRM-1

3.4.5.2 Direct Synthesis of Na^+-BIRM-1

After the success in directly synthesising both the standard ammonium form of BIRM-1 and the potassium form, attention was turned towards the sodium form. Figure 3.20, below, shows the PXRD pattern collected from the product of this attempt in black, compared to that of RT-BIRM-1 in red.

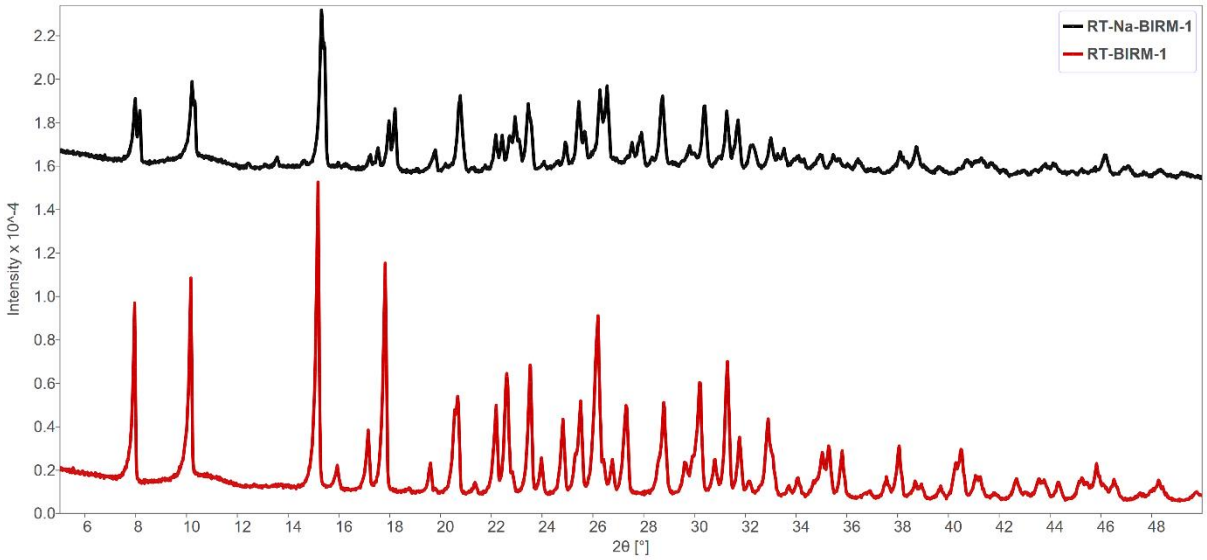

Figure 3.20) Powder X-ray diffraction pattern of RT-Na-BIRM-1 (black) and RT-BIRM-1 (red)

The pattern from RT-Na-BIRM-1 shows the characteristic split peaks of the sodium form which is a result of lower symmetry (sodium form BIRM-1 crystallises in an orthorhombic space group, Pnma) compared to ammonium form BIRM-1. Unfortunately, due to similar electron density and therefore scattering power between N, O and Na it has not thus far been possible to develop a full structural model of Na-BIRM-1 from single crystal diffraction. Therefore, it has not been possible to conduct a full Rietveld refinement of this phase, however, a qualitative assessment can be made by looking at the similarity of the powder patterns displayed in Figure 3.20. The patterns do share similar features and peak positions with a few differences such as RT-Na-BIRM-1 having a peak at $2\theta = 6.5°$ as well as significant differences in relative peak intensities which is not unexpected especially given the splitting of peaks. It should also be noted that the features found in the diffraction pattern of RT-Na-BIRM-1

were also found in Zhao's product of hydrothermal BIRM-1 ion-exchanged with sodium.[115] Using the lattice parameters determined by Zhao, it was possible to conduct a Pawley fit of the data.

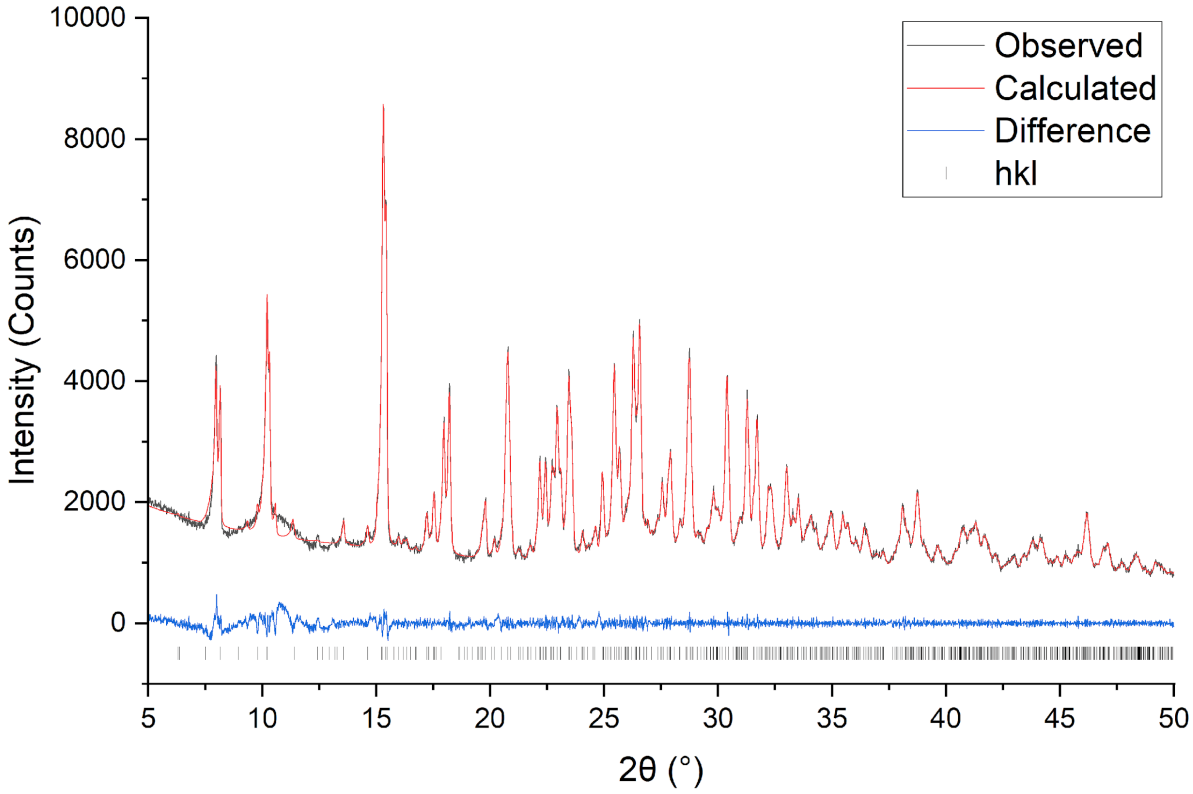

Figure 3.21) Pawley fit of RT-Na-BIRM-1 showing the measured diffraction pattern (black) the calculated Pawley fit (red) and the difference between them (blue). hkl ticks are represented in black at the bottom. R_{wp} =3.77%

Table 3.10) Unit cell parameters obtained from the Pawley fit in Figure 3.21 compared to those reported for Na-BIRM-1 by Zhao[115]

Na-RT-BIRM-1	Refined Parameters	Parameters Reported by Zhao for Na^+ exchanged BIRM-1[115]
a (Å)	22.1686(23)	22.2150(5)
b (Å)	21.6764(19)	21.5250(5)
c (Å)	18.0522(31)	18.0773(3)
Volume ($Å^3$)	8674(2)	8844(4)

Figure 3.21 and Table 3.10, above, show the results of a Pawley fit on the RT-Na-BIRM-1 produced in this work using the lattice parameters from Zhao's indexing of sodium-exchanged hydrothermal BIRM-1 in his work as a starting model.[115] The refined parameters differ slightly from those found by Zhao. There are multiple possible explanations for this, the most obvious one being the cationic content. Sodium cations have a slightly smaller hydrated radius than ammonium cations (2.13 Å and 2.18 Å, respectively). This could lead to the slight reduction in unit cell volume as Zhao's exchanged samples were not 100% sodium form. Another contributor could be differences in hydration such as has already been shown between HT-BIRM-1 and RT-BIRM-1 in section 3.4 from TGA data.

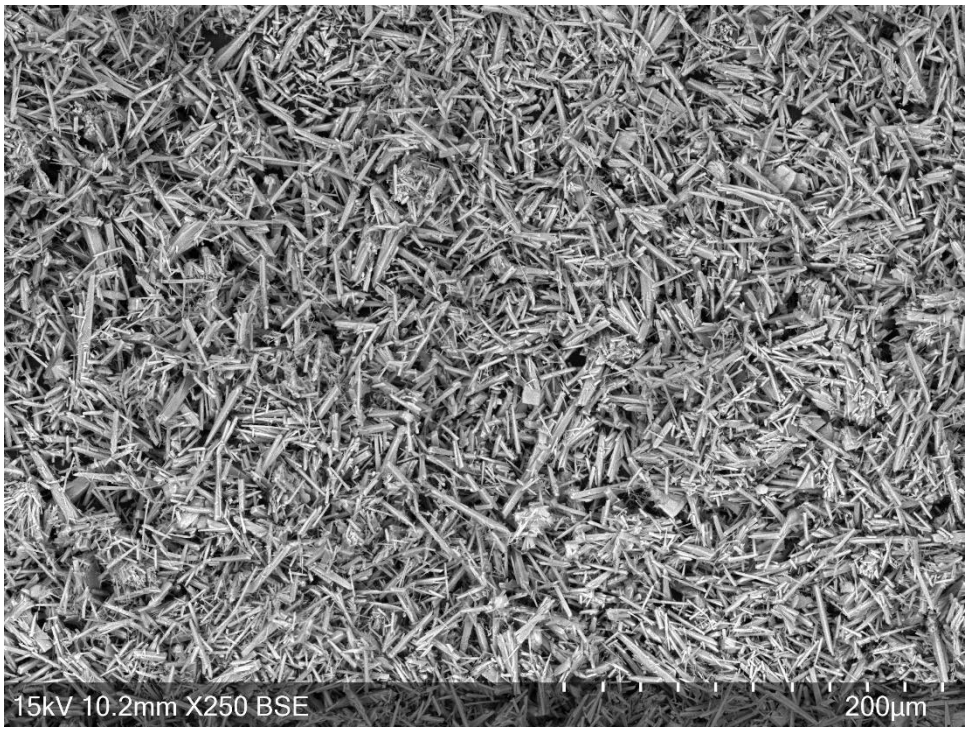

Figure 3.22) SEM image of RT-Na-BIRM-1 taken at 250× magnification

Figure 3.22, above, is an SEM image of directly synthesised RT-Na-BIRM-1 showing that the needle-shape morphology, that all BIRM-1 phases found so far share, has been maintained. The SEM image also shows the small size of the crystals obtained, consistent with those of the ammonium and potassium forms of RT-BIRM-1.

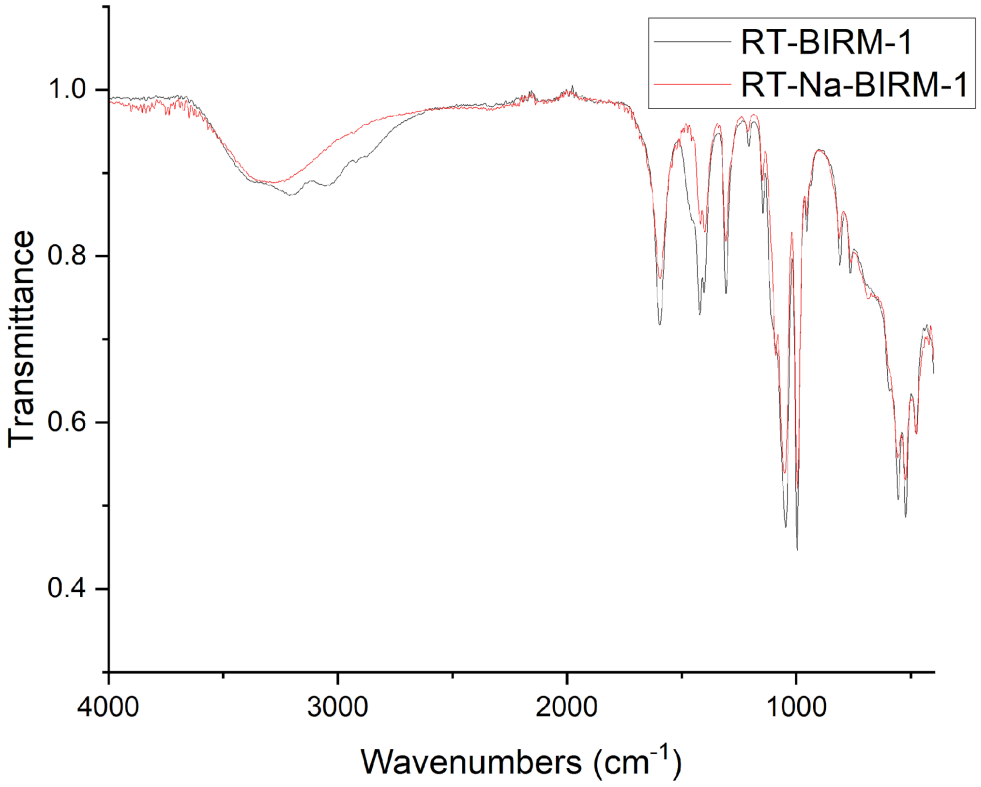

Figure 3.23) ATR-FTIR spectra of RT-BIRM-1 (black) and RT-Na-BIRM-1 (red)

Figure 3.23, above, shows an FTIR spectra of RT-Na-BIRM-1 compared to that of the ammonium form RT-BIRM-1. The lack of ammonium in RT-Na-BIRM-1 is clear from the spectra, due to the loss of the broad peaks in the region around 3000 cm^{-1}. In the ammonium form RT-BIRM-1 N-H stretching vibrations present as peaks in this region, expanding the broad peak at slightly higher wavenumbers that is due to O-H stretching vibrations. Like RT-K-BIRM-1, RT-Na-BIRM-1 also does not have a peak which is present in the FTIR spectra for the ammonium form at around 1450 cm^{-1}. This peak is due to N-H bending vibrations. The rest of the two spectra are quite similar which confirms that the same framework connectivity is present in both materials. This is notable as the powder patterns of each material suggest different crystal structures.

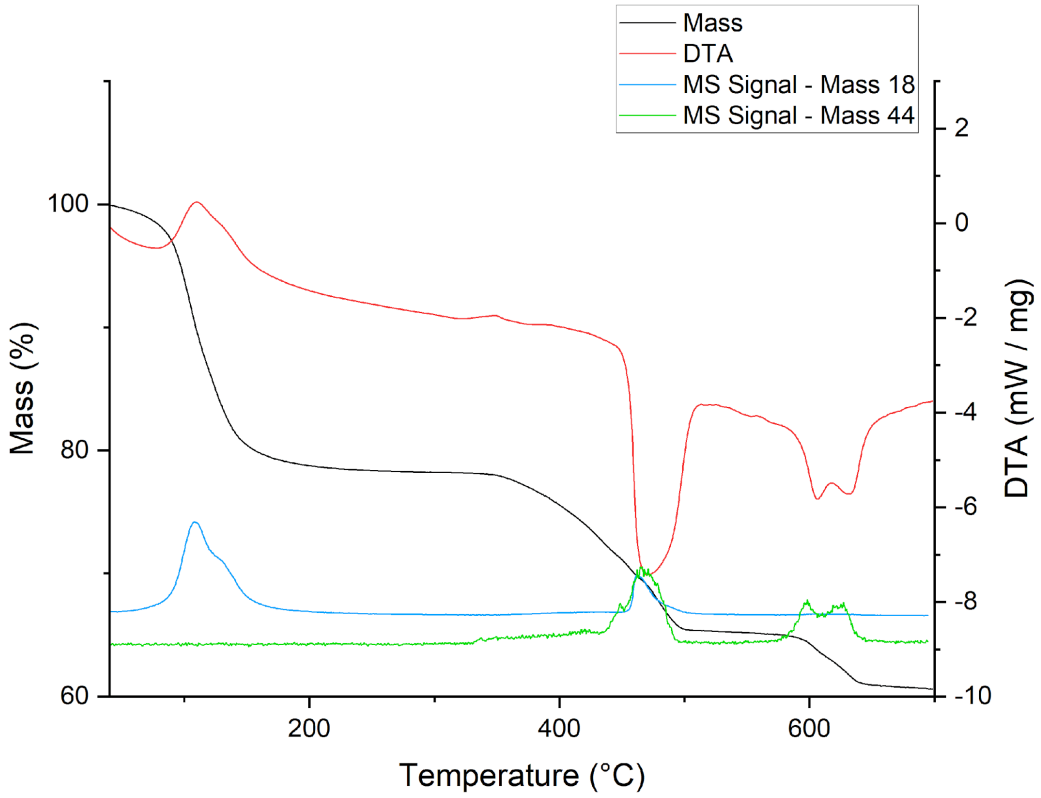

Figure 3.24) Thermogravimetric analysis of RT-Na-BIRM-1

Figure 3.24, above, shows the thermogravimetric analysis of RT-Na-BIRM-1. The overall thermal decomposition appears very similar to that of RT-K-BIRM-1, as well as being very similar to that reported by Zhao for the hydrothermally synthesised and ion-exchanged Na-BIRM-1.[115] The initial mass loss in the dehydration step of 21.7% is consistent with the material containing 2.89 molecules of water per zinc atom, which is slightly higher than the 2.5 that was assumed by Zhao.[115] The last decomposition step shown in Figure 3.24 occurred at a slightly lower temperature than was found for RT-K-BIRM-1. In addition to this, the decomposition step around 400°C is much more exothermic for RT-Na-BIRM-1 compared to RT-K-BIRM-1. The mass loss during the decomposition step around 400°C was also much larger for RT-Na-BIRM-1 compared to RT-K-BIRM-1 (ca. 15% compared to 10%, respectively). This suggests a significant difference in the decomposition pathways of each material.

3.4.6 Titration Curve of RT-K^+-BIRM-1 Synthesis

In order to understand better the formation of BIRM-1 in the room temperature method, the pH was measured whilst known quantities of 2 M KOH were added. This was done in order to see the

deprotonation steps involved in the formation of the material. The titration curve measured is shown in Figure 3.25, below. KOH was chosen as the base due to ammonia solution being quite volatile and hence difficult to get a precise concentration.

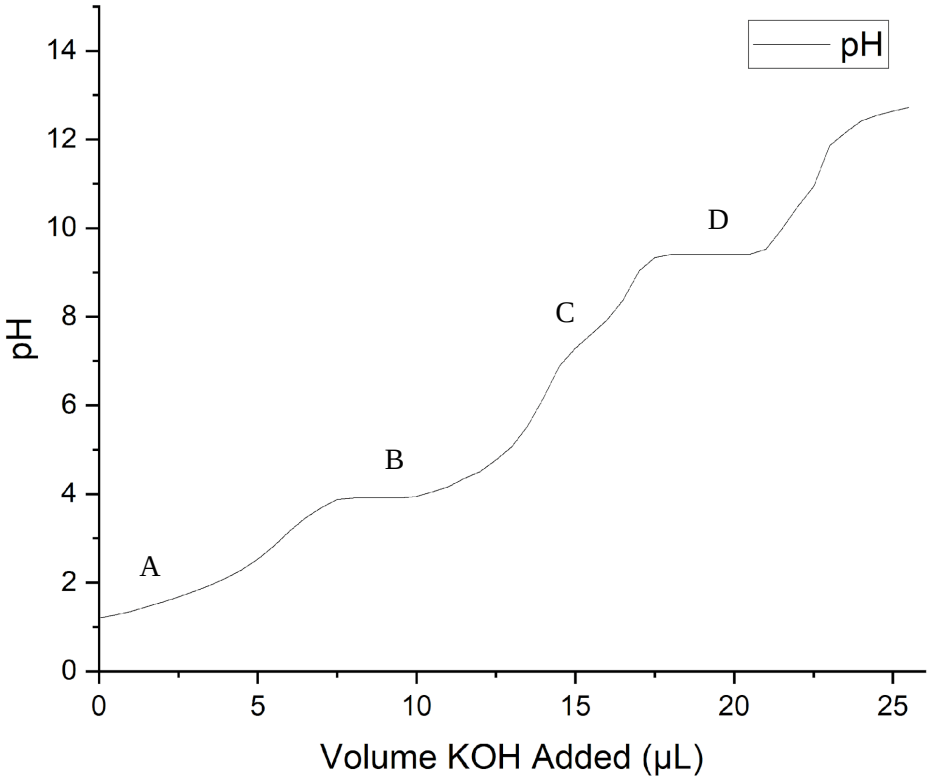

Figure 3.25) A titration curve of RT-K-BIRM-1 synthesis

In the titration curve, at least 4 plateaus, representing a deprotonation occurring can be found, labelled A-D, though C is not a particularly clear plateau there is a definite levelling of the curve. Three of these plateaus are related to deprotonation of the linker and the fourth is likely related to formation of a zinc hydroxide species.[139] Figure 3.26 is the structure of the linker used in the synthesis of BIRM-1 with the acidic protons labelled A, B and C, correlating to the equivalence point on the titration curve at which they are fully deprotonated. RT-BIRM-1 can be obtained at a pH ca. >6, this equates to just before the point labelled C in Figure 3.25, likely at the point where the third proton begins to be removed from the linker. This suggests that BIRM-1 begins to form before the linker is fully deprotonated. Zhao found that ion-exchange of BIRM-1 could be conducted at a pH of 5.5, seemingly below the pH at which the linker would be fully deprotonated.[115] This is likely possible due to coordination to the zinc metal which

would enable some resistance to the linker becoming protonated again. Also of note is that the pK_a of each proton from the linker appears at a slightly lower pH than has been reported in the literature. For example, the plateau of proton 'B' occurs at pH ca. 4, compared to a pK_a of 4.63 in the literature.[139] This is again likely due to the effect of the presence of the zinc ion; stabilising the negative charge of the deprotonation product *via* coordination. Another impact of the presence of the zinc ion is the order in which the protons are removed. Though the second phosphonate proton is the least acidic, BIRM-2 exists as a framework with the phosphonate fully deprotonated but the carboxylic acid remaining protonated. This is likely due to the phosphonates coordination to the zinc allowing the second phosphonate proton to be removed first.

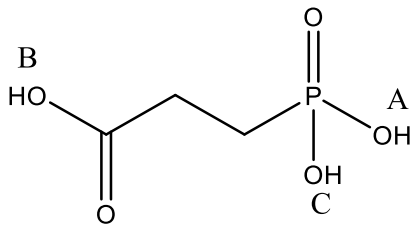

3-phosphonopropionic acid

Figure 3.26) Structure of 3-phosphonopropionic acid with acidic protons labelled A, B and C

The equivalence point labelled D in Figure 3.25 is likely due to deprotonation of water and the formation of zinc hydroxide followed by zinc oxide at high pH. The end product was recovered by vacuum filtration. A PXRD pattern was recorded and the phase was found to be zinc oxide as shown by Figure 3.27.

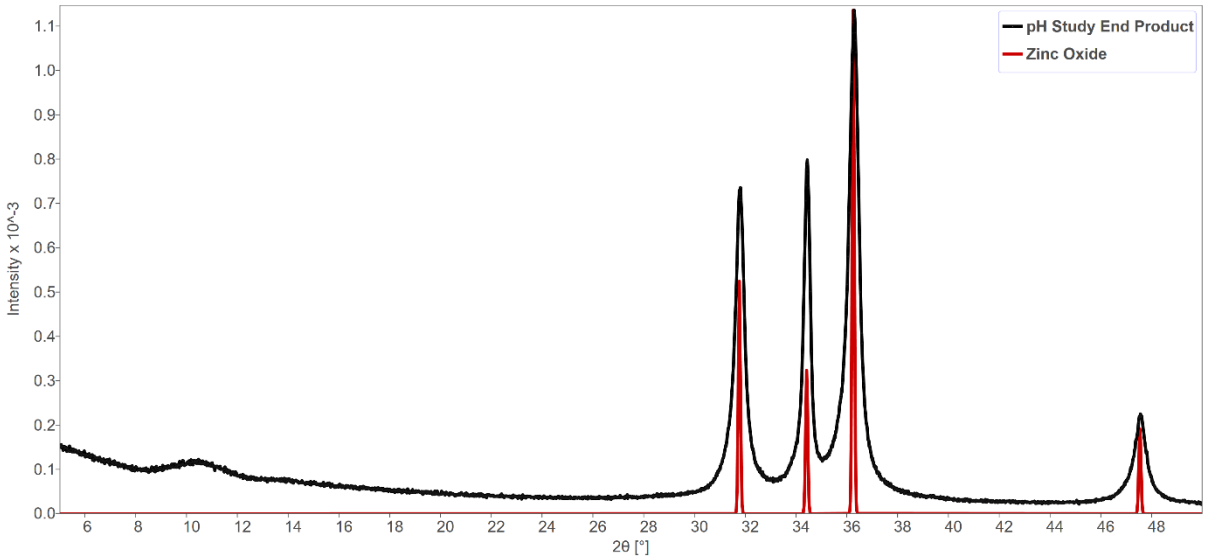

Figure 3.27) The PXRD pattern obtained from the end product of the titration (black) compared to a simulated pattern of zinc oxide (red)

3.4.7 Role of Tetraethylammonium Bromide

The hydrothermal synthesis of BIRM-1 includes the use of the salt tetraethylammonium bromide (TEAB). Originally it was believed the addition of this salt provided a templating effect enabling the formation of BIRM-1. However, BIRM-1 can be obtained *via* the room temperature synthesis regardless of whether TEAB is present or not, suggesting its inclusion is not as crucial as first thought. The presence of TEAB could in fact have an unwanted effect on the material's properties. For example, Zhao found that upon ion-exchange with potassium BIRM-1 would only go to 79% exchange.[59] This could be due to the presence of TEAB and the TEA cation occupying some cation sites. Therefore it is important to establish what, if any, effect TEAB does have on the properties of BIRM-1 The powder diffraction patterns shown below in Figure 3.28 are from the synthesis of RT-K^+-BIRM-1 with and without TEAB present. The diffraction patterns are very similar, indicating little difference in electron density throughout the structure. Though it is worth noting that if the TEA cation was present in the material it

was likely in small amount and subject to a large amount of disorder, leaving little effect on the powder diffraction pattern.

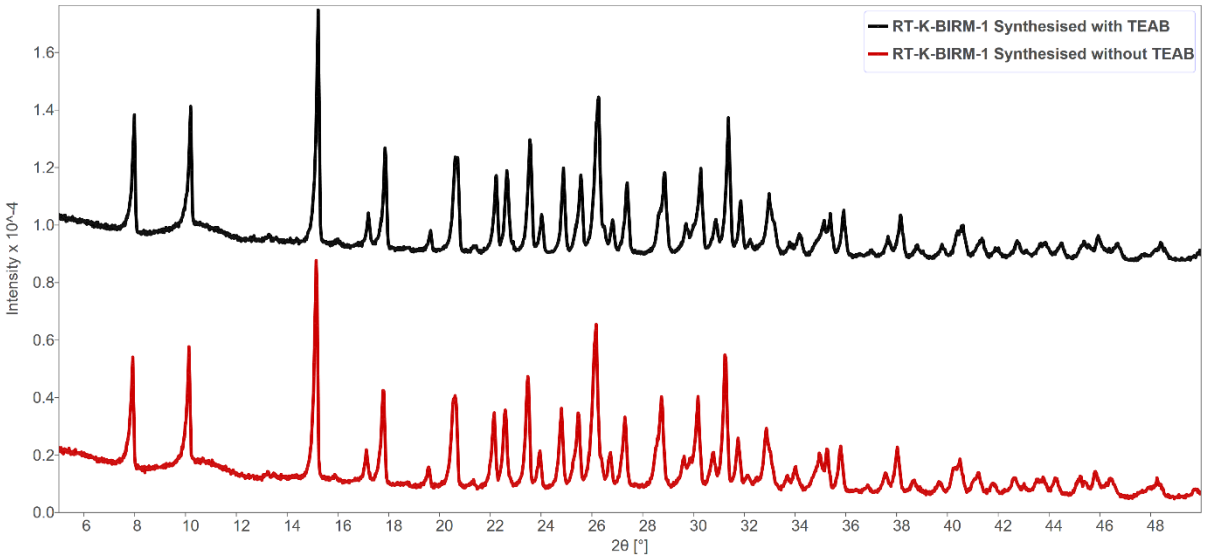

Figure 3.28) Powder X-ray diffraction pattern of K-BIRM-1 made via *the room temperature method, synthesised with TEAB present (black) and without any TEAB present (red)*

A more important matter than whether TEAB is present in the synthesised product is whether this has any effect on the properties of the material. In order to investigate this, EDX analysis of K-BIRM-1 made in various ways, with or without TEAB and either directly or ion-exchanged, was undertaken.

Table 3.11) EDX analysis of K^+-BIRM-1 synthesised in four different ways. Ratios are normalised to the phosphorus content; standard deviation is given as error.

Sample	Zn:P Molar Ratio	K:P Molar Ratio
Potassium Exchanged RT-BIRM-1 (With TEAB)	1.36 ± 0.03	0.60 ± 0.02
Potassium Exchanged RT-BIRM-1 (Without TEAB)	1.08 ± 0.03	0.87 ± 0.02
Directly Synthesised RT-K^+-BIRM-1 (With TEAB)	1.09 ± 0.03	0.87 ± 0.02
Directly Synthesised RT-K^+-BIRM-1 (Without TEAB)	1.16 ± 0.08	1.04 ± 0.11

The data contained within Table 3.11, above, suggests that tetraethylammonium bromide does have an impact on the properties of the material, namely, ion-exchange capability. Both the exchanged product and the product of the direct synthesis contain a higher potassium content when TEAB is not present, suggesting that TEAB is occupying some of the cation sites within the material. Of note is that the

directly synthesised K-BIRM-1 without TEAB has a potassium content around parity with that of phosphorus, suggesting that a 100% potassium form has been achieved in this instance as the theoretical ideal ratio of Zn:P:K is 1:1:1. However, there was a significant amount of error on the measurement and the extent of exchange could be as low as 95% but this is still a significant improvement on the 79% reported by Zhao.[59]

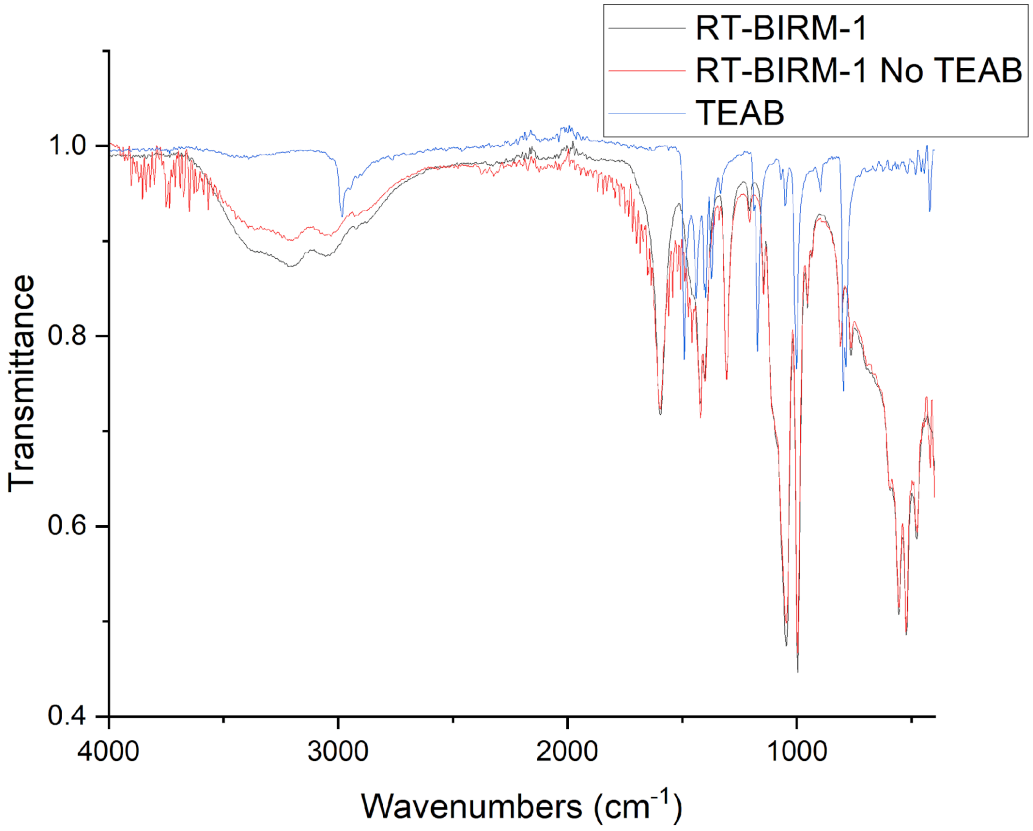

Figure 3.29) ATR-FTIR spectra of RT-BIRM-1 synthesis in the presence of TEAB (black), in the absence of TEAB (red) and the FTIR spectra of TEAB (blue)

Figure 3.29, above, shows a comparison of FTIR spectra from RT-BIRM-1 made in the presence and absence of TEAB alongside the FTIR spectrum of TEAB. The two spectra of RT-BIRM-1 are functionally identical; though the spectrum of RT-BIRM-1 without TEAB has a significant level of noise, this is likely only due to poor contact between the sample and the ATR crystal. None of the peaks from the spectrum of TEAB are visible in the spectra from the RT-BIRM-1 made with TEAB, though this may be because it is only present in small amounts.

From the evidence gathered in this section, it seems likely that the presence of TEAB in the reaction matrix does lead to some of the tetraethylammonium salt occupying the pores of the product and having a negative impact on the material's properties. Given that it is not required for the synthesis of the material anyway, it would seem rather pointless and uneconomical to continue to use tetraethylammonium bromide for the room-temperature synthesis route in the future. That said, the hydrothermal synthesis does seem to rely on the addition of TEAB somewhat as attempts to conduct the synthesis without it have seldom been successful. It is possible it has an effect on the pH of the solution and therefore the product obtained. If this is the case, it should be possible to conduct the hydrothermal synthesis of BIRM-1 without the addition of TEAB on the condition that the quantity of urea and/or the synthesis temperature is adjusted to provide the correct pH conditions.

3.5 Flow Synthesis

The development of the room temperature synthesis opens the path for a continuous flow synthesis of BIRM-1. This would be a very important development if significant scale-up of the material was a goal. For instance, if BIRM-1 is found to excel at a particular application, the scale-up of the material would be crucial to produce the required quantities.

Experiments were conducted with the technical assistance and equipment of Dr Karen Robertson. After an initial proof of concept was run, a series of experiments varying the flow rate of ammonia solution were attempted. The flow rates were calculated such that it would be the equivalent of adding 1.5, 1.7 and 1.8 ml of ammonia solution to an 11 ml precursor solution as per the RT-BIRM-1 preparation method. Figure 3.30, shows the diffraction patterns obtained from the products of these syntheses.

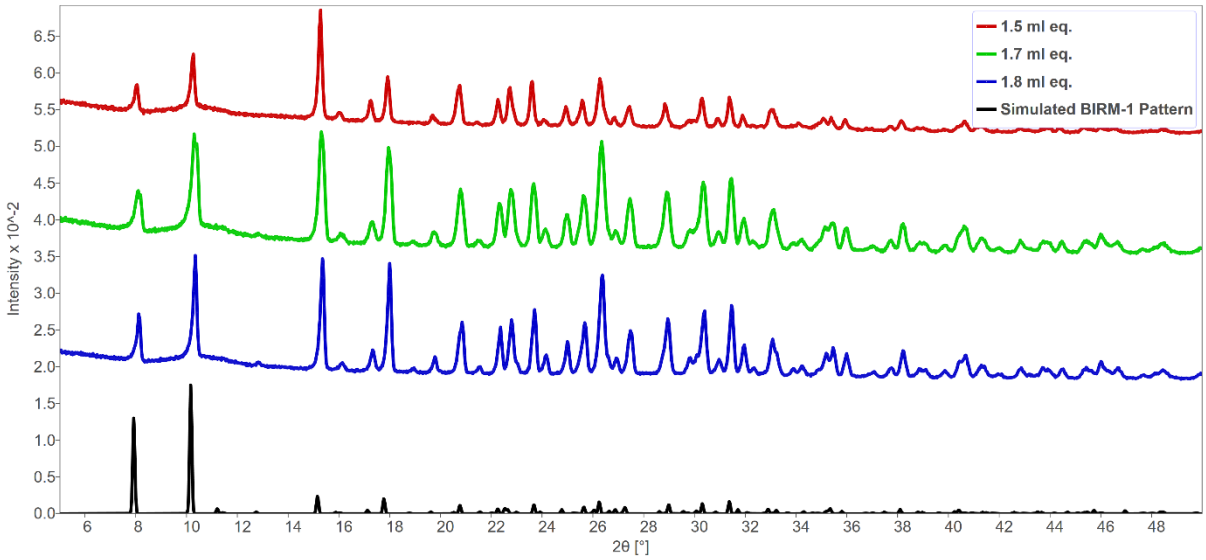

Figure 3.30) PXRD patterns from the products of flow synthesis experiments: 15 ml equivalent (red) 1.7 ml equivalent (green) 1.8 ml equivalent (blue) and a simulated BIRM-1 pattern (black)

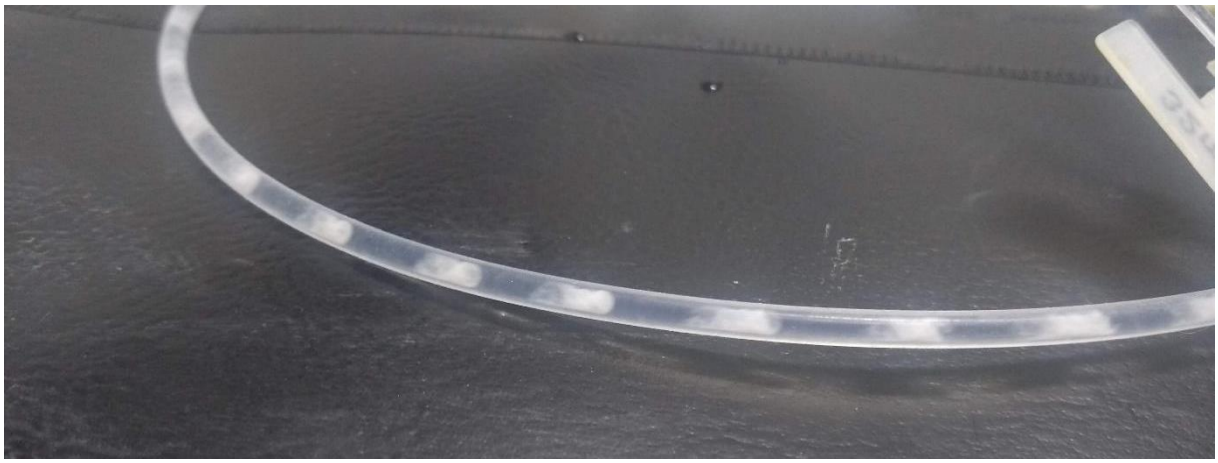

Figure 3.31) A section of tubing with just synthesised BIRM-1 flowing through; this tubing has an inner diameter of 1.5 mm.

It is clear from the diffraction patterns in Figure 3.30 that BIRM-1 was successfully obtained in each experiment, showing it is indeed possible to synthesise the material in a continuous flow set up and Figure 3.31 shows just synthesised BIRM-1 flowing through tubing before being deposited onto filter paper.

Whilst all three flow rates led to phase pure BIRM-1 as the product, it is important to note that for the 1.5 and 1.7 ml equivalent flow rate that when the product exited the tubing onto a filter paper much of the product would redissolve as more solution was deposited on top of it, losing the product in the

process. This was not observed for the 1.8 ml equivalent flow rate suggesting that the low amounts of ammonium hydroxide led to much of the outflowing solution being too acidic.

3.6 Cadmium-Zinc Solid Solution

With cadmium possessing similar coordination chemistry to zinc, it is common in the literature to see either mixed metal framework materials containing Zn-Cd mixes or for zinc-based materials to have cadmium-based analogues synthesised.[140–142] Therefore, an attempt was made to synthesise a cadmium-based analogue of BIRM-1 as well as mixed metal versions. The room-temperature preparation method was used for this in order to eliminate some variables which could cause different phases to form, as the hydrothermal preparation has been found to be difficult to control and highly temperature sensitive.[118] This allows for a much higher throughput when attempting studies which involve a systematic change of variables.

Figure 3.32 shows the diffraction patterns from the synthesis products of a range of Zn:Cd ratios. When only zinc was used without the presence of cadmium, RT-BIRM-1 is produced as normal. With even just 20% cadmium introduced, the outcome was radically different. Whilst there were very small peaks present that correlate with BIRM-1, suggesting it was still present though in small quantities, the dominant features of the diffraction pattern were peaks that do not correlate to either BIRM-1 or the related layered phase that has been previously identified.[115] As the proportion of cadmium was increased to 40% there was no longer any evidence of BIRM-1 present in the samples. With the proportion of cadmium increased further to 60% the diffraction peaks present in the previous samples were lost and few peaks at all remained; this product likely has significant amorphous material present. Finally, when only cadmium was used, a diffraction pattern which shared no peaks with any of the other samples before was the result. The diffraction pattern for this material has a particularly low angle peak which is indicative of a large unit cell, a feature that most crystalline porous materials possess.

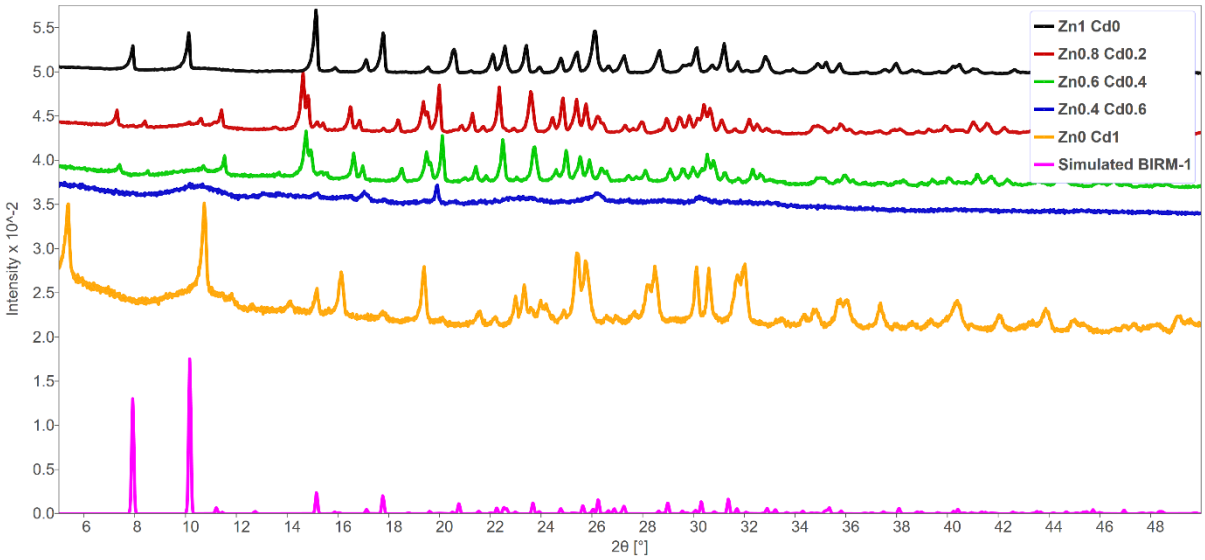

Figure 3.32) PXRD of the products obtained using a range of zinc:cadmium ratios. 1:0 (black) 0.8:0.2 (red), 0.6:0.4 (green), 0.4:0.6 (blue) 0:1 (orange) and a simulated pattern of BIRM-1 (pink)

Attempts were made to index the new products, however, the product of the $Zn_{0.4}$ $Cd_{0.6}$ synthesis did not give any satisfactory results, with low figure of merit (M_{20}) values and most peaks left unindexed. It is possible that there was a mixture of phases present, preventing indexing. The product of the 100% cadmium synthesis was indexed with the results in Table 3.12, below, with more detail provided in the appendix.

Table 3.12) Results of indexing the PXRD pattern obtained from the Zn_0 Cd_1 product

Sample	Zn_0 Cd_1 Product
Space group	Pmmm
a (Å)	9.50587
b (Å)	8.29007
c (Å)	32.65838
Volume (Å^3)	2573.62
FOM (M_{20})[143]	26.44

As indicated by the low angle peak present in the diffraction pattern, this product does indeed have a large unit cell. The extended *c* axis along with the shorter *a* and *b* axis could be an indication that this is a layered material, as many layered materials have one axis much longer than the other two. However, single crystals of this product will be required in order to confirm this and were not obtained in this work. Whilst the figure of merit is not excellent, it is satisfactory. De Wolff who developed the M20

FOM described any value above 20 where there are fewer than 2 unindexed peak as meaning that the indexing is "substantially correct".[143]

3.7 Conclusion

In this chapter, the hydrothermal synthesis of BIRM-1 has been replicated followed by the establishment of an alternative synthetic route at room temperature. This alternative synthetic route can also be used to access at least two other cation versions of BIRM-1 which previously could only be accessed *via* ion-exchange (Na^+ and K^+). The room temperature synthesis also appears to be much more reliable than the hydrothermal route by avoiding the temperature sensitivity and necessary careful temperature control. Additionally, the room temperature route does not require the addition of the TEAB salt which seems to have a negative effect on the material's properties. This is likely due to the TEA cation occupying the pores of the MOF. The room temperature synthesis is also able to be used in a flow synthesis setup, which should allow for relatively easy scale-up of the synthesis. Finally, this new synthesis route can be used to enable higher throughput of samples in systematic studies. A new phase made using cadmium in place of zinc was obtained using the room temperature route. However, this phase was obtained as a powder which highlights the main drawback of the new synthetic method. An item of future work would be to attempt this synthesis *via* the hydrothermal route in order to obtain single crystals for diffraction and subsequent structure solution.

Overall, the work in this section has established a synthetic method for BIRM-1 that is rapid, robust and easy to scale. This is not something that is particularly common within the field of metal-organic frameworks and will allow any researcher expanding upon the work done on the BIRM-1 system to do so with greater speed and ease. Of note is the rapid formation of the material. There are a number of framework materials that have had room temperature synthesis routes developed for them. However, few are as rapidly forming and use as mild conditions as have been established for BIRM-1 here. This also brings in the concept of 'green chemistry', the use of mild synthesis conditions and water as a solvent makes the room-temperature synthesis of BIRM-1 a relatively green one.

4 Properties of BIRM-1 and BIRM-2

4.1 Introduction

An important part of characterisation of metal–organic frameworks is studying their properties with the aim of identifying any potential applications the materials may be useful for. In this chapter various properties and behaviours of the BIRM-1 MOF and BIRM-2 2-dimensional coordination network were examined. Some of these properties are very obviously aimed at applications such as proton conductivity for fuel cell applications, or ammonia uptake measures for gas storage. Others are less direct such as attempting to further understand the dehydration of BIRM-1 or the production of nanosheets from BIRM-2.

4.2 Experimental

4.2.1 Ammonia Adsorption

Ammonia adsorption was achieved using a custom-built ammonia line. The experiment was set up in a fashion similar to temperature programmed desorption but note that only the total ammonia desorption was recorded, not the desorption as a function of temperature. Approximately 0.1 g of material was loaded into the reactor fitted with a glass frit to allow gas to pass through. The reactor was heated to 120 °C for 30 minutes in a 50 ml min^{-1} flow of argon to allow activation of the MOF. The reactor was then cooled to 30 °C. Pure ammonia gas was flowed through the reactor and then overpressurized to 1.5 bar (0.5 bar above atmospheric) and the reactor was then sealed for 60 minutes. After purging the reactor for 10 minutes with 50 ml min^{-1} argon flow the reactor was heated to 350 °C. The outflowing gas during heating was passed through dilute sulphuric acid with a conductance probe submerged in it. The change in conductivity was measured and compared to a calibration taken of the change in conductivity when a known quantity of ammonia was passed through the acid. From this, the quantity of ammonia desorbed was calculated.

4.2.2 Pair Distribution Function Analysis

Total scattering data were collected at Diamond Light Source beamline I15-1. Samples were placed in quartz capillaries with internal diameter of 1.17 mm. Monochromatic X-rays of wavelength 0.161669 Å were used. The detector was a Perkin Elmer 1611 CP3 flat screen detector. In-situ dehydration was achieved with a hot air blower up to 125 °C. Data were processed at Diamond by Dr Phil Chater using the Gudrun software package in order to remove background scattering from air and the capillaries. Data were then processed into pair distribution functions (PDFs) in the D(r) form.

4.2.3 Electrochemical Impedance Spectroscopy

Electrochemical impedance spectroscopy measurements were performed on a Hewlett Packard impedance analyser over a frequency range of 5 Hz to 13 MHz at an amplitude of 100 mV and 0 mV AC rest voltage. Measurements were carried out on pressed pellets of powder samples in a humid atmosphere generated by bubbling nitrogen through deionised water. Pellets were prepared by loading 0.15 g of sample in between 10 mm dies and pressing at ca. 3.5 tonnes.

4.2.4 Synthesis of BIRM-2 Nanosheets and Imaging

For attempted preparations of nanosheets from BIRM-2 material, 0.1 g of hydrothermally synthesised BIRM-2 was placed in glass vials with 10 ml of solvent. The vials were then sonicated for 60 minutes with a cooling coil so the samples were not subjected to significantly elevated temperatures. Sonication was attempted in three solvents: deionised water, acetone and ethanol. After sonication the samples were recovered by vacuum filtration and sent for imaging using atomic force microscopy in order to determine the thickness of the layers. SEM was also used for qualitative evaluation of the sonicated material. This was done using a Hitachi TM4000 plus benchtop electron microscope. For measuring the thickness of the nanosheets a Veeco Dimension 3100 atomic force microscope (AFM) was used. The AFM was fitted with gold-coated Tap150-DLC cantilevers with a nominal spring constant of 5 mN m^{-1}. Images were recorded using a tapping mode. The AFM images were collected by David Burgess of the School of Chemical Engineering, University of Birmingham.

4.3 Adsorption Behaviour of BIRM-1

Zhao previously investigated hydrogen uptake in BIRM-1 as a measure of its accessible internal surface area after dehydration.[115] It was found that a negligible quantity of hydrogen was adsorbed by BIRM-1. This was blamed on the amorphization and apparent pore collapse of BIRM-1 upon dehydration. With the development of the room temperature synthesis route to BIRM-1, which does not require the addition of TEAB, the surface area of BIRM-1 was assessed using nitrogen adsorption and the BET method. This was done in order to confirm Zhao's assessment and ensure it holds when TEAB is not used in the synthesis, as it could be that it blocks pores and prevents internal surface area being accessed. The potassium form of BIRM-1 was chosen for this adsorption experiment. This choice was made as K^+-BIRM-1 has a plateau in its decomposition profile which marks a point at which the pores are emptied of any volatile content. The adsorption isotherm is shown in Figure 4.1.

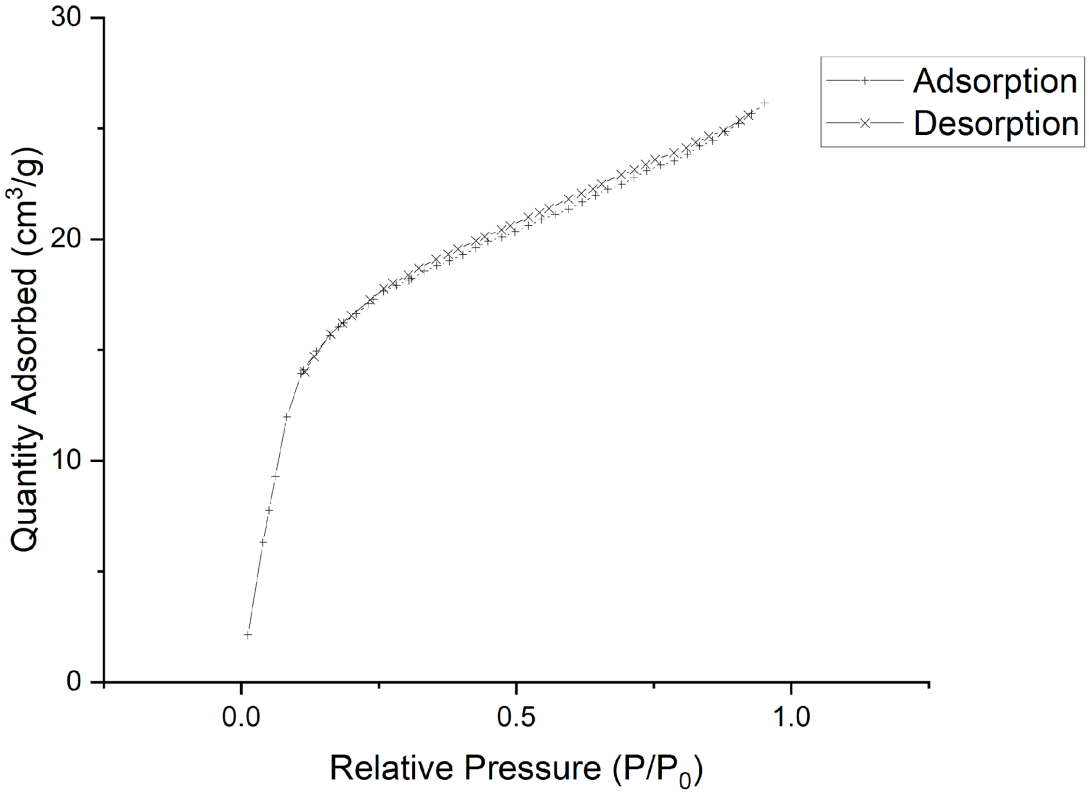

Figure 4.1) N2 adsorption isotherm of RT-K^+-BIRM-1

The recorded isotherm matches that of a 'type I' isotherm which is indicative of a microporous solid.[136] However, the BET surface area calculated *via* the Rouquerol approach gave a very low value of 77 m^2

g^{-1} seemingly confirming Zhao's assessment of a lack of porous porosity in the BIRM-1 materials.[115,137] It seems that whilst there are micropores present in the material, they are small in number, likely due to the majority of pores becoming blocked when the structure distorts upon dehydration. Leading to the 'type I' isotherm shape that is reported but relatively very little surface area remaining accessible.

Zhao stated at the end of his thesis that an item of future work would be to attempt dehydration of BIRM-1 *via* a freeze-drying method as a way potentially to circumvent amorphization.[115] For metal–organic frameworks this is typically achieved by solvent exchange with benzene prior to the freeze-drying.[144] However, BIRM-1 only possesses small pores and the Van der Waals radius of benzene (4.8 Å) is notably larger than the small channel in BIRM-1 (4.0 Å).[115,144] In addition to this, the hydrophobic nature of benzene would mean it is unlikely it would displace water in the pores of BIRM-1 as the partly uncoordinated carboxylate group leaves the large channel of BIRM-1 hydrophilic in nature. Therefore, a freeze-drying attempt was carried out without prior solvent exchange. A PXRD pattern was taken of the freeze-dried material to establish whether activation was achieved without amorphization of the material; this is shown in Figure 4.2.

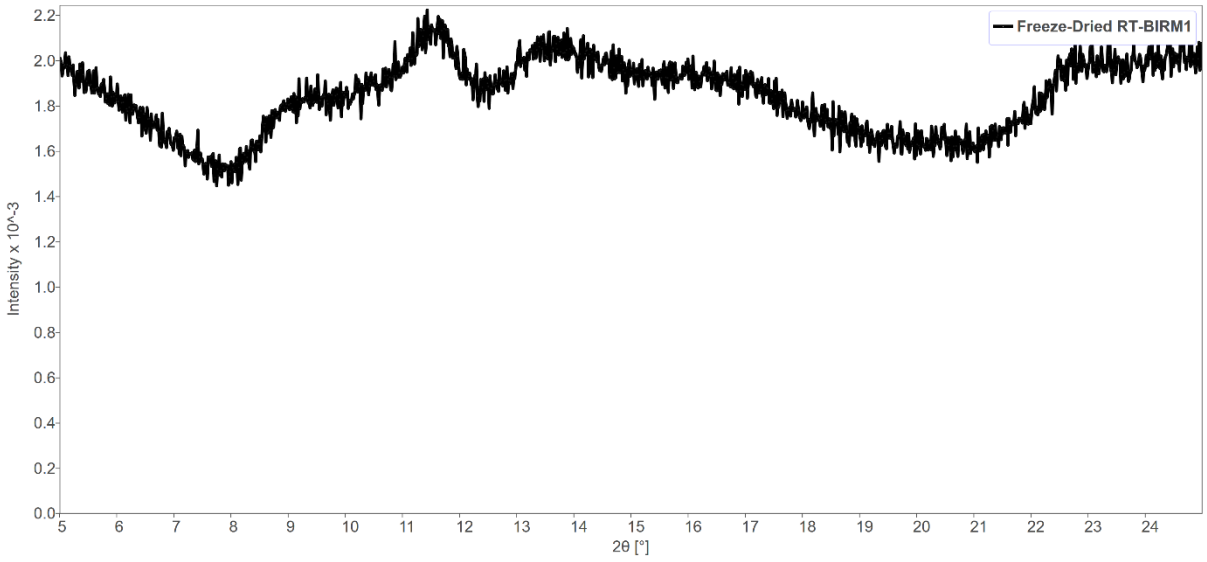

Figure 4.2) PXRD pattern of the freeze-dried material

The PXRD pattern of the freeze-dried material confirms its amorphization. The last method by which it may be possible to dehydrate BIRM-1 whilst retaining the crystalline structure is supercritical CO_2

drying. This method has seen some success in activating other porous framework materials without degradation of the structure.[145] This is an area for future work.

Although the structure was not maintained, this does not mean it would not be possible to utilize the internal space of the material. Zhao found that BIRM-1 would reversibly dehydrate, with the crystalline structure returning upon reuptake of water. As it is possible to do that with water, it may also be possible to 'rehydrate' the structure with ammonia in its place. The presence of cations within the pores of BIRM-1 would likely enhance this behaviour as ammonia would be able to coordinate to the extra-framework cations as well as just filling the pores as a solvent would.

An experiment was designed and set up as detailed in section 4.2.1. This experiment was envisioned as a proof of concept rather than a detailed study of the potential for BIRM-1 in ammonia storage. For this adsorption experiment RT-K^+-BIRM-1 which was synthesised without TEAB present was chosen.

The calibration gave the following relationship: μmol of ammonia = change in conductivity / 0.48. Through the course of the desorption step the conductivity dropped by 31 μS cm^{-1} corresponding to an ammonia desorption of 64.58 μmol of ammonia. For the experiment 0.1009 g of MOF was used giving an absorbance of 0.64 mmol g^{-1} or 0.011 g g^{-1}. As the sample was dehydrated in the reactor vessel to not expose it to humid air post dehydration, giving no opportunity to weigh the dried sample, the gravimetric capacity based on the activated MOF could be up to 20% higher from assessment of the TGA data shown previously. Although the uptake values recorded in this work are poor compared to those for other MOFs in literature,[96,146] there are several experimental factors which may lead to higher uptake being achieved. Firstly, dehydration under vacuum would likely achieve more effective activation of the MOF. Longer exposure to ammonia would also likely lead to higher uptake. As the pores of BIRM-1 are collapsed upon dehydration it is likely that the ammonia uptake is severely kinetically limited as these pores reopen. Lastly, an important feature of BIRM-1 is its ion-exchange ability and potential for tuning to particular applications.[59] Whilst potassium compounds are not particularly heralded for their ability to coordinate ammonia, magnesium ones are. It has not proved possible to directly synthesise a magnesium

form of BIRM-1 so far owing to magnesium hydroxide being a relatively weak base. However, ion-exchange attempts have been successful.[115]

Overall, this experiment has proved it is possible for ammonia to be adsorbed by BIRM-1 but there are experimental factors which should be resolved to achieve higher uptake. However, as a proof of concept this experiment was successful.

4.4 Pair distribution function analysis of in-situ dehydration of BIRM-1

Zhao established the reversible dehydration of BIRM-1 where the material can be dehydrated into an amorphous form which shows little uptake of hydrogen gas followed by recrystallisation back to BIRM-1 on exposure to moist air.[59] Little is understood of the structural changes that occur during this process. An experiment was planned using pair distribution function analysis to attempt to study and characterise the amorphous phase that is formed and the mechanisms involved. The purpose of this was that it may help in the design of materials with permanent porosity as well as understanding the changes that occur within the material and how it affects the framework connectivity. Such an understanding is important for potential applications that involve dehydration of the material, for example gas or water sorption.

The PDFs of ammonium form HT-BIRM-1 produced from total scattering data collected at temperatures between 25 and 125 °C are shown in Figure 4.3. For the data collected at 25 °C, order can be seen in the form of peaks in the PDF to at least 50 Å, which is the distance the PDF was processed up to. Upon heating the material to 125 °C, most the longer-range order was lost and above ca. 12 Å the function became a randomly fluctuating background with no distinct peaks or features. For the distance between 5 and 12 Å there were significant differences to the PDF with notable changes to peak intensities and widths. Finally, below 5 Å there were limited changes upon dehydration. The peaks at ca. 1.5 and 1.9 Å showed little change. These peaks correspond to C–O and P–O bonds for the 1.5 Å peak and Zn–O bonds for the 1.9 Å peak. This supports the theory that the framework stays intact upon dehydration which allows for the reversible dehydration. As for intermediate temperatures, a gradual change in peak intensities was observed as the material was heated, slowly lost intrapore water and long-range order.

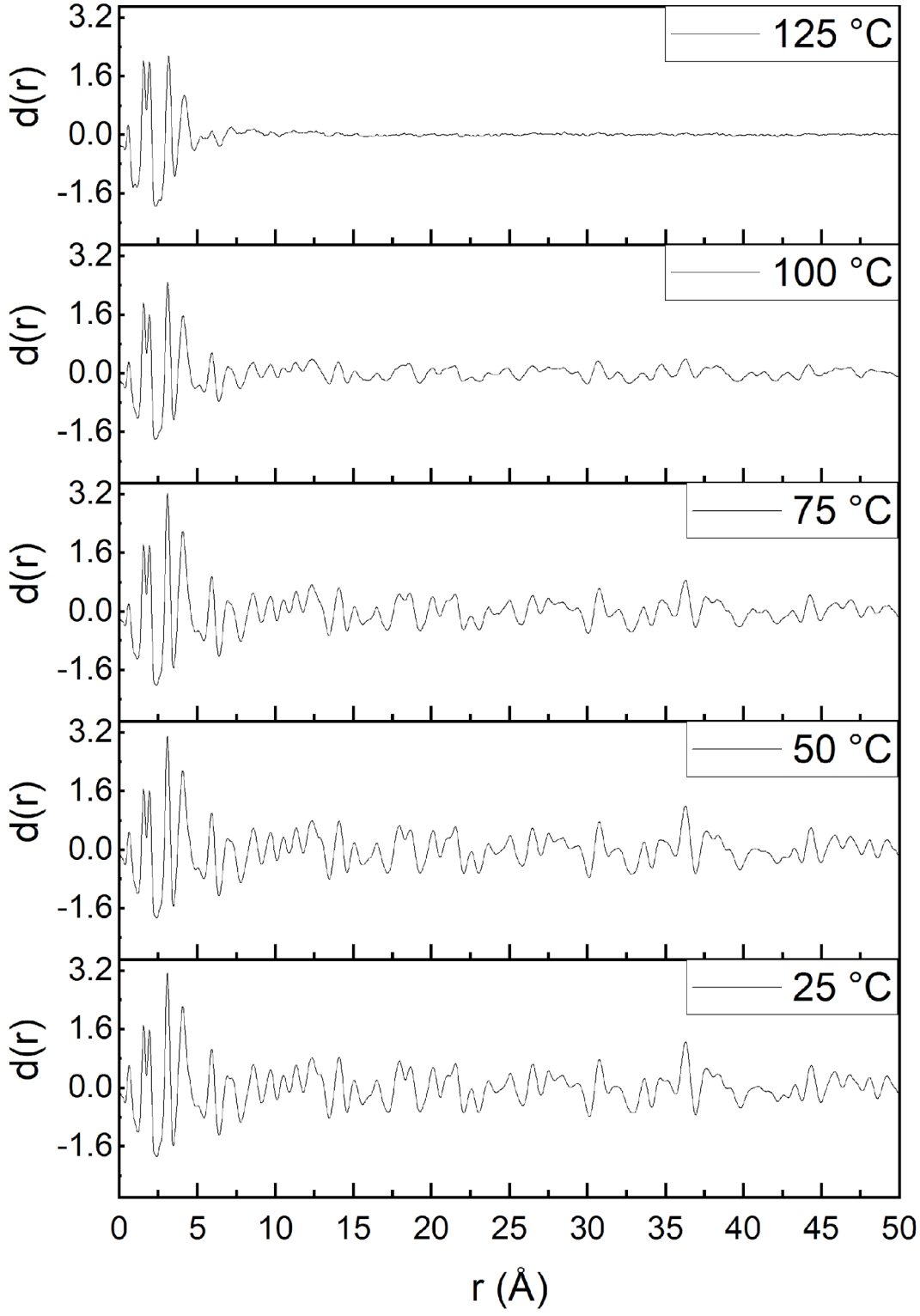

Figure 4.3) Pair distribution functions for ammonium form HT-BIRM-1 produced from data collected at temperatures between 25-125 °C

The first data collection at 25 °C was fitted to the HT-BIRM-1 structural model developed by Zhao.[59]

The plotted fit is shown in Figure 4.4. The refined structure (Figure 4.5) is not significantly different

from the starting model. There are slight differences in atom positions and a dampening function had to be applied to these during refinement. This was to prevent atoms refining far from their original positions to nonsensible locations. As the refinement progressed, the weighting on the dampening function was successfully lowered. A variable was also used to account for differences in pore contents both from the starting model and as dehydration started to occur. Rather than refining each occupancy separately, the initial occupancies were multiplied by this new variable with a starting value of 1. Refinement of the data collected at 25 °C led to this variable settling at a value of 1.3. By the end of the refinement process, there was good agreement between model and data as shown by the fit in Figure 4.4. The intensities of some low angle peaks are not fitted well but this region of a PDF typically has a high level of noise, making it difficult to fit the peaks perfectly.

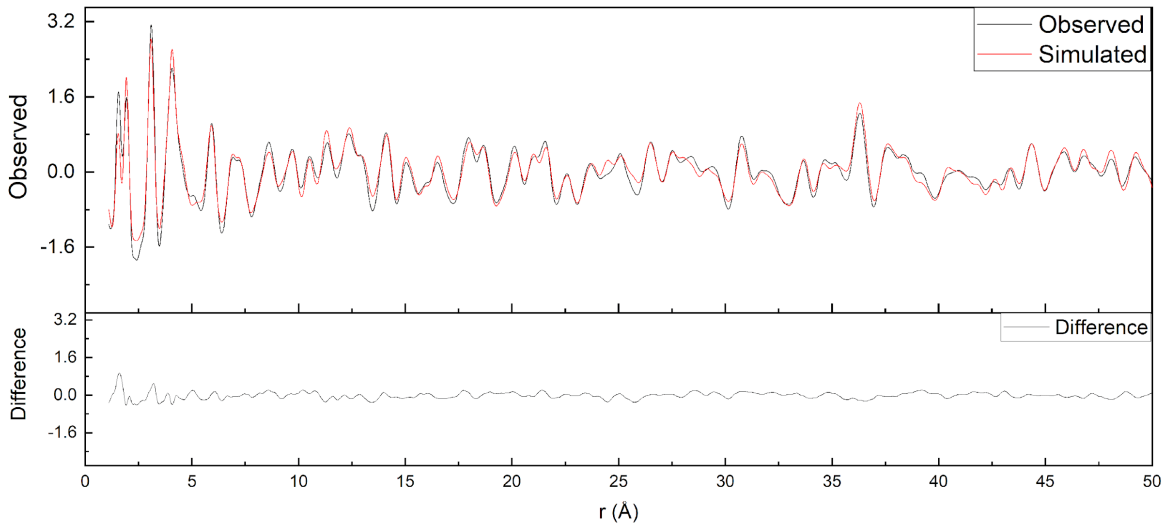

Figure 4.4) PDF fitted to a model of BIRM-1. Data collected at 25 °C

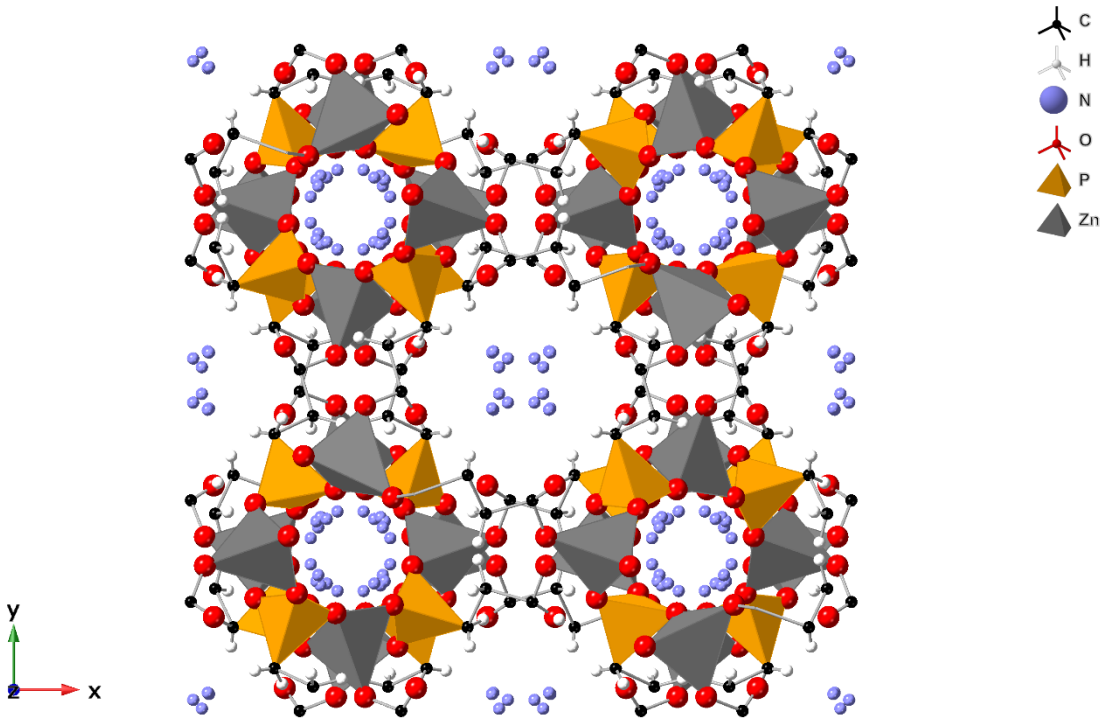

Figure 4.5) Structure as refined from PDF data; oxygen atoms corresponding to intrapore water have been removed for clarity

Iterative fittings were then conducted on each subsequent data collection at the various temperatures, using the model produced from the previous set of data. The fits for temperatures 50 – 100 °C are included in the appendix. The main changes in each iteration were related to the pore contents as would be expected during dehydration. However, counterintuitively the solvent occupancy variable previously mentioned increased as temperature increased. There was a moderate increase to 1.56 at 50 °C and then a further small increase to 1.59 at 75 °C. This was followed by a more significant increase to 1.95 at 100 °C and 2.21 at 125 °C. Clearly this cannot possibly be reflecting the actual change of pore contents in the material. A closer investigation into the refinements found that the thermal parameters for the pore contents also refined to very high values, reflecting increased motion of the water and ammonium within the pores. This increased motion of the solvent with increasing temperature is to be expected. This is the likely cause of the counterintuitive increase in pore occupancies as the two variables are correlated. Therefore, the pore occupancy variable should not be treated as a value that is physically meaningful. However, it was kept in the refinements to help model the changes that are occurring even if the value

is not directly usable. The contributions by pore contents to the overall fit are minimal as shown by Figure 4.6. The peak at ca. 3.2 roughly corresponds to the N-O distance in solvated ammonium cations.[147] This could correspond to either residual coordinated water or the ammonium coordinating to framework oxygens. The rest of the fit simulated from pore contents alone is composed of broad features that effectively form part of the background of the PDF.

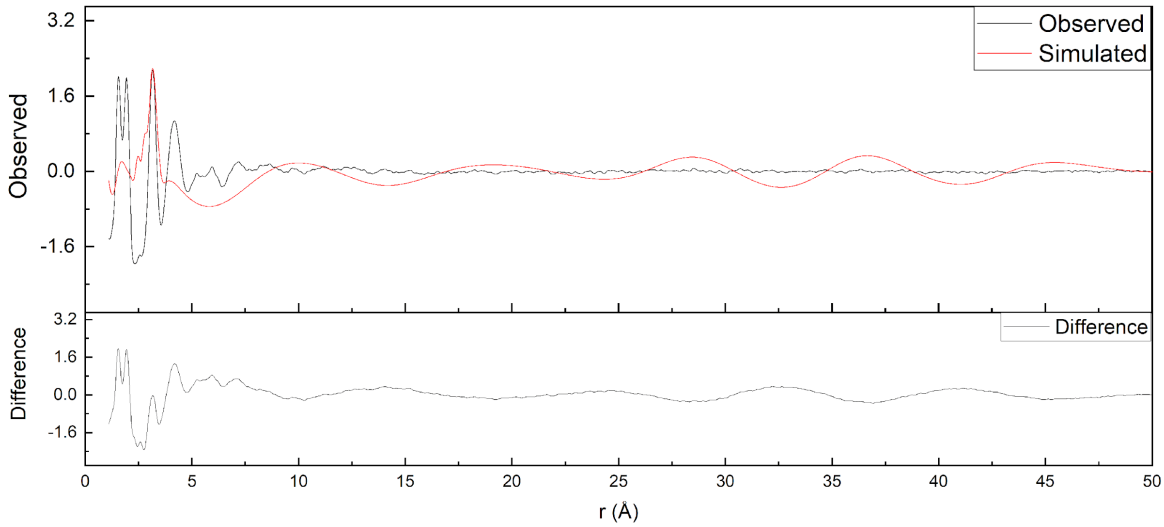

Figure 4.6) PDF fitted to a model of BIRM-1 consisting of only the pore contents; data collected at 125°C

For the data collected at 125 °C a spherical dampening variable was used for the PDF fit. This treats the structural model as smaller regions of short-range order rather than using the unit cell as a whole. The fit is shown in Figure 4.7. The spherical dampening variable refined to a value of 9.77 ±0.55 Å, meaning it is an area of the structure around this size which remained relatively intact after dehydration. The use of this variable is also why the broad contributions from pore contents are not observed in Figure 4.7 as they are in Figure 4.6.

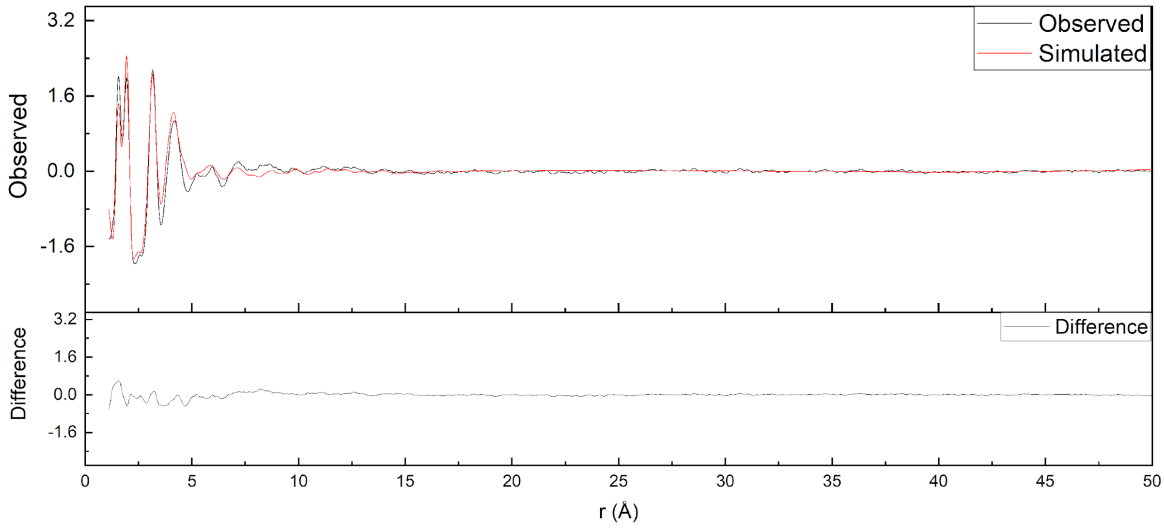

Figure 4.7) PDF fitted to a model of BIRM-1; data collected at 125 °C

As described in the literature review section of this thesis, BIRM-1 is made up of helical double chains of ZnO_4 and CPO_3 tetrahedra. The helical chains are then connected through the organic linker. Usually in MOFs the most flexible part of the material is the organic linker, especially when alkyl chains are used such as in BIRM-1. However, on inspection of the structure to find a segment approximately 9.8 Å large which looks like it would remain relatively rigid upon dehydration the inorganic helical chains do not look sufficiently rigid. The tetrahedra are only connected by corner sharing and one could picture the helical chains behaving somewhat like springs which could be compressed, elongated, twisted and bent. Further to this, no success was found in searching for an atom-atom distance around 9.8 Å in the inorganic section of the material without crossing pores which are very unlikely to remain intact. This is evidenced by the materials lack of porosity upon dehydration. Instead, atom-atom distances across the area in which the linker connects the helical chains were found as shown in Figure 4.8. These atom distances are between zinc and phosphorus atoms which are by far the heaviest atoms in the structure and would be contributing to the scattering data more than the lighter organic parts of the structure. in contrast to the helical chains as a whole, the organic linkers likely impart some rigidity on this part of the structure. As the double chains twist or bend at the corner sharing connections between tetrahedra, the organic linkers will come closer to one another introducing steric effects. The relatively short alkyl chain would also have less flexibility than a longer one would have but would not be completely rigid.

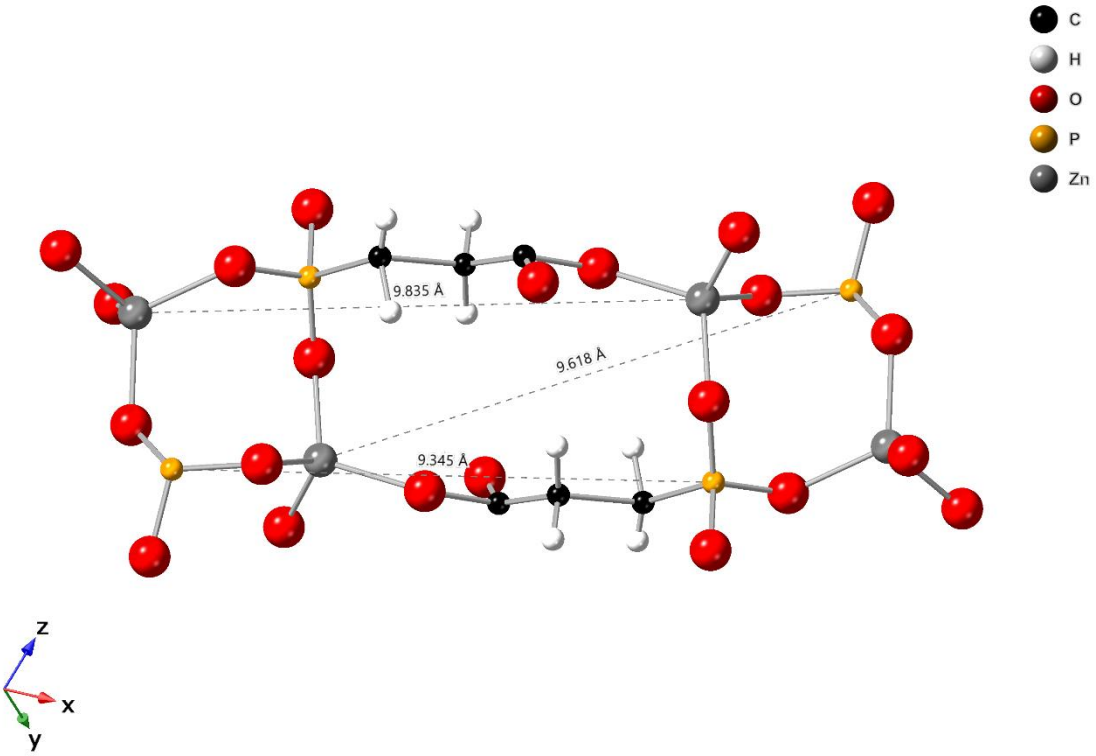

Figure 4.8) A section of the BIRM-1 structure with organic linkers connecting the two helical chains; three atom-atom distances are labelled.

This part of the structure was fitted to the PDF generated from data collected at 125 °C. A unit cell containing only the above section and with very large lattice parameters was generated to ensure that only contributions from this part of the structure were considered. A function was used which takes into account the rest of the structure for fitting at low r, as contributions from atoms one or two bonds away still needed to be accounted for. The fit is shown in Figure 4.9.

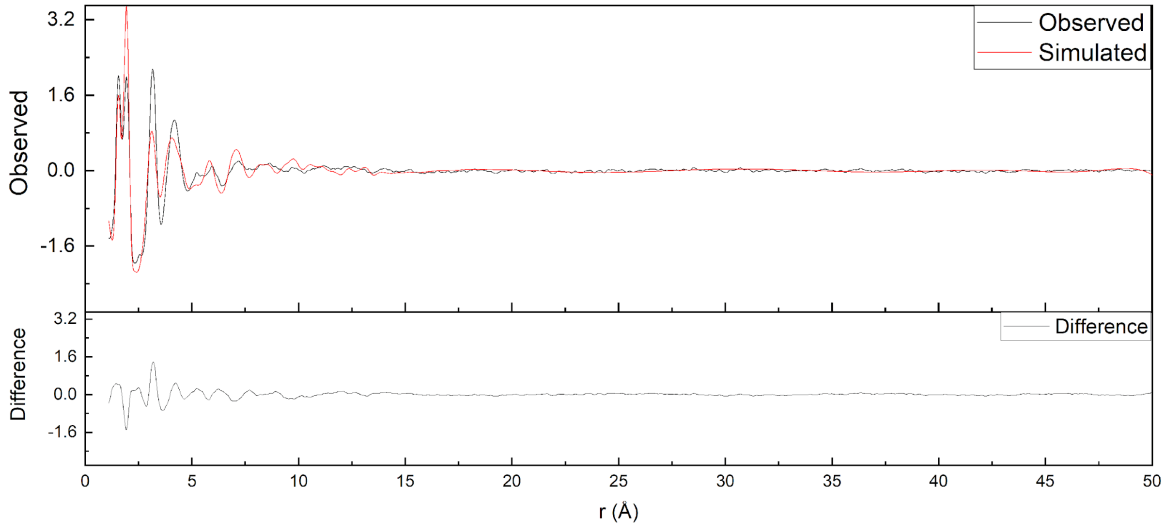

Figure 4.9) PDF fitted to a section of BIRM-1, shown in Figure 4.8; data collected at 125 °C

The fit is not perfect with a lot of peak intensity quite poorly matched. However, most if not all peaks have at least some of their intensities accounted for. The difference can be explained by a number of factors. The peak at 3.2 Å is likely from cation coordination, which is not included in the structural model used for this fit. Another fit was attempted with a cation site included but did not appear to improve the fit, possibly because the location of coordinated atoms is not known in the dehydrated structure and therefore this could not be modelled other than to include the nearest cation site to the small section modelled in Figure 4.8. The mismatched intensity from the rest of the peaks could be due to flexibility in this section of the structure. Whilst it seems likely that the small section modelled here is the most rigid part of the structure, that does not mean it is entirely rigid. The alkyl chain would be able to twist and flex to a degree and there would still be some flexibility in the connected part of the helical chains. All of this makes producing a satisfactory model and fit particularly difficult. However, from the data available it is likely that this part of the structure remains relatively undistorted during dehydration compared to the rest of the structure, and that the connectivity of the framework remains largely unaffected. This latter point was also evidenced by FTIR data collected by Zhao.[115] To conclude this section, the flexibility and reversible amorphization of the material on dehydration is most likely imparted by the chains of corner-sharing tetrahedra which form helixes. These chains are likely to be

able to twist, flex, compress and elongate much like a spring. A graphical depiction of these chains is included in Figure 4.10.

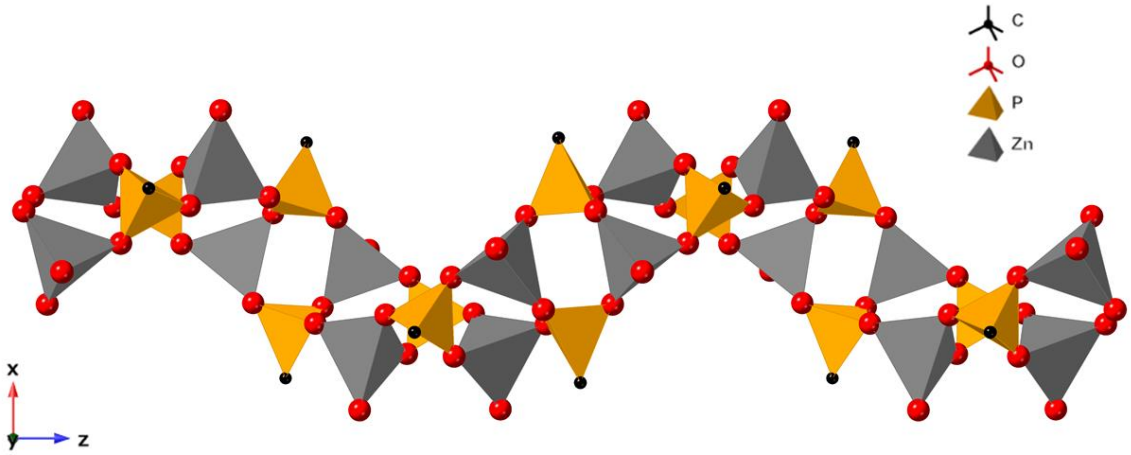

Figure 4.10) Helical double chains of ZnO_4 and CPO_3 tetrahedra which form part of the BIRM-1 structure

4.5 Proton Conductivity of BIRM-1

The proton carrying groups in the form of water and especially ammonium within the pores of BIRM-1 raise the possibility that the material may be able to conduct protons. There are similar materials, such as other phosphonate or ammonium containing MOFs, in the literature which have been proven to facilitate the conduction of protons through their structures.[98,148] For this reason, electrochemical impedance spectroscopy (EIS) was used in order to assess samples of BIRM-1 for conductivity. The ammonium form RT-BIRM-1 was chosen as the test material for this, as ammonium is an effective proton carrier and the room-temperature variant can be made reliably with or without TEAB. It was predicted that a sample with TEAB should have lower conductivity as TEA^+ cations block conduction pathways within the pores of the material. Table 4.1 shows the conductivity values measured by EIS for RT-BIRM-1 synthesised without TEAB as well as with TEAB. For the material synthesised without TEAB the conductivity increased as the material was heated from room temperature, peaked at 50 °C and then began to decrease. Above 65 °C the conductivity value was below the value at room temperature. The initial increase of conductivity with temperature is the expected response and typical of proton conductive materials, as proton carriers become more mobile as well as acidic protons

becoming more labile. The decrease in conductivity at higher temperatures can be explained by the loss of water and possibly some ammonia from the material, which can take part in conductive pathways so naturally removal of the water leads to lower conductivity. It is also established that the pores and channels of BIRM-1 are inaccessible when the material is dehydrated, indicating the conductive pathways could be broken. This explains why the conductivity value at the higher end of temperatures measured in this work was lower than the conductivity at room temperature. The conductivity values recorded show that BIRM-1 is comparable to other similar materials.[98,149] However, the conductivity of BIRM-1 is still two orders of magnitude lower than the industry-leading material Nafion with a conductivity value of 0.2 S cm^{-1}.[150] The important feature that BIRM-1 has is that it has been proven that a variety of cations can be held within the pores and channels of the material. This allows a degree of tunability which makes it a very interesting material for further research in this area.

Table 4.1) Conductivity measurements from EIS at various temperatures for RT-BIRM-1 synthesised without and with TEAB

Temperature (°C)	Conductivity of RT-BIRM-1 Synthesised without TEAB (S cm^{-1})	Conductivity of RT-BIRM-1 Synthesised with TEAB (S cm^{-1})
30	5.87×10^{-4}	1.60×10^{-5}
35	6.83×10^{-4}	1.94×10^{-5}
40	7.85×10^{-4}	1.96×10^{-5}
45	8.71×10^{-4}	2.05×10^{-5}
50	9.20×10^{-4}	2.01×10^{-5}
55	8.95×10^{-4}	1.96×10^{-5}
60	7.75×10^{-4}	2.02×10^{-5}
65	6.10×10^{-4}	1.93×10^{-5}
70	3.96×10^{-4}	1.67×10^{-5}

In order to provide a comparison as well as to further establish the effects that TEAB has on the properties of BIRM-1, a sample of RT-BIRM-1 synthesised with the presence of TEAB was also tested with EIS. The conductivity values for this sample are also shown in Table 4.1. Overall, a similar trend was observed. However, the conductivity for this sample, as expected, was much decreased. The higher temperature conductivity values did not decrease to lower than those taken at room temperature, however, possibly as many conductive pathways were already blocked by TEA^+. This lessens the impact

of pores and channels collapsing on dehydration and provides further evidence that TEA^+ cations do indeed occupy some cation sites within the BIRM-1 structure.

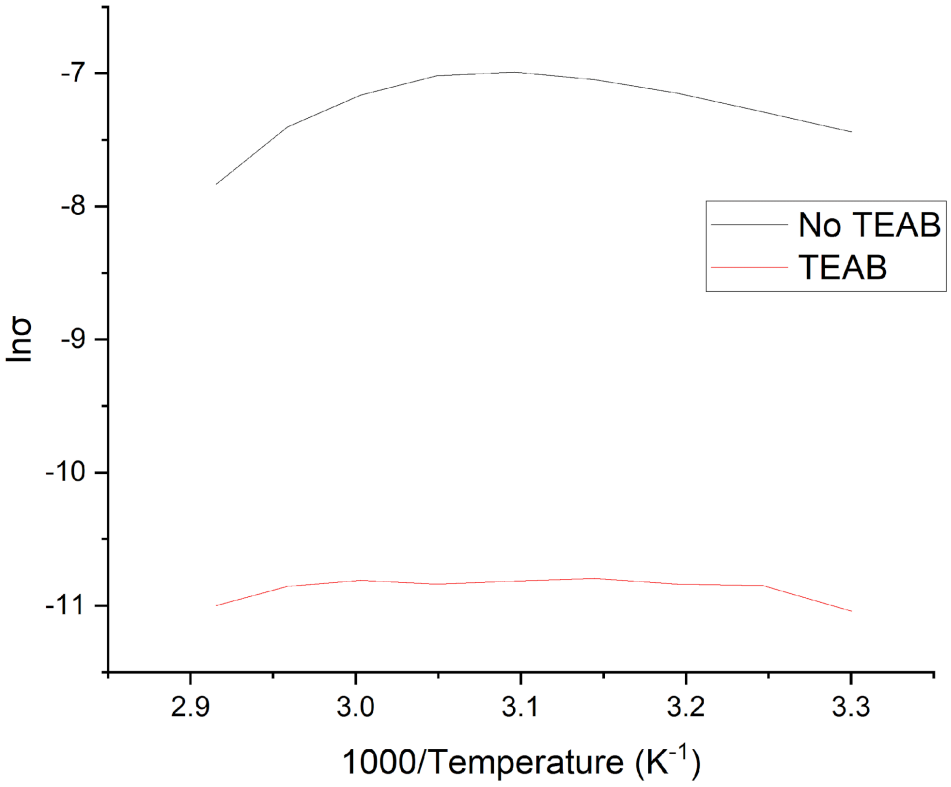

Figure 4.11) Arrhenius plot of the conductivity data for RT-BIRM-1 with and without TEAB

Owing to the unusual relation conductivity has with temperature for this system, it is not possible to get a reliable activation energy using an Arrhenius plot (Figure 4.11) due to the lack of linearity. Therefore, it is not easy to deduce by which mechanism the conductivity occurs, Grotthuss or vehicular. Grotthuss mechanism is also known as 'proton jumping' as it involves the exchange of protons between water molecules and other proton carriers such as ammonium cations. The Grotthuss mechanism is associated with a relatively low activation energy. In comparison, the vehicular mechanism involves the movement of a whole molecule which can act as a proton carrier, which intrinsically has a greater energy barrier than the movement of a proton between molecules.

4.6 Formation of BIRM-2 Nanosheets

There is significant interest in the formation of metal–organic nanosheets for a range of applications including catalysis and sensing.[151] The formation of nanosheets can be achieved in multiple ways which can be placed into two broad categories. Top-down methods involve breaking apart a material post-synthesis into nanosheets whereas bottom-up methods are those where the material is synthesised as a nanosheet in the first instance.[151] The structure of BIRM-2, with its 2-dimensional layers held together by hydrogen bonding, looks like a potential material to form into nanosheets by top-down methods. Additionally, its metal centres which have one water molecule coordinated may become accessible upon formation of nanosheets. These metal centres could then be used in applications like catalysis or sensing, especially as the BIRM-2 structure is known with Mn(II) in place of the Zn(II), suggesting isostructural materials with a range of metals may be possible.[120]

Sonication of BIRM-2 was undertaken by the procedure set out in section 4.2.4. The sonicated materials as well as the starting BIRM-2 sample were imaged using SEM, as shown below.

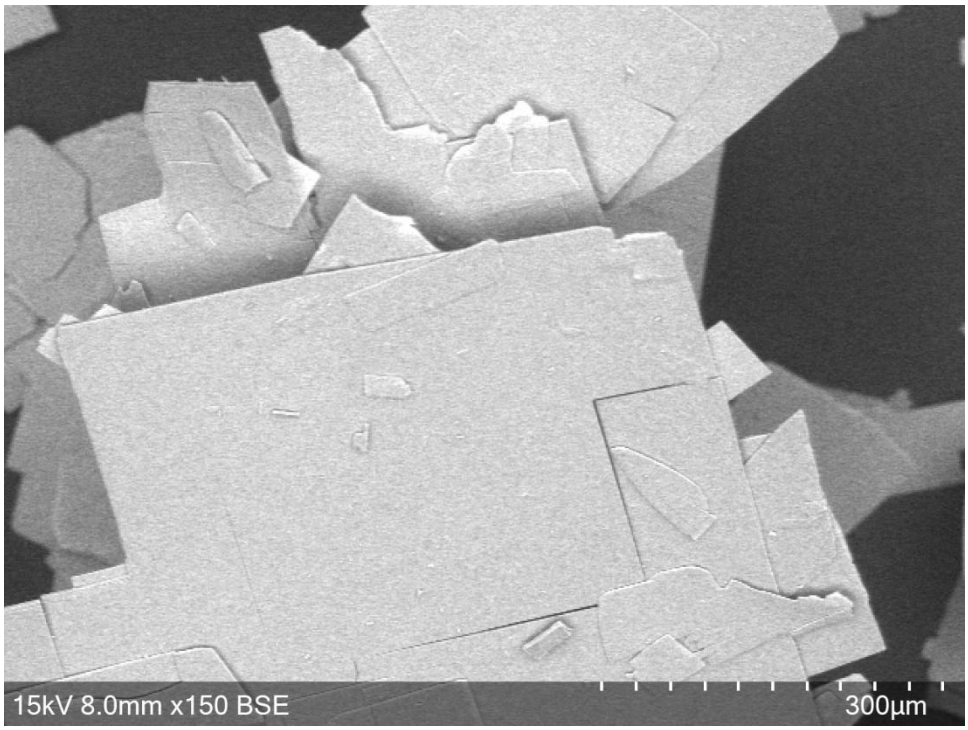

Figure 4.12) SEM image of as-synthesised BIRM-2 at 150× magnification

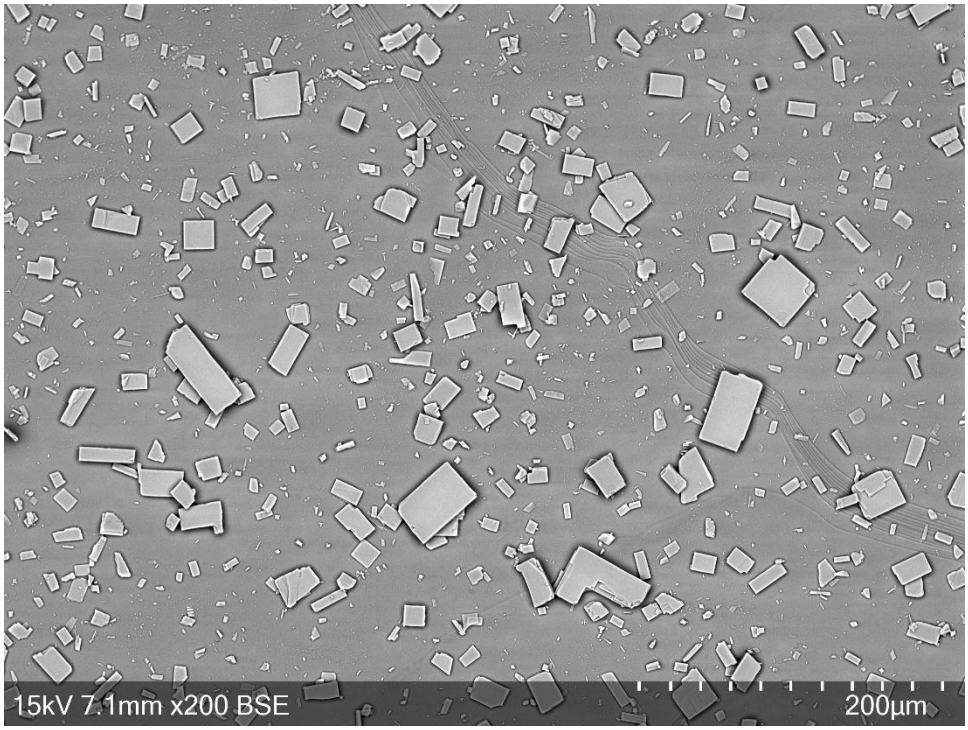

Figure 4.13) SEM image of BIRM-2 sheets after sonication in acetone at 200× magnification

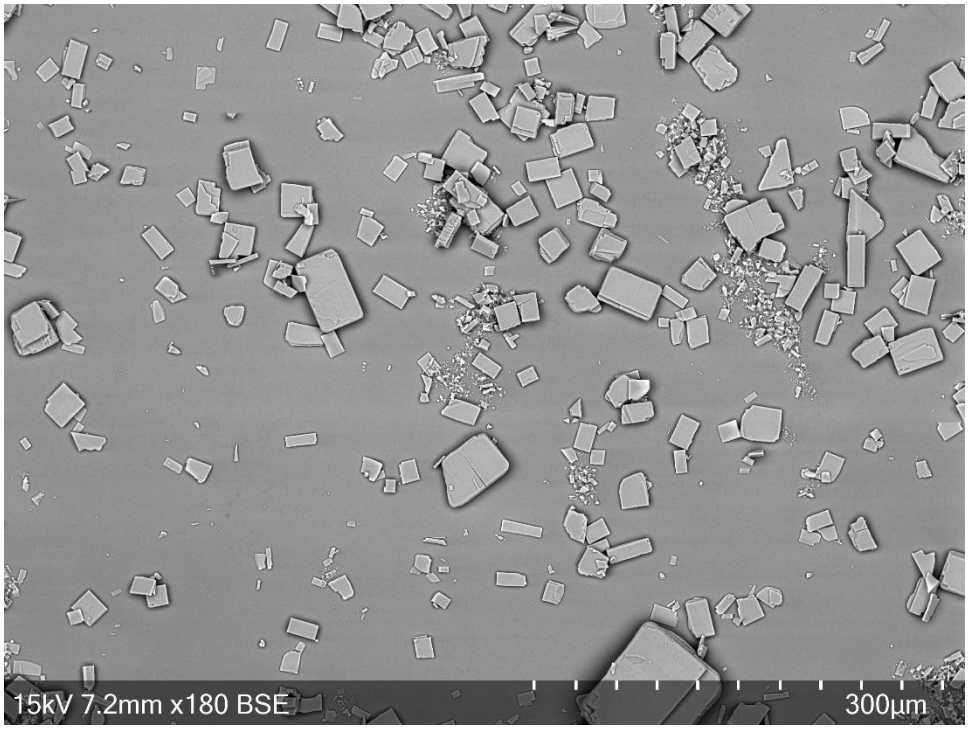

Figure 4.14) SEM image of BIRM-2 sheets after sonication in ethanol at 180× magnification

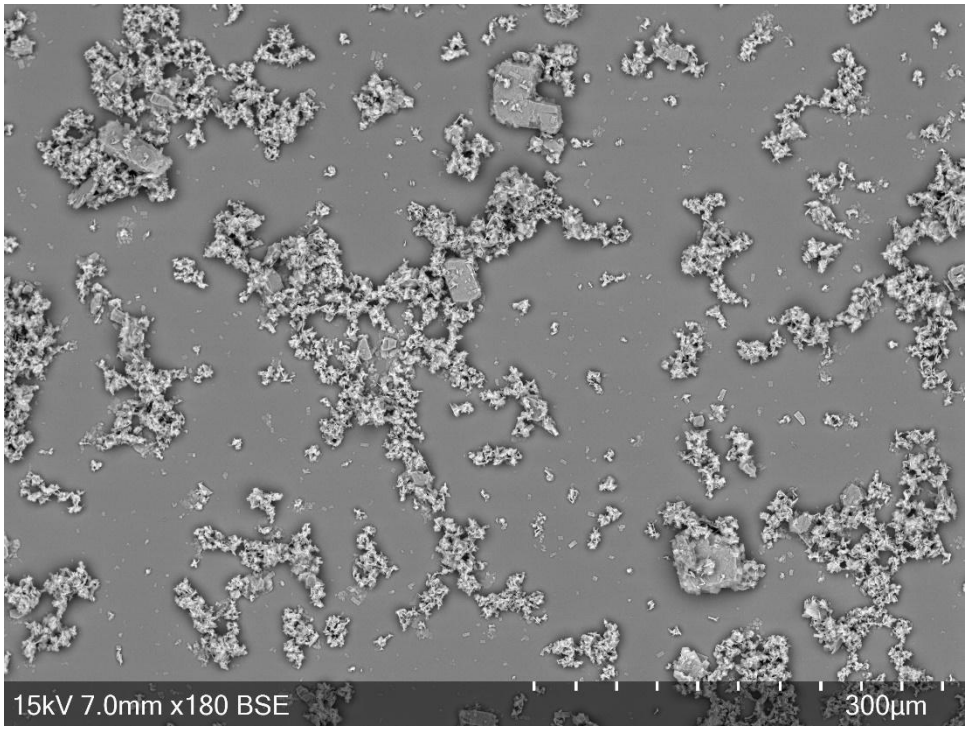

Figure 4.15) SEM image of BIRM-2 after sonication in water at 180× magnification

The sonication process led to significant breakdown of the material and appears to have affected the material along multiple axes rather than just splitting into nanosheets. This is not unexpected as the thinner a crystallite gets the more susceptible it will be to breaking. An interesting observation is the extent to which the material breaks down in the different solvents. The material sonicated in acetone (Figure 4.13) largely reflects the morphology of the as-synthesised material, just with much smaller plates, whereas significant breakdown into unrecognisable material can be seen after sonication in ethanol (Figure 4.14). This is alongside the more familiar plate morphology with some crystals, such as in the bottom centre of the image, appearing quite large still. The product sonicated in water (Figure 4.15) appears to have almost completely broken down into unrecognisable material with only a few larger crystallites remaining. It seems like the extent of breakdown may be related to the ability of the solvent to undergo hydrogen bonding, with water seeing the highest degree of breakdown and acetone the least.

In order to measure the thickness of the sonicated sheets, they were sent for measurements using AFM. An AFM image of one such sheet, sonicated in acetone is shown in Figure 4.16. The samples which

were sonicated in ethanol and water gave very noisy images from which it was not possible to extract height information. The thickness of the sheet in Figure 4.16 was measured by taking the change in height along the line labelled 1. This gave a thickness of ca. 190 nm, confirming the formation of nanosheets. This can be compared to the height of the nanosheets prior to sonication which were too large to measure with the AFM indicating a sheet thickness of > 5 μm.

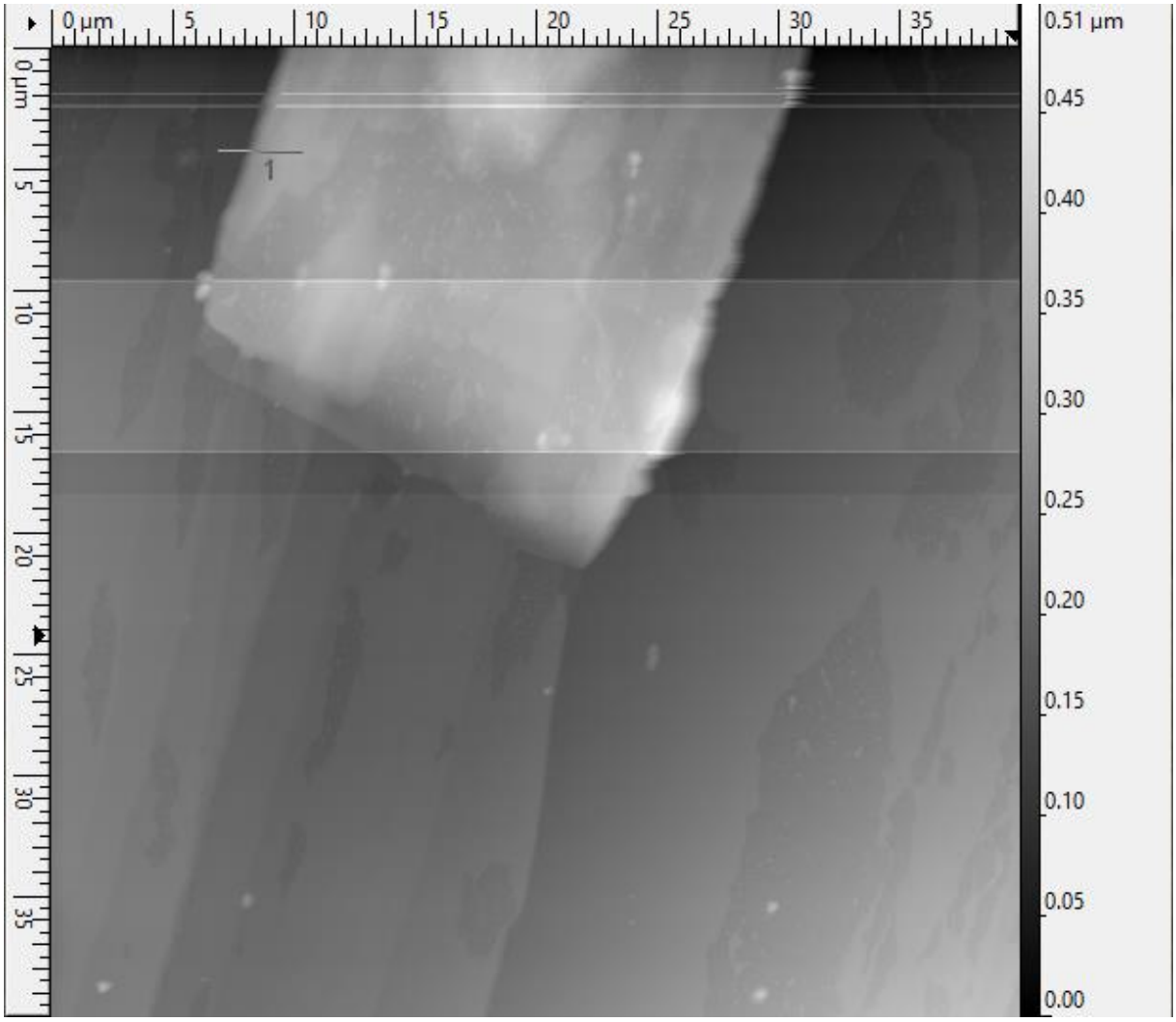

Figure 4.16) AFM image of sonicated sheets of BIRM-2; height scale shown right. Sheet thickness was measured by taking the change in height along line labelled 1.

4.7 Conclusion

Some properties of BIRM-1 and BIRM-2 have been evaluated in this section. It has been shown that BIRM-1 is capable of conducting protons to a reasonable extent and is at least as conductive as other similar materials which have been reported.[98] It may be possible to further enhance this property through

further functionalisation of the linker and inclusion of different proton carriers within the pores. Further, the dehydration and amorphization of BIRM-1 has been characterised by PDF and it seems that the flexibility of the structure is actually caused by the inorganic double chains being able to flex rather than the organic linker, though this is not completely rigid either. Data were also collected observing the recrystallisation process, though not included here. An item of future work would be to fit the recrystallisation data to a model. Ammonia adsorption was attempted on BIRM-1 as a proof of concept experiment and indeed some ammonia was adsorbed. However, it was a very small quantity and tuning of experimental variables would need to be conducted in order to see if it is possible to store more ammonia within the material. This is another area for future work. Finally, nanosheets of BIRM-2 have been synthesised with a thickness of ca. 190 nm. These nanosheets may be useful for applications such as catalysis if the formation of the sheets renders the metal sites accessible.

5 Synthesis of a Magnesium-Based Carboxyphosphonate Metal–Organic Framework

5.1 Introduction

After the development and characterisation of the zinc-based BIRM-1, it was decided that an attempt to expand the family of carboxyethylphosphonate framework materials should be made, to structures based on different metal ions. Magnesium was chosen as a candidate in part due to the low mass and high abundance of the element. One area in which MOFs are of particular interest is gas storage, and for this application low mass framework materials are of particular importance as well as low cost.[152] Therefore, the work presented in this chapter was conducted with the aim of discovery of new, lightweight and porous framework materials. The hydrothermal synthesis of BIRM-1 was used as a starting point with the zinc nitrate substituted with the magnesium equivalent.

5.2 Experimental

5.2.1 Hydrothermal Synthesis

The initial attempt at synthesising a magnesium-based framework using 3-phosphonopropionic acid was conducted using the same method as developed by Zhao for the synthesis of BIRM-1 but replacing zinc nitrate hexahydrate with magnesium nitrate hexahydrate. The quantities of reagents used are shown in Table 5.1, below.

Table 5.1) Quantities of reagents used in the hydrothermal synthesis attempt at a magnesium-based framework, adapted from Zhao's 'method III' for BIRM-1[115]

	Zinc nitrate hexahydrate	3-phosphonopropionic acid	Tetraethylammonium bromide	Urea
Molar Ratio	1	1.75	1.3	9
Mass (g)	1.436	1.5098	1.5342	3.0631

Subsequent experiments varied the ratios of the above reagents as well as introducing additional additives to act as modulators. The aim of this was to study the effect on crystal morphology in order to grow larger, single crystals for diffraction experiments and subsequent structure solution.

5.2.2 Diffusion Methods

For slow crystallisations vapour and layered diffusion techniques were attempted. The product from the hydrothermal synthesis was tested for solubility in a range of solvents. It was found to be insoluble in acetone and therefore this was selected as the antisolvent in these experiments. An aqueous solution of the reagents was made and adjusted to pH 6.5 with 28% w/w aqueous ammonia solution. Acetone was either layered on top of the precursor solution, or the solution was left in an atmosphere of acetone vapour as set out in the methodology section of this thesis.

5.3 Initial Product

The initial attempt at synthesising a magnesium-based framework material did indeed yield a crystalline product. The product obtained was in the form of crystals stuck together forming roughly spherical clumps. These proved very difficult to break apart for single crystal diffraction experiments. The powder diffraction pattern from the product is shown in Figure 5.1.

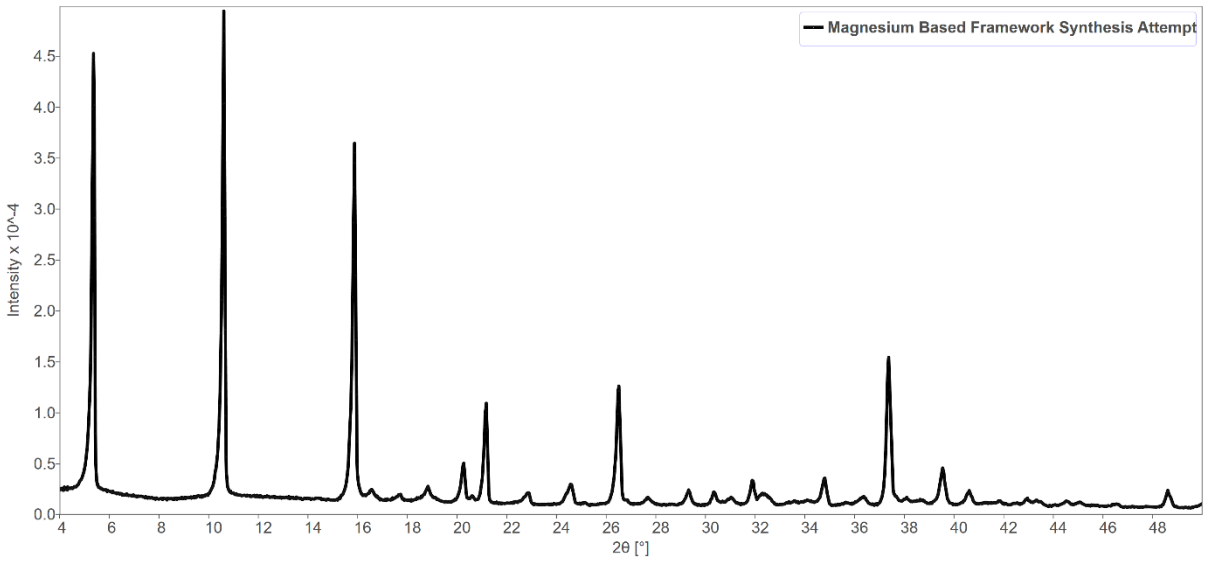

Figure 5.1) PXRD pattern obtained from the product of the synthesis attempt of a magnesium-based framework material

It proved not possible to separate out a suitable single crystal for diffraction experiments. Each crystal attempted was either badly twinned or far too small and weakly scattering to provide data good enough for structure solution. An attempt at indexing the powder pattern was made and the results of this are shown in Table 5.2.

Table 5.2) Results of indexing the product of the hydrothermal synthesis, further detail is included in the appendix

Sample	Mg-Based Synthesis Attempt
Bravais Lattice	*Ammm*
a (Å)	33.7543
b (Å)	17.7876
c (Å)	9.5952
Volume (Å^3)	5761
M20	40.13

The lattice parameters show a unit cell with one elongated axis, at 33.75 Å long, whilst the other two axes are of more moderate length. Unit cells with one axis significantly elongated compared to the others are often found in layered materials but it is not possible to confirm this is a layered material from the lattice parameters alone. It is also of note that the lattice parameters bear a resemblance to those of the cadmium product in the previous chapter, with the b-axis being just over doubled. It seems plausible that these two materials could be similar in structure as both metal ions are known to coordinate octahedrally.

5.3.1 Attempts to Control Crystallisation

5.3.1.1 Reagent Ratios

Reagent ratios were adjusted in order to see if these influence the crystal size. It was hypothesised that an increase in linker concentration may encourage framework growth and have an effect on the pH of the synthesis solution, slowing down either nucleation or crystal growth and allowing larger crystals to be obtained. Similar arguments can be made for urea, as this reagent also affects the pH of the synthesis solution. The synthesis was also attempted without TEAB to check whether it is necessary in order to obtain this phase as it may have unintended effects on the crystallisation. The quantities of ratios used

in each experiment are set out in Table 5.3 and the powder diffraction patterns obtained from the products are shown in Figure 5.2.

Table 5.3) List of reagent ratios used for synthesis attempts of larger crystals, the molar ratio is a ratio of the listed reagent to magnesium nitrate as shown in Table 5.1

Reagent Changed	Mass of Reagent Used (g)	Molar Ratio to Magnesium
Less urea	2.8033	8
More urea	3.25	9.5
Less linker	1.294	1.5
More linker	1.7255	2
No TEAB	0	0

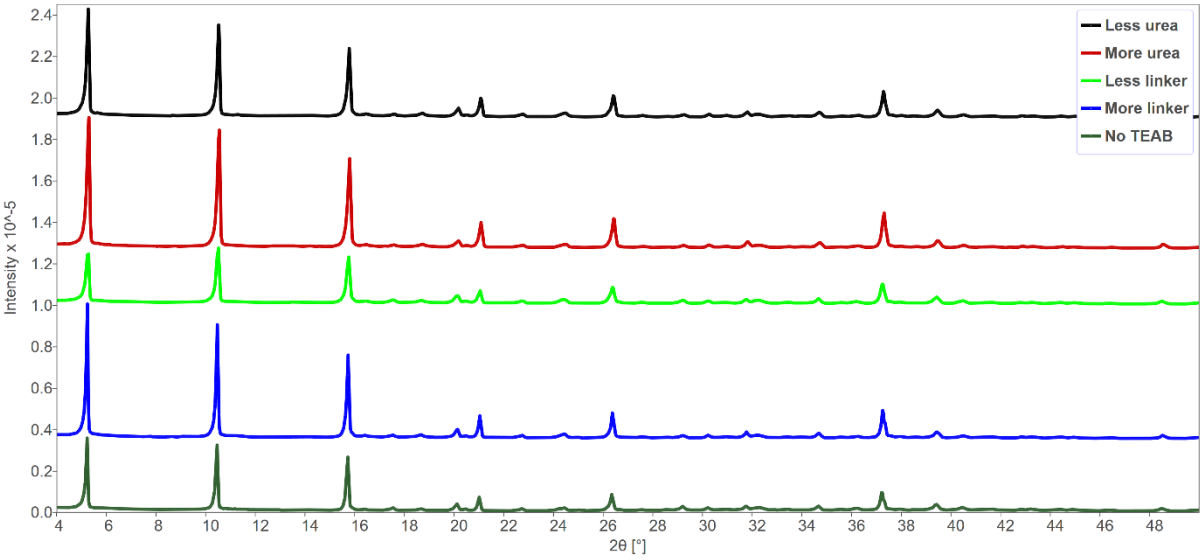

Figure 5.2) PXRD patterns obtained from the products of synthesis attempts with varying ratios of reagents as set out in Table 5.3

No effect on crystal morphology or phase outcome was observed. Though it is notable that this synthesis does seem be quite resilient to difference in synthesis conditions, as opposed to BIRM-1 which has been found to be a rather sensitive synthesis. Also of note is that the presence of TEAB does not have any effect on the phase outcome of the synthesis, as was found for BIRM-1.

5.3.1.2 Temperature

The synthesis was tried at a range of temperatures from 80-120 °C to see if this would affect the growth of crystals. The powder diffraction patterns of the products of these syntheses are shown in Figure 5.3;

the synthesis conducted at 80 °C yielded no product. The synthesis conducted at 90 and 100 °C yielded the same product as the initial synthesis, however, there was no change in crystal size and no single crystals suitable for diffraction experiments were obtained. Conducting the synthesis at higher temperatures yielded at least two new phases based on the emergence of different peaks in the corresponding powder diffraction patterns. These syntheses also did not yield large single crystals therefore structure solution of those phases was not possible. Indexing attempts were not made as the samples appear to be a mixture of phases which complicates indexing greatly. A further synthesis attempt was made at 90 °C but with a slow ramp rate up to that temperature; the product was the same as when the synthesis was conducted at a steady 90 °C and there was no effect on crystal size.

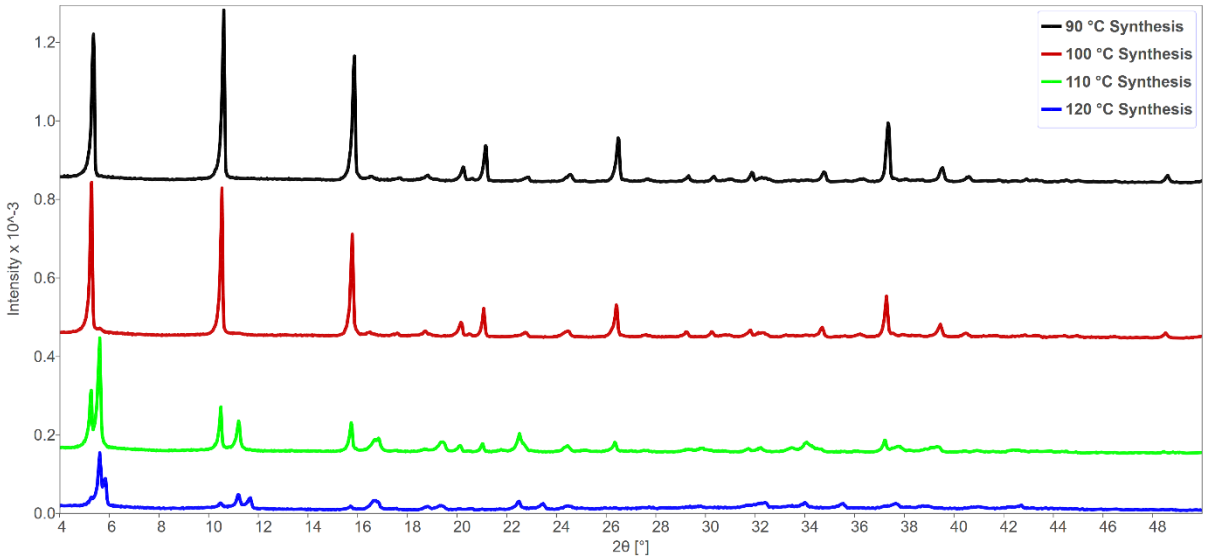

Figure 5.3) PXRD patterns of the products obtained from the attempted synthesis of a magnesium-based MOF at different temperatures

5.3.1.3 Using Moderating Counterions

Use of magnesium acetate as the metal salt was hypothesised to lead to larger crystals as the acetate should coordinate more strongly to the magnesium than nitrate does, leading to slower nucleation and crystal growth. Likewise, a synthesis attempt was also made using acetic acid within the reaction matrix to act as a modulator. The addition of acetic acid should both slow down the rate of change of pH and compete for coordination to the magnesium ions. The product of both these syntheses was the same as the initial synthesis (shown by Figure 5.4), with some differences in relative peak intensity. An increase

in crystal size was not achieved. An area of future work would be to try a similar experiment but attempt to control coordination of the phosphonate group rather than the carboxylate end of the linker. This may be possible through addition of modulators such as phosphonic acid or an alkylphosphonic acid as the acidic protons of these would be closer in pK_a to those from the phosphonate group on the linker used in this work.

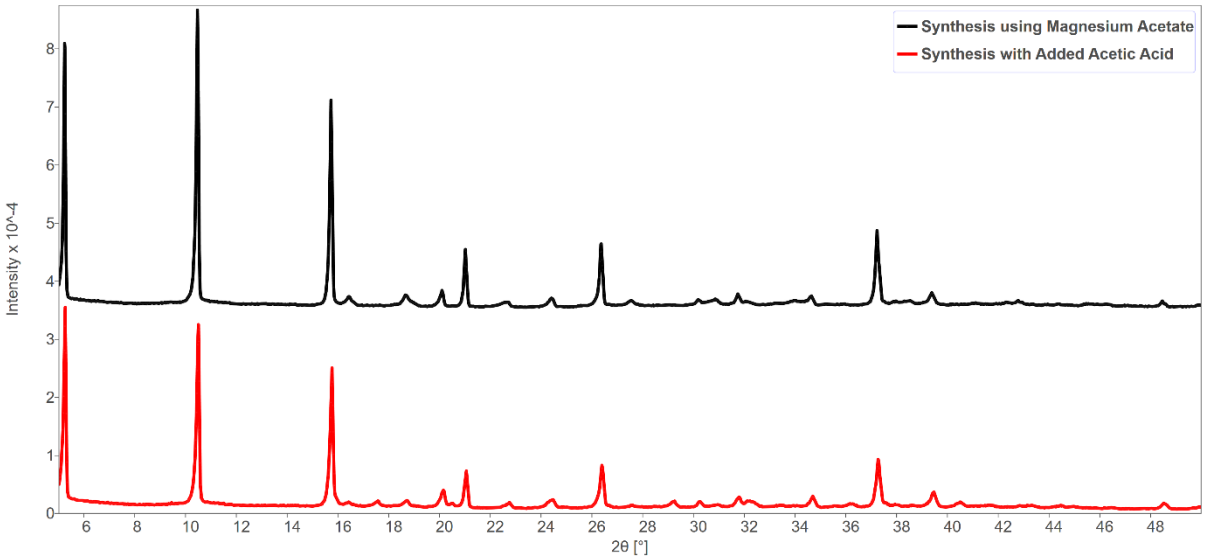

Figure 5.4) PXRD pattern of the product obtained from the attempted synthesis of a magnesium-based MOF using magnesium acetate as the metal salt (black) and from use of acetic acid as a modulator (red)

5.3.1.4 Diffusion Crystallisations

Following from the lack of success of the previous experiments in forming suitable single crystals, a radically different approach was designed. Rather than hydrothermal synthesis, much slower diffusion crystallisations were attempted instead. The product from previous experiments was left in various solvents in order to assess solubility. It was found that the product was least soluble in acetone; this was then selected as the antisolvent for these experiments.

The layered diffusion crystallisation experiment was tried first, however, this yielded no product. It could be that not enough acetone was used or that much of it evaporated rather than mixing with the aqueous precursor solution. Next, the vapour diffusion crystallisation was attempted. This crystallisation yielded a very small amount of product. The powder diffraction pattern obtained from this product is

shown in Figure 5.5. It is clear that this is a different product to that of the hydrothermal synthesis attempt.

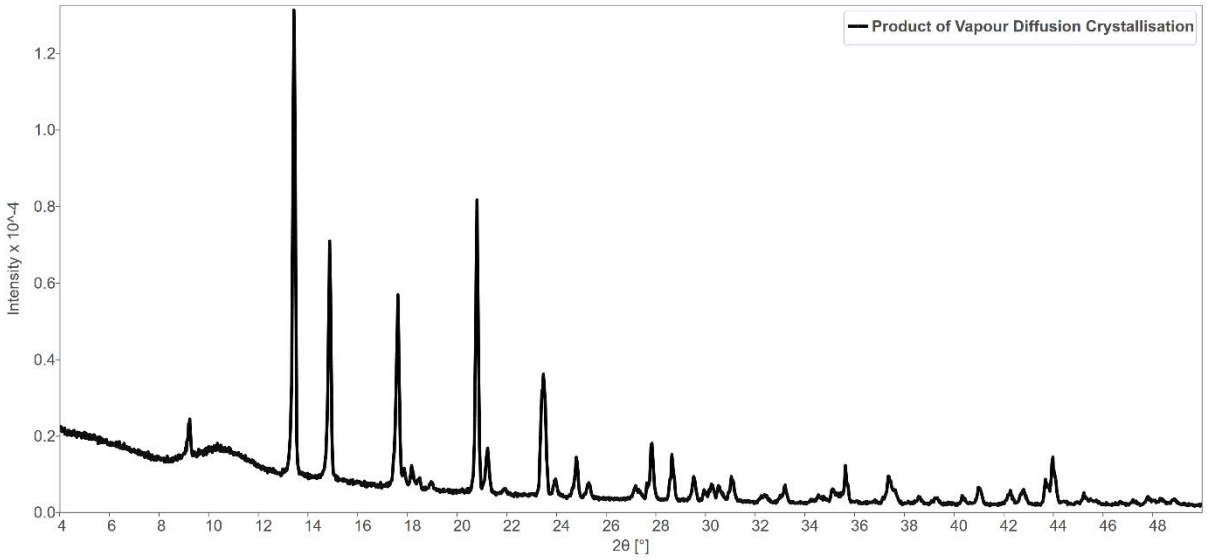

Figure 5.5) PXRD pattern obtained from the product of the vapour diffusion crystallisation

The sample was submitted to the School of Chemistry's single crystal diffraction service run by Dr Louise Male. Dr Male identified a crystal within the sample suitable for diffraction. Data was collected, processed and analysed by Dr Male and a structure was returned. The light atoms contained within the material led to weak scattering, coupled with some disorder within the material, and low symmetry led to difficulties in collecting a dataset with 100% completeness (83% was achieved) and subsequent problems with some atoms not refining anisotropically. Additionally, the location of hydrogen atoms bonded to water molecules in the structure could not be determined.

5.4 1-Dimensional Magnesium Coordination Polymer

The structure was solved and revealed the material to be a coordination polymer, the asymmetric unit of which is shown in Figure 5.6, with the full structure in Figure 5.7. The structure can be described as a 1-dimensional coordination polymer consisting of chains of phosphorus-centred CPO_3 tetrahedra and magnesium-centred MgO_6 octahedra.[153] Each magnesium octahedron is corner-sharing with two CPO_3 tetrahedra with the other 4 oxygen atoms being from water molecules. The chains of magnesium atoms and linker molecules extend along the y-axis.

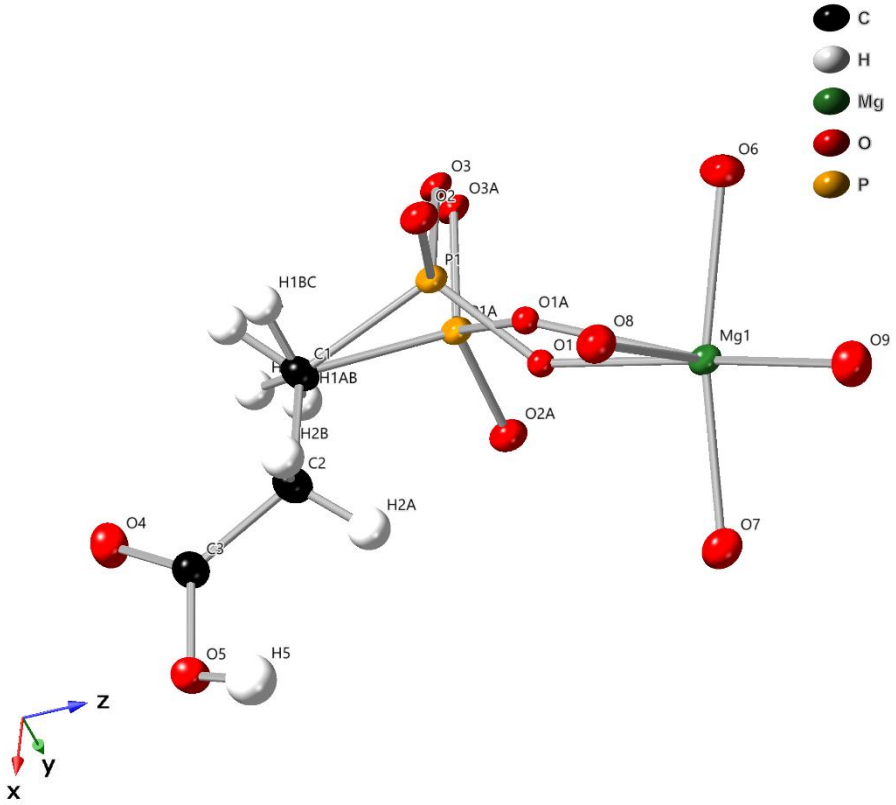

Figure 5.6) Asymmetric unit of the product obtained from the vapour diffusion crystallisation. Ellipsoids are drawn at 50% probability. Atoms P1, O1-O3 / P1A,O1A-O3A are disordered over two positions at a refined percentage occupancy ratio of 93.2:6.8. Atoms O1 and O1A could not be refined anisotropically. A mirror plane runs through Mg1, O1, O6, O7 and O9 which generates a symmetry equivalent oxygen to O8 completing the octahedral coordination.

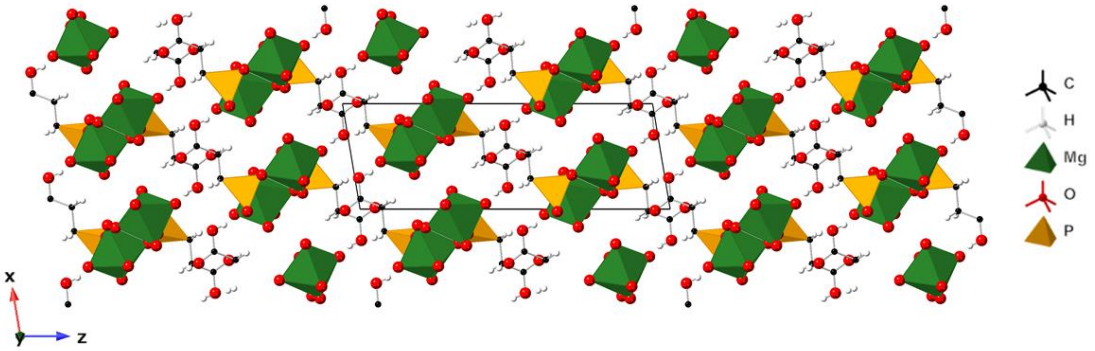

Figure 5.7) Structure of the product obtained from the vapour diffusion crystallisation looking down the y-axis. Disorder has been removed for clarity. Unit cell is indicated by the black outline

The structure crystallises in the $P2_1/n$ monoclinic space group. The lattice parameters, as well as measures of fit for the model and data, are given in Table 5.4. The dataset used to solve this structure was not of particularly high quality, as shown by the poor goodness-of-fit and wR_2, as such, higher

quality crystals were sought. This material, with formula $Mg(O_3PCH_2CH_2CO_2H)\cdot 4H_2O$, will henceforth be referred to as BIRM-6.

Table 5.4) Basic Crystallographic details of BIRM-6

Sample	BIRM-6
Space group	$P2_1/n$
a (Å)	6.6904(7)
b (Å)	7.5524(6)
c (Å)	19.426(2)
β (°)	99.493(11)
Volume (Å^3)	968.13(17)
Goodness-of-fit on F^2	1.201
wR_2	0.3077
Largest peak/hole (e Å^{-3})	1.00/−0.74

5.4.1 Synthesis Optimisation

Whilst the previous synthesis provided a product from which a rough crystal structure was obtained, it provided neither good yield nor high-quality crystals. Therefore, experiments were planned with the aim to improve the synthesis in both yield and crystal quality. A slow evaporative crystallisation from water was attempted. The precursor solution was made in the same fashion as previously with the exception of the TEAB salt which was not used. With the material being a coordination polymer, it was deemed unnecessary to continue adding a templating agent. This is because there is no framework to template. The pH was adjusted to ca. 6.5 with 28% w/w aqueous ammonia solution, as before. The solution was then left to crystallise, which took two weeks. The result was an apparent significantly higher yield of material. The PXRD pattern obtained from the material is shown in Figure 5.8, in black.

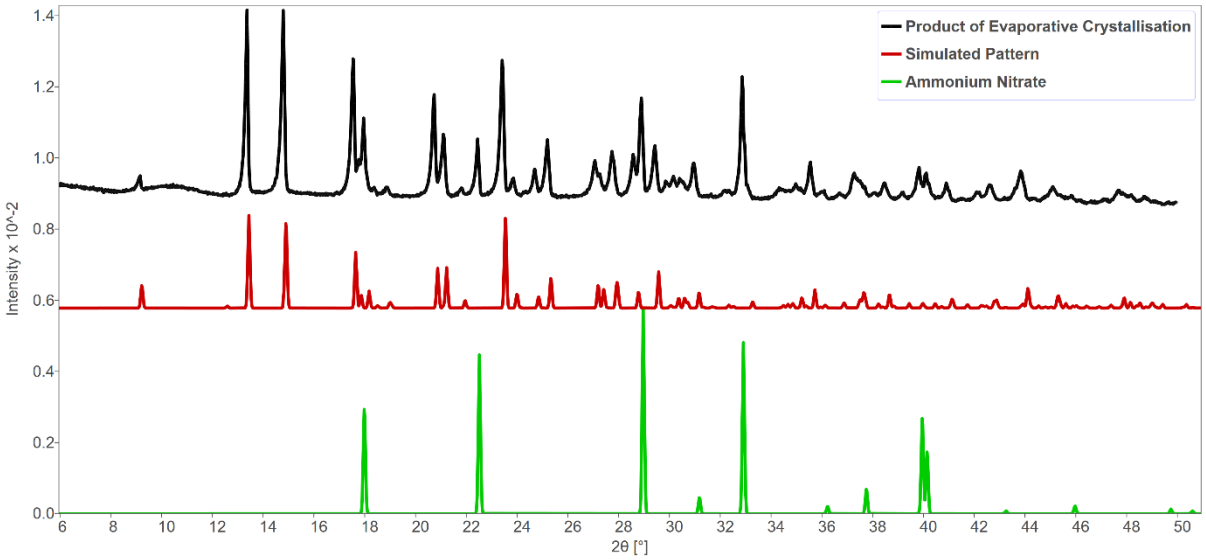

Figure 5.8) PXRD pattern of the product obtained from the evaporative crystallisation (black) compared to a pattern simulated from the previous single crystal structure (red) and a simulated pattern of ammonium nitrate in its room temperature polymorph (green)[154]

It is apparent from the powder diffraction pattern that the same phase was obtained via this route, however, additional peaks were also present. These peaks were phase matched to ammonium nitrate, an expected by product of the reaction. Attempts to wash the ammonium nitrate out of the product were made. An attempt with cold deionised water led to the product dissolving with the ammonium nitrate. An attempt with methanol did not successfully remove all the ammonium nitrate, and led to the appearance of an additional phase, as can be seen in Figure 5.9.

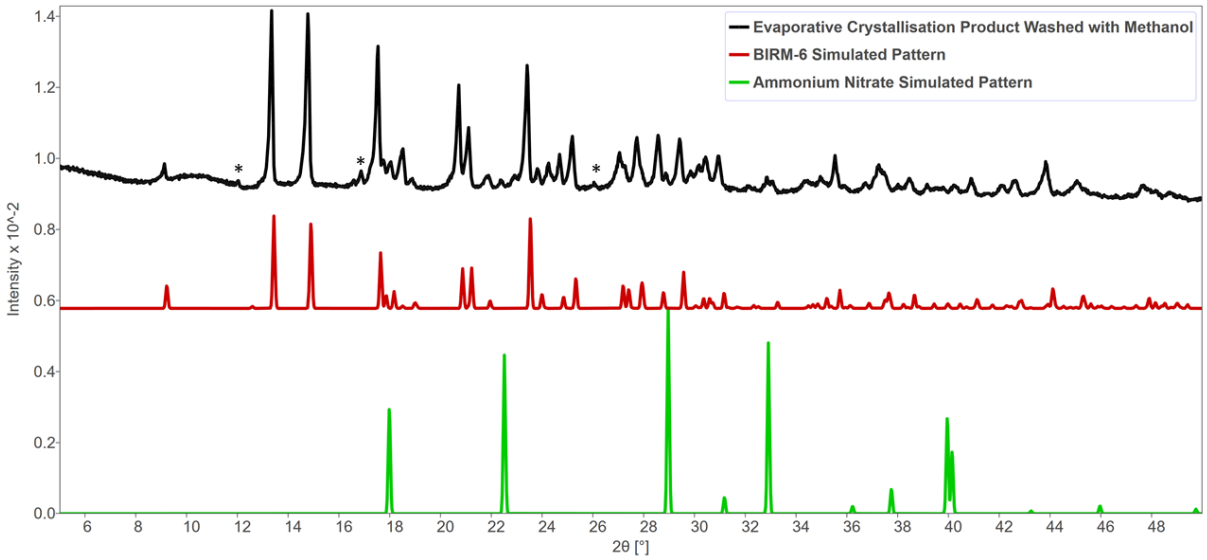

Figure 5.9) PXRD of the same evaporative crystallisation product after washing with methanol. Some peaks from the new impurity are marked with an asterisk.

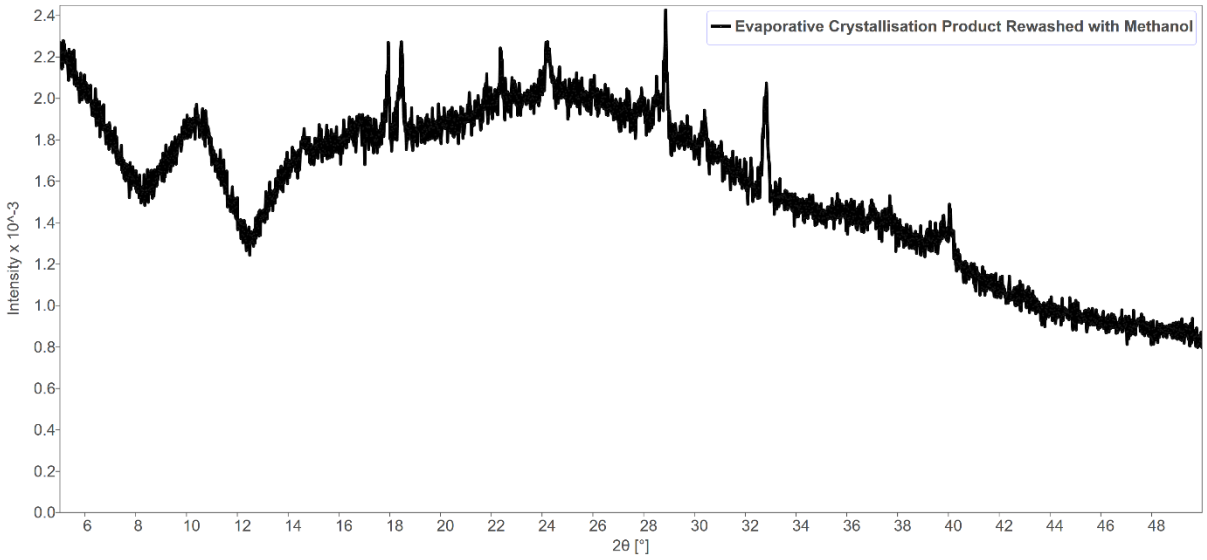

Figure 5.10) PXRD of the same evaporative crystallisation product after a second, longer, washing with methanol

A second, longer wash was attempted but the outcome, as can be seen in Figure 5.10 is the loss of most peak intensity. Most peaks that remain correspond to ammonium nitrate rather than the product.

One other washing attempt was made on the original evaporative crystallisation product using acetone. The outcome from washing with acetone was a thick gel which was left to see if it would crystallise. Concurrent with these experiments, another antisolvent experiment was being run. Rather than a slow diffusion method, this synthesis was done by directly adding antisolvent to the precursor solution in a

rapid fashion. It was thought whilst this may not provide large crystals, it may produce a significant amount of product. Upon adding acetone to the precursor solution, the solution turned to a milky appearance. Attempts to recover product via vacuum filtration were unsuccessful with the milky solution passing through the filter paper, however, as with the attempted wash with acetone of the previous product, a thick gel was left at the bottom of the beaker. This gel was left to crystallise. The result of the crystallisation of these gels was a hard, glassy product, the powder diffraction pattern of which is given in Figure 5.11

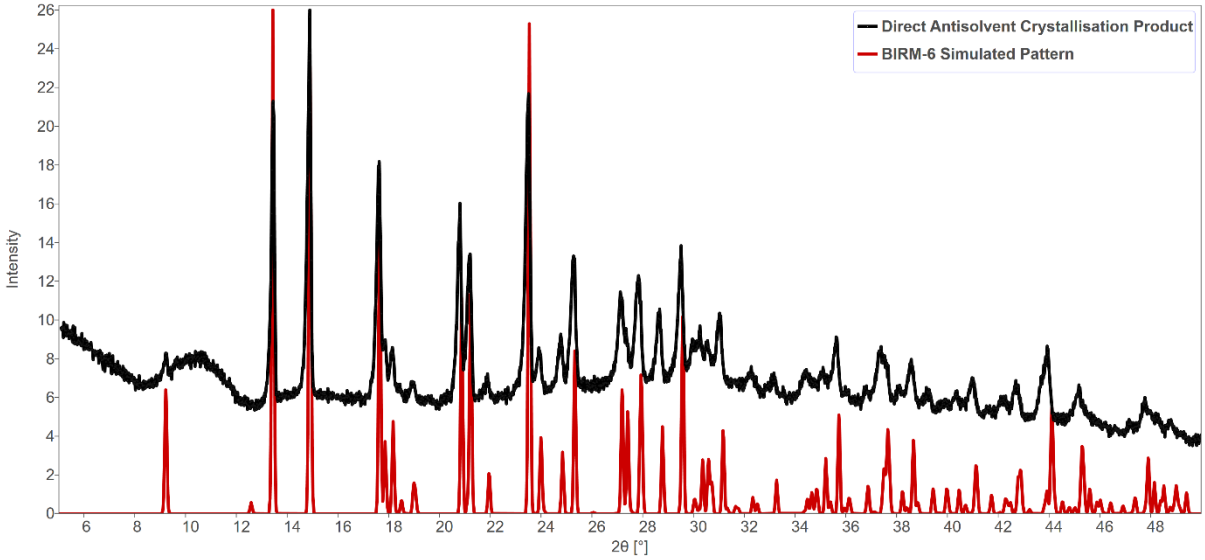

Figure 5.11) PXRD pattern obtained from the product of the direct antisolvent crystallisation

The product contained large clear crystals. A sample was submitted to the single crystal service run by Dr Louise Male and much higher quality data than previously was obtained; this dataset had 100% completeness. The full structure, including positions of hydrogen atoms, was able to be solved.

5.4.2 Characterisation

5.4.2.1 Structure

Figure 5.12, Figure 5.13 and Figure 5.14 show the structure of BIRM-6, the structure solved from this dataset is very similar to the structure obtained previously but the location of hydrogen atoms from water molecules have been determined here. The structure is confirmed as a 1-dimensional coordination polymer made up of chains consisting of CPO_3 and MgO_6 polyhedra. The asymmetric unit has a mirror

plane which runs through the magnesium, perpendicular to the Mg1 O9 bond. The sixth coordinated oxygen is thus symmetry equivalent to O9 and is not shown within the asymmetric unit. The chains of CPO_3 and MgO_6 polyhedra are particularly visible in Figure 5.14 extending along the y-axis, though note that these chains are not interconnected by anything more than hydrogen bonds.

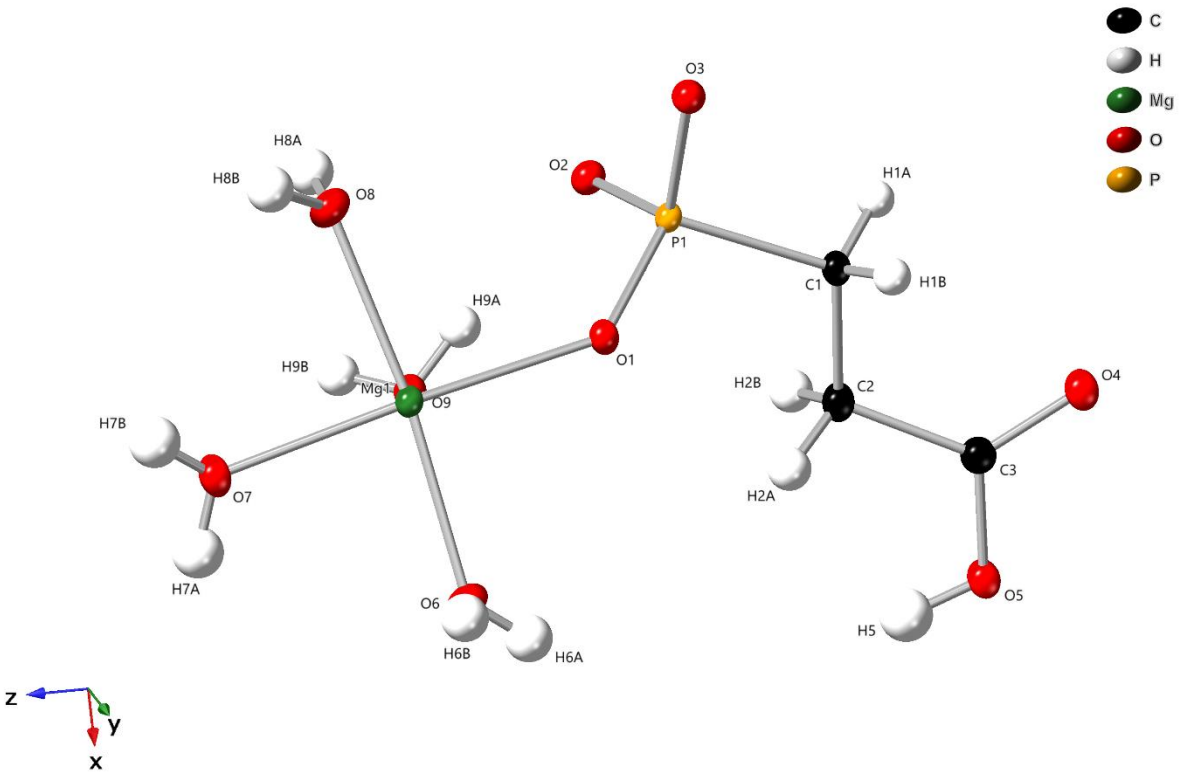

Figure 5.12) Asymmetric unit of the BIRM-6 structure, ellipsoids drawn at 50% probability level.

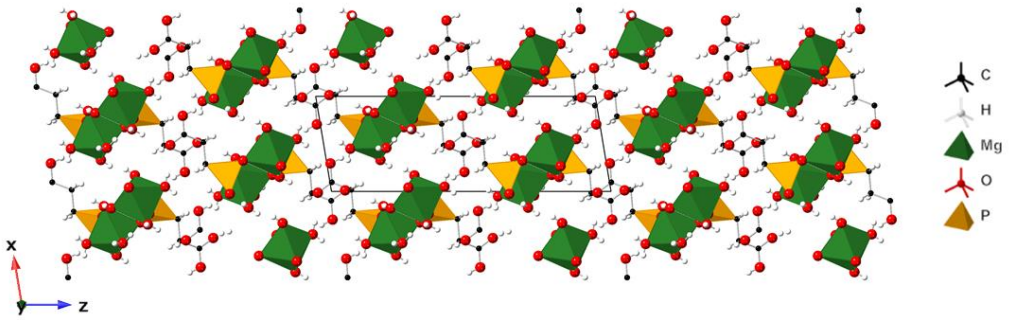

Figure 5.13) Structure of BIRM-6 looking down the y-axis. Unit cell is indicated by the black outline

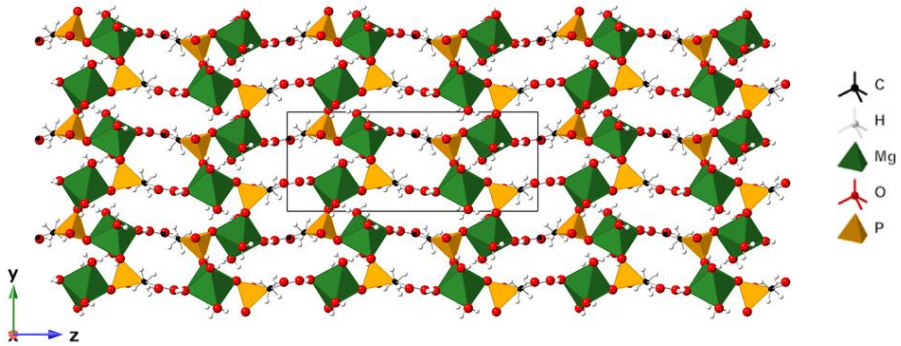

Figure 5.14) Structure of BIRM-6 looking down the x-axis. Unit cell indicated by the black outline

Table 5.5 gives the lattice parameters and measures of fit for the BIRM-6 structure obtained from the higher quality crystal. They show good agreement with the values originally obtained but with much better measures of fit. There was no evidence of disorder within the structure from the higher quality data obtained. Full crystallographic detail is given in the appendix. Using the formula weight from the solved structure, the yield of this synthesis was 66.4%.

Table 5.5) Basic structural and crystallographic details of BIRM-6

Sample	BIRM-6
Molecular Formula	$Mg(O_3PCH_2CH_2CO_2H)\cdot 4H_2O$
Formula Weight	248.41
Space group	$P2_1/n$
a (Å)	6.69070(10)
b (Å)	7.54360(10)
c (Å)	19.4168(4)
β (°)	99.449(2)
Volume ($Å^3$)	966.71(3)
Goodness-of-fit on F^2	1.076
wR_2	0.0785
Largest peak/hole (e $Å^{-3}$)	0.45/-0.37

5.4.2.2 SEM-EDX

SEM images of the crystals (Figure 5.15) were taken. Though no clear regular morphology is visible in the image, the crystal used for single crystal diffraction was a plate with dimensions 0.011 × 0.052 × 0.137 mm.

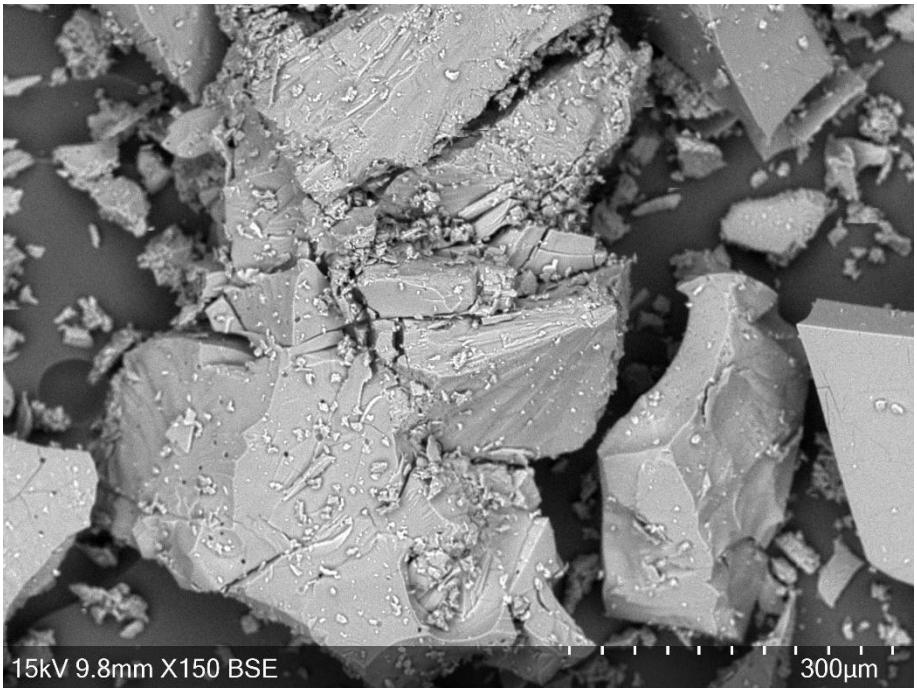

Figure 5.15) SEM image of crystals of BIRM-6 at 150× magnification. Image taken using BSE detector

The BSE detector was used in order to show any impurities, as patches of material containing lighter elements will show darker and heavier elements will appear as bright spots. The image does contain some dark spots which may be some other phase made up of lighter elements, such as excess organic material, or could be features of the crystal surface.

EDX analysis was also performed on the sample, finding a phosphorus to magnesium ratio of 1:1.04, in good agreement with the structure solved through single crystal diffraction.

5.4.2.3 FTIR Spectroscopy

Figure 5.16 gives the FTIR spectrum whilst Table 5.6 lists notable bands and assignments to functional groups. This FTIR spectrum is rather complex, with many overlapping peaks. Whilst all the expected peaks are present some are much weaker than expected, such as the 1701 cm^{-1} peak arising from the carboxylic acid group which is usually a very strong absorption band. There are also some peaks that were not expected: there may be residual ammonia left in the sample as apparent from the 3474 cm^{-1} peak. The ammonia could be present as a coordinating group to the magnesium in place of water in some instances or could be present in some amorphous content. The PXRD pattern of the material in

Figure 5.11 has quite a high background suggestive of significant amorphous content. Additionally, there are some peaks which are evidence of deprotonation of the carboxylic acid proton which is not shown in the solved structure, such as the peak at 1556 cm^{-1} which is indicative of a deprotonated carboxylate group. Overall, the FTIR provides evidence that there is a phase present with different connectivity compared to BIRM-6, as this phase is not apparent from x-ray diffraction data in Figure 5.11 beyond a notable background signal, it is likely this phase is amorphous.

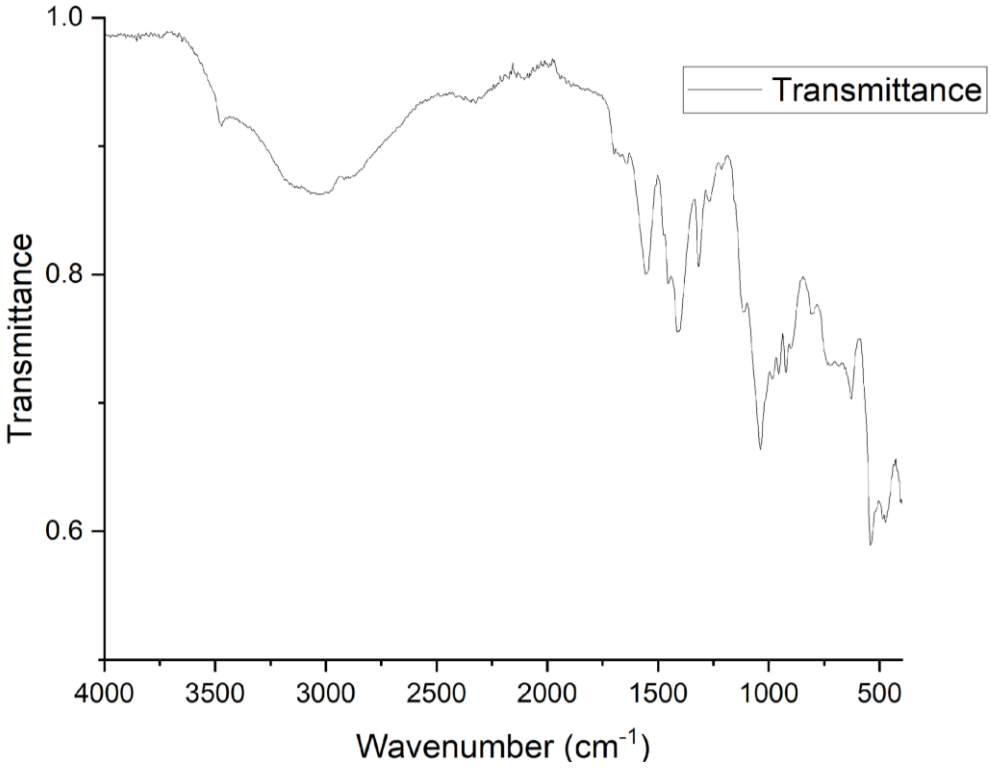

Figure 5.16) FTIR spectra collected from BIRM-6

Table 5.6) FTIR peak assignments for BIRM-6

Peak (cm^{-1}), profile, intensity	Assignment
3474, sharp, weak	Possible ammonia N–H
3120, broad, weak	Water O-H, carboxylic acid O–H
1701, sharp, weak	Carboxylic acid C=O
1556, medium	Possible carboxylate C–O
1454, sharp, medium	Possible carboxylate C–O
1413, sharp, medium	Phosphonate P–C
1401, sharp, medium	Possible carboxylate C–O

1319, sharp, medium	Carboxylic acid C–O
1397, shoulder, medium	Carboxylic acid C–O
1040, sharp, strong	Phosphonate P–O

5.4.2.4 Thermogravimetric Analysis

The TGA-MS decomposition profile of BIRM-6 is shown in Figure 5.17. There was continuous loss in mass from the start of the heating program at 40 °C up to around 600 °C where the mass loss plateaued. The mass loss appeared to continue just before the end of the heating program at 700 °C where there is also a sharp peak in the mass 44 MS signal and a sharp exothermic peak in the DTA trace, both indicating the burning of organic components of the material. The start of the decomposition has two emissions of mass 18, corresponding to water coming off, with two endothermic peaks in the DTA trace. The mass loss after the second emission of water is approximately 28.2% which is in good agreement with the theoretical 28.98% from loss of water from the structural formula. The further mass 18 emissions coincide with mass 44 emissions and exothermic peaks which suggest they are from combustion of organic components. The final mass percentage that is recorded at 700 °C is 55.34%, ie. 44.66% mass loss.

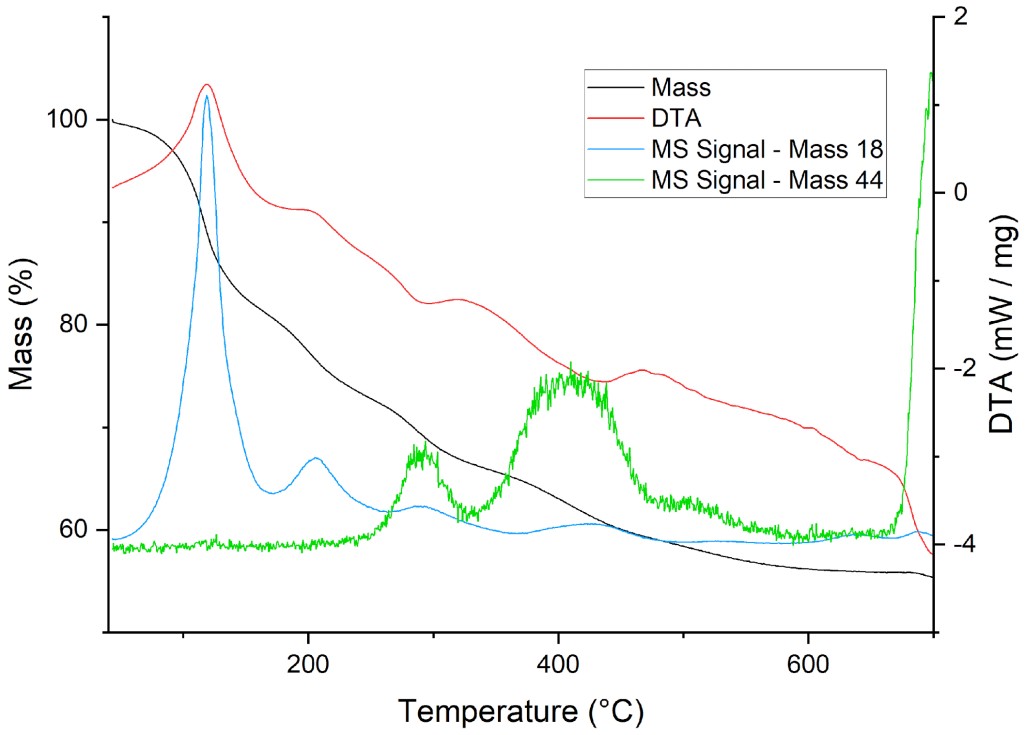

Figure 5.17)TGA-MS analysis of BIRM-6

The product of the TGA (Figure 5.18) was a black powder. The powder diffraction pattern obtained from this product (Figure 5.19) did not contain many features but the most notable is a broad peak around 30° 2θ. This broad peak corresponds to two peaks found in the same region in the diffraction pattern for magnesium pyrophosphate, therefore the product does seem to contain this phase. The broad peaks may indicate very small crystallite size of the TGA product. The theoretical mass loss if magnesium pyrophosphate were the only material left at the end of the TGA is 55.21% which leaves a discrepancy of 10.55% likely due to residual amorphous organic material giving the TGA product its black appearance.

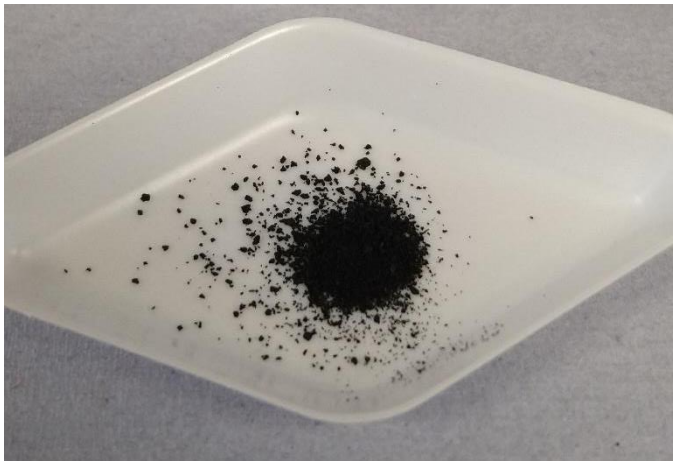

Figure 5.18) Image of the post-TGA product of BIRM-6

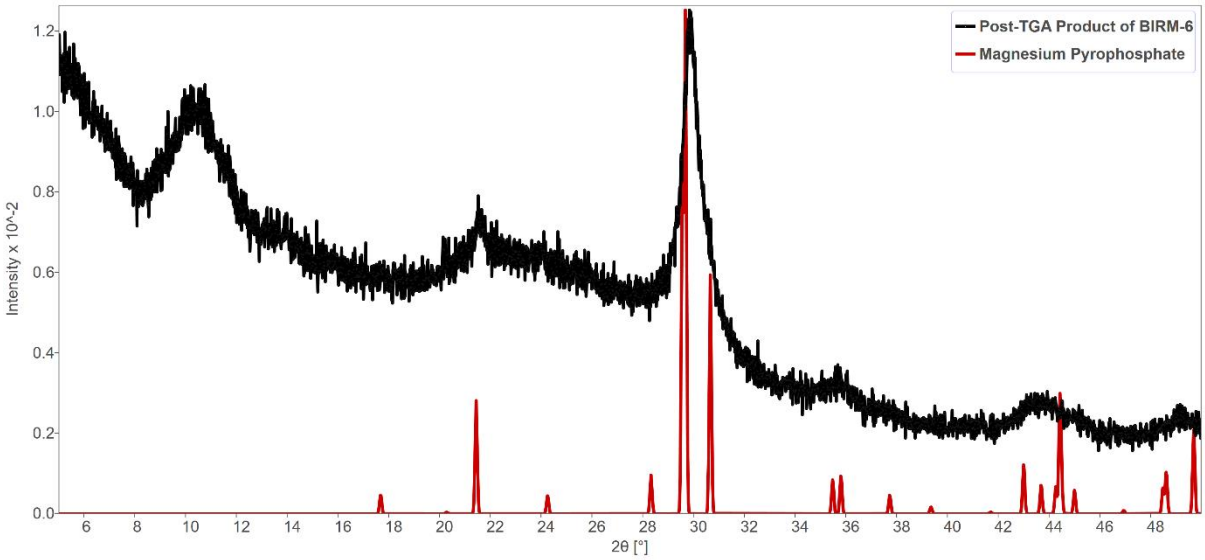

Figure 5.19) Powder diffraction pattern of the post-TGA product from BIRM-6 (black) compared to a simulated pattern of magnesium pyrophosphate[155] *(red)*

5.4.3 Heating Phase Change Attempt

With so many of the ligands coordinated to magnesium being water, a hypothesis was formed that heating the material in order to dehydrate it may lead to the formation of another novel framework. With the carboxylic end of the linker molecule being uncoordinated one could imagine a scenario where removal of the water ligands from the magnesium would lead to the coordination of the linker at both ends. This could lead to an interesting material being formed, such as a porous MOF; there are examples of MOFs being made this way in literature.[156] Therefore, the material was left in a drying oven overnight at a moderate temperature of 60 °C. It was planned that the material would be heated at this relatively

low temperature first to see if there is an effect and later go to higher temperatures, however, even at 60 °C a phase change was observed.

The diffraction pattern (Figure 5.20) of the product is evidently very different to that of the material before heating, indicating a significant structural difference. Unfortunately, a side effect of this significant structural change was the complete degradation of the single crystals obtained in the initial synthesis. It was not possible to obtain any usable single crystal diffraction data and therefore it has not been possible to solve the structure in this work. Indexing attempts were made, however; possibly due to the broad peaks and high background, no reasonable indexing result was found.

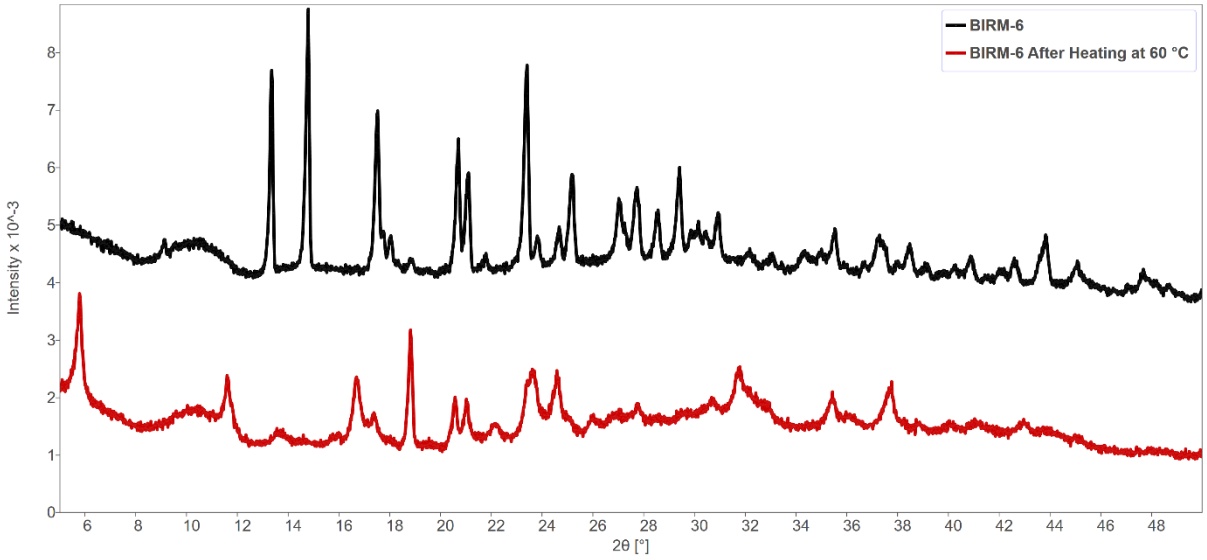

Figure 5.20) PXRD pattern of the product obtained from heating BIRM-6 at 60 °C (red) with the original powder diffraction pattern from BIRM-6 (black)

5.5 New Attempts

Owing to the lack of success in producing single crystals of new MOF materials based on magnesium in this work so far, a change in strategy was sought. After a search for literature on the synthesis of phosphonate-based MOFs in aqueous solutions, a method developed by Farha et al. was found.[149] This synthesis was a one-pot hydrothermal method, however, it involved the formation of linker in situ. The basic principles of pH adjustment of the solution prior to heating at a significantly higher temperature were used for this work. As a result, a series of experiments (Table 5.7) was set up, inspired by this

method but also designed to examine a broad range of variables and their effect on the synthesis outcome in order to identify any conditions that may lead to novel materials.

Table 5.7) List of experimental conditions used in search of novel materials

Method	Magnesium nitrate hexahydrate	3-phosphonopropionic acid	Base	Water	Heating
I	1.48 mmol	4.08 mmol	NaOH to pH 7	5 ml	150 °C 48 Hours
II	0.98 mmol	2.04 mmol	Urea 3.07 mmol	5 ml	170 °C 24 Hours
III	0.98 mmol	2.04 mmol	NaOH to pH 4	5 ml	170 °C 24 Hours
IV	1.48 mmol	2.04 mmol	NH_4OH to pH 7	5 ml	170 °C 24 Hours
V	1.48 mmol	2.04 mmol	Urea 2.59 mmol	5 ml	170 °C 24 Hours
VI	1.48 mmol	2.04 mmol	Urea 3.29 mmol	5 ml	170 °C 24 Hours

Of these synthetic methods, I and III produced no product. Figure 5.21 contains the diffraction patterns from the products of the remaining 4 methods.

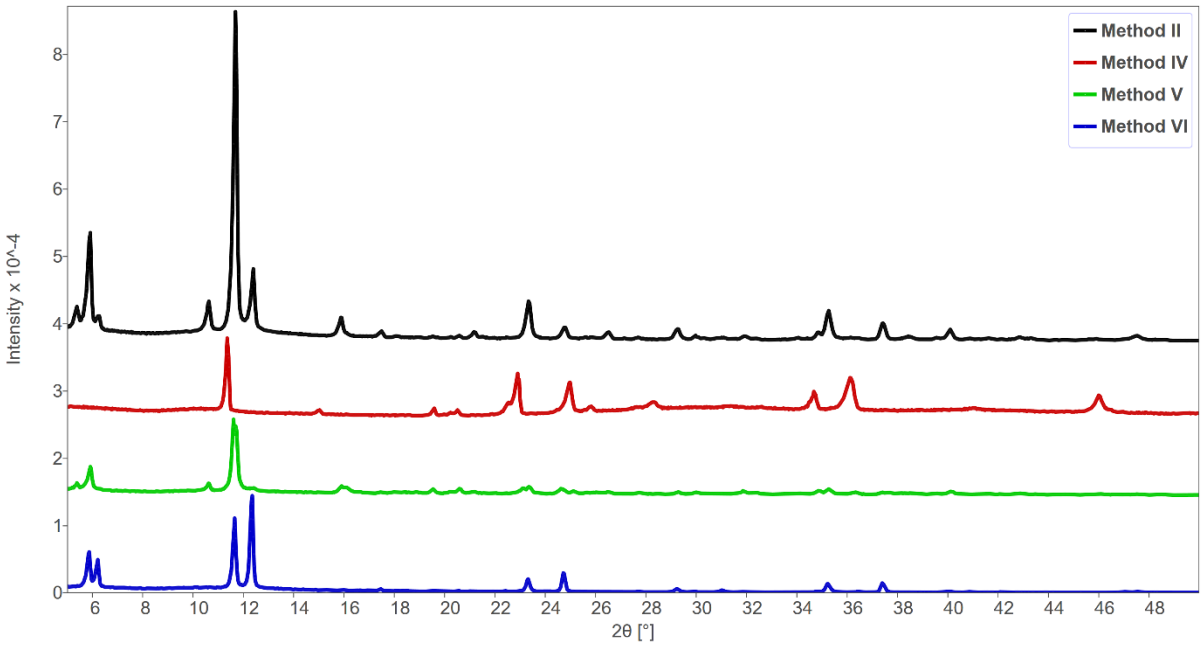

Figure 5.21) Diffraction patterns from the products obtained from methods II (black), IV (red), V (green) and VI (blue)

From the diffraction patterns it appears that there are multiple phases that have been made and that some products seem to be a mixture of phases. This is based on the presence of some peaks in multiple products whilst other peaks in the pattern are different. For example, all of the peaks present in the diffraction pattern for product VI also appear in the diffraction pattern for product II with some additions. The pattern for product VI also seems to be a mix of phases as it contains peaks which are present in product V with the addition of some extra peaks. Products IV and V appear as though they could be made of single phases whilst II and VI seems to be a combination of phases found in the former as well as other phases due to additional peaks being present. This makes the indexing of products II and VI quite difficult, with an attempt being made but no satisfactory solution found. Method II gave a sample that was powdery, unsuitable for single crystal diffraction. The other three samples were submitted to the single crystal diffraction facility of the School of Chemistry. The products of method V and VI did not give high quality single crystal data, light scattering and small crystals being factors in this. The product of method IV gave twinned crystals, however, the crystals diffracted better than the products of the other samples. The sample was sent to the UK National Crystallography Service (NCS) at the University of Southampton in search for better data. The NCS returned a twinned dataset with a roughly solved structure but with poor measures of fit.

5.5.1 New Phase Obtained

The product of method IV (henceforth called BIRM-7) has the formula $Mg_3(O_3PCH_2CH_2CO_2)_2$, the structure is shown in Figure 5.22 as the asymmetric unit as well as the expanded structure in Figure 5.23 and Figure 5.24. The structure is made up of magnesium and phosphorus oxide polyhedra linked together to form extended sheets which are in turn bound together by the linker molecule. This forms a pillared-layered type structure. Interestingly, Mg1 and Mg3 are both in a relatively unusual 5-coordinate square pyramidal configuration. There are plausible channels and pores within the structure; in between the interconnected sheets, however, the entrances are rather narrow so whether they would actually be accessible will be investigated by recording adsorption isotherms. Compared to BIRM-6, both ends of the linker (both the phosphonate and carboxylate groups) are now deprotonated and coordinated to

magnesium cations. This allows for greater dimensionality of the framework and BIRM-7 is indeed a 3-dimensional framework.

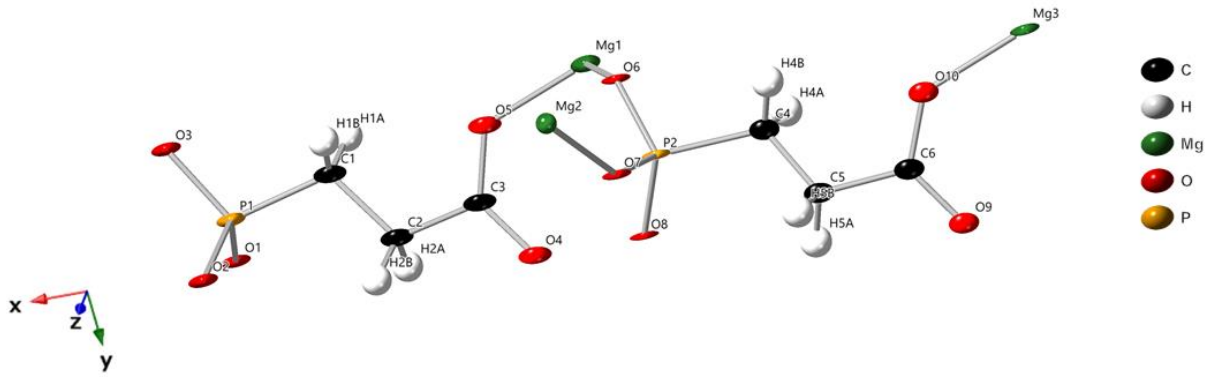

Figure 5.22) Asymmetric unit of BIRM-7. Atoms are drawn at 50% probability level. Atom Mg2 could not be refined anisotropically.

Table 5.8) Basic crystallographic details of the product from method IV

Sample	BIRM-7
Molecular Formula	$Mg_3(O_3PCH_2CH_2CO_2)_2$
Formula Weight	374.99
Space group	$P2_1/c$
a (Å)	15.4935(8)
b (Å)	9.0290(5)
c (Å)	9.0152(4)
β (°)	92.154(5)
Volume (Å^3)	1260.25(11)
Goodness-of-fit on F^2	2.982
wR_2	0.6025
Largest peak/hole (e Å^{-3})	4.98/-3.02

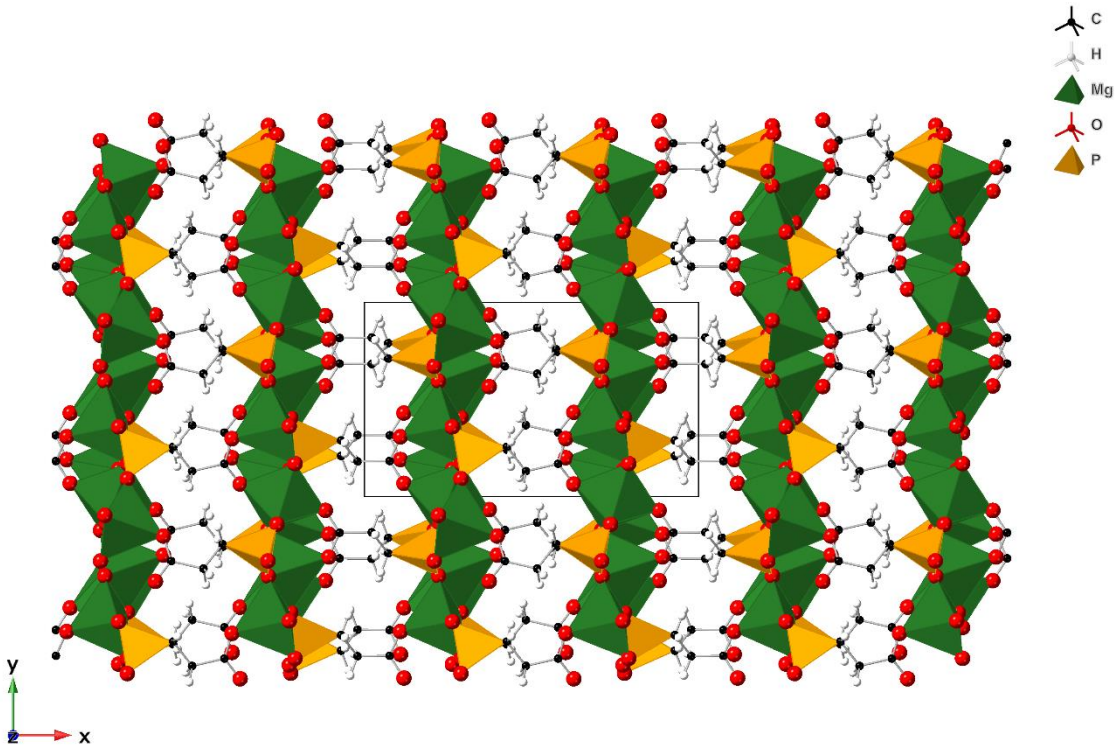

Figure 5.23) Structure of BIRM-7 looking along the z-axis. Unit cell indicated by black outline

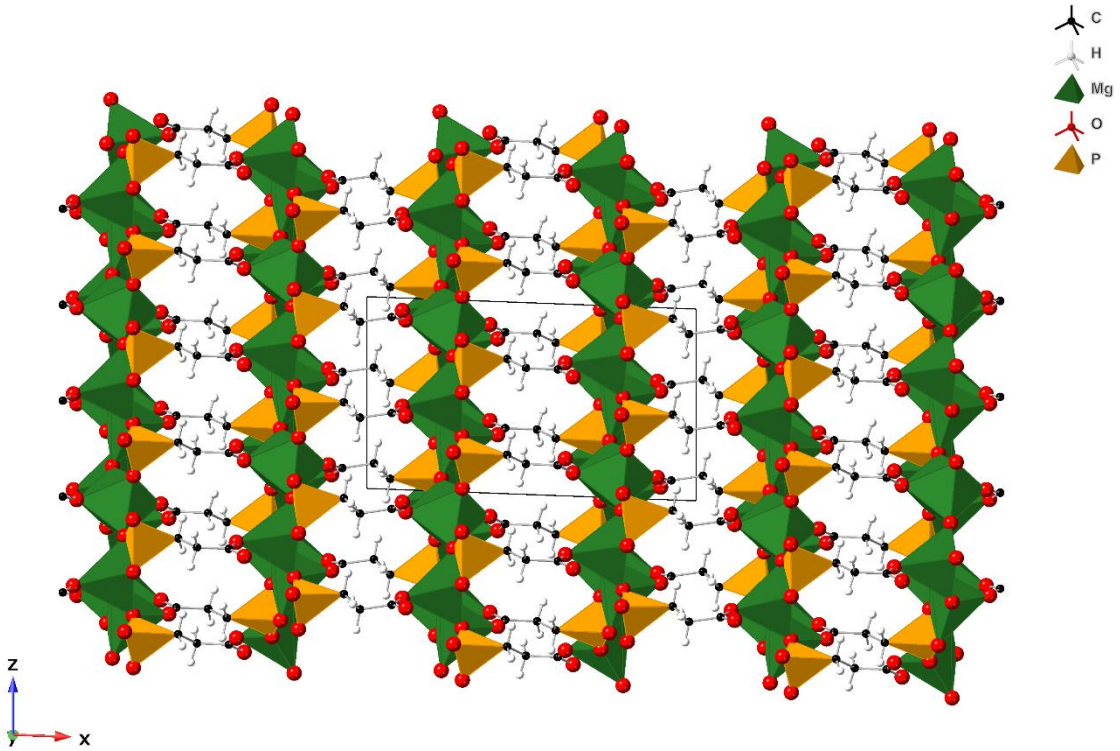

Figure 5.24) Structure of BIRM-7 looking along the y-axis. Unit cell indicated by black outline

5.5.2 Synthesis Optimisation

Before further characterisation would be conducted on the material, experiments were set out to optimise the synthesis of the material. The aim was to increase the quality of crystals so that better single crystal diffraction data could be collected to give more confidence in the solved structure.

The initial attempt was to adjust the metal:linker ratio to equal that of the product (3:2) with 3.078 mmol of magnesium nitrate hexahydrate, and all other variables the same as used in method IV. The powder diffraction pattern obtained from the product of this synthesis is shown in Figure 5.25. Whilst showing a large decrease in background, many peaks had drastically reduced intensity or were missing altogether compared to both the simulated pattern and the product of the original synthesis, possibly due to a preferred orientation effect. It is also worth noting that the pattern from the product of the original synthesis is somewhat different to the simulated pattern. Again, this could be due to a preferred crystal orientation effect. There are no additional peaks in the product pattern so there is no suggestion of impurities being present.

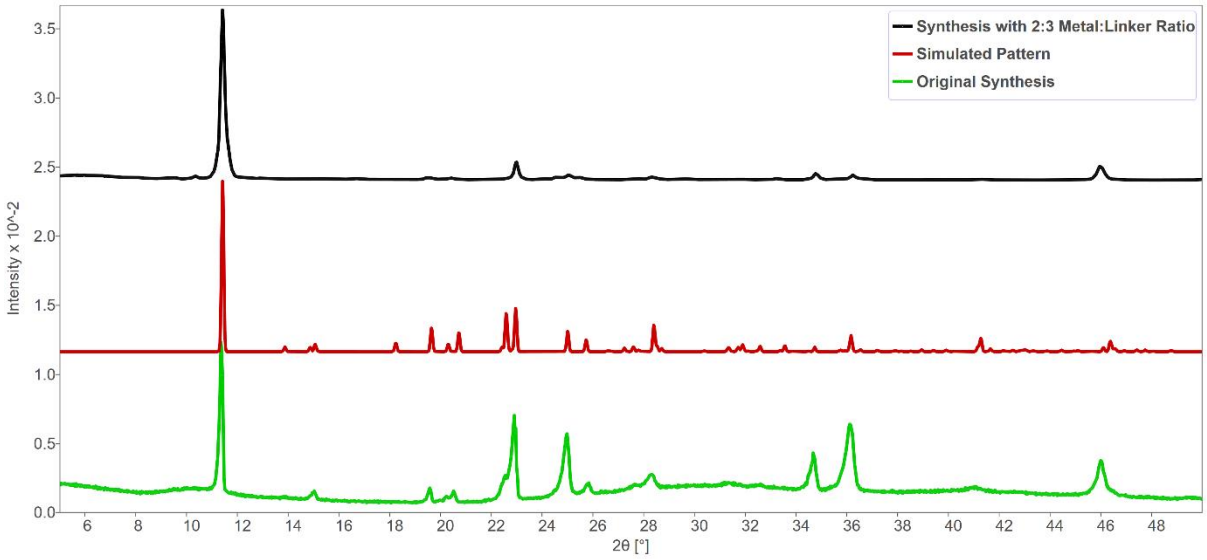

Figure 5.25) A comparison of PXRD patterns obtained from using a 2:3 metal:linker ratio (black), a simulated pattern of BIRM-7 (red) and the pattern from the original synthesis (green).

The method IV synthesis was also attempted again but with the addition of tetraethylammonium bromide (TEAB) as a structure directing agent in order to observe if this had any effect on the phase outcome. The powder diffraction pattern from this synthesis is shown in Figure 5.26.

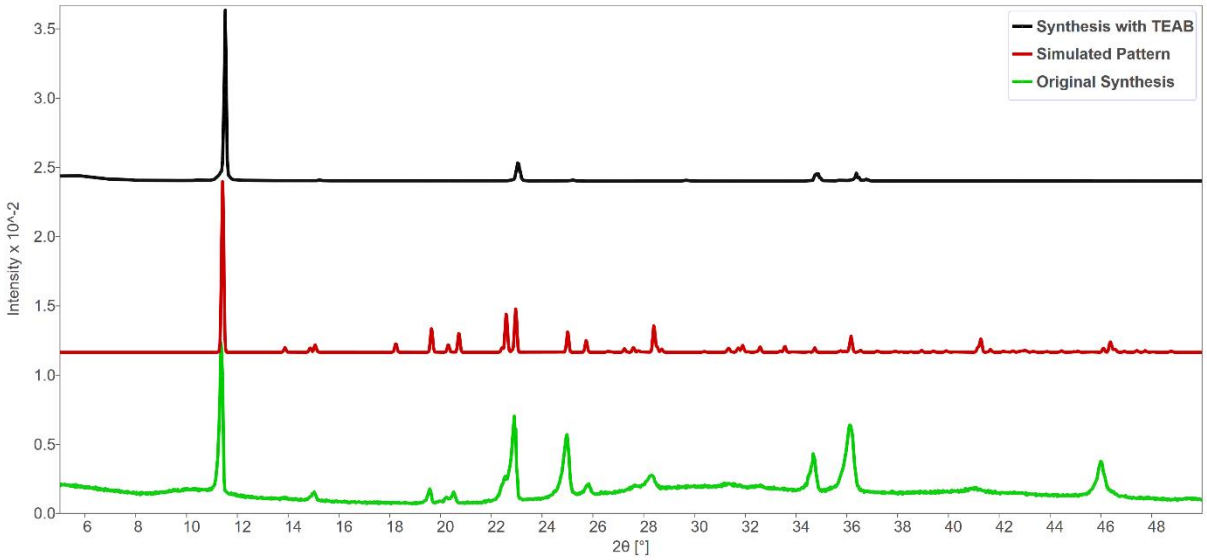

Figure 5.26) A comparison of PXRD patterns obtained from the BIRM-7 synthesis with TEAB (black), a simulated pattern (red) and the pattern from the original synthesis (green).

The addition of TEAB seems to have had a similar effect on the powder diffraction pattern of the product as increasing the metal:linker ratio did. However, in this instance the crystals obtained were much larger. Whereas previously they were clumps of small crystals with morphology that was difficult to discern by the naked eye, now they were larger individual plates. This could be the source of the radically different relative intensities of the peaks, as large plates will have a significant preferred crystal orientation. The crystals were screened for single crystal diffraction and were found to diffract well with no twinning. The quality of the crystals seemed much improved compared to the original synthesis and the optimisation was deemed successful.

5.5.3 Characterisation

5.5.3.1 Structure

Although some of the lattice parameters (Table 5.9) and the asymmetric unit (Figure 5.27) look quite different at first glance to those that were obtained previously, the different space group found ($P2_1$

compared to $P2_1/c$) means that the expanded structure (Figure 5.28) is actually very similar to that which was solved originally. In addition, the measures of fit for this dataset and model were drastically improved compared to before, giving confidence that this the correct space group and structure. This dataset and corresponding structure also confirm the unusual 5-coordinate square pyramidal magnesium. The unit cell obtained from the higher quality crystals is approximately twice the volume of the initially solved unit cell. Supporting that it is the same structure but with lower symmetry and a larger unit cell.

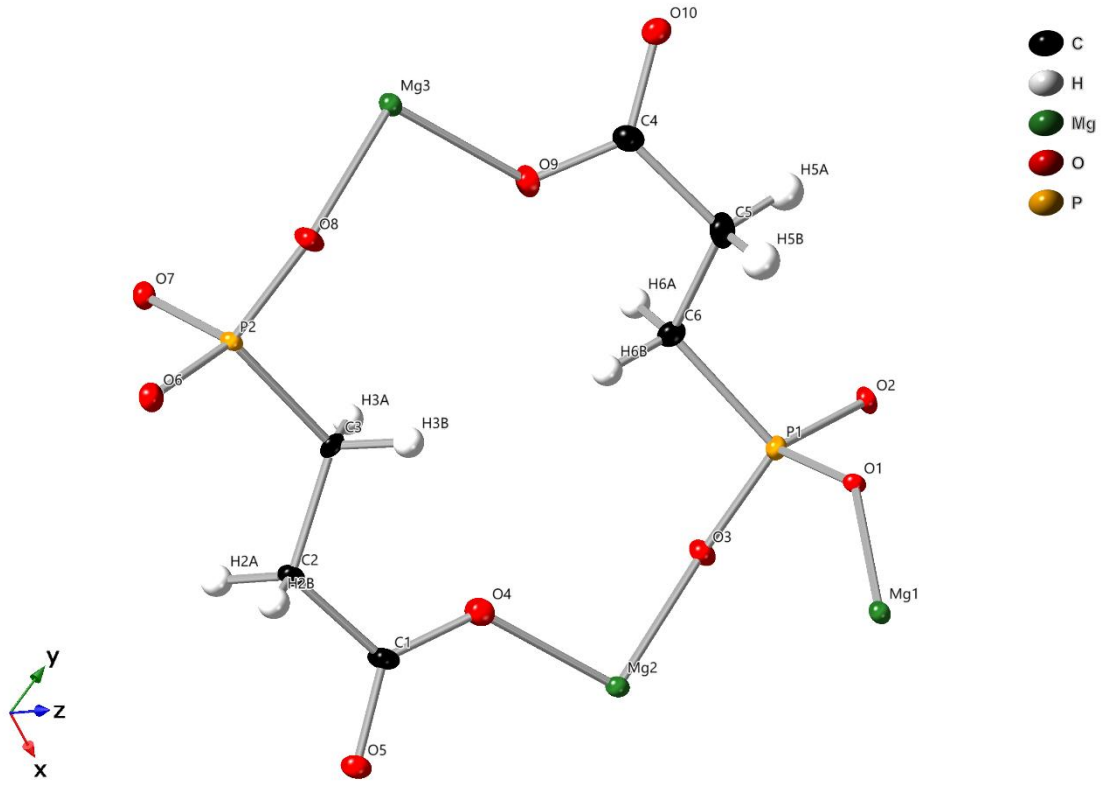

Figure 5.27) Actual asymmetric unit obtained from the higher quality crystals of BIRM-7. Atoms are drawn at 50% probability levels

Table 5.9) Actual basic crystallographic details of BIRM-7

Sample	BIRM-7
Formula	$Mg_3(O_3PCH_2CH_2CO_2)_2$
Formula Weight	374.99
Space group	$P2_1$
a (Å)	8.1016(3)
b (Å)	9.0014(3)
c (Å)	9.0443(4)
β (°)	107.744(4)
Volume (Å^3)	628.19(4)
Goodness-of-fit on F^2	1.079
wR_2	0.1243
Largest peak/hole (e Å^{-3})	1.73/-0.7

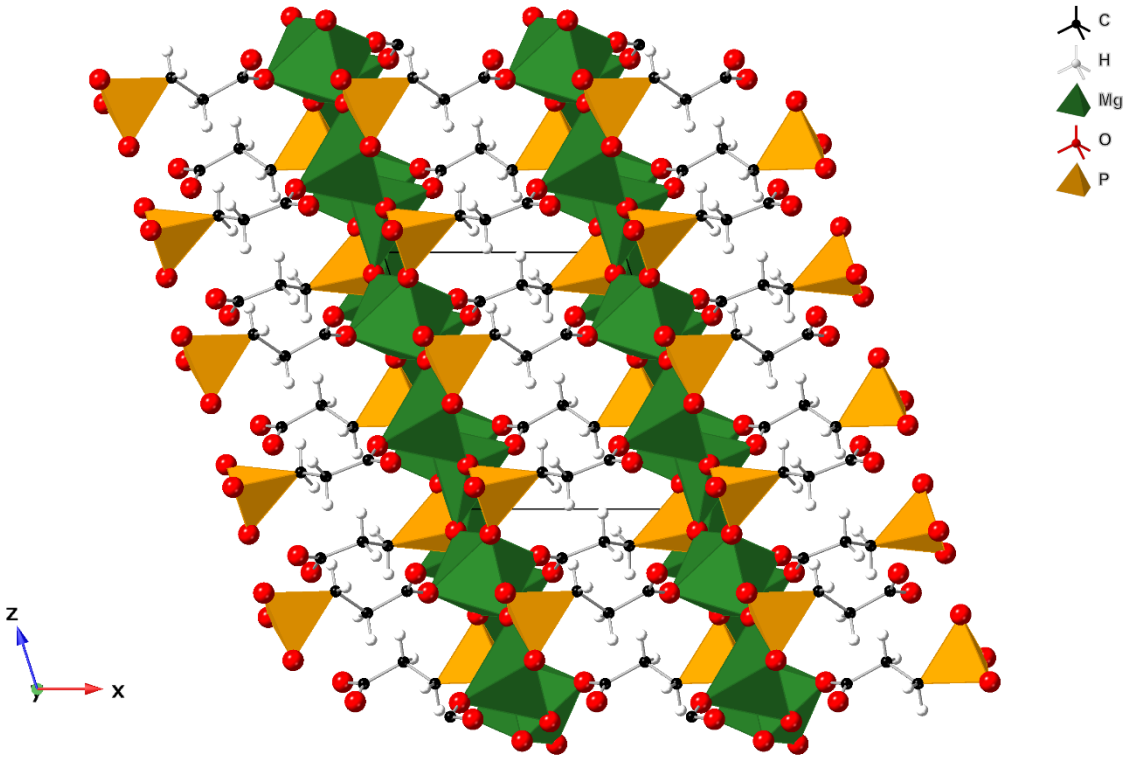

Figure 5.28) Actual structure of BIRM-7 looking along the y-axis

5.5.3.2 SEM-EDX

The plate shape morphology of BIRM-7 is apparent in the SEM images shown in Figure 5.29. Strangely, the crystals are all covered in many cracks and gaps. The reason for these is unclear, it could be that the material has a significant thermal expansion coefficient and so when the product is cooled after the hydrothermal synthesis these cracks develop. This could also explain why finding a suitable crystal for

single crystal diffraction was a challenge. The absence of brighter or darker patches of material (other than where there are obvious cracks or gaps) supports phase purity of the product.

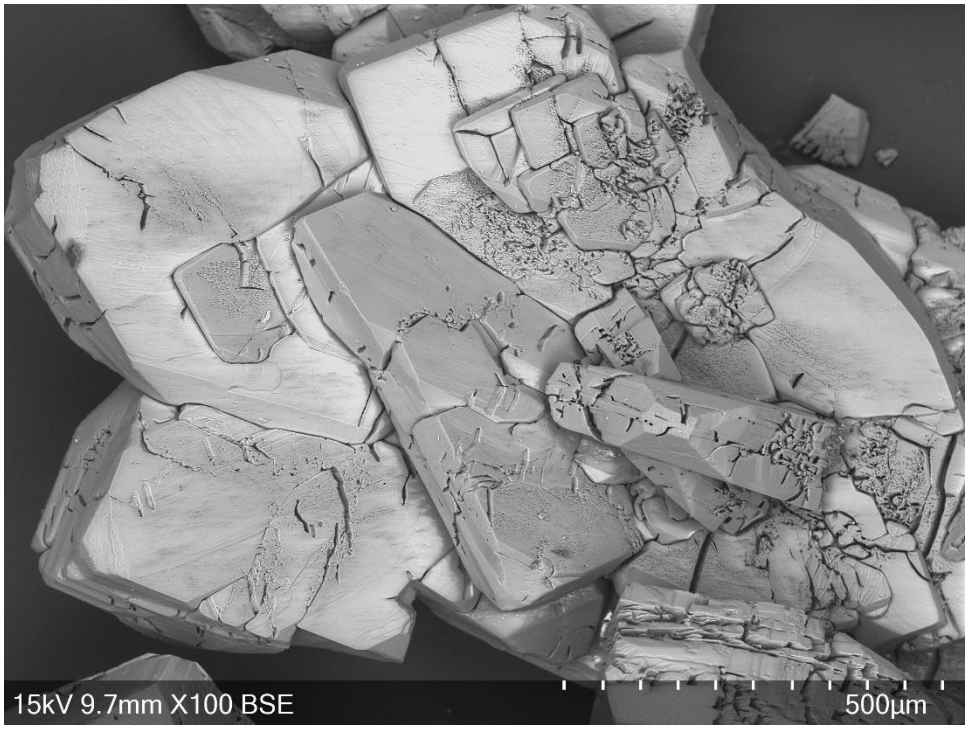

Figure 5.29) SEM image of crystals of BIRM-7 using a BSE detector to identify phase purity

The EDX analysis of the same sample found that the average magnesium: phosphorus ratio across 7 sites was 3:1.87 which is in reasonable agreement with the 3:2 predicted by the solved structure, especially when considering that EDX is usually used as an estimation rather than a full quantitative answer.

5.5.3.3 FTIR

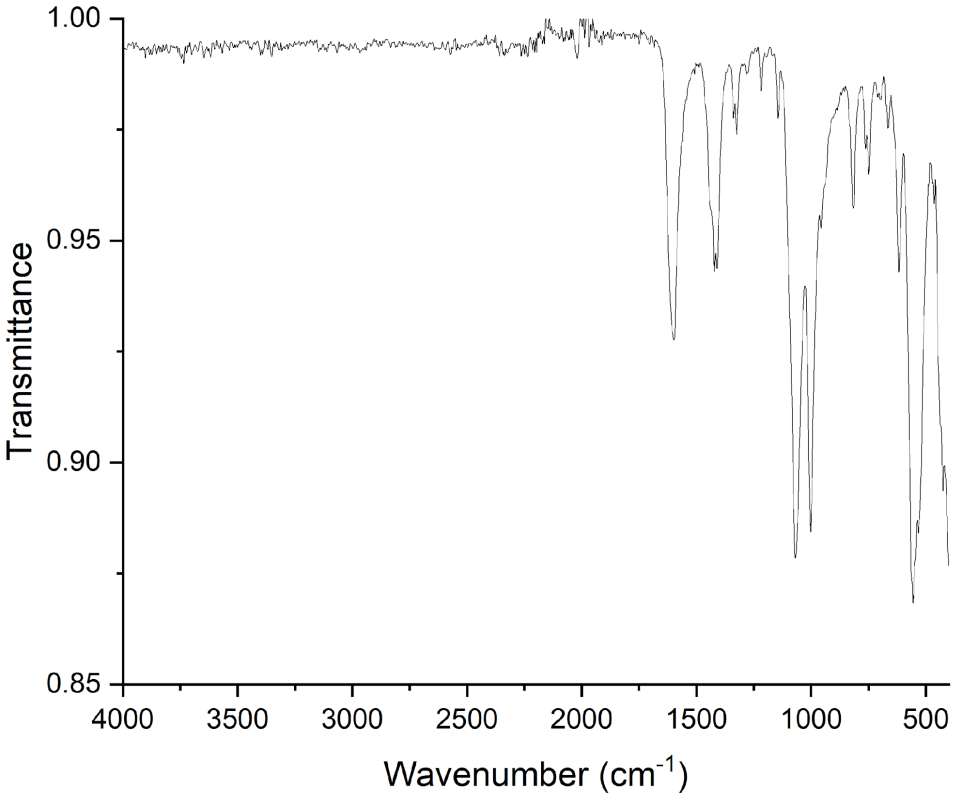

Figure 5.30) FTIR spectra of BIRM-7

Table 5.10) FTIR peak assignments for BIRM-7

Peak (cm^{-1}), profile, intensity	Assignment
1597, sharp, medium	Carboxylate C–O
1422, sharp, medium	Carboxylate C–O
1413, sharp, medium	Phosphonate P–C
1323, sharp, weak	Phosphonate P=O
1069, sharp, strong	Phosphonate P–O
1001, sharp, strong	Phosphonate P–O
957, shoulder, medium	Phosphonate P–O

The FTIR spectrum for BIRM-7 is given in Figure 5.30 with notable peak assignments in Table 5.10, assignments for the phosphonate bands were made with comparison to previously published magnesium phosphonate materials.[157] The most significant observation is the lack of a broad peak at high wavenumbers corresponding to O–H vibrations and giving evidence of water molecules being present. This suggests that the small pores mentioned previously in this materials structure are in fact too small

to contain even small molecules, otherwise one would expect them to be filled with water molecules from the synthesis and see evidence of this in the FTIR spectrum. The peaks that are present all support the solved structure with deprotonated carboxylate and phosphonate groups all evident in the FTIR data.

5.5.3.4 TGA-MS

The thermogravimetric analysis (Figure 5.32) data confirm the lack of solvent water within the material. No mass loss was observed in the TGA until almost 600 °C along with no MS signal corresponding to water in the emission from the material until this temperature. The fact that no mass loss was observed until 600 °C does, however, demonstrate the remarkable thermal stability that is possible with carboxyphosphonate materials and shows that BIRM-7 is a quite stable material itself. When BIRM-7 did decompose the mass loss occurred in a sharp step of about 20% followed by a slower but constant loss in mass which was still ongoing at 700 °C, the upper temperature limit of the measurement. The 20% mass loss was accompanied by an exothermic peak in the DTA as well as in the MS signals of *m/z* 18 and 44 indicating emission of water and carbon dioxide, respectively. The product left after the TGA is a black powder as shown in Figure 5.31.

Figure 5.31) Image of the post-TGA product of BIRM-7

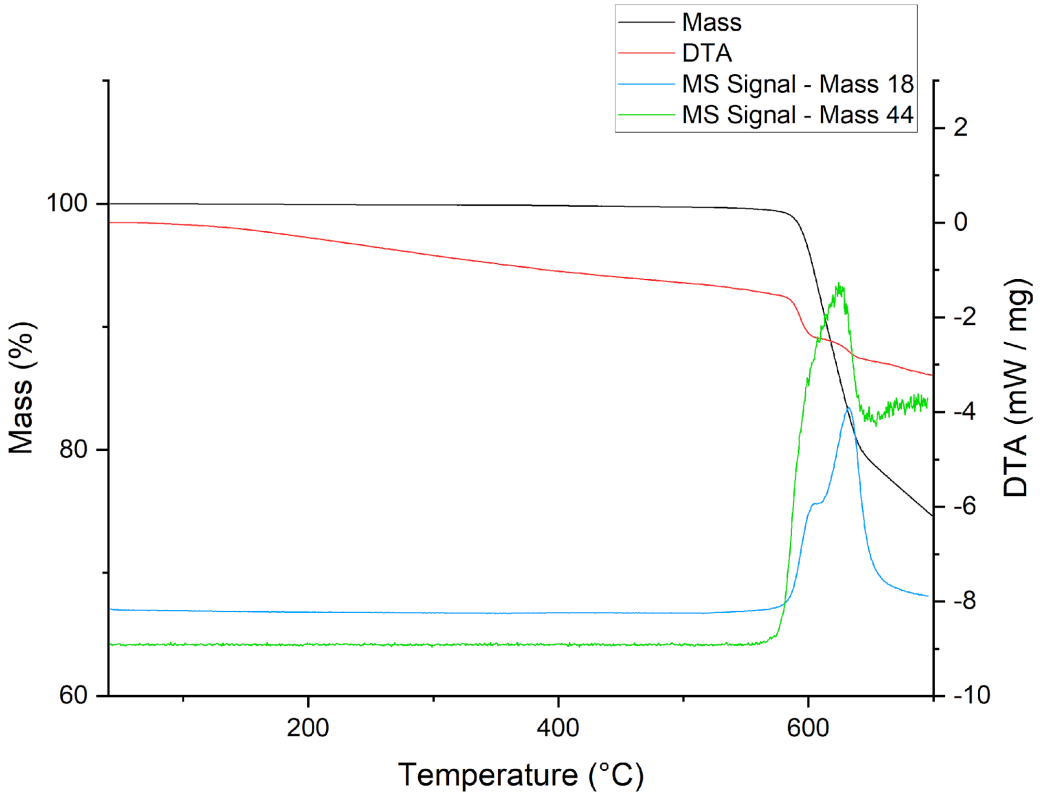

Figure 5.32) TGA-MS Analysis of BIRM-7

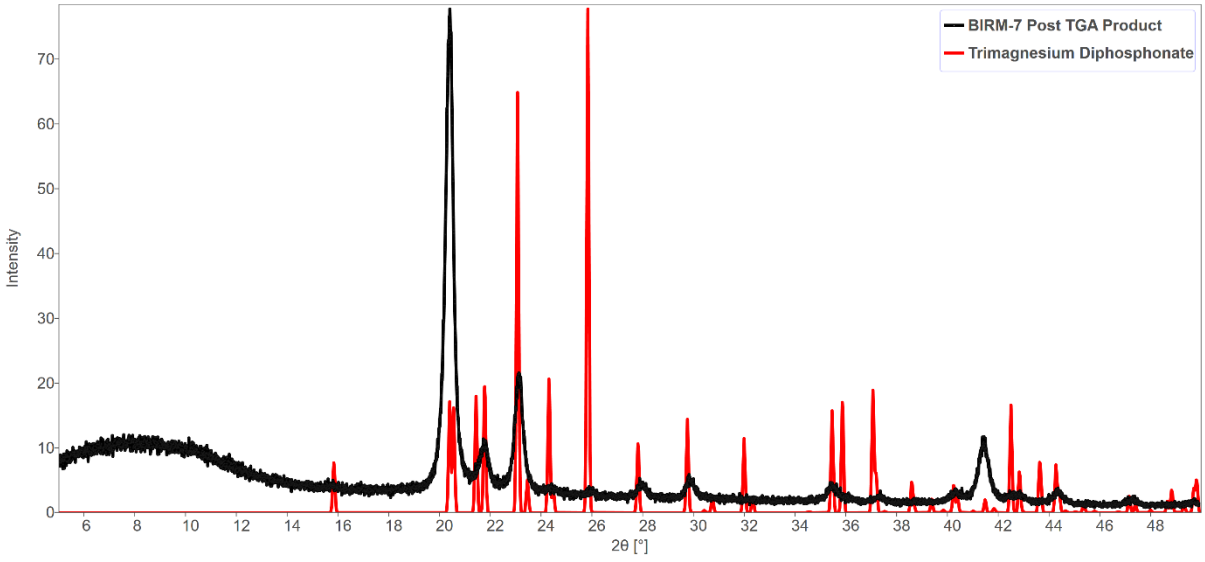

Figure 5.33) PXRD pattern of the TGA product from BIRM-7 (black) with a simulated pattern of trimagnesium diphosphate[158] (red)

Figure 5.33 shows a PXRD pattern of the TGA product of BIRM-7 which has been phase matched to a trimagnesium diphosphate phase.[158] Though the relative intensities are quite different the positions

match rather well. The different TGA product compared to BIRM-6 is likely the result of the different metal:linker ratio. This is yet further evidence supporting the structure solution from the single crystal data as this confirms the 3:2 magnesium:linker ratio of BIRM-7.

5.5.3.5 BET Surface Area Analysis

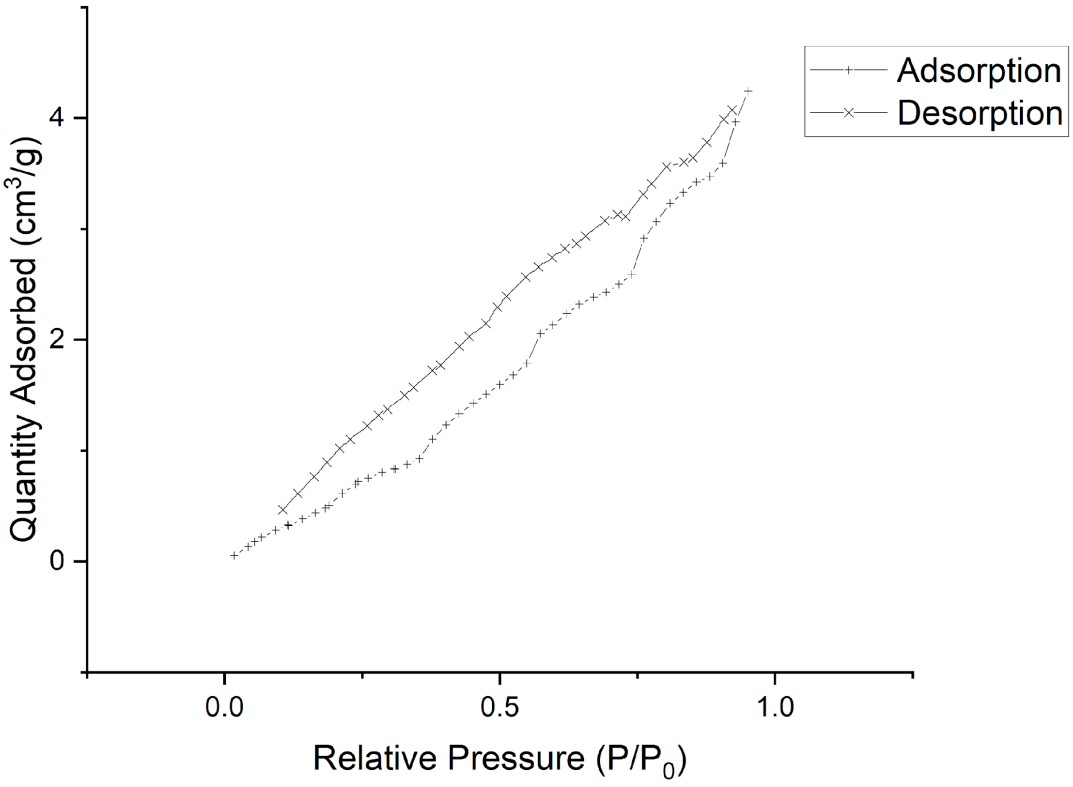

Figure 5.34) Isotherm of nitrogen adsorption on BIRM-7 at 77 K

The isotherm recorded of nitrogen adsorption on BIRM-7 at 77 K (Figure 5.34) correlates to a 'type VI' isotherm.[136] A type VI isotherm is indicative of adsorption on a uniform non-porous solid. The calculated BET surface area of the material also confirms non-porosity with a meagre 4.95 $m^2 g^{-1}$. The noisy shape of the isotherm is due to the very small quantities of gas adsorbed, leading to large errors. The confirmation of the lack of porosity means that BIRM-7 can most accurately be described as a 3-dimensional coordination network rather than a metal–organic framework.[153]

5.5.4 Porous Phase

Towards the end of this project a similar synthetic procedure to that of BIRM-7 was tried where urea was also added to the precursor solution after pH adjustment with ammonium hydroxide. This resulted

in a powder diffraction pattern (Figure 5.35) that did not match any of the phases previously made in this work. The sample was analysed for porosity and this led to the discovery that the material has a notable surface area of 476 m^2 g^{-1}. The recorded isotherm (Figure 5.36) takes the shape of a 'type I' reversible isotherm which is indicative of a porous material,[136] and the expected isotherm from a MOF with permanent porosity. Unfortunately, this discovery came towards the end of this project. Attempts were made to find a single crystal in this sample, but none were discovered. There were also attempts to index the powder pattern, but these were also unsuccessful. Therefore, this will be an area for future researchers to look at.

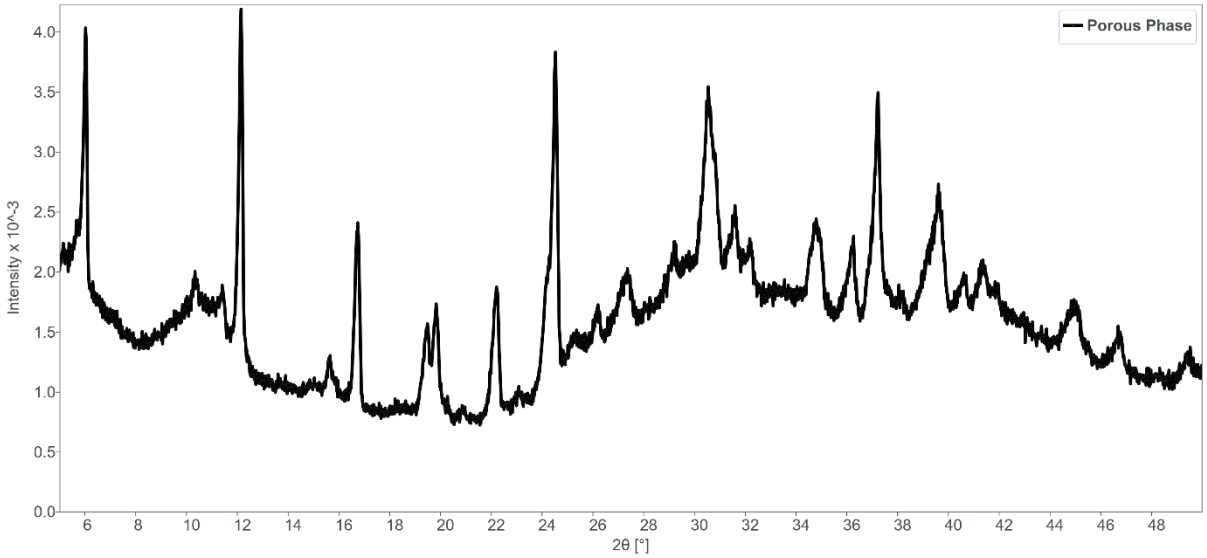

Figure 5.35) PXRD pattern of the porous phase

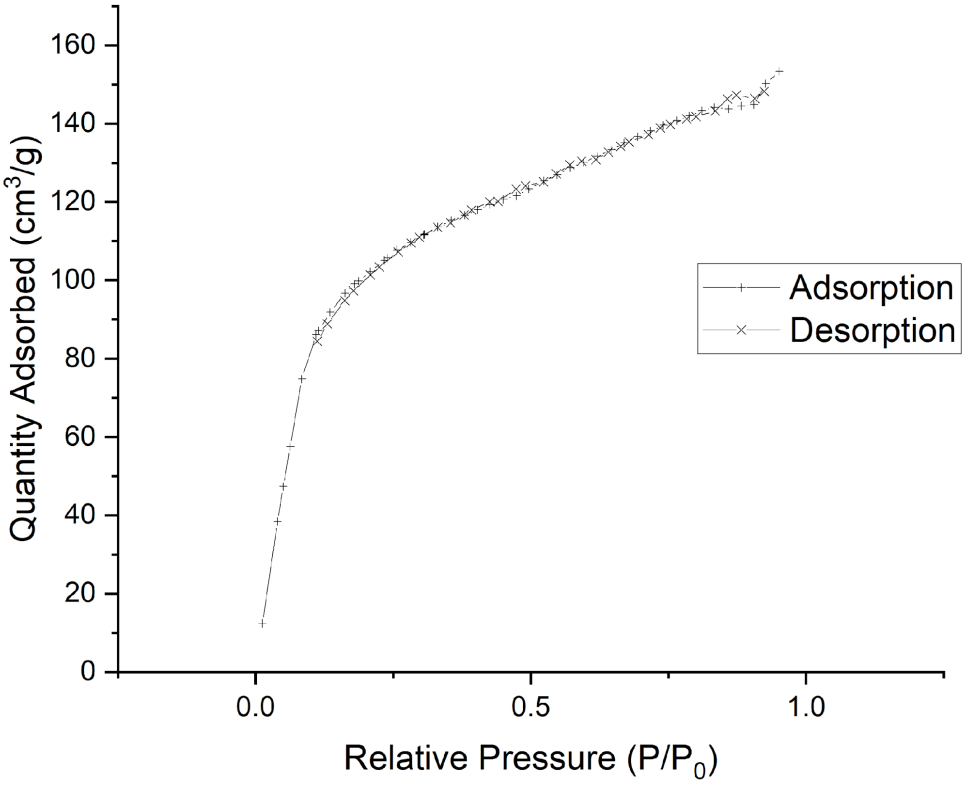

Figure 5.36) Nitrogen isotherm of the porous phase

5.6 Conclusion

Multiple magnesium-based phases have been successfully synthesised in this work. However, it has only been possible to solve the structure of two of them. The first phase synthesised in this chapter as well as the last, which is confirmed to have a notable surface area indicative of porosity, have not been successfully solved. The solving of the structures of these materials should form the basis of any future work continuing from the results presented here. The two structures that were solved, BIRM-6 and BIRM-7, and presented in this work can be described as a 1-dimensional coordination polymer and a 3-dimensional coordination network with a pillared-layered type structure respectively. As they do not appear to contain potential voids, it would not be accurate to describe them as metal–organic frameworks.[153] The differences in structure between BIRM-6 and BIRM-7 are likely determined by the degree of deprotonation of the linker, with BIRM-6 retaining a proton on the carboxylic acid whereas the linker in BIRM-7 is fully deprotonated. The fully deprotonated linker in BIRM-7 enables coordination at both ends of the linker molecule leading to a 3-dimensional framework material.

The porous phase may well be a new lightweight framework which is of particular interest for applications such as gas storage. If, like BIRM-1, the pores contain a significant concentration of proton carriers such as ammonium cations and water it may also be capable of proton conduction. Lightweight proton conductors are of great interest in powering vehicles, as greater mass limits the efficiency of these power sources. As discussed in the literature review chapter of this thesis, the potential applications of MOFs are extremely broad, and without knowing the structure of this porous phase it is difficult to speculate on what other applications it may be suitable for. BIRM-7 contains a 5-coordinate magnesium metal centre, other magnesium-based frameworks with coordinatively unsaturated metal centres have been proven capable in electrocatalytic applications.[159]

6 Synthesis of Novel Metal–Organic Frameworks Using a Rigid Aromatic Carboxyphosphonate Linker

6.1 Introduction

Following on from the work on BIRM-1 and the magnesium-based phases, the next logical item of study in the search for new, useful phases, and potentially synthesising a novel MOF, was by changing the linker used. As has been established, BIRM-1 does not show any notable permanent porosity and in fact undergoes reversible amorphization when dehydrated, due to the flexibility of the structure. In order to obtain a MOF with permanent porosity, the best chance would come from the use of more rigid constituent parts. In this case the aromatic linker 4-phosphonobenzoic acid was chosen, the chemical structure of which is shown in Figure 6.1. Other chemicals considered include those with alkene carbon chains, for example 3-phosphonoacrylic acid, but these are not readily commercially available. As there was limited success with the formation of magnesium-based materials in this work, zinc was chosen as the metal once again.

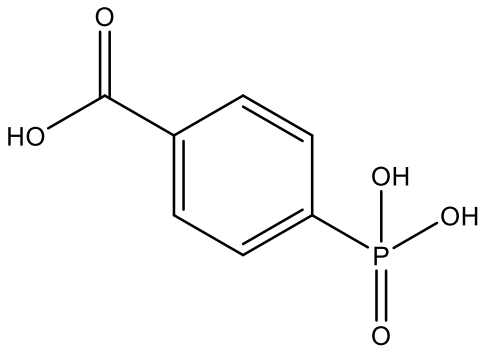

Figure 6.1) Chemical structure of 4-phosphonobenzoic acid, the linker used in this work

6.2 Experimental

6.2.1 Hydrothermal Synthesis

As with the magnesium based framework in the previous chapter, the synthesis ‘method III’ developed by Zhao for BIRM-1 was used as a starting point for the synthesis in this work, however, quantities were

scaled down significantly as well as a slightly lower synthesis temperature used.[115] The decision for a slightly lower synthesis temperature was based on the lower pK_a values of the acidic protons on 4-phosphonopropionic acid compared to 3-phosphonopropionic acid (Table 6.1) and an understanding of the relationship between synthesis temperature, urea decomposition and subsequent pH of the synthesis solution.

Table 6.1) pK_a values of the acidic protons on 3-phosphonopropionic acid and 4-phosphonobenzoic acid [139,160]

Linker	Temperature	pK_1	pK_2	pK_3
3-phosphono-propionic acid[139]	25 °C	2.26	4.63	7.75
4-phosphonobenzoic acid[160]	24.3 °C	1.32	3.84	6.77

The 4-phosphonobenzoic acid was purchased from abcr UK. All other reagents were sourced from Sigma-Aldrich. For the initial synthesis the quantities of reagents in Table 6.2 were dissolved in 11 ml of deionised water. The solution was stirred until all the reagents were dissolved; 4-phosphonobenzoic acid has limited solubility in water so some gentle heating was applied to encourage dissolution. The solution was then transferred into a 23 ml teflon lined stainless steel autoclave and placed in an oven at 83 °C for 24 hours. The product was recovered by vacuum filtration and washed with deionised water. Further experiments varied both quantities of reagents, volume of water, presence of TEAB and synthesis temperature.

Table 6.2) Quantities of reagents used in the initial synthesis attempt of a framework material using 4-phosphonobenzoic acid

	Zinc Nitrate Hexahydrate	4-phosphono-benzoic acid	Tetraethylammonium Bromide (TEAB)	Urea
Mass (g)	0.0841	0.1	0.0772	0.1528
Molar Ratio	1	1.75	1.3	9

6.3 Initial Attempt

The initial synthesis attempt yielded a product composed of white needle-shaped crystals approximately 2-3 mm long. The pH of the supernatant liquid was found to be ca. 6. The powder diffraction pattern

from the product can be seen in Figure 6.2. The sample was submitted to the School of Chemistry's single crystal diffraction service run by Dr Louise Male.

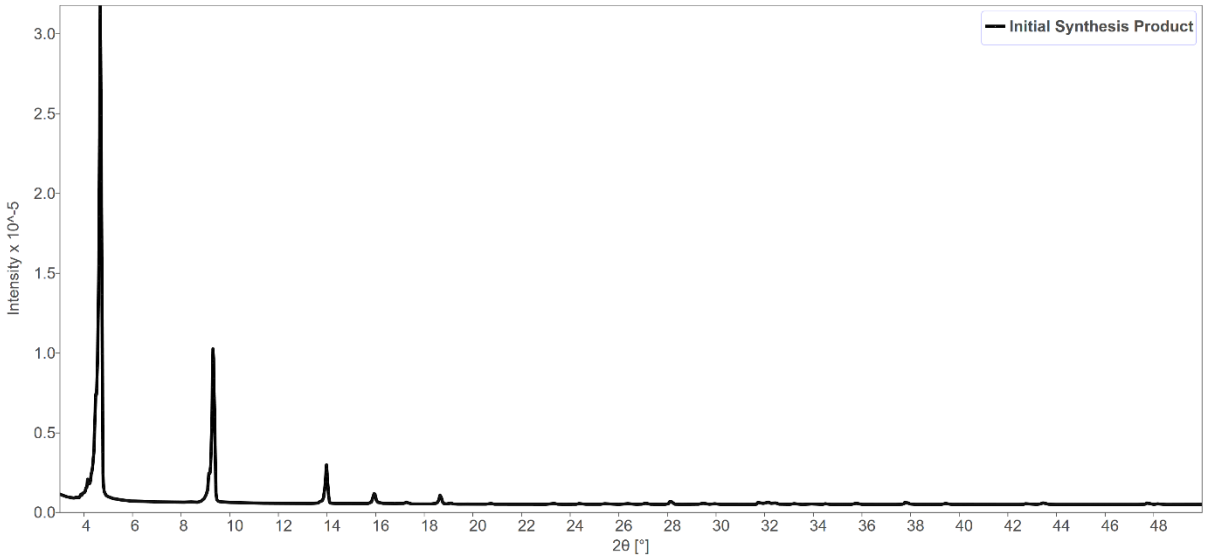

Figure 6.2) PXRD pattern obtained from the product of the initial synthesis attempt

6.4 Layered Structure

A suitable single crystal was found and diffracted well. A structure was solved from the data which is shown in Figure 6.3 with some of the basic crystallographic details in Table 6.3. More extensive crystallographic information is given in the appendix. The expanded structure is shown in Figure 6.4. This material will now be named as BIRM-8 going forward, it has the formula $Zn(O_3PC_6H_4COOH)\cdot H_2O$. Of note is that the carboxylic acid group remains protonated. There is a significant amount of disorder in the structure with the aromatic ring and the carboxylate group disordered over three positions. The disordered positions have 50% occupancy in C2, C3, C4 and O4, and 25 % occupancy in the equivalent 'a' and 'b' positions.

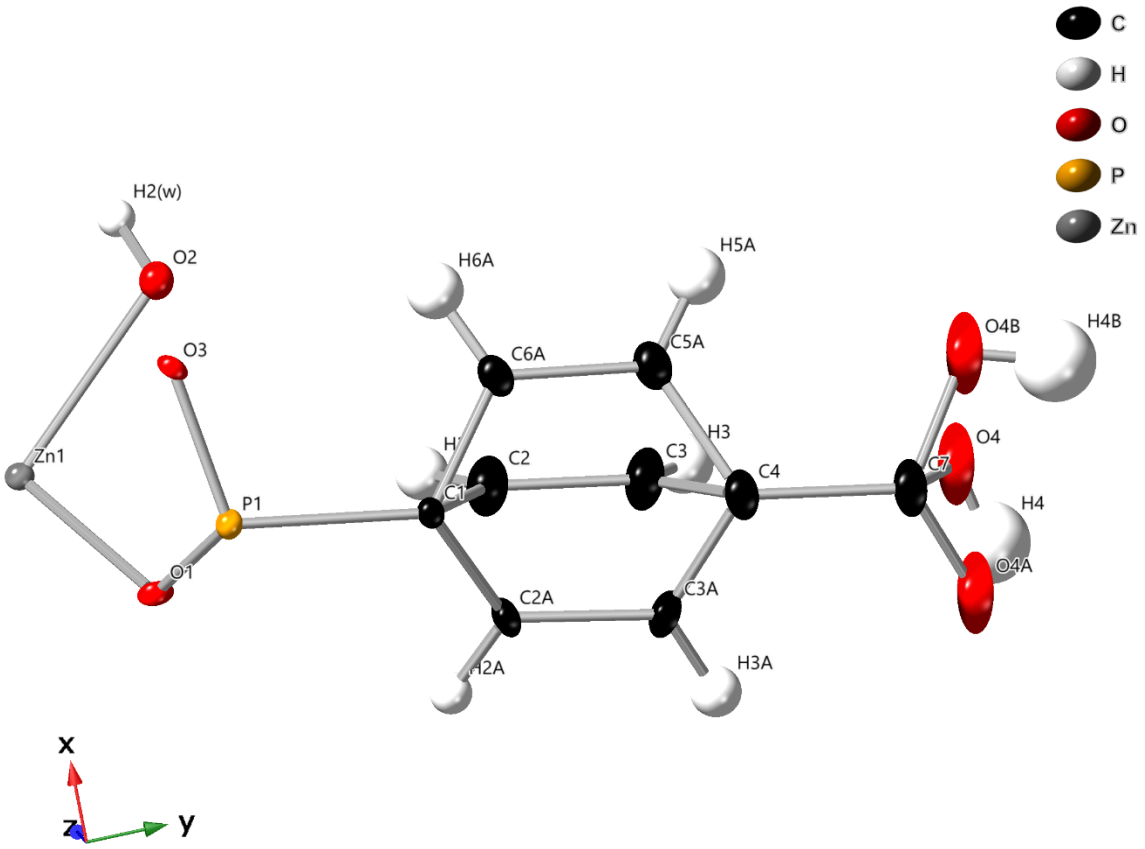

Figure 6.3) Asymmetric unit of BIRM-8, ellipsoids are drawn at 50% probability level. The aromatic ring and carboxylate units are disordered over three positions and across a mirror plane that runs through C1, C4 and C7, O3, P1 and Zn1. The water oxygen, O2, is also located on the mirror plane

Table 6.3) Basic crystallographic details of the product of the initial synthesis

Sample	BIRM-8
Formula	$Zn(O_3PC_6H_4COOH)\cdot H_2O$
Formula Weight	283.47
Space group	*Pnnm*
a (Å)	4.7698(3)
b (Å)	38.0812(15)
c (Å)	5.6235(4)
Volume ($Å^3$)	1021.45(11)
Goodness-of-fit on F^2	1.231
wR_2	0.117
Largest peak/hole (e $Å^{-3}$)	0.91/-1.46

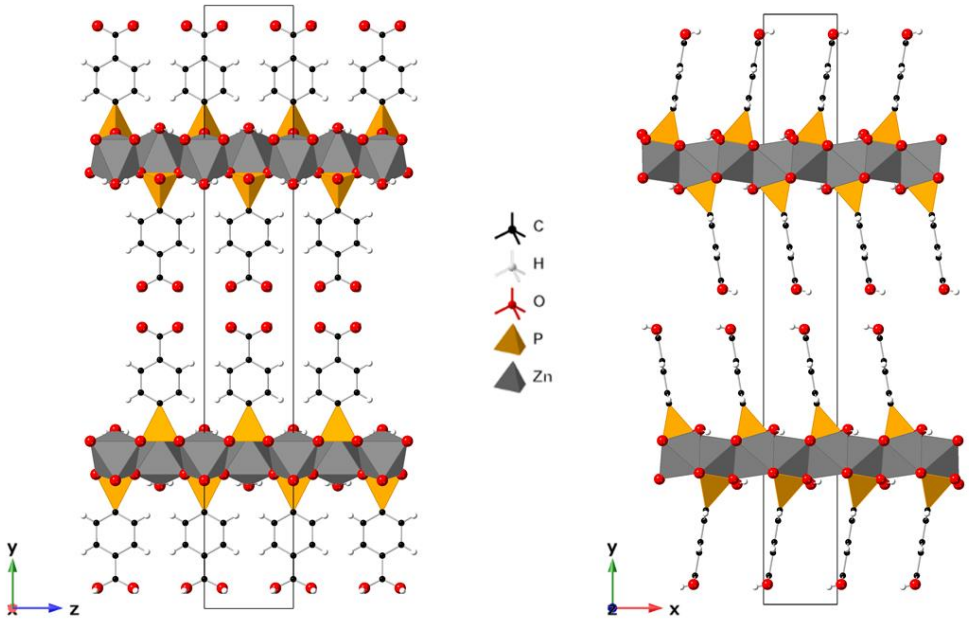

Figure 6.4) Structure of BIRM-8 viewed along the x-axis (left) and the z-axis (right). Unit cells are indicated by the black outlines. Disorder has been removed for clarity

The structure of BIRM-8 is that of a layered coordinated framework. It is composed of sheets of ZnO_6 octahedra and CPO_3 tetrahedra which are edge-sharing and extend out along two dimensions. The linker then extends outwards from this sheet along the *y*-axis and the layers are linked together by hydrogen bonding from the carboxylic acid group. The structure is in fact very similar to the layered phase, BIRM-2, which was found by Zhao[115] and also features in the first results chapter of this thesis. This was notable as it has been established that through control of synthetic variables such as temperature and pH of the synthesis solution for the BIRM-1 system the layered phase can be obtained, or the BIRM-1 MOF can be generated. Therefore, a sensible next step would be to increase the synthesis temperature in an attempt to obtain a MOF.

6.4.1 FTIR

The FTIR spectrum of BIRM-8 is given in Figure 6.5 along with peak assignments in Table 6.4. The FTIR data confirm the structure solved from single crystal diffraction with evidence of the carboxylic acid being left protonated whilst the phosphonate group has been deprotonated.

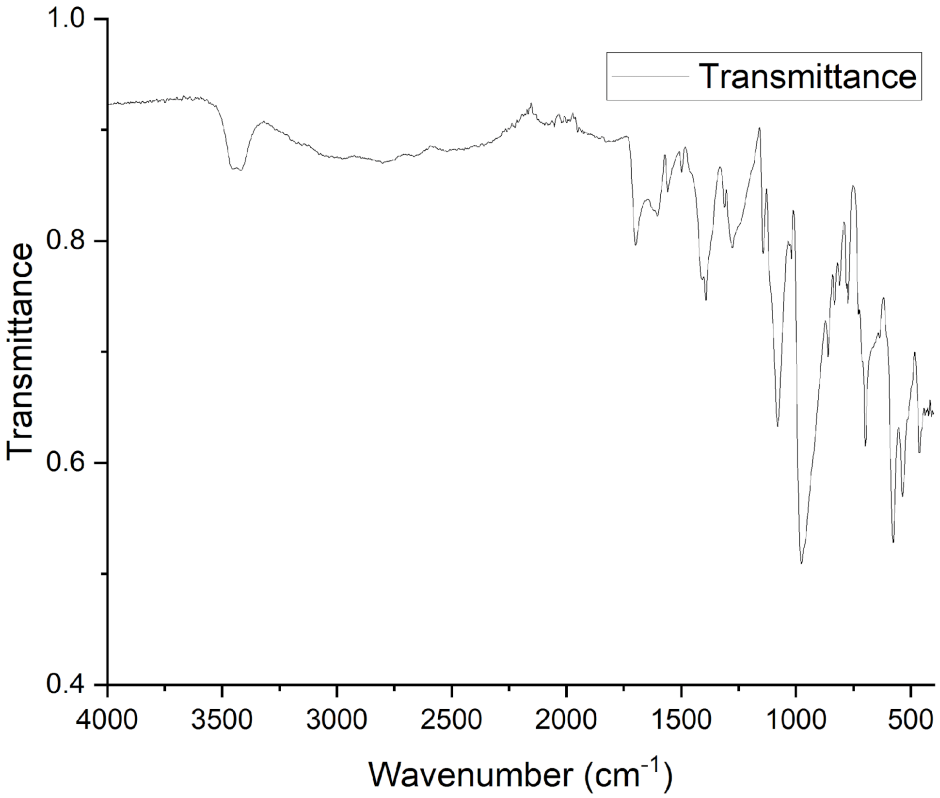

Figure 6.5) FTIR spectra of BIRM-8

Table 6.4) List of notable FTIR peaks and their assignments to functional groups in BIRM-8

Peak (cm^{-1}), profile, intensity	Assignment
3450, medium	Carboxylic acid O–H
3421, medium	Aromatic ring C–H
2800, broad, weak	Water O–H
1698, sharp, medium	Carboxylic acid C=O
1277, medium	Carboxylic acid C–O
1144, medium	Phosphonate P–O
1081, sharp, strong	Phosphonate P–O
976, strong	Carboxylic acid O–H

6.4.2 SEM-EDX

Figure 6.6 is an SEM image of BIRM-8 at 100× magnification. Although initially described as needle-shaped crystals, under the magnification of the SEM it was clear they are actually plate-shaped crystals with one sheet dimension much longer than the other. The absence of brighter or darker areas of material

indicates the sample is homogenous in terms of elemental distribution. EDX analysis found an average Zn:P ratio of 1:0.87, which is a lower level of phosphorus than would be expected from the solved structure (1:1). The powder diffraction data had a low background and all peaks were accounted for by BIRM-8 so there was no evidence of impurities which could account for this discrepancy.

Figure 6.6) SEM image of BIRM-8 at 100× magnification

6.4.3 TGA-MS

TGA-MS was used to characterise the decomposition profile of BIRM-8; this is shown in Figure 6.7. The decomposition occurred in 4 mass loss steps, with the last step being somewhat eclipsed by the penultimate step. The first mass loss occurs around 100 °C. It is a loss of 6.3% accompanied by an endothermic DTA peak and an MS signal for mass 18 corresponding to water. The mass loss of 6.3% is what would be expected with the loss of the coordinated water from the structure. The next step in the decomposition is a small mass loss of 2.7% at around 200 °C, again accompanied by a small MS signal for mass 18 and a slight upwards 'bump' in the DTA trace indicating a small endotherm. It is not clear from the structure what the exact cause of this step is but it is a very minor feature of the overall

decomposition profile. The next decomposition step is the largest mass loss overall with 30%, closely followed by a second step of 8.5%. Both of these steps are accompanied by exothermic peaks in the DTA trace and MS signals for both masses 18 and 44, indicating emission of water and carbon dioxide. This is likely due to the combustion of organic material within the structure. The overall mass loss amounts to 47.5%. The final decomposition product is a crystalline material (as shown by the PXRD pattern in Figure 6.8) however, attempts to phase match it to known phases have been unsuccessful. The end product of the TGA is a grey powder, shown in Figure 6.9.

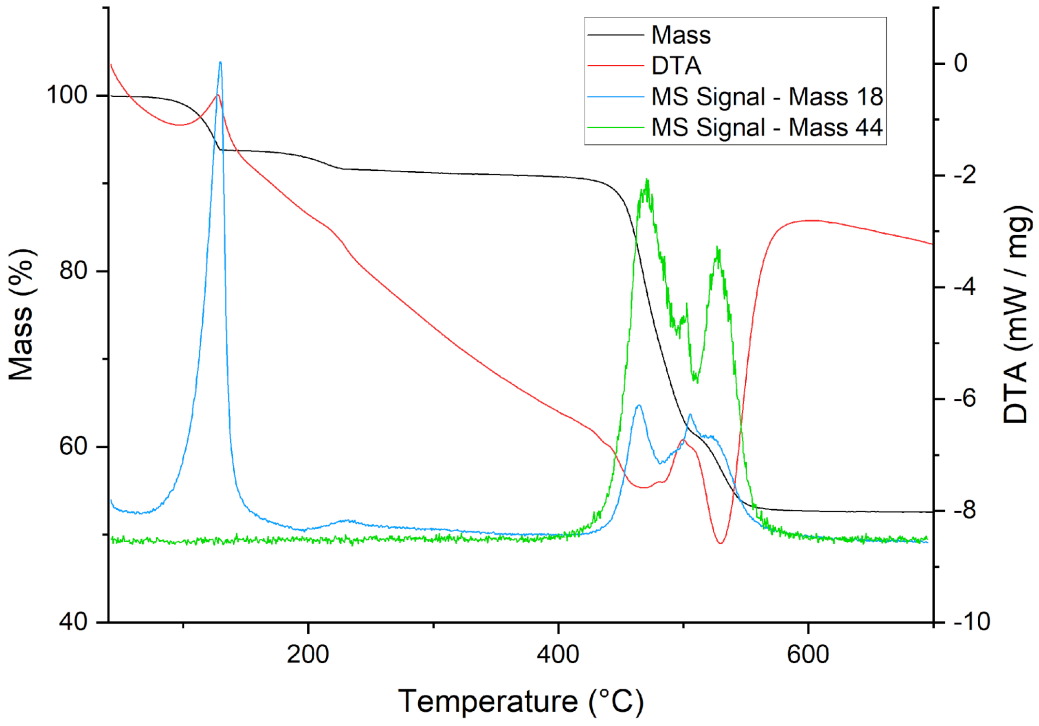

Figure 6.7) TGA-MS analysis of BIRM-8

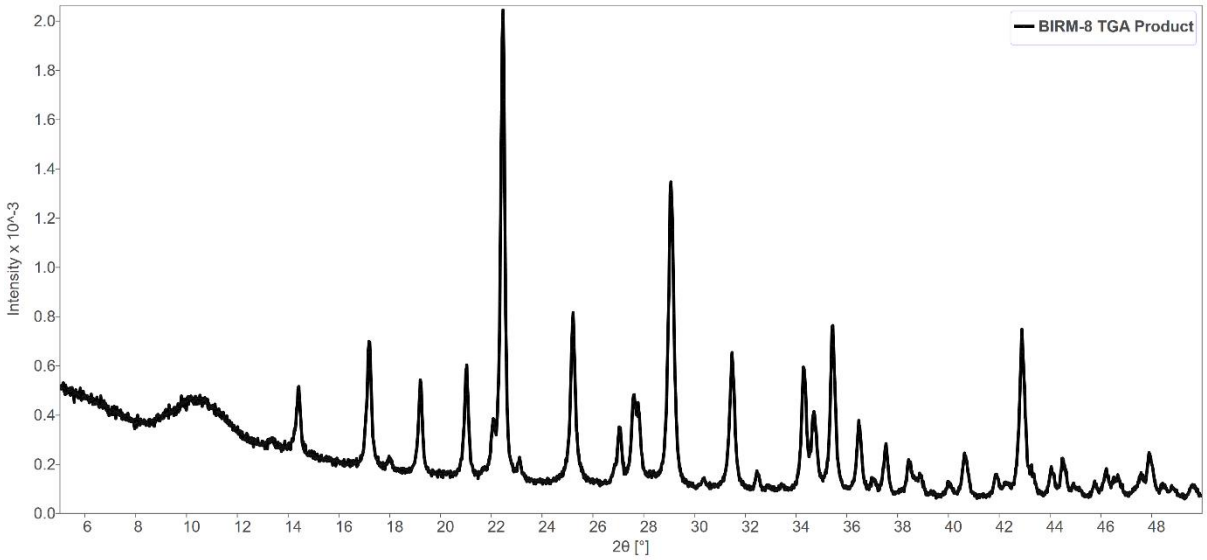

Figure 6.8) PXRD pattern of the TGA product from BIRM-8

Figure 6.9) Image of the TGA product of BIRM-8

6.5 Adjusting the Synthesis Temperature

The synthesis was attempted at a range of temperatures with 2 °C intervals between 83 and 89 °C and then once it was established that no new phases were being produced in that range the temperature was increased significantly more to 110°C with additional attempts at 115 and 120 °C. The PXRD patterns from the products of these syntheses are shown in Figure 6.10. It is clear that each synthesis in the 83-89 °C range produced the previously identified layered material, BIRM-8. Although the synthesis conducted at 87 °C showed a diffraction pattern with additional peaks and different relative intensities compared to other BIRM-8 products, this is likely a preferred orientation effect as those peaks are also in the simulated pattern for BIRM-8. At higher temperatures between 110 and 120 °C at least two

different phases were obtained. The syntheses at 110 and 115 °C appeared to produce a mix of phases based of the presence of two sets of peaks which slightly varied in relative intensity between the two patterns. In contrast, the PXRD pattern of the product made at 120 °C only contained one of these sets of peaks indicating the material was composed of a single crystalline phase.

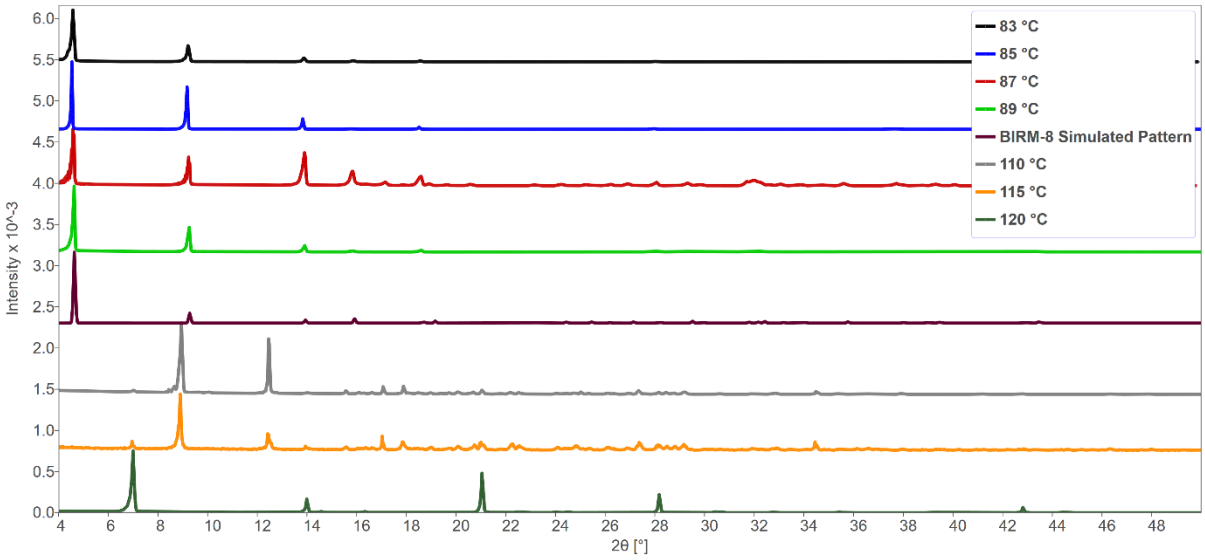

Figure 6.10) PXRD patterns from products of a range of syntheses across a temperature scale with a simulated pattern of BIRM-8 for comparison.

As the product of the 120 °C synthesis appeared to be a single phase, this sample was chosen first for further examination.

6.6 Second Layered Phase

The product of the 120 °C sample was composed of plate-shaped crystals, appearing white in bulk. A sample was sent to the National Crystallography Service at the University of Southampton after unsuccessful attempts to collect data of sufficient quality for structure solution at Birmingham. A dataset was returned for analysis with the assistance of Dr Louise Male. A twinned dataset was obtained with a very high R_{int} of 42.46%, but despite this a reasonable structure (Figure 6.11 & Figure 6.12) with good measures of fit (Table 6.5) was found. This phase will now be referred to as BIRM-9, with formula $Zn_4(O_3PC_7H_4COO)_2(OH)_2 \cdot 2H_2O$. More detailed crystallographic information can be found in the appendix.

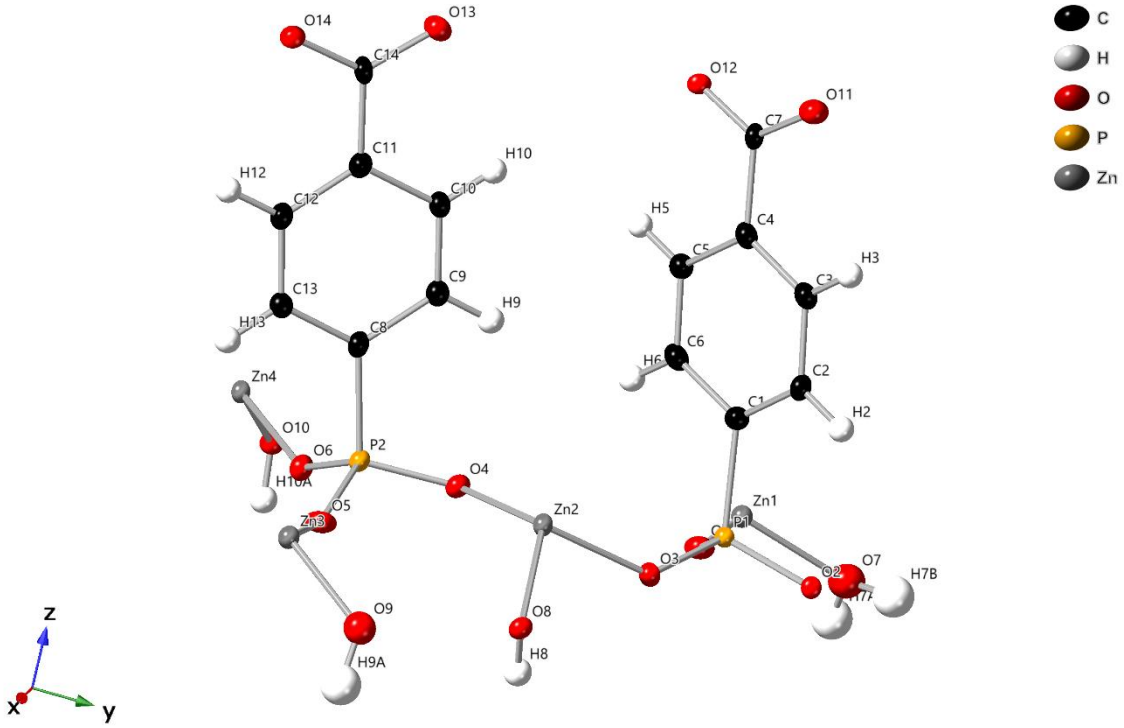

Figure 6.11) Asymmetric unit of BIRM-9, ellipsoids are drawn at the 50% probability level

Table 6.5) Basic crystallographic details of BIRM-9

Sample	BIRM-9
Formula	$Zn_4(O_3PC_7H_4COO)_2(OH)_2 \cdot 2H_2O$
Formula Weight	728.66
Space group	*P*21/*c*
a (Å)	7.6382(2)
b (Å)	10.8640(2)
c (Å)	25.2711(6)
β (°)	90.379(2)
Volume (Å^3)	2096.99(8)
Goodness-of-fit on F^2	1.127
wR_2	0.1319
Largest peak/hole (e Å^{-3})	1.04/-0.85

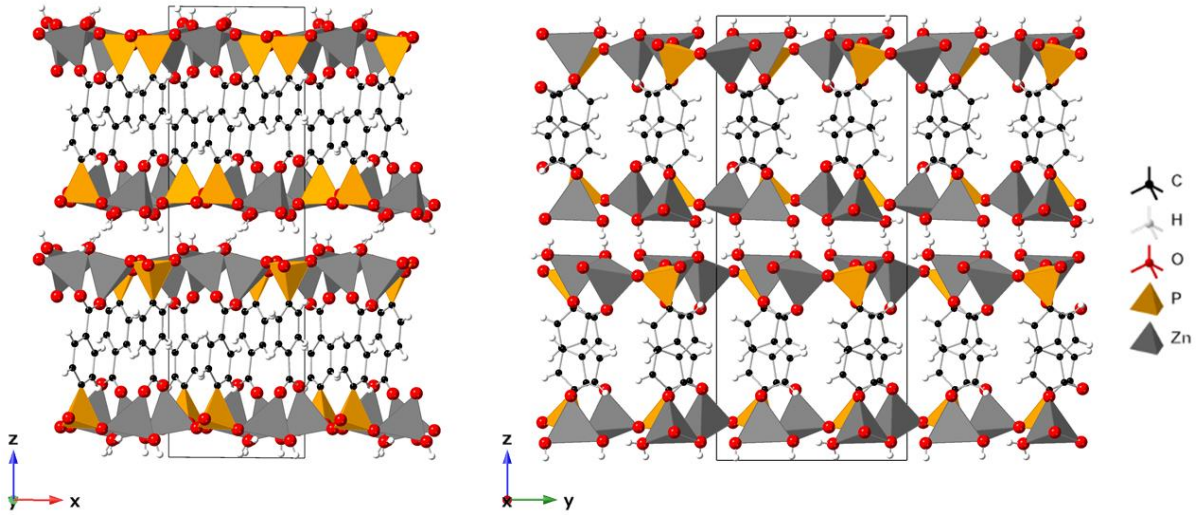

Figure 6.12) Structure of BIRM-9 viewed along the y-axis (left) and the x-axis (right). Unit cell is indicated by the black outlines

The structure of BIRM-9 is a coordination network consisting of two layers of corner sharing ZnO_4 and CPO_3 tetrahedra joined together via deprotonated 4-phosphonobenzoic acid linkers. These structural units then form layers which are joined together *via* hydrogen bonding. Each phosphorus-centred CPO_3 tetrahedron is corner-sharing with 3 zinc-centred ZnO_4 tetrahedra with the fourth corner being a carbon from the benzene ring of the linker. The ZnO_4 tetrahedra which contain Zn1 and those which contain Zn3 are each corner-sharing with a CPO_3 tetrahedron and a ZnO_4 tetrahedron. Of the other two oxygens one is from the carboxylate group of the linker and the other is a coordinated water molecule. The Zn2 and Zn4 tetrahedra are corner-sharing with 2 CPO_3 and a ZnO_4 tetrahedron with the final oxygen coming from the carboxylate group of the linker. Where two ZnO_4 tetrahedra are corner-sharing this is *via* a bridging hydroxyl group. The structure of the inorganic layers in shown in Figure 6.13, showing there are not any gaps within the layers which are large enough to be considered pores or channels.

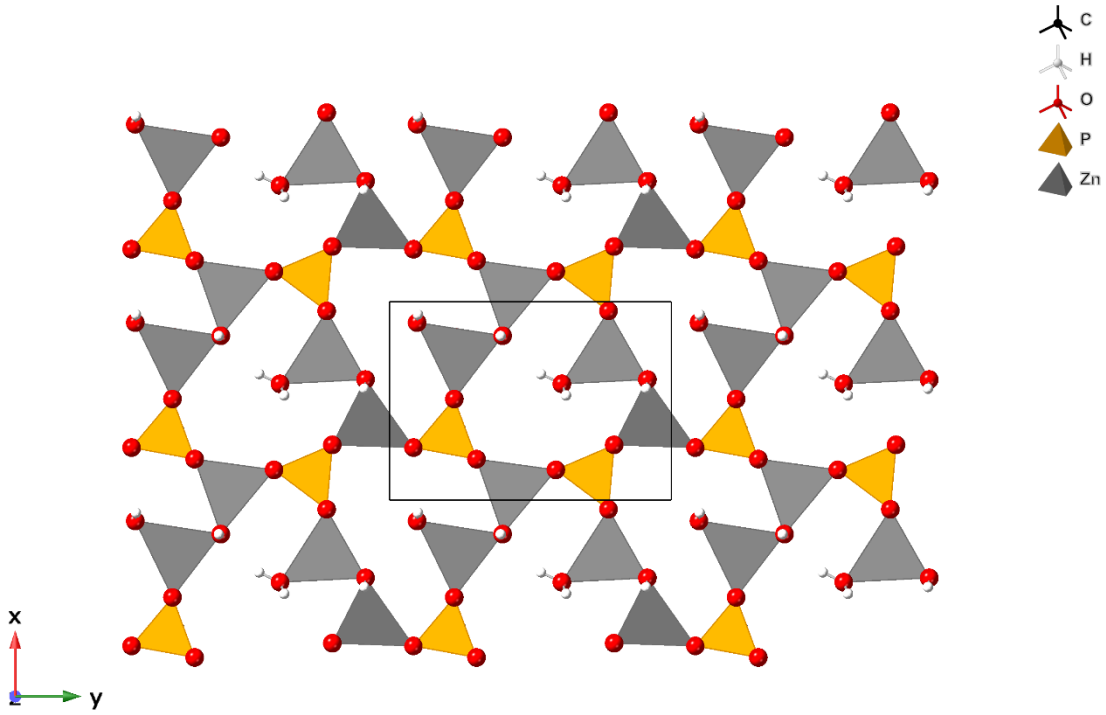

Figure 6.13) The structure of the inorganic layers of BIRM-9. Unit cell indicated by the black outline.

6.6.1 FTIR

The FTIR spectrum for this new material, BIRM-9, is shown in Figure 6.14 with notable peak assignments in Table 6.6. All the expected peaks from the functional groups contained within the material are present. The broad peak from coordinated water is somewhat obscured by peaks from the bridging hydroxyl and aromatic C-H groups.

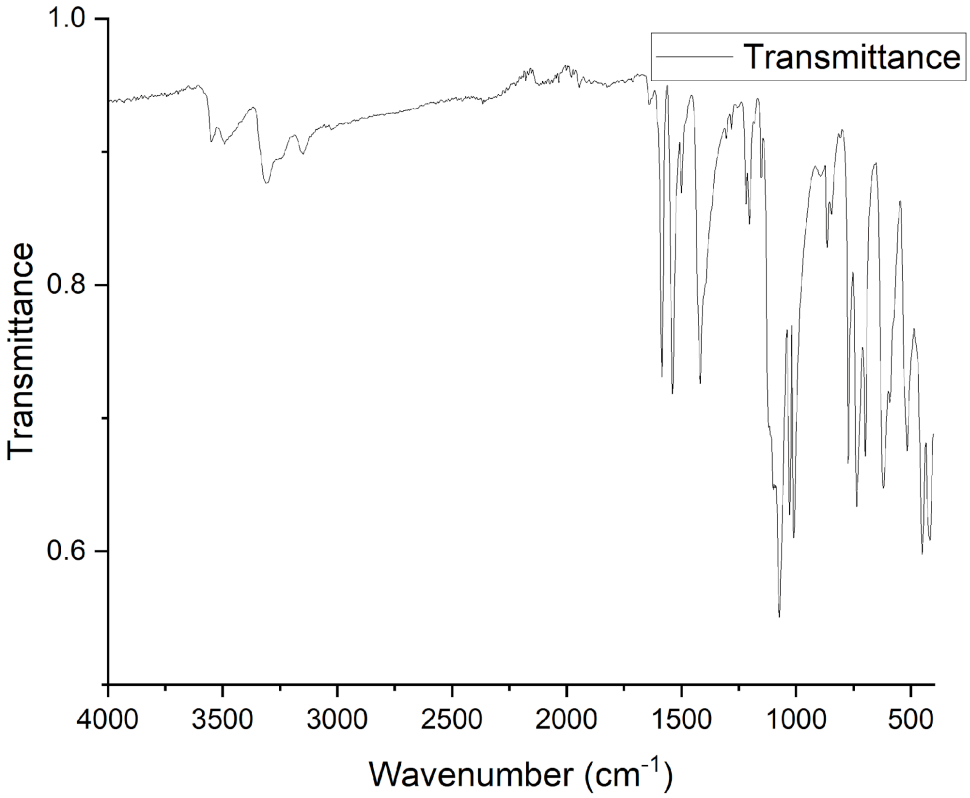

Figure 6.14) FTIR Spectra of BIRM-9

Table 6.6) List of FTIR peaks for BIRM-9 and their assignments

Peak (cm^{-1}), profile, intensity	Assignment
3554, sharp, weak	Hydroxyl O–H
3252, broad, weak	Water O–H
3154, broad, weak	Aromatic ring C–H
1585, sharp, strong	Carboxylate C–O
1538, sharp, strong	Aromatic ring C–C
1418, sharp, strong	Carboxylate C–O
1120, shoulder, medium	Phosphonate P–O
1099, shoulder, strong	Phosphonate P–O
1073, sharp, strong	Phosphonate P–O

6.6.2 SEM-EDX

The SEM image of BIRM-9 (Figure 6.15) confirms the plate-shape morphology of the material. It is also clear that there are few distinct single crystals of appropriate size and most crystallites appear to have twins attached, indicating why sufficiently high quality single crystal diffraction data were difficult to obtain. The plates also appear to be extremely thin. Some edges of the material appear to be slightly

lighter than the bulk and this may indicate the presence of material which is, on average, composed of lighter elements such as the organic linker. Alternatively, it may be that the edges of the crystals are particularly thin. Likewise, there are a couple areas in the SEM image which are a darker shade, likely indicating a higher proportion of heavier elements such as zinc.

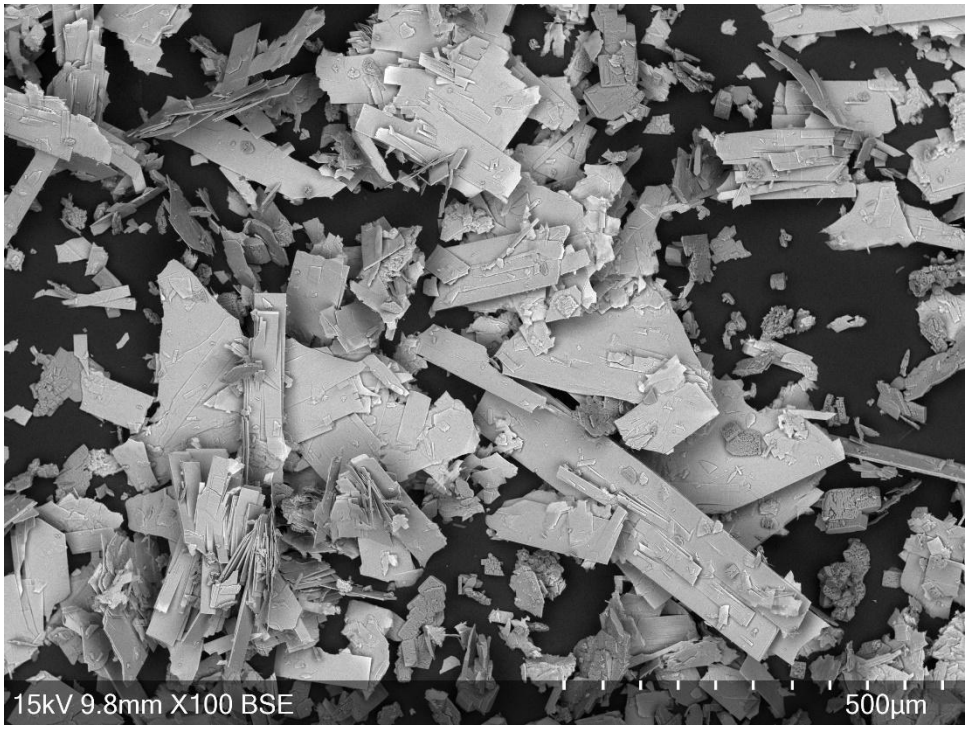

Figure 6.15) SEM image of BIRM-9 at 100× magnification

EDX analysis indicates an average Zn:P ratio of 2.27:1 across 6 different sites which is slightly higher than expected from the solved structure, this could be due to the darker areas mentioned previously.

6.6.3 TGA-MS

TGA-MS (Figure 6.16) was used to characterise the decomposition profile of the BIRM-9 material. The analysis shows the material is quite stable up to 400 °C with a mass loss of only 3% in this range and no clear evolution of water or carbon dioxide from the sample at these temperatures. At 400 °C there is a small mass loss of about 5.8% accompanied by an endothermic peak in the DTA and an emission of water as shown by the MS signal. The 5.8% loss is roughly equivalent to the expected loss from the coordinated water, though 400 °C is a very high temperature for this to occur at. More likely is that this is the loss of the bridging hydroxyl groups which are only slightly less massive. The coordinated water

is likely accounted for in the 4% mass loss prior to 400 °C but may have occurred gradually, hence the lack of a peak in the MS signal. It could be that some water does remain trapped within the structure hence why the mass loss at 400 °C is larger. At 500 °C the next decomposition step starts. This is a mass loss of 28.6% with an exothermic peak in the DTA and a peak in the MS signal for masses 18 and 44 corresponding to water and carbon dioxide, respectively. The mass loss then plateaus for the rest of the recorded decomposition which ends at 700 °C.

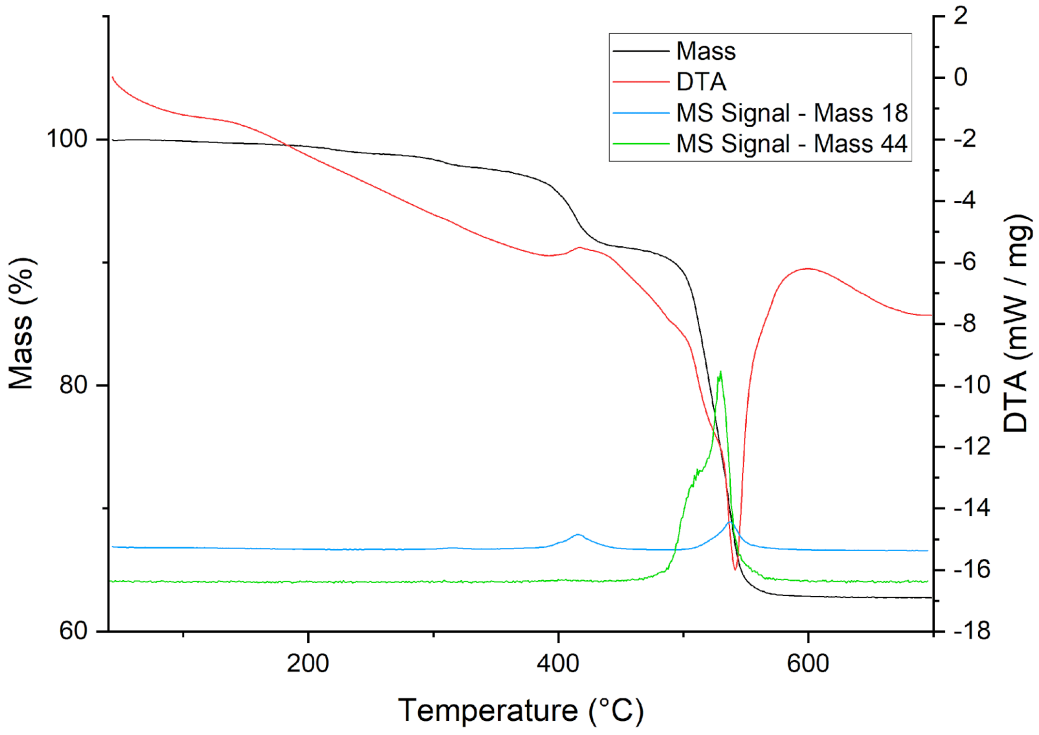

Figure 6.16) TGA-MS analysis of BIRM-9

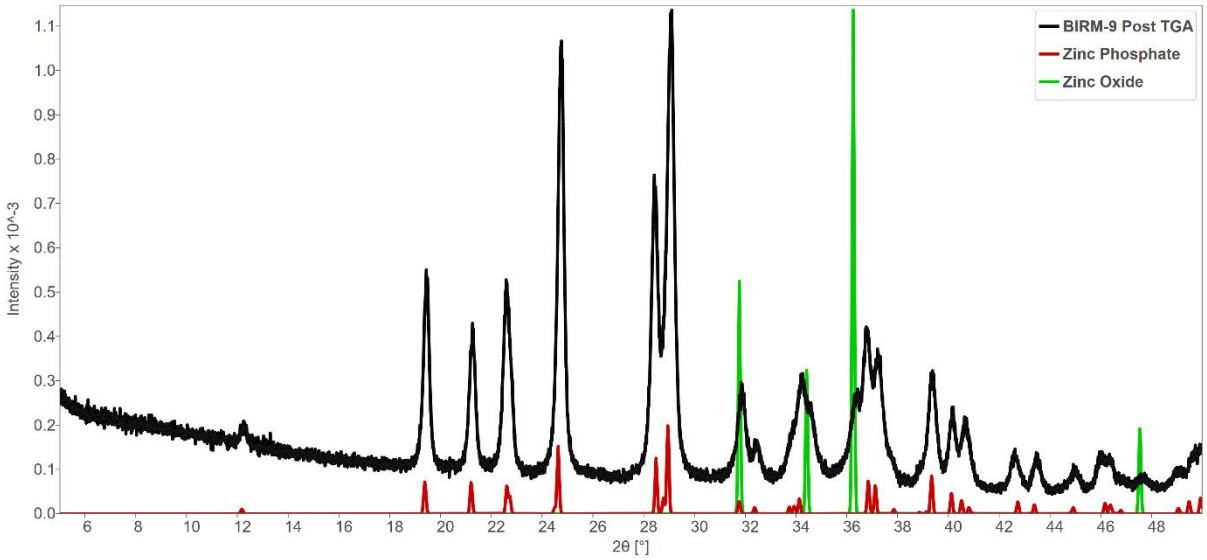

Figure 6.17) PXRD Pattern showing the decomposition product of BIRM-9 (black) compared to simulated patterns for zinc phosphate (red) and zinc oxide (green)

Figure 6.18) Image of the TGA product of BIRM-9

Figure 6.17 shows the PXRD pattern for the final decomposition product of BIRM-9, compared to simulated patterns for zinc phosphate and zinc oxide. The peaks for the simulated patterns account for all the peaks in the recorded pattern from the decomposition product. From these decomposition products the calculated mass of the final decomposition step is 30.5%. This is in fairly good agreement with the 28.6% mass loss which was observed. The TGA product is a light brown powder as shown in Figure 6.18. As both zinc oxide and zinc phosphate are white solids this suggests there is some other amorphous phase still present.

6.7 Porous Framework

With the previous structure solved and characterised, attention moved to the products from section 6.5 which contained mixed phases. Under an optical microscope, these samples were visibly a mix of phases. The previously solved BIRM-9 with plate-like crystals was visible but also present were crystals with completely different morphology. These crystals were prism-shaped with pointed ends.

6.7.1 Structure

One of the prism-shaped crystals was mounted for single crystal diffraction and was found to be untwinned and diffracted well. A good quality dataset was collected with an R_{int} of 3.3%. Figure 6.19 displays the asymmetric unit of the solved structure. Atom labels have not been included for clarity due to the large number of atoms present. The structure consists of 2-dimensional layers of ZnO_4 and CPO_3 tetrahedra which are then connected *via* coordinating linkers to form an extended 3-dimensional network. There are potential pores present within which ammonium cations and water molecules reside meaning that this material meets the definition of a metal–organic framework.[153] Although from the solved structure and corresponding chemical formula ($Zn_{1.1}(O_3PC_7H_4COO)(OH)_{0.1}(NH_4)_{0.9}\cdot 0.33H_2O$) there does not seem to be much water present within the material, there may be a significant amount more that is poorly ordered and hence determining a defined crystallographic location for those molecules is not possible. There is a noticeable amount of disorder present within the structure. One of the linker molecules is disordered over two positions except for the phosphorus atom which is not disordered; two of the oxygen atoms from the two disordered carboxylate groups also share a common position. There is a disordered zinc atom at 1/3 occupancy which is visible in the lower right corner of Figure 6.19 close to a disordered ammonium cation site which is at 1/2 occupancy. This zinc atom is coordinated to three framework oxygen atoms, a water molecule and a hydroxyl group which is important for charge balance of the overall structure. A coordination number of 5 is relatively unusual for zinc, however, from the structure there does not appear to be an accessible open metal site. This is due to the potential site being blocked by a linker molecule. Table 6.7 provides some basic crystallographic detail of the structure whilst Figure 6.20, Figure 6.21 and Figure 6.22 display the

extended structure. This material will be known as BIRM-10. CHNS analysis was conducted to confirm the ammonium content of the material as it was not always obvious from the single crystal data whether a particular atom site was from water or ammonium due to their similar electron density. CHNS returned a C:N ratio of 7:0.889 which is in excellent agreement with the theoretical value of 7:0.88 from the structure determined in this work.

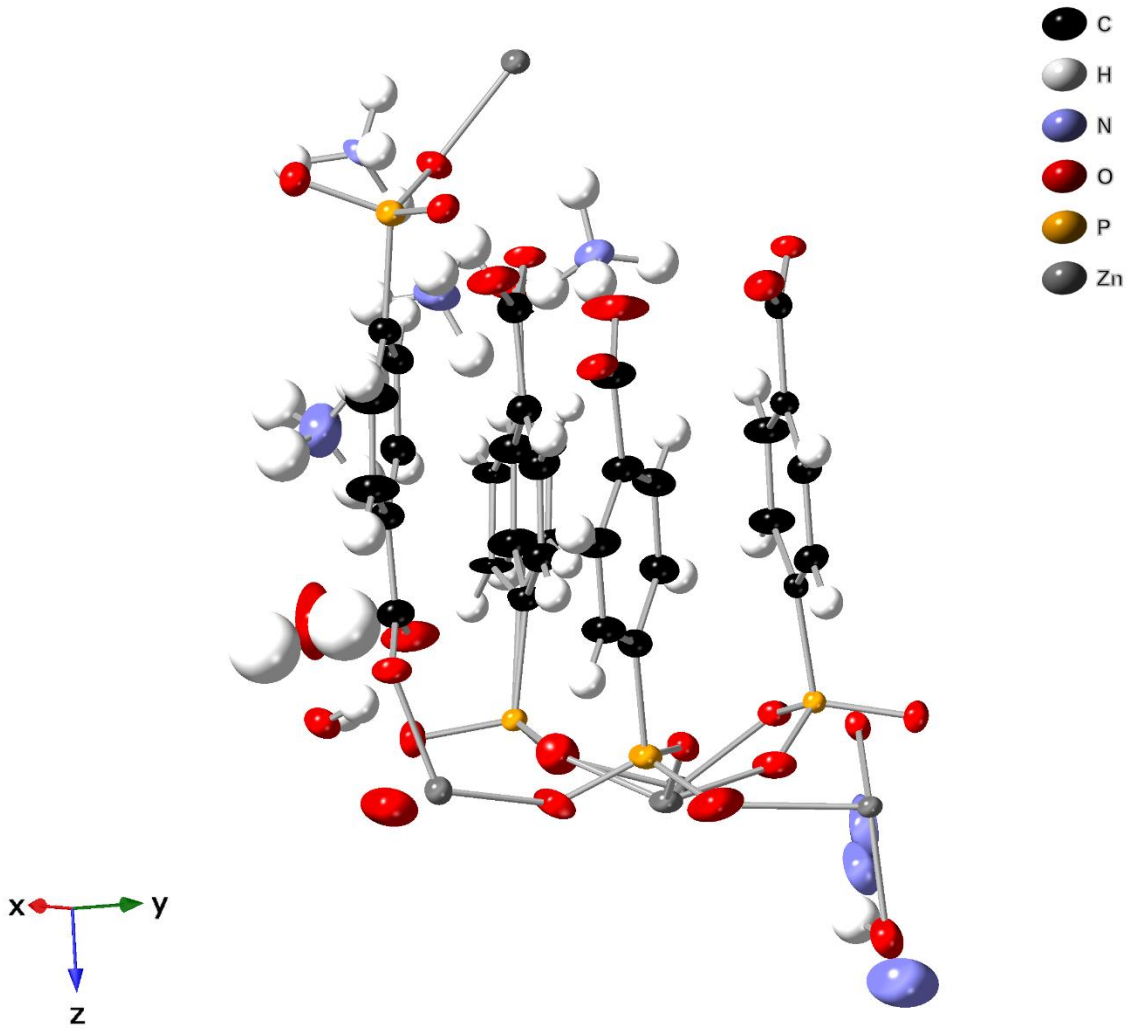

Figure 6.19) Asymmetric unit of the third phase identified from PXRD patterns. Ellipsoids are drawn at the 50% probability level. Atom labels have not been included here for clarity, due to the number of atoms in the asymmetric unit. One of the aromatic rings is disordered other two positions but the phosphorus is not disordered and two of the carboxylate oxygen atoms share a common position. Thermal parameters of hydrogen atoms are fixed as a function of the parent's thermal parameter.

Table 6.7) Basic crystallographic details of BIRM-10

Sample	BIRM-10
Formula	$Zn_{1.1}(O_3PC_7H_4COO)(OH)_{0.1}(NH_4)_{0.9}\cdot 0.33H_2O$
Formula Weight	293.42
Space group	*P*21/*c*
a (Å)	10.4124(1)
b (Å)	19.4412(2)
c (Å)	19.8815(2)
β (°)	92.282(1)
Volume ($Å^3$)	4021.41(7)
Goodness-of-fit on F^2	1.042
wR_2	0.0683
Largest peak/hole (e $Å^{-3}$)	0.91/-0.73

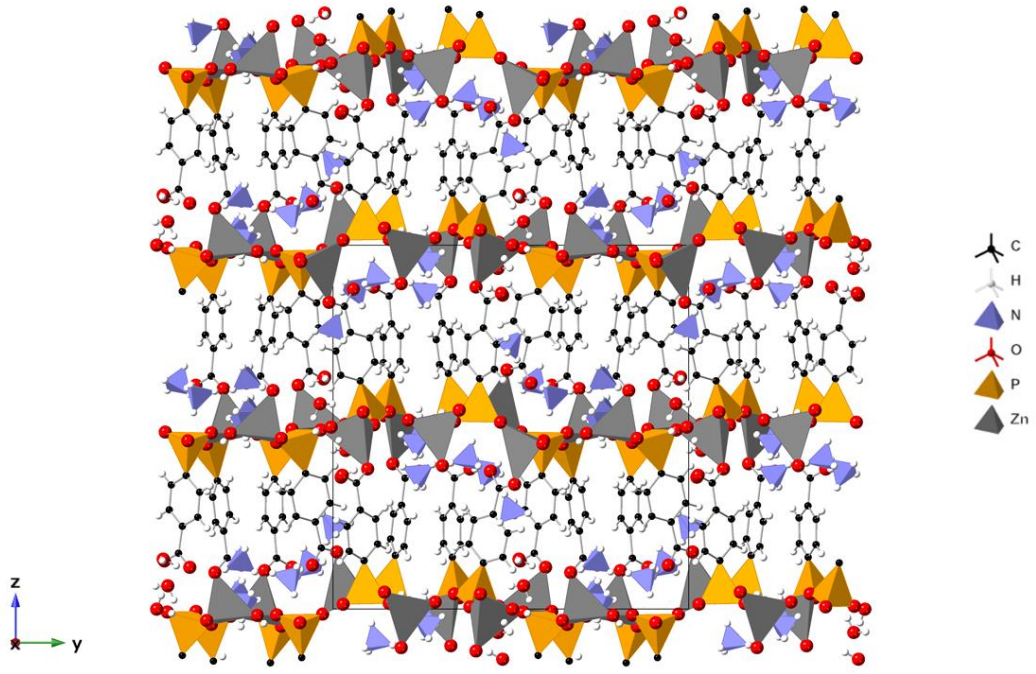

Figure 6.20) A view of the extended structure of BIRM-10 with disordered zinc and linkers removed for clarity, looking along the x-axis. Unit cell is shown by the black outline

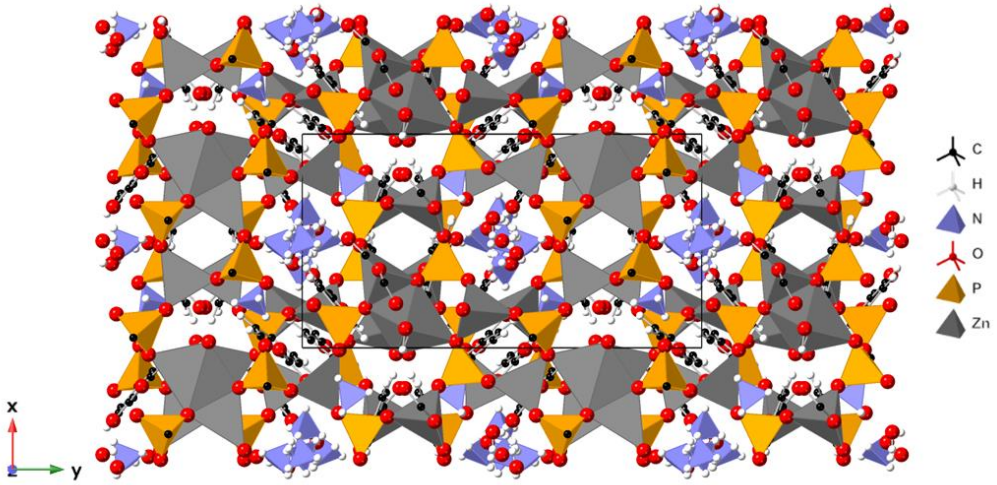

Figure 6.21) A view of the extended structure of BIRM-10 with the disordered zinc and linker removed for clarity, looking down the z-axis. Unit cell is shown by the black outline

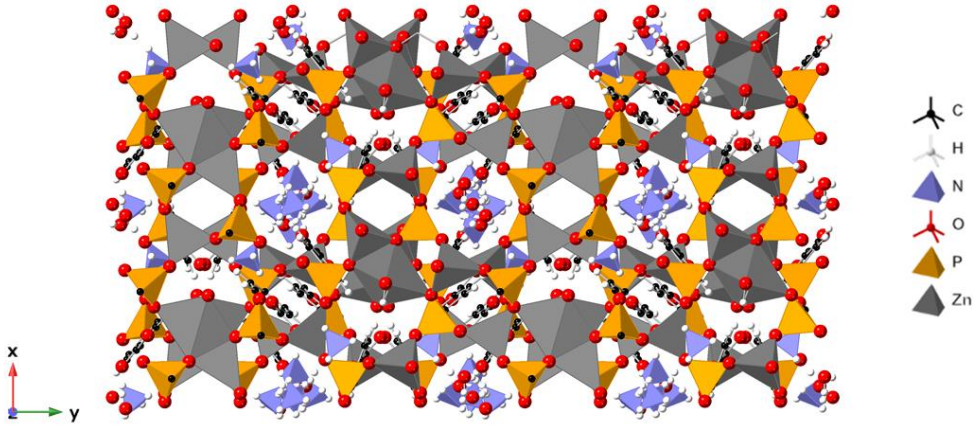

Figure 6.22) A view of the extended structure of BIRM-10, looking down the z-axis with the disordered zinc included in the structure; the disordered linker is not shown for clarity.

The extended structure is shown in Figure 6.20, Figure 6.21 and Figure 6.22, with various amounts of disorder displayed. It is significant that the disordered zinc sits within the channels of the structure, presumably decreasing the amount of accessible internal surface area. There are multiple crystallographically distinct channels which run the length of the structure. Some of these contain disordered zinc atoms, however, all appear to contain water and ammonium cations. To give a clearer view of the channels and potential internal surface area of the material, Figure 6.23 displays the structure with the pore contents removed and the channels marked with green rods. There is clearly a significant amount of potential internal surface area if it can be accessed despite the cations present. The channels

are also located quite close together and there seem to be plausible 'windows' between them from spacings between the organic linkers. This indicates that the porosity of the material may not merely be 1-dimensional and would ensure that a significant proportion of the internal surface area remains accessible despite the presence of disordered zinc and ammonium cations which may otherwise block the internal porosity.

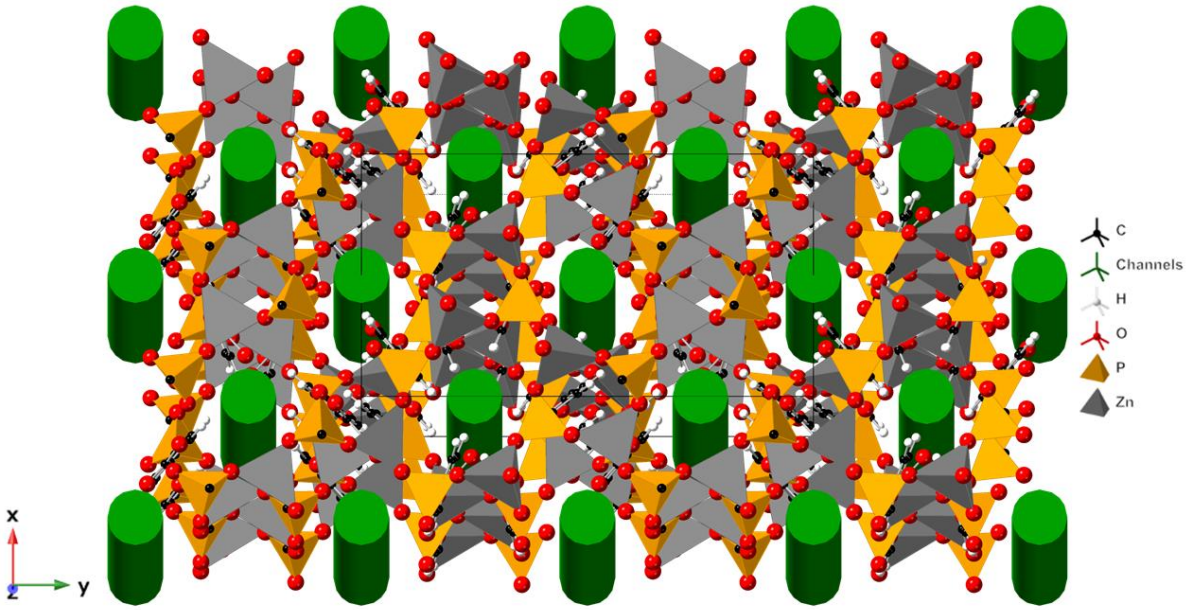

Figure 6.23) A view of the extended structure of BIRM-10, looking at a 5° tilt from straight down the z-axis; the disordered zinc and linker as well as ammonium cations and water are removed to highlight the channels within the structure, represented by green rods.

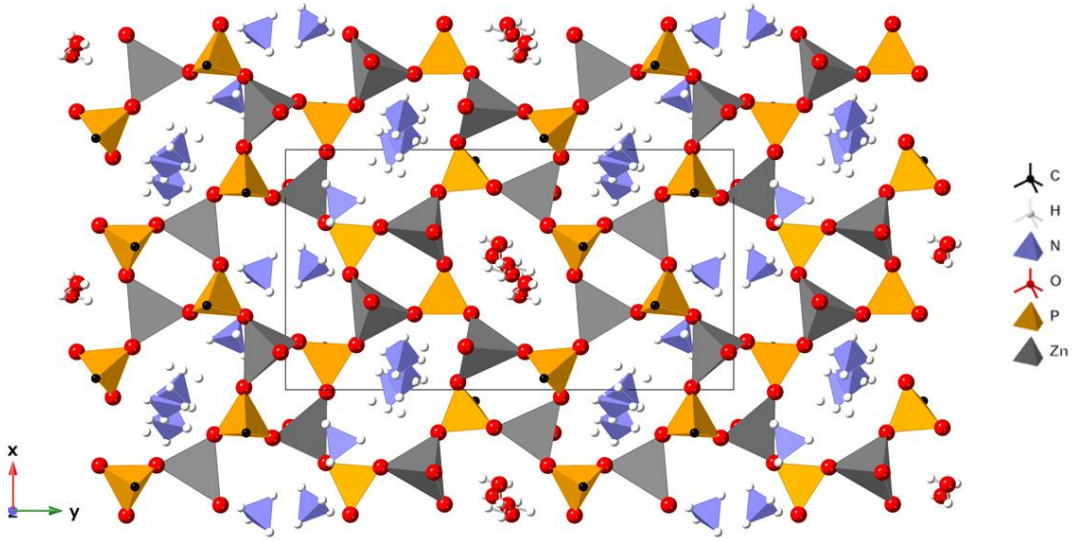

Figure 6.24) A cross-section of the extended structure of BIRM-10 to show the layers of ZnO_4 and CPO_3 tetrahedra. The unit cell is shown by the black outline

Figure 6.24 shows a cross section of the material to better visualise the layers of ZnO_4 and CPO_3 tetrahedra. Ammonium cations and water molecules can be seen within apertures in the layers which allow the channels to pass through and extend through the structure ad infinitum. These apertures are made up of 8-membered rings of ZnO_4 and CPO_3 tetrahedra (not counting the disordered zinc that is occasionally present). The framework oxygens that make up the edges of these apertures can coordinate to the ammonium cations contained within. If the material is capable of ion-exchange it seems likely that these apertures will enact a selectivity for certain ions due to the shape and size of the openings. This could make this material a prime candidate for applications like waste remediation. In addition to possibly enabling the selective ion-exchange of certain cations these apertures may also impart a size-exclusion property allowing selective adsorption of certain gases or small molecules. The channel structure of the material is similar to the zeolite gismondite which has known phosphate analogues, including BIRM-3.[63,115,121]

6.7.2 Synthesis Optimisation

Recalling that the single crystal which was used for structure solution was in fact pulled from a sample that contained a mixture of phases, namely BIRM-9 and BIRM-10, it is crucial for characterisation and applications testing that a pure phase is obtained. For this, a study of synthesis variables must be conducted in order to establish a methodology which reliably leads to a pure sample of BIRM-10 being obtained. It was theorised that the bridging hydroxyl groups present in BIRM-9 would form under high pH due to coordinated water being deprotonated, therefore the first variable that was changed was the amount of urea present. In the first chapter of this thesis, it was established that the presence of TEAB was not required for the synthesis of BIRM-1. As part of the optimisation of the synthesis of this material, it was thought prudent to determine whether TEAB is a crucial part of the synthesis matrix and so it was removed as a variable. An additional objective of this optimisation was to scale the synthesis up somewhat as a very small quantity of product was obtained in the previous syntheses. As the limiting reagent is zinc nitrate the quantity used was increased compared to the initial synthesis. The quantities of reagents used are shown in Table 6.8, reagents were dissolved in 6 ml of deionised water and the

hydrothermal bomb was heated to 110 °C. It is important to note for this synthesis that the reduction in urea added leads to the 4-phosphonobenzoic acid being less soluble in the synthesis solution. This leads to not all of the linker being dissolved prior to being poured into the hydrothermal bomb but this was done with the hypothesis that, once heated, the increase in temperature and decomposition of urea would ensure it readily dissolves.

Table 6.8) List of reagents and amounts added in the first synthesis optimisation experiment

	Zinc Nitrate Hexahydrate	4-phosphono-benzoic acid	Tetraethylammonium Bromide (TEAB)	Urea
Mass (g)	0.1481	0.1	0	0.1543
Molar Ratio	1	1	0	5

The PXRD pattern of the product is shown in Figure 6.25. There was clearly still a mix of phases. However, the product was obtained in a higher yield than previously with 0.075 g compared to 0.029 g. Two lessons can be learnt from this synthesis attempt: first is that TEAB is in fact not required for the synthesis of either phase and its use is superfluous. Secondly, that whilst increasing the quantity of zinc nitrate does seem to have led to higher yield as predicted, a mix of phases was obtained. It was expected that the phase outcome of this synthesis would be drastically different as the reduction in urea and increase in zinc should have led to a much more acidic synthesis solution. The fact that the BIRM-10 phase was still obtained, albeit as part of a mixture, suggests that pH and temperature are not the only important variables in phase control. One possibility is that the more zinc added to the synthesis solution the more favourable it is that the zinc-rich product (BIRM-9) will form.

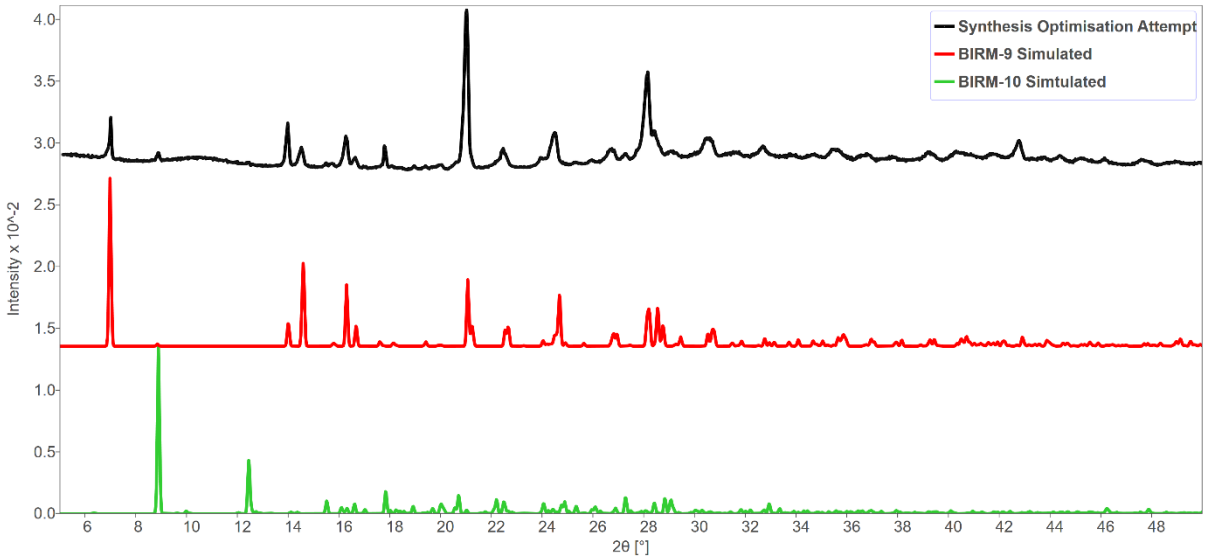

Figure 6.25) PXRD pattern of the product of the first synthesis optimisation attempt (black) with simulated patterns of BIRM-9 (red) and BIRM-10 (green)

With that hypothesis, another synthesis optimisation was planned: the urea ratio was kept lower than the initial synthesis (though higher than the previous experiment) and the zinc nitrate reverted to the original quantity. It was unlikely this would lead to an improved yield, as the zinc was the limiting reagent, but the main objective of phase purity might be achieved. The quantities used are shown in Table 6.9 and the synthesis was again conducted at 110 °C.

Table 6.9) List of reagents and amounts added in the second synthesis optimisation experiment

	Zinc Nitrate Hexahydrate	4-phosphono-benzoic acid	Tetraethylammonium Bromide (TEAB)	Urea
Mass (g)	0.0873	0.1	0	0.12
Molar Ratio	1	1.75	0	6.8

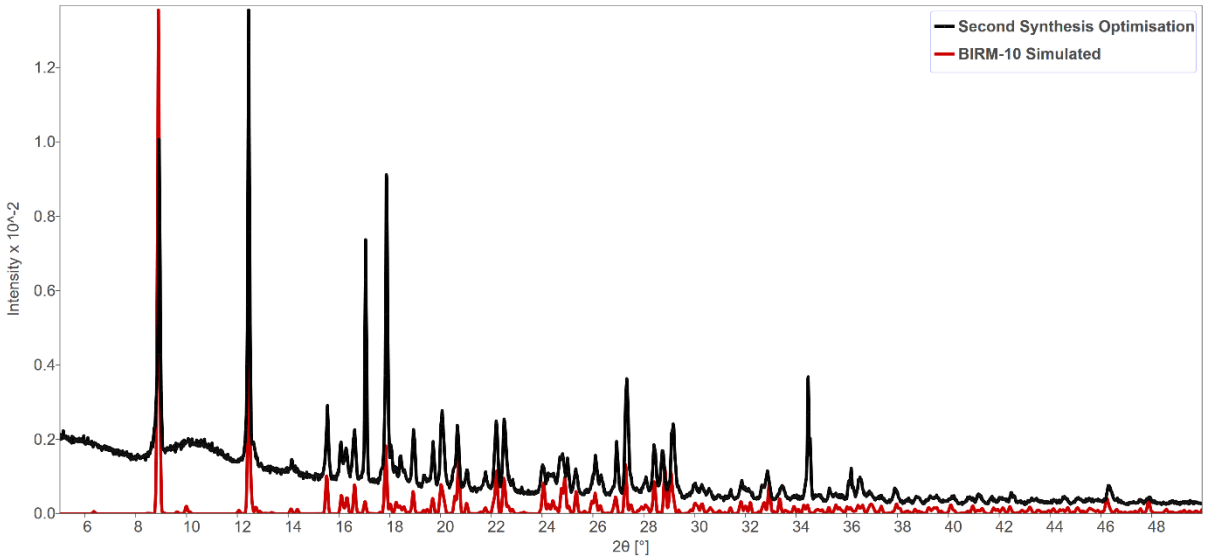

Figure 6.26) PXRD pattern of the product of the second synthesis optimisation attempt (black) with simulated patterns of BIRM-10 (green)

From the PXRD pattern in Figure 6.26 it can be established that a pure phase sample of BIRM-10 was successfully synthesised. Figure 6.26 contains a comparison of a PXRD pattern from the product of the second synthesis optimisation attempt to a simulated pattern of BIRM-10, showing that all peaks are accounted for and in the correct position, indicating a pure phase. Only 0.03 g of product was obtained, (ca. 35% yield) which is just as poor as the original synthesis, however, obtaining a pure phase is a crucial step forward. To ensure reliability as well as to obtain sufficient product for thorough characterisation, this synthesis was attempted an additional 3 times with the same outcome.

6.7.2.1 Synthesis-Phase Relationship

Table 6.10 contains a list of a few synthesis conditions tried in this work with a metal-to-linker ratio of 1:1.75.

Table 6.10) A list of some of the synthesis conditions tried in this work, the pH of the resulting supernatant liquid and the phase outcome; all of these reactions had a zinc:linker ratio of 1:1.75

Temperature (°C)	Urea Molar Ratio	Final Solution pH	Phase Outcome
83	9	6	BIRM-8
110	6.8	8	BIRM-10
115	8.75	9	Mixed BIRM-9 & -10
120	8.75	8.5	BIRM-9

For the given metal-to-linker ratio, a complicated relation between synthesis temperature and pH, and phase outcome was observed. The full range of phases found with this linker, in this work, can be obtained at this ratio by only changing the quantity of urea added and the synthesis temperature. As with the phases related to BIRM-1, the layered phase with a still protonated carboxylic acid group formed at low temperatures where the extent of urea breakdown into ammonium carbonate was low, leading to a lower pH. As the synthesis temperature was increased, even if the quantity of urea added was decreased, an increase in pH was observed as more urea decomposed into ammonium carbonate. The formation of a new phase occurred, and the porous MOF, BIRM-10 was obtained. As temperature was increased further, the other layered phase (BIRM-9) was obtained in a mixture with BIRM-10, and the supernatant liquid had a notably higher pH as would be expected. The BIRM-9 phase has three hydroxyl groups in the asymmetric unit which is evidence of the more basic conditions in which it forms as water molecules coordinated to zinc can be deprotonated. At this point, further increasing the synthesis temperature had a rather unexpected effect on the supernatant pH with a decrease being observed. This can be explained by the BIRM-9 phase forming preferentially at higher temperatures and the previously mentioned deprotonation of coordinated water molecules leading to the supernatant liquid becoming less basic. Therefore, a complicated relationship between pH and temperature, and the phase outcome can be put forward, with the increase in pH being responsible for the formation of the initial layered phase and the porous BIRM-10 phase, but the synthesis temperature being the determining factor for the formation of the BIRM-9 phase. This means BIRM-9 is likely the thermodynamically favourable product.

6.7.3 FTIR

Evident from the FTIR spectra (Figure 6.27, with assignments in Table 6.11) is the presence of water and ammonium within the structure from the broad overlapping peaks which are centred around 3000 cm^{-1}. Moreover, the FTIR spectra displays all the peaks expected from the functional groups within the structure, such as those arising from deprotonated carboxylate and phosphonate groups.

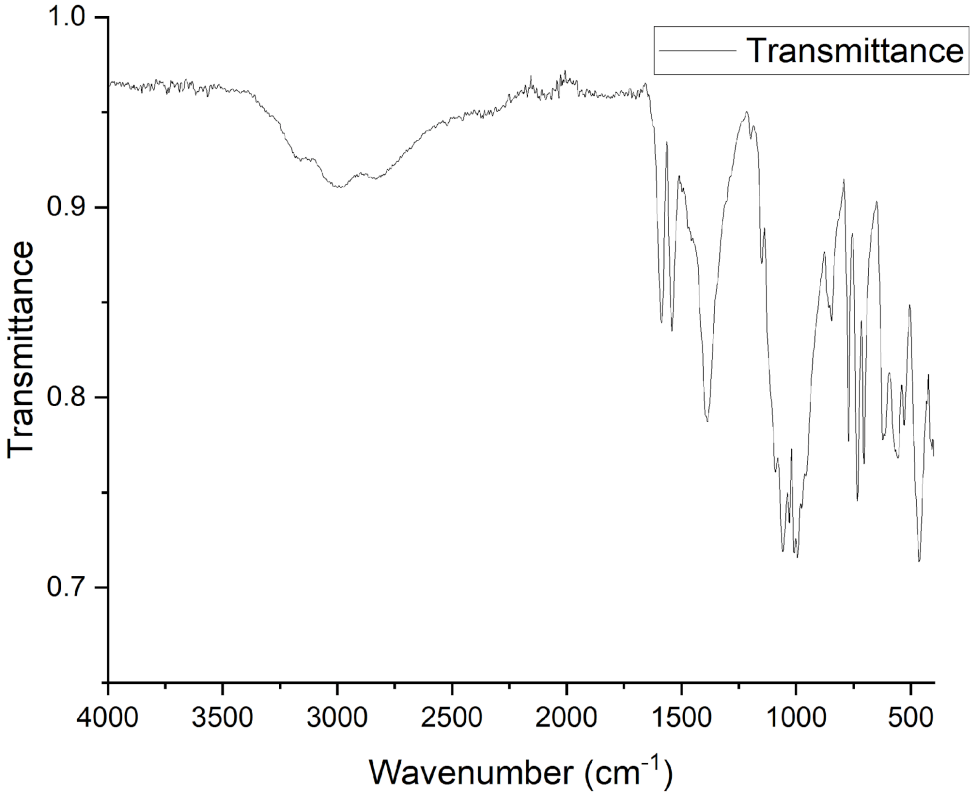

Figure 6.27) FTIR spectra of BIRM-10

Table 6.11) Table of FTIR peaks and assignments for BIRM-10

Peak (cm^{-1}), profile, intensity	Assignment
3000, broad, weak	Water O-H, Ammonium N^{+}-H, Aromatic C-H
1587, sharp, strong	Carboxylate C-O
1540, sharp, strong	Aromatic ring C-C
1387, sharp, strong	Carboxylate C-O
1150, shoulder, medium	Phosphonate P-O
1090, shoulder, strong	Phosphonate P-O
1058, sharp, strong	Phosphonate P-O

6.7.4 SEM-EDX

The SEM images (Figure 6.28) show the previously described crystal morphology of BIRM-10. A more powerful magnification is provided on the right of the figure for a clearer view. The crystals are rectangular prisms terminating with a truncated pyramid shape on the ends of the prism.

Figure 6.28) Two SEM images of BIRM-10 at 100× magnification (left) and 400× magnification (right)

EDX analysis found an average Zn:P ratio of 1.35:1 across 6 sites. This is a higher ratio than the theoretical 1.1:1 value, however, it seems that EDX analysis is either always overestimating the zinc content of samples in this work or all the materials made in this work have higher levels of zinc than expected. The latter seems unlikely especially when considering that most the materials synthesised in this work were done so with an excess of the linker (and hence phosphorus) present. As the heavier atom, zinc would be expected to more efficiently absorb electrons when compared to phosphorus and this may contribute to the apparent overestimation of zinc content.

6.7.5 TGA-MS

The TGA-MS analysis (Figure 6.29) shows the decomposition profile of the material. The start of the TGA involves a slow and steady loss of mass with a corresponding MS signal for mass 18, representing water. This is likely due to water being removed from the internal structure of the material, with the water that is present deeper within pores coming off at higher temperatures, hence the steady loss of mass. There is also a slight upwards bend in the DTA trace indicating a small endotherm in this region, which would be expected with the removal of water. Some of the loss is also likely attributable to the removal of ammonia. The loss of pore contents is confirmation of the porous nature of the material. The most sudden mass loss attributable to emission of water is about 3.5% at 325 °C, evidenced by the MS signal for mass 18 and an endothermic DTA peak. Around 520 °C the material appears to start to undergo a dramatic decomposition, likely due to combustion of the organic components, as evidenced

by the exothermic peak in the DTA trace and MS signals of mass 18 and 44, corresponding to water and carbon dioxide. The total mass loss up to 700 °C is 48.4%. Figure 6.30 shows the PXRD pattern of the decomposition product of the material. Whilst at a first glance it bears resemblance to the pattern for the decomposition product of BIRM-9, closer inspection reveals it is a unique pattern with a different set of peaks. Attempts to phase match the pattern to likely decomposition products such as zinc phosphates, pyrophosphates and oxides were not successful. An image of the TGA product is shown in Figure 6.31. The product was largely composed of a dark grey powder with some white product also present. This suggests the composition was not made up of a single phase.

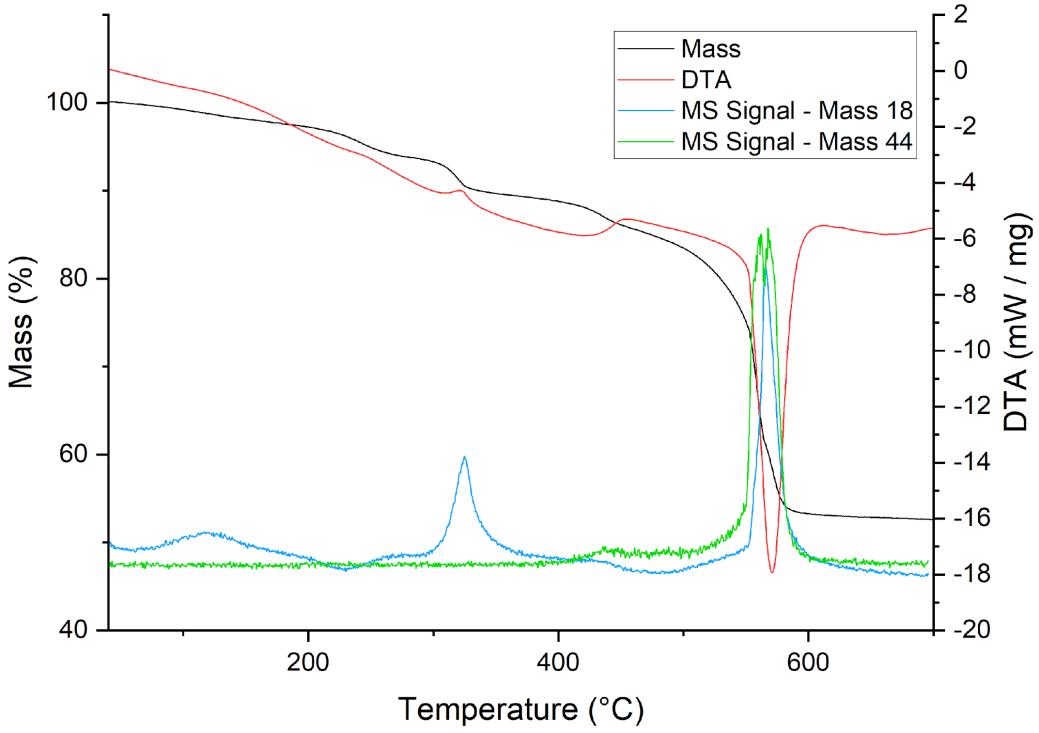

Figure 6.29) TGA-MS Analysis of BIRM-10

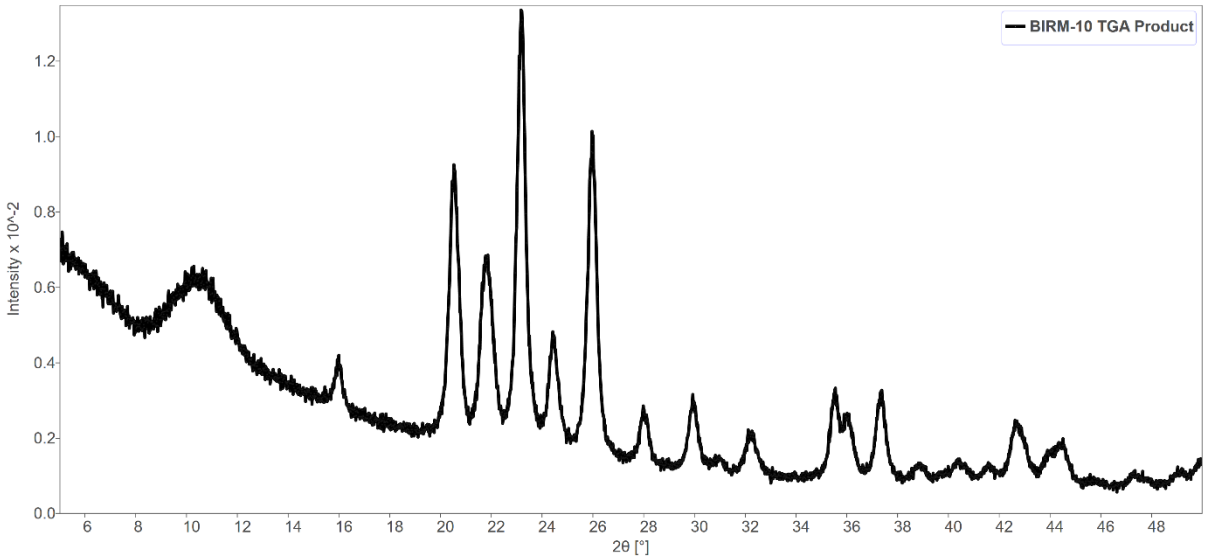

Figure 6.30) PXRD pattern of the post TGA product of BIRM-10

Figure 6.31) Image of the TGA product of BIRM-10

6.7.6 Porosimetry

Due to the evidence from the solved structure and the TGA-MS analysis that this material may contain accessible pores, a nitrogen adsorption isotherm (Figure 6.32) was recorded. The isotherm takes the shape of a 'type I' reversible isotherm, indicating microporosity.[136] The measured surface area using the Rouquerol BET approach for microporous materials was calculated as 813 m^2 g^{-1}.[137] Whilst there are many MOFs in literature that have a much greater surface area,[161] this is a substantial value and certainly confirmation of the material's porosity.

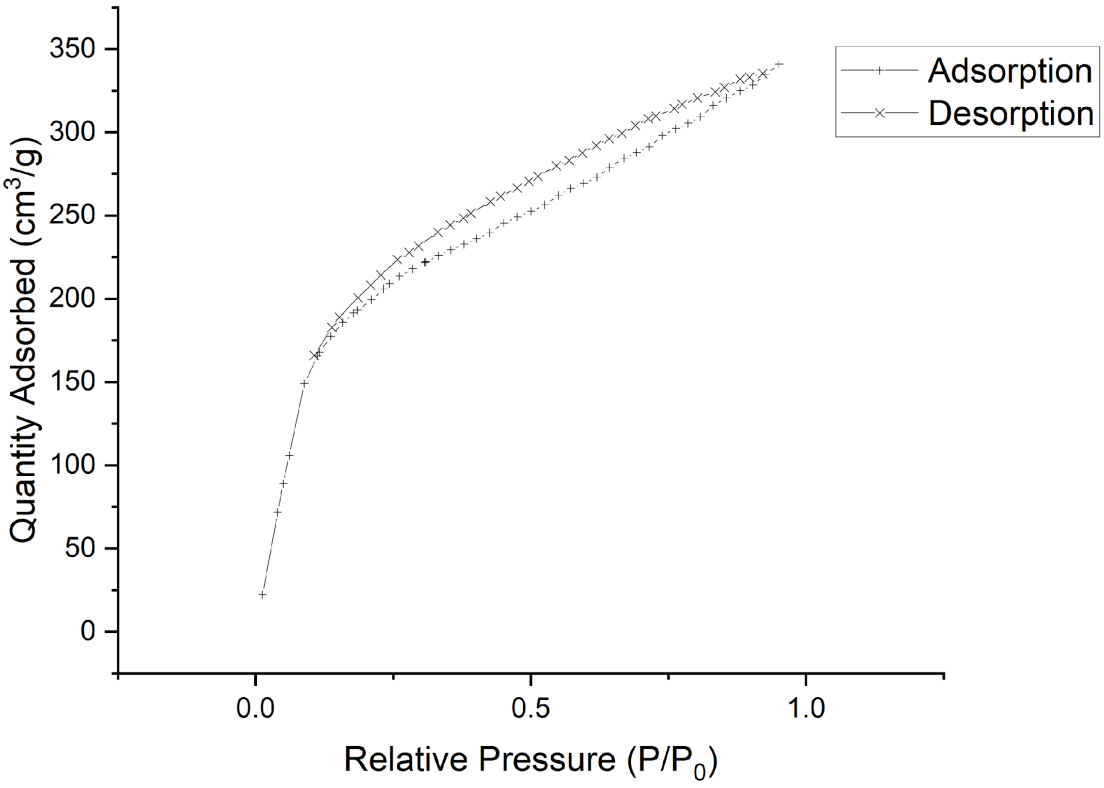

Figure 6.32) N_2 adsorption isotherm of BIRM-10

6.7.7 Ion-Exchange

The presence of extra-framework ammonium cations within the pores of BIRM-10 raises the possibility of ion-exchange of the material, such as can be observed in BIRM-1. Successful ion-exchange would open up a wide range of possible applications as well as the opportunity to tune the material and enhance properties suited to particular applications. An experiment was designed to test if it was possible for BIRM-10 to undergo ion-exchange. Potassium was chosen as the exchange cation due to its similar hydrated radius to ammonium.[162] In the experiment, 0.02 g of BIRM-10 was placed in a glass vial with 20 ml of 0.2 M aqueous potassium acetate and left on an orbital shaker for 24 hours. The pH of this exchange solution was found to be around 8; no pH adjustment was conducted as only a small quantity of BIRM-10 was available and there was a perceived risk of dissolution of the sample if acid were added as the pH stability range of the material had not yet been assessed.

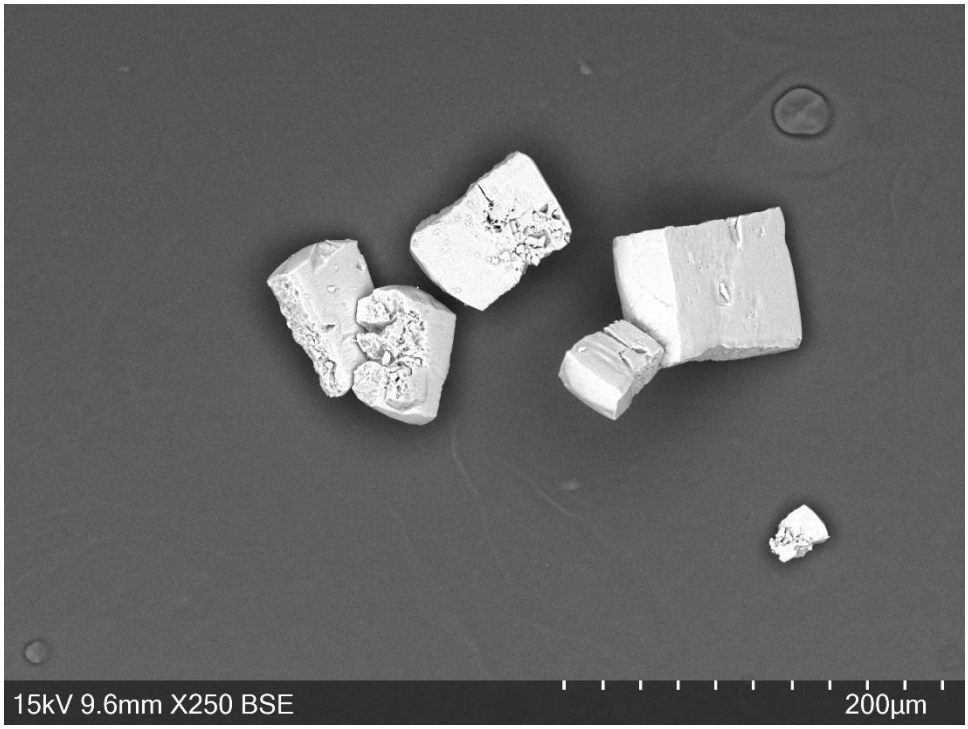

Figure 6.33) SEM image of BIRM-10 post ion-exchange attempt with potassium

An SEM image of some of the recovered product is shown in Figure 6.33. From, the image it is visible that the crystal morphology looks as if it has been retained, though the few crystals that are shown do appear to have some defects. EDX analysis found no evidence of potassium in the sample at all, providing evidence that the ion-exchange was not successful. Additional analysis came in the form of single crystal diffraction which also found no evidence of change in the electron density of the cation sites, further proving that ion-exchange was not successful. Table 6.10 lists the lattice parameters of the as-synthesised and the post-exchange attempt sample showing there is little difference between them and there is no evidence of ion-exchange.

Table 6.12) Lattice parameters of as-synthesised and post-exchange attempt BIRM-10

Lattice Parameter	As-Synthesised BIRM-10	Post-exchange attempt BIRM-10
a (Å)	10.4124(1)	10.4106(1)
b (Å)	19.4412(2)	19.4443(3)
c (Å)	19.8815(2)	19.8841(2)
β (°)	92.282(1)	92.324(1)
Volume ($Å^3$)	4021.41(7)	4021.76(8)

A further attempt at ion-exchange was undertaken, this time the solution used was 2 M potassium acetate and was slightly acidified to pH 6 with 1 M hydrochloric acid. This led to the slow dissolution of the sample and was therefore unsuccessful. It does, however, provide information about the pH stability range of the material.

It could still be that ion-exchange of BIRM-10 is possible under the right conditions. It could be that with application of heat it is possible to ion-exchange or perhaps with a different cation. The disordered zinc within some channels of the material indicates that a range of cations could sit within those sites and it is just a matter of determining the correct conditions for ion-exchange to be conducted.

6.7.8 Room Temperature Synthesis Attempt

As there was success in making BIRM-1 at room temperature, the same principles were applied to this material in the hope that it would be made more easily and possibly in greater yield and overall quantity. A precursor solution of 0.0873 g zinc nitrate hexahydrate and 0.1 g of 4-phosphonobenozic acid was made in 10 ml of deionised water. To this 2 M ammonium hydroxide solution was added dropwise. A precipitate was observed forming from pH 5 onwards and the addition of base was stopped at pH 7, at which point the linker should be deprotonated. The product was not recoverable *via* vacuum filtration as it kept passing through the filter paper used, so instead centrifugation was used. The product was centrifuged at 4000 rpm for 5 minutes three times, with the water being decanted and replaced with 10 ml deionised water between each run to wash the product. After the final centrifugation the product was left in a weighing boat to dry in air. The PXRD pattern of the product is shown in Figure 6.34.

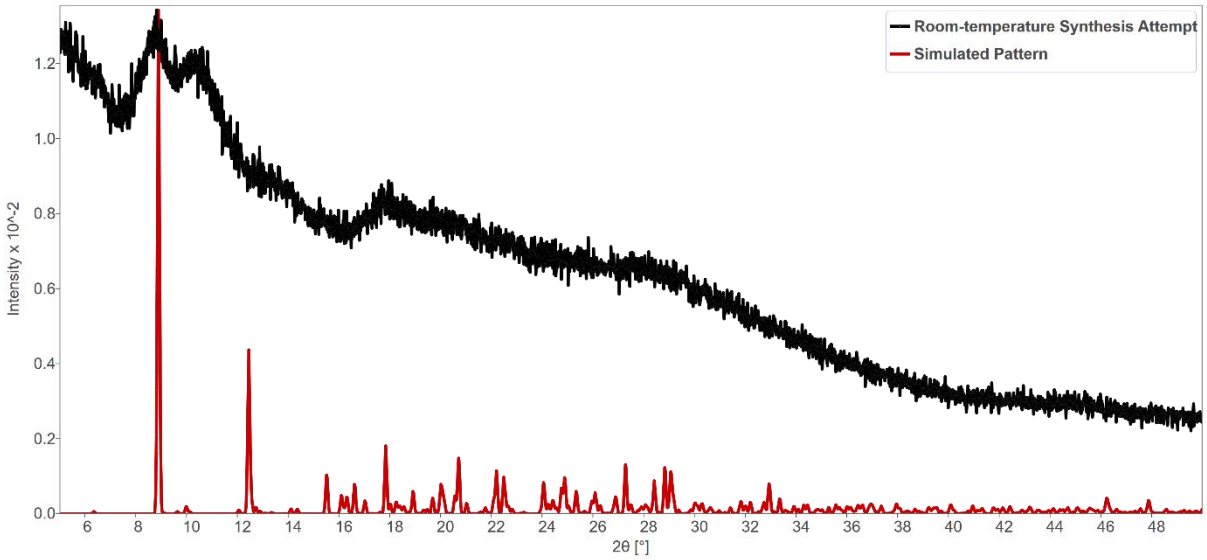

Figure 6.34) PXRD pattern of the product of the room temperature synthesis attempt (black) and a simulated pattern of BIRM-10 (red)

The collected diffraction pattern indicates a product without significant long-range order as evidenced by the broad peaks. The lack of long-range order can either be due to the material being amorphous or nanoparticulate in nature. A notable feature of the diffraction pattern is that the broad peaks do seem to line up with peaks in the simulated pattern, with the exception of the broad peak around 10° which is an artifact associated with the diffraction instrument used. SEM images of the material were taken to see if the particle size was discernible; an image at 600× magnification is shown in Figure 6.35.

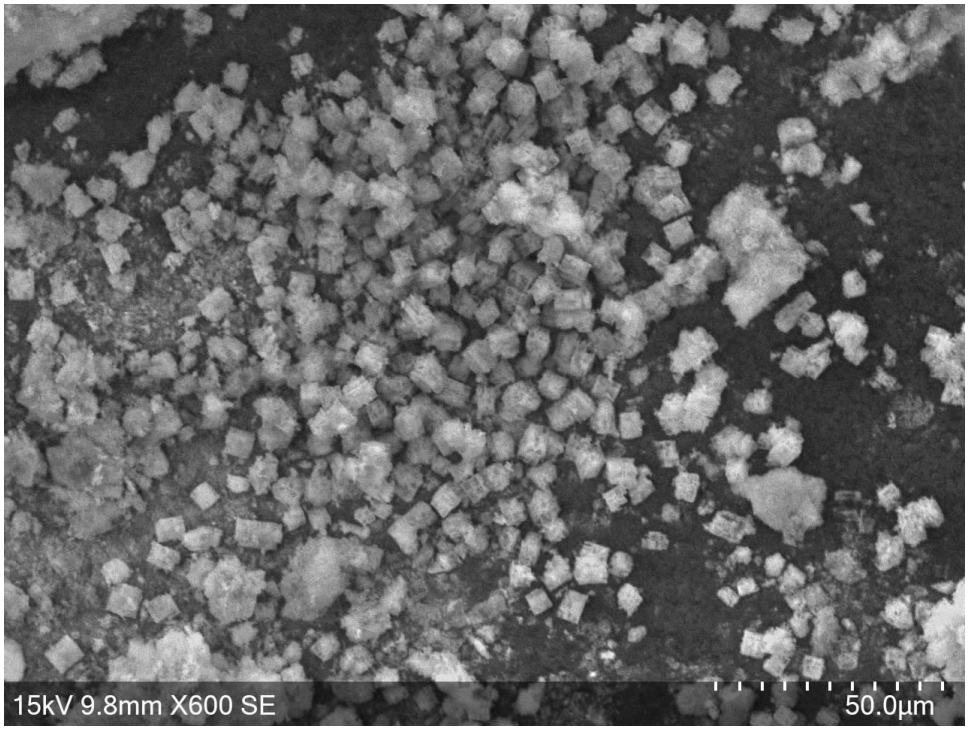

Figure 6.35) SEM images of the product synthesised at room-temperature, 600× magnification

In the SEM image most crystallites appear to be a similar size with the exception of some larger particles which could be aggregated material. The majority of particles appear to be roughly 5 µm in size, about 50× larger than the generally accepted upper limit of the definition of a nanoparticle. 5 µm is also far too large to cause the extreme broadening of peaks observed in the PXRD pattern of the material. It is possible that these particles are all aggregates of smaller crystallites, and smaller particles can be seen in the SEM image. However, there is a relatively consistent size for the majority of the particles in the image which would not be indicative of them being aggregates. Higher resolution SEM or TEM images are required to conclusively prove whether these are nanoparticles or not, however, with the data available it seems more likely that it is amorphous material and not nanocrystalline.

6.8 Novelty of Materials

Previously, zinc and 4-phosphonobenzoic acid based MOFs and related frameworks have been synthesised and published, such as those by Chen et al.[63] However, the synthesis of these materials has some key differences such as different templating agents which are still present in the material post-synthesis, different zinc salts and different solvents. The outcome is that the materials synthesised in

this work are distinct from any found in previous literature and are thus novel. Indeed, a search of the CCDC database found no match to these structures.

6.9 Conclusion

In this chapter, three novel framework materials (BIRM-8, 9 & 10) have been synthesised with BIRM-10 being particularly interesting as a porous MOF. The three materials have had their syntheses optimised in order to give phase pure samples. The synthesis-phase relationships of these materials have also been linked together by a proposed complex relationship of both synthesis pH and temperature. As a result of this, and especially the differences in synthesis pH, the three materials have significantly different structures. In BIRM-8 the carboxylic acid group remains protonated whereas in BIRM-9 and BIRM-10 the acidic group is deprotonated allowing coordination at both ends of the linker. BIRM-9 contains hydroxy groups, likely due to a higher synthesis pH leading to the deprotonation of coordinated water molecules. Metal hydroxide–organic frameworks have recently been shown to be of interest for electrocatalytic reactions.[163] As a consequence of the hydroxy groups presence, BIRM-9 has a metal:linker ratio of 2:1 which is different to the other materials made in this chapter which have around a 1:1, ratio. BIRM-10, with a synthesis pH between the other two, possesses a fully deprotonated linker and a rather complicated chemical formula which equates to slightly less than 1 hydroxy groups for every 10 zincs in the framework.

BIRM-10 may also be able, under the right conditions, to undergo ion-exchange, however, that has not proven possible in this work. This material also contains disordered zinc atoms within the channels with a 1/3 occupancy, presumably blocking some channels and limiting the accessible internal surface area. Examining if there is a way to make this material without the aforementioned zinc would be a priority for future work.

The synthesis, structure solution and characterisation of a permanently porous novel metal–organic framework is a major milestone of this work. The development of novel MOFs is a widely held goal in the field due to their wide range of potential applications. It is of significant note that the novel MOF

developed in this chapter, BIRM-10, also contains extra-framework cations as the number of MOFs which contain such guests within their pores but are also structurally stable and exhibit permanent porosity is very limited. The presence of these cations could enable a wider variety of applications such as proton conductivity, as explored earlier in this thesis, or waste remediation. They can also enable the tuning of a materials properties *via* ion-exchange for enhanced potential for applications such as gas storage by allowing gas molecules to bind to cations within the structure.

7 Conclusions

This thesis explores the synthesis, structure and properties of a range of metal carboxyphosphonate frameworks, as well as relationships between these. These relationships include the effect of synthesis pH on structure, and the effect of the presence of additives such as TEAB during synthesis on the properties of the materials. The development of novel frameworks and their characterisation is a significant achievement in this work and the formation of new MOF materials is a widely held goal by many researchers due to their wide range of potential applications.

The first chapter focused on the synthesis of the MOF BIRM-1, $(NH_4)_2[Zn_2(O_3P(CH_2)_2COO)_2]\cdot 5H_2O$, developing a new synthetic route which is more reliable and can directly access forms of the material which could previously only be made *via* ion-exchange. The new synthesis method uses mild synthesis conditions, simply adding base to a precursor solution without the requirement of additional energy input in the form of heat. This synthetic route can also be used without the need for the addition of TEAB, which appears to have unwanted effects on the material's properties as established in this work. Further, the new synthetic procedure leads to a sample of BIRM-1 with much smaller crystallite size. This can be both a positive and a negative depending on what is desired of the material. Small crystallites are often preferred for many applications, however, the structures of many ion-exchanged versions of BIRM-1 remain unsolved and this requires large crystals for single crystal diffraction experiments. The mild conditions of the new synthesis method allow the material to be synthesised in a flow set up, which would make the scale-up of the synthesis relatively straight forward. The layered phase, BIRM-2 $Zn(O_3P(CH_2)_2COOH)\cdot H_2O$, can also be accessed by this new synthesis method. Rietveld refinement was used in order to confirm that the BIRM-1 material synthesised at room-temperature is indeed the same structure as the hydrothermally synthesised product. The framework was confirmed to be isostructural with only slight differences in pore contents. Though the pore contents are difficult to model due to light scattering atoms and disorder. A cadmium-based phase was also produced using the room temperature synthesis method. This phase was obtained as a powder and therefore single crystal diffraction was not possible. However, an indexed unit cell was obtained from the powder pattern.

The properties of BIRM-1 have been further explored with a nitrogen BET isotherm recorded showing the material lacks surface area but does seem to possess a small number of micropores. Proton conductivity in the material has been measured and shows that the material is capable of moderate conductivity comparable to similar materials in literature.[98] A proof of concept experiment for ammonia adsorption in BIRM-1 was attempted and did show some, albeit low, uptake. Steps were set out on how to improve the uptake through both experimental design and from using different forms of BIRM-1. PDF analysis was used in order to characterise the dehydration and amorphization of the BIRM-1 material. This analysis determined that despite the theorised cause of the framework flexibility being the short aliphatic linker, it is likely the inorganic double chains of CPO_3 and ZnO_4 tetrahedra which are distorting most. Nanosheets of BIRM-2 were synthesised and characterised by SEM and AFM. The thickness of the sheets was determined to be approximately 190 nm.

The project focus then moved on to developing novel carboxyphosphonate materials. Initially with a different, lighter, metal in order to produce lightweight frameworks. At least 4 magnesium phases were synthesised, however, only 2 of the structures were solved in this work. One of the unsolved structures appears to have significant surface area and could be a MOF. The other unsolved phase was indexed from its powder pattern. The unit cell has one axis which is much longer than the other two, which is common in layered phases, but it is not possible to tell what form the structure takes from that alone. BIRM-6 is a one-dimensional coordination polymer with formula $Mg(O_3PCH_2CH_2CO_2H)\cdot 4H_2O$. Note that the carboxylic acid group remains protonated, limiting the coordination of the linker to the phosphonate end. Meanwhile BIRM-7, $Mg_3(O_3PCH_2CH_2CO_2)_2$, is a three-dimensional framework with a fully deprotonated linker. Unlike BIRM-1 or BIRM-10, the other three-dimensional frameworks focused on in this work, BIRM-7 does not contain extra-framework cations or pore water as it is a dense framework without a porous structure.

Work progressed to synthesising novel frameworks using a different linker. 4-Phosphonobenzoic acid was chosen for this as the longer, rigid linker should be able to produce structures with larger internal voids. Three novel phases were produced. One of these, BIRM-8 $Zn(O_3PC_6H_4COOH)\cdot H_2O$, is similar

in structure to the layered BIRM-2, while the second, BIRM-9 $Zn_4(O_3PC_7H_4COO)_2(OH)_2 \cdot 2H_2O$, is also a layered material but has a significantly different structure. The third and final phase is a novel porous MOF named BIRM-10 with the formula ($Zn_{1.1}(O_3PC_7H_4COO)(OH)_{0.1}(NH_4)_{0.9} \cdot 0.33H_2O$). BIRM-10 contains channels along one axis which contain ammonium cations. The material shows significant surface area measured using the BET Roquerol method on a nitrogen isotherm, confirming its porosity. Attempts to ion-exchange the ammonium cations for potassium were unsuccessful, though it may be possible given the right conditions. A room temperature synthesis attempt yielded a white powder with extremely broad features in the PXRD pattern. It was not clear whether this material was amorphous or nanoparticulate in nature. BIRM-10 contains disordered zinc atoms within some of the channels in the structure, this is almost certainly restricting the full potential porosity of the material. This material is a significant discovery, if ion-exchange can be achieved it will likely have many potential applications as the extra framework cations and permanent porosity will make it a good material for a range of adsorption applications. Regardless, the presence of ammonium cations may allow it to be a good proton conductor as shown already for BIRM-1. The synthesised of a MOF with extra-framework cations and permanent porosity is notable in itself as there is a very limited number of such materials.

The work presented in this thesis has expanded the understanding of the formation of carboxyphosphonate materials, for each group of materials made (zinc based aliphatic linker, magnesium based aliphatic linker, and zinc based rigid linker) careful control of synthesis pH *via* reagent ratios and temperature appears crucial. For the materials made by a hydrothermal synthesis method the balance of pH and temperature is further complicated with the appearance of phases which are not obtained at room temperature, likely the thermodynamic products of the reaction, such as BIRM-3 and BIRM-4 in the zinc based aliphatic linker system. The development of the room temperature synthesis route avoids this problem but produces product in a powder form. The use of urea decomposing in-situ for pH adjustment allowed for the production of single crystals large enough for diffraction experiments and structure solution which is notably difficult in phosphonate systems.

MOFs are usually produced with rigid linkers as it is often believed that an aliphatic linker will lead to a framework which is too flexible to allow for permanent porosity. However, the pair-distribution function work in chapter two produced unexpected results in showing that it is likely the inorganic double chains within BIRM-1 which are flexing upon dehydration and leading to collapse of the internal porosity. The production of a porous magnesium-based phase in chapter three which was synthesised with the aliphatic linker shows that it is indeed possible to obtain a material with permanent porosity using such a linker.

Overall, 5 novel phases have been developed, including a novel porous MOF. Three additional phases with unsolved structures have been produced, at least one of which may be a MOF. A new synthetic method for BIRM-1 and BIRM-2 has been established and the properties and structure of BIRM-1 have been further explored.

8 Future Work

The highest priority item for future work is likely synthesising the porous unsolved magnesium phase as single crystals and as a pure phase. This is likely to be a porous MOF which could possess a relatively lightweight framework, possibly making it a candidate for gas storage applications. There is also the other unsolved magnesium phase for which a unit cell was determined. Many attempts were made to synthesise this material as a single crystal with no success, including the use of modulators. However, one idea which did not have time to be tested was to use phosphorous acid rather than acetic acid as the modulator. The formation of phases where the phosphonate group coordinates first (BIRM-2 and BIRM-8) suggests control of coordination of that group may have a stronger effect on crystallisation. However, as a phosphonate group has multiple coordinating oxygen atoms it is possible the outcome would be a structure that incorporates the deprotonated phosphorous acid rather than the acid just competing and slowing down nucleation.

Other future work should include a study of the effect of TEAB on the hydrothermal synthesis of BIRM-1. As it is possible to synthesise BIRM-1 at room temperature without its addition, it should be possible

via the hydrothermal route also, given the right conditions are found. Ideas for improving the ammonia adsorption uptake in BIRM-1 were also put forward in the corresponding section of this thesis.

There is also scope for attempting synthesis with a wide array of different elements. Copper, aluminium and the lanthanide series are popular choices for MOF scientists. Similarly, related linkers could be used to produce frameworks in a reticular fashion. For example, it may be possible to produce a framework similar to BIRM-10 with greater porosity by using a linker with two aromatic rings arranged in series.

A large range of total scattering data of the in-situ dehydration and rehydration of BIRM-1 and its cations forms were collected but only a small amount of that data was fitted and analysed in this work. Fitting of the rehydration may give evidence to why Zhao found that the material only returns to ca. 80% of its original crystallinity upon rehydration.

Finally, studying the synthesis and properties of BIRM-10 in greater detail. For example: whether it can undergo proton conductivity, finding whether there are conditions which allow for ion-exchange and measuring uptake of different gasses. Improving yield and synthesising the material without the disordered zinc blocking channels would also be a desirable aim. Alongside development of a room temperature synthesis of BIRM-10, imaging of the product of the room temperature synthesis done in this work using higher resolution SEM in order to determine whether the product is amorphous and/or nanocrystalline should be carried out. Spectroscopy, total scattering and small-angle scattering would also be suitable for characterisation of that material.

9 References

1 O. M. Yaghi, G. Li and H. Li, *Nature*, 1995, **378**, 703–706.

2 N. L. Rosi, J. Eckert, M. Eddaoudi, D. T. Vodak, J. Kim, M. O'Keeffe and O. M. Yaghi, *Science*, 2003, **300**, 1127–9.

3 H. Furukawa, K. E. Cordova, M. O'Keeffe and O. M. Yaghi, *Science*, 2013, **341**, 974.

4 Y. Kinoshita, I. Matsubara, T. Higuchi and Y. Saito, *Bull. Chem. Soc. Jpn.*, 1959, **32**, 1221–1226.

5 B. F. Hoskins and R. Robson, *J. Am. Chem. Soc.*, 1989, **111**, 5962–5964.

6 B. F. Hoskins and R. Robson, *J. Am. Chem. Soc.*, 1990, **112**, 1546–1554.

7 M. Eddaoudi, J. Kim, N. Rosi, D. Vodak, J. Wachter, M. O'Keeffe and O. M. Yaghi, *Science*, 2002, **295**, 469–472.

8 O. M. Yaghi, M. O'Keeffe, N. W. Ockwig, H. K. Chae, M. Eddaoudi and J. Kim, *Nature*, 2003, **423**, 705–714.

9 J. L. C. Rowsell and O. M. Yaghi, *Microporous Mesoporous Mater.*, 2004, **73**, 3–14.

10 Z. J. Lin, J. Lü, M. Hong and R. Cao, *Chem. Soc. Rev.*, 2014, **43**, 5867–5895.

11 K. J. Gagnon, H. P. Perry and A. Clearfield, *Chem. Rev.*, 2012, **112**, 1034–1054.

12 G. K. H. Shimizu, R. Vaidhyanathan and J. M. Taylor, *Chem. Soc. Rev.*, 2009, **38**, 1430.

13 K. Maeda, *Microporous Mesoporous Mater.*, 2004, **73**, 47–55.

14 J. Le Bideau, C. Payen, P. Palvadeau and B. Bujoli, *Inorg. Chem.*, 1994, **33**, 4885–4890.

15 K. Maeda, J. Akimoto, Y. Kiyozumi and F. Mizukami, *Angew. Chemie Int. Ed. English*, 1995, **34**, 1199–1201.

16 S. R. Miller, E. Lear, J. Gonzalez, A. M. Z. Slawin, P. A. Wright, N. Guillou and G. Férey, *Dalt. Trans.*, 2005, **34**, 3319.

17 Y. Y. Zhang, Y. Qi, Y. Zhang, Z. Y. Liu, Y. F. Zhao and Z. M. Liu, *Mater. Res. Bull.*, 2007, **42**, 1531–1538.

18 D. L. Lohse and S. C. Sevov, *Angew. Chemie Int. Ed. English*, 1997, **36**, 1619–1621.

19 K. Barthelet, C. Merlier, C. Serre, M. Riou-Cavellec, D. Riou and G. Férey, *J. Mater. Chem.*, 2002, **12**, 1132–1137.

20 Q. Gao, N. Guillou, M. Nogues, A. K. Cheetham and G. Férey, *Chem. Mater.*, 1999, **11**, 2937–2947.

21 M. P. Attfield, Z. Yuan, H. G. Harvey and W. Clegg, *Inorg. Chem.*, 2010, **49**, 2656–2666.

22 W. Ouellette, H. Y. Ming, C. J. O'Connor and J. Zubieta, *Inorg. Chem.*, 2006, **45**, 3224–3239.

23 R. B. Fu, X. T. Wu, S. M. Hu, J. J. Zhang, Z. Y. Fu and W. X. Du, *Polyhedron*, 2003, **22**, 2739–2744.

24 C. A. Merrill and A. K. Cheetham, *Inorg. Chem.*, 2007, **46**, 278–284.

25 C. A. Merrill and A. K. Cheetham, *Inorg. Chem.*, 2005, **44**, 5273–5277.

26 M. Tuikka, M. Haukka and M. Ahlgrén, *Solid State Sci.*, 2007, **9**, 535–541.

27 D. M. Poojary, B. Zhang and A. Clearfield, *J. Am. Chem. Soc.*, 1997, **119**, 12550–12559.

28 D. I. Arnold, X. Ouyang and A. Clearfield, *Chem. Mater.*, 2002, **14**, 2020–2027.

29 K. J. Gagnon, S. J. Teat, Z. J. Beal, A. M. Embry, M. E. Strayer and A. Clearfield, *Cryst. Growth Des.*, 2014, **14**, 3612–3622.

30 D. M. Poojary, B. Zhang, P. Bellinghausen and A. Clearfield, *Inorg. Chem.*, 1996, **35**, 5254–5263.

31 D. M. Poojary, B. Zhang, P. Bellinghausen and A. Clearfield, *Inorg. Chem.*, 1996, **35**, 4942–4949.

32 D. K. Cao, S. Gao and L. M. Zheng, *J. Solid State Chem.*, 2004, **177**, 2311–2315.

33 A. Subbiah, N. Bhuvanesh and A. Clearfield, *J. Solid State Chem.*, 2005, **178**, 1321–1325.

34 P. O. Adelani and T. E. Albrecht-Schmitt, *Inorg. Chem.*, 2009, **48**, 2732–2734.

35 A. A. Ayi, A. D. Burrows, M. F. Mahon and V. M. Pop, *J. Chem. Crystallogr.*, 2011, **41**, 1165–1168.

36 J. M. Taylor, K. W. Dawson and G. K. H. Shimizu, *J. Am. Chem. Soc.*, 2013, **135**, 1193–1196.

37 J. A. Groves, S. R. Miller, S. J. Warrender, C. Mellot-Draznieks, P. Lightfoot and P. A. Wright, *Chem. Commun.*, 2006, **42**, 3305.

38 C. Serre, J. A. Groves, P. Lightfoot, A. M. Z. Slawin, P. A. Wright, N. Stock, T. Bein, M. Haouas, F. Taulelle and G. Férey, *Chem. Mater.*, 2006, **18**, 1451–1457.

39 M. T. Wharmby, J. P. S. Mowat, S. P. Thompson and P. A. Wright, *J. Am. Chem. Soc.*, 2011, **133**, 1266–1269.

40 M. Taddei, F. Costantino and R. Vivani, *Eur. J. Inorg. Chem.*, 2016, **2016**, 4300–4309.

41 G. Yücesan, Y. Zorlu, M. Stricker and J. Beckmann, *Coord. Chem. Rev.*, 2018, **369**, 105–122.

42 M. Taddei, F. Costantino, F. Marmottini, A. Comotti, P. Sozzani and R. Vivani, *Chem. Commun.*, 2014, **50**, 14831–14834.

43 T. Rhauderwiek, K. Wolkersdörfer, S. Øien-ØDegaard, K. P. Lillerud, M. Wark and N. Stock, *Chem. Commun.*, 2018, **54**, 389–392.

44 T. Rhauderwiek, H. Zhao, P. Hirschle, M. Döblinger, B. Bueken, H. Reinsch, D. De Vos, S. Wuttke, U. Kolb and N. Stock, *Chem. Sci.*, 2018, **9**, 5467–5478.

45 S. J. I. Shearan, N. Stock, F. Emmerling, J. Demel, P. A. Wright, K. D. Demadis, M. Vassaki, F. Costantino, R. Vivani, S. Sallard, I. Ruiz Salcedo, A. Cabeza and M. Taddei, *Crystals*, 2019, **9**, 270.

46 S. Drumel, P. Janvier, P. Barboux, M. Bujoli-Doeuff and B. Bujoli, *Inorg. Chem.*, 1995, **34**, 148–156.

47 M. Riou-Cavellec, M. Sanselme, N. Guillou and G. Férey, *Inorg. Chem.*, 2001, **40**, 723–725.

48 A. Cabeza, M. A. G. Aranda and S. Bruque, *J. Mater. Chem.*, 1998, **8**, 2479–2485.

49 G. B. Hix, D. S. Wragg, P. A. Wright and R. E. Morris, *J. Chem. Soc. Dalt. Trans.*, 1998, 3359–3362.

50 N. Stock, S. A. Frey, G. D. Stucky and A. K. Cheetham, *J. Chem. Soc. Dalt. Trans.*, 2000, **29**, 4292–4296.

51 F. Serpaggi and G. Férey, *Inorg. Chem.*, 1999, **38**, 4741–4744.

52 D. A. Burwell and M. E. Thompson, *Chem. Mater.*, 2002, **3**, 14–17.

53 E. M. Sabbar, M. E. De Roy, A. Ennaqadi, C. Gueho and J. P. Besse, *Chem. Mater.*, 1998, **10**, 3856–3861.

54 E. M. Sabbar, M. E. De Roy and J. P. Besse, *Mater. Res. Bull.*, 1999, **34**, 1023–1037.

55 A. Distler and S. C. Sevov, *Chem. Commun.*, 1998, **34**, 959–960.

56 G. B. Hix, A. Turner, B. M. Kariuki, M. Tremayne and E. J. MacLean, *J. Mater. Chem.*, 2002, **12**, 3220–3227.

57 E. Fernández-Zapico, J. Montejo-Bernardo, A. Fernández-González, J. R. García and S. García-Granda, *J. Solid State Chem.*, 2015, **225**, 285–296.

58 G. B. Hix, A. Turner, L. Vahter and B. M. Kariuki, *Microporous Mesoporous Mater.*, 2007, **99**, 62–69.

59 C. Zhao, L. Male, T. Chen, J. A. Barker, I. J. Shannon and P. A. Anderson, *Chem. – A Eur. J.*, 2019, **25**, 13865–13868.

60 R. M. P. Colodrero, K. E. Papathanasiou, N. Stavgianoudaki, P. Olivera-Pastor, E. R. Losilla, M. A. G. Aranda, L. León-Reina, J. Sanz, I. Sobrados, D. Choquesillo-Lazarte, J. M. García-Ruiz, P. Atienzar, F. Rey, K. D. Demadis and A. Cabeza, *Chem. Mater.*, 2012, **24**, 3780–3792.

61 N. Stock and T. Bein, *Angew. Chemie Int. Ed.*, 2004, **43**, 749–752.

62 S. Bauer, T. Bein and N. Stock, *J. Solid State Chem.*, 2006, **179**, 145–155.

63 Z. Chen, Y. Zhou, L. Weng and D. Zhao, *Cryst. Growth Des.*, 2008, **8**, 4045–4053.

64 J. T. Li, D. K. Cao, T. Akutagawa and L. M. Zheng, *Dalt. Trans.*, 2010, **39**, 8606–8608.

65 J. T. Li, L. R. Guo, Y. Shen and L. M. Zheng, *CrystEngComm*, 2009, **11**, 1674–1678.

66 J. T. Li, D. K. Cao, B. Liu, Y. Z. Li and L. M. Zheng, *Cryst. Growth Des.*, 2008, **8**, 2950–2953.

67 N. Hermer, H. Reinsch, P. Mayer and N. Stock, *CrystEngComm*, 2016, **18**, 8147–8150.

68 P. Ramaswamy, N. E. Wong, B. S. Gelfand and G. K. H. Shimizu, *J. Am. Chem. Soc.*, 2015, **137**, 7640–7643.

69 M. Deng, X. Liu, Q. Zheng, Z. Chen, C. Fang, B. Yue and H. He, *CrystEngComm*, 2013, **15**, 7056–7061.

70 M. Deng, Y. Ling, B. Xia, Z. Chen, Y. Zhou, X. Liu, B. Yue and H. He, *Chem. – A Eur. J.*, 2011, **17**, 10323–10328.

71 Z. Chen, Y. Zhou, L. Weng, C. Yuan and D. Zhao, *Chem. – An Asian J.*, 2007, **2**, 1549–1554.

72 C. Heering, B. Nateghi and C. Janiak, *Crystals*, 2016, **6**, 22.

73 P. Garczarek, J. K. Zaręba, M. Duczmal, J. Janczak, J. Zoń, M. Samoć and M. Nyk, *Cryst. Growth Des.*, 2017, **17**, 1373–1383.

74 R. M. P. Colodrero, I. R. Salcedo, M. Bazaga-Garciá, A. Cuesta, E. R. Losilla, K. D. Demadis,

P. Olivera-Pastor and A. Cabeza, *Dalt. Trans.*, 2020, **49**, 3981–3988.

75 C. Liu, W. Yang, N. Qu, L. J. Li, Q. J. Pan and Z. M. Sun, *Inorg. Chem.*, 2017, **56**, 1669–1678.

76 Y. Y. Zhu, X. Zhang, Y. N. Zhou, Z. G. Sun and C. Q. Jiao, *Transit. Met. Chem.*, 2021, **46**, 593–600.

77 K. S. Park, Z. Ni, A. P. Côté, J. Y. Choi, R. Huang, F. J. Uribe-Romo, H. K. Chae, M. O'Keeffe and O. M. Yaghi, *Proc. Natl. Acad. Sci. U. S. A.*, 2006, **103**, 10186–10191.

78 N. Stock and S. Biswas, *Chem. Rev.*, 2011, **112**, 933–969.

79 L. Huang, H. Wang, J. Chen, Z. Wang, J. Sun, D. Zhao and Y. Yan, *Microporous Mesoporous Mater.*, 2003, **58**, 105–114.

80 D. J. Tranchemontagne, J. R. Hunt and O. M. Yaghi, *Tetrahedron*, 2008, **64**, 8553–8557.

81 J. Cravillon, S. Münzer, S. J. Lohmeier, A. Feldhoff, K. Huber and M. Wiebcke, *Chem. Mater.*, 2009, **21**, 1410–1412.

82 S. Bauer and N. Stock, *Angew. Chemie Int. Ed.*, 2007, **46**, 6857–6860.

83 F. Millange, R. El Osta, M. E. Medina and R. I. Walton, *CrystEngComm*, 2010, **13**, 103–108.

84 J. Klinowski, F. A. Almeida Paz, P. Silva and J. Rocha, *Dalt. Trans.*, 2010, **40**, 321–330.

85 T. Friščić, *J. Mater. Chem.*, 2010, **20**, 7599.

86 S. Noro, S. Kitagawa, M. Kondo and K. Seki, *Angewante Chemie Int. Ed.*, 2000, **39**, 2082–2084.

87 H. Furukawa, N. Ko, Y. B. Go, N. Aratani, S. B. Choi, E. Choi, A. Ö. Yazaydin, R. Q. Snurr, M. O'Keeffe, J. Kim and O. M. Yaghi, *Science*, 2010, **329**, 424–428.

88 O. K. Farha, A. Özgür Yazaydın, I. Eryazici, C. D. Malliakas, B. G. Hauser, M. G. Kanatzidis, S. T. Nguyen, R. Q. Snurr and J. T. Hupp, *Nat. Chem.*, 2010, **2**, 944–948.

89 B. Chen, X. Zhao, A. Putkham, K. Hong, E. B. Lobkovsky, E. J. Hurtado, A. J. Fletcher and K. M. Thomas, *J. Am. Chem. Soc.*, 2008, **130**, 6411–6423.

90 M. Kandiah, M. H. Nilsen, S. Usseglio, S. Jakobsen, U. Olsbye, M. Tilset, C. Larabi, E. A. Quadrelli, F. Bonino and K. P. Lillerud, *Chem. Mater.*, 2010, **22**, 6632–6640.

91 M. T. Kapelewski, T. Runčevski, J. D. Tarver, H. Z. H. Jiang, K. E. Hurst, P. A. Parilla, A. Ayala, T. Gennett, S. A. Fitzgerald, C. M. Brown and J. R. Long, *Chem. Mater.*, 2018, **30**, 8179–8189.

92 Mercedes-Benz F125! Research Vehicle Technology | eMercedesBenz, https://emercedesbenz.com/autos/mercedes-benz/concept-vehicles/mercedes-benz-f125-research-vehicle-technology/, (accessed 18 March 2022).

93 Z. Chen, M. R. Mian, S. J. Lee, H. Chen, X. Zhang, K. O. Kirlikovali, S. Shulda, P. Melix, A. S. Rosen, P. A. Parilla, T. Gennett, R. Q. Snurr, T. Islamoglu, T. Yildirim and O. K. Farha, *J. Am. Chem. Soc.*, 2021, **143**, 18838–18843.

94 S.-M. Wang, M. Shivanna and Q.-Y. Yang, *Angew. Chemie*, 2022, **134**, e202201017.

95 BASF Develops Method for Industrial-Scale MOF Synthesis; Trials Underway in Natural Gas Vehicle Tanks - Green Car Congress, https://www.greencarcongress.com/2010/10/basf-develops-method-for-industrial-scale-mof-synthesis-trials-underway-in-natural-gas-vehicle-tanks.html, (accessed 19 March 2022).

96 A. J. Rieth and M. Dinca, *J. Am. Chem. Soc.*, 2018, **140**, 3461–3466.

97 H. G. W. Godfrey, I. da Silva, L. Briggs, J. H. Carter, C. G. Morris, M. Savage, T. L. Easun, P. Manuel, C. A. Murray, C. C. Tang, M. D. Frogley, G. Cinque, S. Yang and M. Schröder, *Angew. Chemie*, 2018, **130**, 14994–14997.

98 S.-S. Bao, G. K. H. Shimizu and L.-M. Zheng, *Coord. Chem. Rev.*, 2019, **378**, 577–594.

99 Y. Nagao, R. Ikeda, S. Kanda, Y. Kubozono and H. Kitagawa, *Mol. Cryst. Liq. Cryst.*, 2002, **379**, 89–94.

100 A. Shigematsu, T. Yamada and H. Kitagawa, *J. Am. Chem. Soc.*, 2011, **133**, 2034–2036.

101 M. Sadakiyo, T. Yamada, K. Honda, H. Matsui and H. Kitagawa, *J. Am. Chem. Soc.*, 2014, **136**, 7701–7707.

102 M. A. Hickner, H. Ghassemi, Y. S. Kim, B. R. Einsla and J. E. McGrath, *Chem. Rev.*, 2004, **104**, 4587–4611.

103 Z. Chen, Z. Lv, Z. Lin, J. Chen, Y. Zhang, C. Wang, G. Qing, Y. Sun and Z. Chi, *J. Mater. Chem. B*, 2021, **9**, 638–647.

104 J. J. Liu, J. J. Fu, G. J. Li, T. Liu, S. B. Xia and F. X. Cheng, *CrystEngComm*, 2021, **23**, 7628–7634.

105 P. Kumar, A. Pournara, K.-H. H. Kim, V. Bansal, S. Rapti and M. J. Manos, *Prog. Mater. Sci.*, 2017, **86**, 25–74.

106 N. Hanikel, X. Pei, S. Chheda, H. Lyu, W. S. Jeong, J. Sauer, L. Gagliardi and O. M. Yaghi, *Science*, 2021, **374**, 454–459.

107 Q. Wang, J.-Y. Liu, T.-T. Wang, Y.-Y. Liu, L.-X. Zhang, J.-Z. Huo and B. Ding, *Spectrochim. Acta Part A Mol. Biomol. Spectrosc.*, 2022, **274**, 121132.

108 J. Lei, R. Qian, P. Ling, L. Cui and H. Ju, *TrAC Trends Anal. Chem.*, 2014, **58**, 71–78.

109 N. Panagiotou, K. Evangelou, A. Psalti, N. Varnava, G. K. Angeli, P. N. Trikalitis, J. C. Plakatouras, T. Lazarides and A. J. Tasiopoulos, *Mol. Syst. Des. Eng.*, 2020, **5**, 1077–1087.

110 J.-Y. Yeh, S. S. Chen, S. Li, C. H. Chen, T. Shishido, D. C. W. Tsang, Y. Yamauchi, Y.-P. Li and K. C.-W. Wu, *Angew. Chemie*, 2021, **133**, 634–639.

111 J. Lee, O. K. Farha, J. Roberts, K. A. Scheidt, S. T. Nguyen and J. T. Hupp, *Chem. Soc. Rev.*, 2009, **38**, 1450–1459.

112 G. R. F. Orton, B. S. Pilgrim and N. R. Champness, *Chem. Soc. Rev.*, 2021, **50**, 4411–4431.

113 S. Bai, X. Liu, K. Zhu, S. Wu and H. Zhou, *Nat. Energy*, 2016, **1**, 16094.

114 X. Wen, Q. Zhang and J. Guan, *Coord. Chem. Rev.*, 2020, **409**, 213214.

115 C. Zhao, *PhD Thesis*, University of Birmingham, 2012.

116 A. Karmakar, A. V. Desai and S. K. Ghosh, *Coord. Chem. Rev.*, 2016, **307**, 313–341.

117 M. Williams, *Master's Dissertation*, University of Birmingham, 2016.

118 J. A. Barker, *Master's Dissertation*, University of Birmingham, 2018.

119 E. Lewis, *Master's Dissertation*, University of Birmingham, 2015.

120 M. M. Gómez-Alcantara, M. A. G. G. Aranda, P. Olivera-Pastor, P. Beran, J. L. García-Muñoz and A. Cabeza, *Dalt. Trans.*, 2006, 577–585.

121 P. Feng, X. Bu and G. D. Stucky, *Nature*, 1997, **388**, 735–741.

122 R. E. Dinnebier and S. J. L. Billinge, *Powder Diffraction Theory and Practice*, Royal Society of Chemistry, Cambridge, 2008.

123 W. Massa, *Crystal Structure Determination*, Springer, Berlin, Second Eng., 2004.

124 Vitalij K. Pecharsky and Peter Y. Zavalij, *Fundamentals of Powder Diffraction and Structural Characterization of*, Springer, 2008.

125 B. H. Toby and R. B. Von Dreele, *J. Appl. Crystallogr.*, 2013, **46**, 544–549.

126 A. A. Coelho, *J. Appl. Crystallogr.*, 2003, **36**, 86–95.

127 G. S. Pawley, *J. Appl. Crystallogr.*, 1981, **14**, 357–361.

128 A. Coelho, *TOPAS Academic (Version 6)*, Coelho Software, Brisbane, 2018.

129 H. M. Rietveld, *J. Appl. Crystallogr.*, 1969, **2**, 65–71.

130 Goodhew, *J. Microsc.*, 1998, **190**, 392–393.

131 B. H. Toby, *Powder Diffr.*, 2006, **21**, 67–70.

132 G. M. Sheldrick, *Acta Crystallogr. A*, 2015, **71**, 3–8.

133 O. V. Dolomanov, L. J. Bourhis, R. J. Gildea, J. A. K. Howard and H. Puschmann, *J. Appl. Crystallogr.*, 2009, **42**, 339–341.

134 G. M. Sheldrick, *Acta Crystallogr. C*, 2015, **71**, 3–8.

135 D. A. Keen, *J. Appl. Crystallogr.*, 2001, **34**, 172–177.

136 M. Thommes, K. Kaneko, A. V. Neimark, J. P. Olivier, F. Rodriguez-Reinoso, J. Rouquerol and K. S. W. Sing, *Pure Appl. Chem.*, 2015, **87**, 1051–1069.

137 J. Rouquerol, P. Llewellyn and F. Rouquerol, *Stud. Surf. Sci. Catal.*, 2007, **160**, 49–56.

138 B. F. C Kracek, *J. Phys. Chem*, 1932, **33**, 23.

139 P.-H. C. Heubel and A. I. Popov, *J. Solution Chem.*, 1979, **8**, 615–625.

140 M. EL Kassaoui, M. Lakhal, A. Benyoussef, A. El Kenz and M. Loulidi, *J. Alloys Compd.*, 2021, **874**, 159902.

141 A. F. Sapnik, H. S. Geddes, E. M. Reynolds, H. H. M. Yeung and A. L. Goodwin, *Chem. Commun.*, 2018, **54**, 9651–9654.

142 K. W. P. Orr, S. M. Collins, E. M. Reynolds, F. Nightingale, H. L. B. Boström, S. J. Cassidy, D. M. Dawson, S. E. Ashbrook, O. V. Magdysyuk, P. A. Midgley, A. L. Goodwin and H. H. M. Yeung, *Chem. Sci.*, 2021, **12**, 4494–4502.

143 P. M. de Wolff, *J. Appl. Crystallogr.*, 1968, **1**, 108–113.

144 X. Zhang, F. Rösicke, V. Syritski, G. Sun, J. Reut, K. Hinrichs, S. Janietz and J. Rappich, *Zeitschrift für Phys. Chemie*, 2014, **228**, 557–573.

145 J. E. Mondloch, O. Karagiaridi, O. K. Farha and J. T. Hupp, *CrystEngComm*, 2013, **15**, 9258.

146 T. Islamoglu, Z. Chen, M. C. Wasson, C. T. Buru, K. O. Kirlikovali, U. Afrin, M. R. Mian and O. K. Farha, *Chem. Rev.*, 2020, **120**, 8130–8160.

147 L. X. Dang, *Chem. Phys. Lett.*, 1993, **213**, 541–546.

148 M. Sadakiyo, T. Yamada and H. Kitagawa, *Chempluschem*, 2016, **81**, 691–701.

149 U. Afrin, M. R. Mian, K. I. Otake, R. J. Drout, L. R. Redfern, S. Horike, T. Islamoglu and O. K. Farha, *Inorg. Chem.*, 2021, **60**, 1086–1091.

150 Y. Sone, P. Ekdunge and D. Simonsson, *J. Electrochem. Soc.*, 1996, **143**, 1254–1259.

151 D. J. Ashworth and J. A. Foster, *J. Mater. Chem. A*, 2018, **6**, 16292–16307.

152 B. M. Connolly, D. G. Madden, A. E. H. Wheatley and D. Fairen-Jimenez, *J. Am. Chem. Soc.*, 2020, **142**, 8541–8549.

153 S. R. Batten, N. R. Champness, X.-M. Chen, J. Garcia-Martinez, S. Kitagawa, L. Öhrström, M. O'Keeffe, M. Paik Suh and J. Reedijk, *Pure Appl. Chem.*, 2013, **85**, 1715–1724.

154 S. B. Hendricks, E. Posnjak and F. C. Kracek, *J. Am. Chem. Soc.*, 2002, **54**, 2766–2786.

155 C. Calvo, *Can. J. Chem.*, 1965, **43**, 1139–1146.

156 H. Li, M. Eddaoudi, T. L. Groy and O. M. Yaghi, *Angew. Chem., Int. Ed. Engl*, 1998, **33**, 8571–8572.

157 K.-R. Ma, C.-L. Wei, Y. Zhang, Y.-H. Kan, M.-H. Cong and X.-J. Yang, *J. Spectrosc.*, 2013, **2013**, 1–9.

158 J.-H. Hong, S.-W. Song and S.-T. Hong, *Acta Crystallogr. C*, 2011, **67**, i1–i3.

159 K. Dong, J. Liang, Y. Wang, L. Zhang, Z. Xu, S. Sun, Y. Luo, T. Li, Q. Liu, N. Li, B. Tang, A. A. Alshehri, Q. Li, D. Ma and X. Sun, *ACS Catal.*, 2022, **10**, 6092–6099.

160 R. G. Franz, *AAPS PharmSci*, 2001, **3**, 1–13.

161 O. K. Farha, I. Eryazici, N. C. Jeong, B. G. Hauser, C. E. Wilmer, A. A. Sarjeant, R. Q. Snurr, S. T. Nguyen, A. Ö. Yazaydın and J. T. Hupp, *J. Am. Chem. Soc.*, 2012, **134**, 15016–15021.

162 Y. Marcus, *Chem. Rev.*, 1988, **88**, 1475–1498.

163 S. Yuan, J. Peng, B. Cai, Z. Huang, A. T. Garcia-Esparza, D. Sokaras, Y. Zhang, L. Giordano, K. Akkiraju, Y. G. Zhu, R. Hübner, X. Zou, Y. Román-Leshkov and Y. Shao-Horn, *Nat. Mater.*, 2022, **21**, 673–680.

10 Appendix

Crystallographic Details

HT-BIRM-1 Crystallographic Details from Zhao

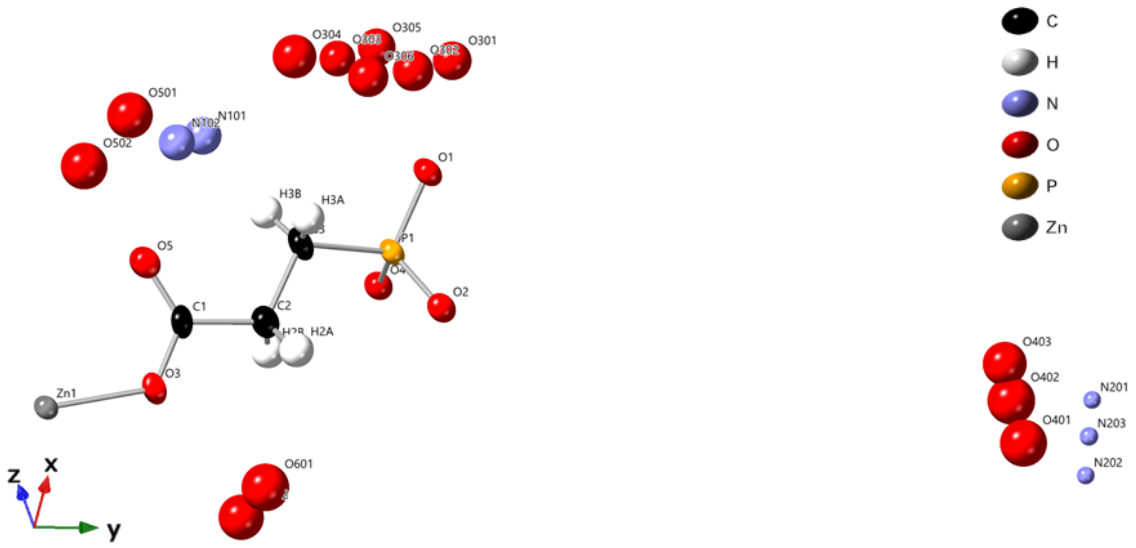

Figure 10.1) Asymmetric unit of BIRM-1 as reported by Zhao. Ellipsoids drawn to 50% probability level.

Table 10.1) Crystal data and structure refinement for BIRM-1 from Zhao's work

Identification code	BIRM-1
Empirical formula	$C_3H_{13}NO_{7.5}PZn$
Formula weight	279.48
Temperature/K	120(2)
Crystal system	tetragonal
Space group	$I4_1/acd$
a/Å	22.3019(17)
b/Å	22.3019(17)
c/Å	17.7384(11)
α/°	90
β/°	90
γ/°	90
Volume/Å^3	8822.6(11)
Z	32
ρ_{calc}g/cm^3	1.683
μ/mm^{-1}	2.385
F(000)	4576
Crystal size/mm^3	0.3 × 0.06 × 0.05
Radiation	MoKα (λ = 0.71073)
2Θ range for data collection/°	5.86 to 55.02
Index ranges	$-28 \leq h \leq 22,\ -28 \leq k \leq 16,\ -22 \leq l \leq 23$
Reflections collected	20693
Independent reflections	2541 [R_{int} = 0.0828, R_{sigma} = 0.0554]
Data/restraints/parameters	2541/0/159
Goodness-of-fit on F^2	1.099
Final R indexes [I>=2σ (I)]	R_1 = 0.0718, wR_2 = 0.1649
Final R indexes [all data]	R_1 = 0.1110, wR_2 = 0.1889
Largest diff. peak/hole / e Å^{-3}	0.78/-0.59

Table 10.2) Fractional Atomic Coordinates ($\times 10^4$) and Equivalent Isotropic Displacement Parameters ($Å^2 \times 10^3$) for BIRM-1 from Zhao's work

Atom	X	Y	Z	U(eq)
C1	3057(3)	2338(3)	1694(4)	27.0(15)
C2	3031(3)	3018(3)	1788(4)	31.6(16)
H2A	3076	3205	1285	38
H2B	2628	3127	1980	38
C3	3495(3)	3285(3)	2308(4)	29.4(15)
H3A	3896	3252	2073	35
H3B	3501	3058	2787	35
O1	3853(2)	4313(2)	2956(3)	28.4(11)
O2	3270(2)	4381(2)	1739(3)	31.7(11)
O3	2658(3)	2133(2)	1256(3)	49.5(17)
O4	2738(2)	4093(2)	2917(3)	25.8(10)
O5	3410(3)	2026(2)	2047(4)	47.0(15)
P1	3333.3(7)	4060.7(7)	2498.1(10)	24.1(4)
Zn1	2496.5(4)	1281.2(3)	1143.3(4)	23.0(2)
N101	4672(14)	2285(15)	2062(18)	46(8)
N102	4684(14)	2062(15)	1919(17)	42(7)
N201	2923(6)	9577(6)	1250	10(4)
N202	2683(11)	9473(11)	425(15)	10(5)
N203	2803(13)	9528(14)	859(17)	11(6)
O301	5098(12)	4285(15)	2733(14)	48(6)
O302	5047(16)	3970(20)	2630(20)	53(9)
O303	4776(13)	3473(16)	3219(17)	41(7)
O304	4840(20)	3110(20)	3120(20)	61(12)
O305	4980(30)	3740(30)	3090(40)	46(16)
O306	4920(30)	3640(30)	2710(40)	52(17)
O401	3272(10)	8829(9)	-56(13)	71(6)
O402	3455(17)	8744(15)	320(20)	73(9)
O403	3680(30)	8680(20)	540(30)	62(15)
O501	3972(13)	1974(13)	3482(16)	67(7)
O502	3400(20)	1710(20)	3570(30)	70(13)
O601	2500	2905(13)	0	73(7)
O602	2110(40)	2790(30)	140(40)	66(19)

Table 10.3) Anisotropic Displacement Parameters ($Å^2 \times 10^3$) for BIRM-1 from Zhao's work

Atom	U_{11}	U_{22}	U_{33}	U_{23}	U_{13}	U_{12}
C1	41(4)	17(3)	23(3)	1(3)	2(3)	-7(3)
C2	35(4)	24(3)	36(4)	-5(3)	-2(3)	-2(3)
C3	36(4)	20(3)	32(4)	-10(3)	0(3)	-6(3)
O1	24(2)	23(2)	38(3)	-10(2)	-5(2)	-0.4(19)
O2	37(3)	28(3)	30(3)	0(2)	-7(2)	-7(2)
O3	76(4)	19(2)	53(3)	-2(2)	-36(3)	-12(3)
O4	25(2)	25(2)	27(2)	-4(2)	-0.1(19)	-0.3(19)
O5	47(3)	25(3)	69(4)	-11(3)	-24(3)	3(2)
P1	24.3(8)	19.1(8)	28.8(8)	-6.4(7)	-4.3(7)	-3.0(6)
Zn1	20.5(4)	18.1(4)	30.5(4)	-2.9(3)	-6.1(3)	-0.8(3)

Table 10.4) Atomic Occupancies for BIRM-1 from Zhao's work

Atom	Occupancy	Atom	Occupancy	Atom	Occupancy
N101	0.25	N102	0.25	N201	0.35
N202	0.18	N203	0.15	O301	0.25
O302	0.2	O303	0.2	O304	0.15
O305	0.1	O306	0.1	O401	0.38
O402	0.27	O403	0.15	O501	0.25
O502	0.15	O601	0.4	O602	0.1

HT-BIRM-1 (refined)

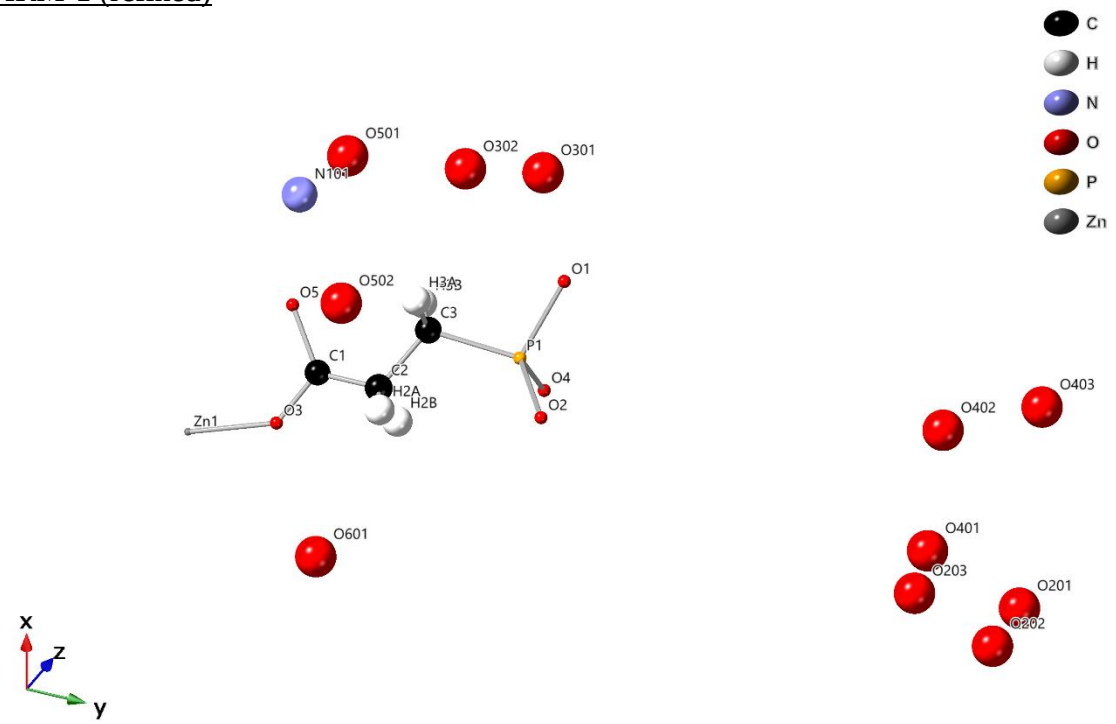

Figure 10.2) Asymmetric unit of HT-BIRM-1 from the Rietveld refinement conducted in this work. Ellipsoids draw to 50% probability level.

Table 10.5) Crystal data and structure refinement for HT-BIRM-1

Identification code	HT-BIRM-1
Empirical formula	$C_3H_{13}NO_{9.4}PZn$
Formula weight	317.31
Temperature/K	120
Crystal system	tetragonal
Space group	$I4_1/acd$
a/Å	22.3196(5)
b/Å	22.3196(5)
c/Å	17.7629(8)
α/°	90
β/°	90
γ/°	90
Volume/Å^3	8848.8(8)
Z	32
ρ_{calc}g/cm^3	1.8093
Radiation	CuKα1 (λ = 1.5406)
2θ range for data collection/°	5 to 50
Goodness-of-fit	3.348
Final R index	Rwp = 2.31

Table 10.6) Fractional Atomic Coordinates ($\times 10^4$) and Equivalent Isotropic Displacement Parameters ($Å^2 \times 10^3$) for refined HT-BIRM-1

Atom	X	Y	Z	U(eq)
C1	3103	2359	1716	27
C2	3100	2955	1698	31.6
H2A	3145	3142	1195	38
H2B	2697	3064	1890	38
C3	3484	3212	2320	29.4
H3A	3885	3179	2085	35
H3B	3490	2985	2799	35
O1	3987	4305	2929	9.44(674)
O2	3203	4532	1664	9.44(674)
O3	2699	2106	1314	9.44(674)
O4	2811	4107	2936	9.44(674)
O5	3583	2015	2011	9.44(674)
P1	3355	4053	2435	17.66(683)
Zn1	2482	1310	1153	10.30(341)
N101	4747	2089	1994	68.72(1854)
O201	2774	9400	940	67.40(960)
O202	2609	9335	394	67.40(960)
O203	3313	8815	-251	67.40(960)
O301	5140	4158	2774	67.40(960)
O302	4827	3298	3087	67.40(960)
O401	3416	8696	435	67.40(960)
O402	4095	8445	1559	67.40(960)
O403	4456	9323	1776	67.40(960)
O501	4375	1960	3653	67.40(960)
O502	2939	1961	3468	67.40(960)
O601	2130	2962	-24	67.40(960)

Table 10.7) Atomic Occupancies for refined HT-BIRM-1

Atom	Occupancy	Atom	Occupancy	Atom	Occupancy
O201	0.47029	O202	0.45233	O203	0.32049
O301	0.64087	O302	0.80077	O401	0.45367
O402	0.25953	O403	0.12459	O501	0.20733
O502	0.24248	O601	0.45805		

RT-BIRM-1

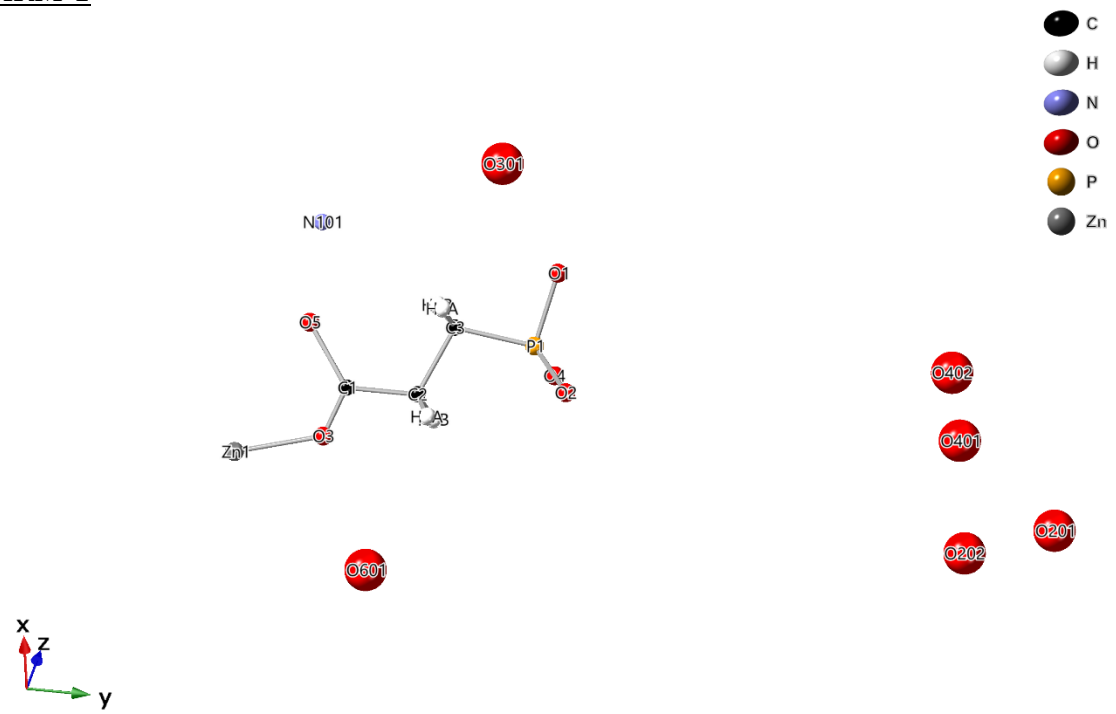

Figure 10.3 Asymmetric unit of RT-BIRM-1 from the Rietveld refinement conducted in this work. Ellipsoids draw to 50% probability level. Other than framework oxygen, phosphorous and zinc for which thermal parameters refined to very low levels

Table 10.8) Crystal data and structure refinement for RT-BIRM-1

Identification code	RT-BIRM-1
Empirical formula	$C_3H_{13}NO_{8.4}PZn$
Formula weight	299.30
Temperature/K	120
Crystal system	tetragonal
Space group	$I4_1/acd$
a/Å	22.2433(10)
b/Å	22.3433(10)
c/Å	17.85066(15)
α/°	90
β/°	90
γ/°	90
Volume/Å^3	8831.9(11)
Z	32
ρ_{calc}g/cm^3	1.7108
Radiation	CuKα1 (λ = 1.5406)
2θ range for data collection/°	5 to 50
Goodness-of-fit	3.474
Final R index	Rwp = 2.25

Table 10.9) Fractional Atomic Coordinates ($\times 10^4$) and Equivalent Isotropic Displacement Parameters ($Å^2 \times 10^3$) for refined RT-BIRM-1

Atom	X	Y	Z	U(eq)
C1	3072.5	2343.9	1705.2	12.98(2375)
C2	3025.2	3020.3	1783.7	12.98(2375)
H2A	3076	3205	1285	15.58
H2B	2628	3127	1980	15.58
C3	3524.4	3309.7	2336.8	12.98(2375)
H3A	3896	3252	2073	15.58
H3B	3501	3058	2787	15.58
O1	3917.6	4221.7	2943.5	0.304(11501)
O2	3231.8	4478.6	1752.7	0.304(11501)
O3	2703.2	2170.6	1323.4	0.304(11501)
O4	2724.8	4145.2	2899.3	0.304(11501)
O5	3544.5	1933.4	2136.4	0.304(11501)
P1	3327	4056.7	2451.6	0.009(12383)
Zn1	2519.3	1327.5	1158.3	0.009(6009)
N101	4777.2	2115.8	2085.6	12.68(1754)
O201	2661.6	9358.6	908.9	85.49(1802)
O202	2547.4	8552.7	486.2	85.49(1802)
O301	5047	3701.4	3117.9	85.49(1802)
O401	3762	8526	676.3	85.49(1802)
O402	4181.9	8359.9	1299.4	85.49(1802)
O601	1784.2	2721.8	299.7	85.49(1802)

Table 10.10) Atomic Occupancies for refined RT-BIRM-1

Atom	Occupancy	Atom	Occupancy	Atom	Occupancy
O201	0.83782	O202	0.25528	O301	0.7113
O401	0.51456	O402	0.37991	O601	0.6724

BIRM-6

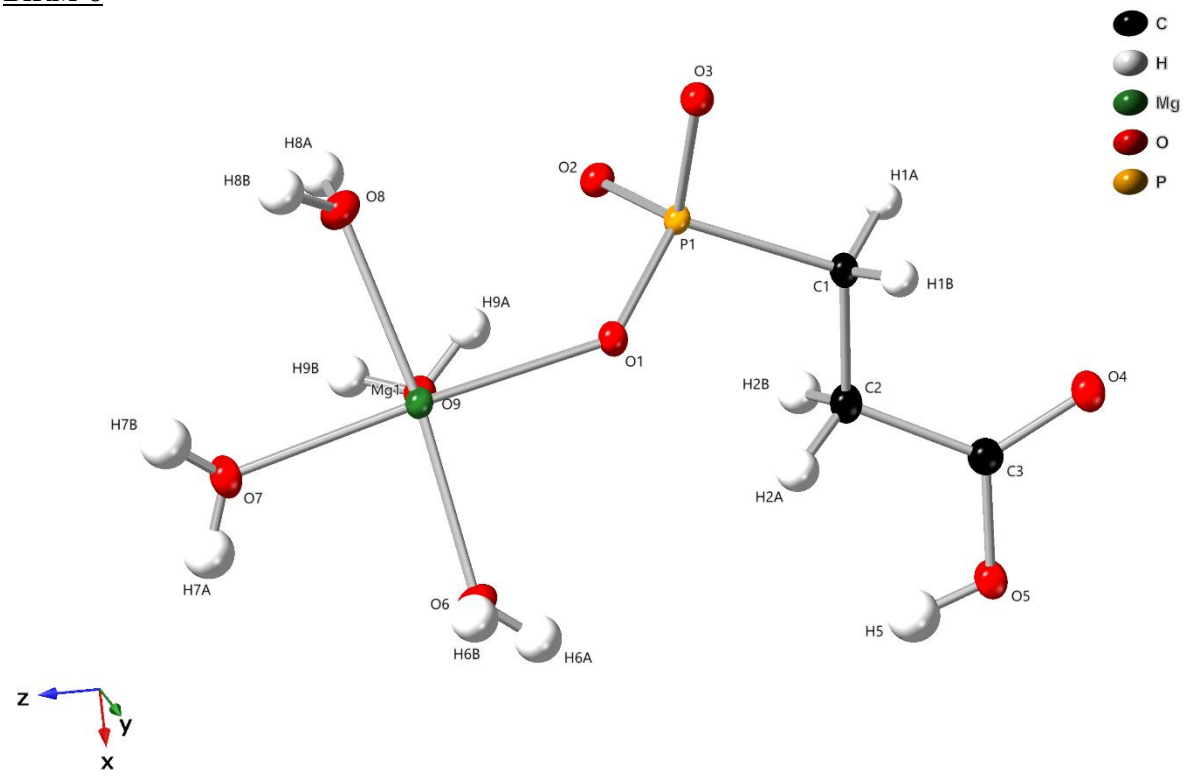

Figure 10.4) Asymmetric unit of BIRM-6. Ellipsoids drawn at 50% probability level.

Table 10.11) Crystal data and structure refinement for BIRM-6

Identification code	BIRM-6
Empirical formula	$C_3H_{13}MgO_9P$
Formula weight	248.41
Temperature/K	100.01(10)
Crystal system	monoclinic
Space group	*P*21/*n*
a/Å	6.69070(10)
b/Å	7.54360(10)
c/Å	19.4168(4)
α/°	90
β/°	99.449(2)
γ/°	90
Volume/Å^3	966.71(3)
Z	4
ρcalc g/cm^3	1.707
μ/mm^{-1}	3.519
F(000)	520.0
Crystal size/mm^3	0.137 × 0.052 × 0.011
Radiation	Cu Kα (λ = 1.54184)
2Θ range for data collection/°	9.234 to 147.18
Index ranges	$-8 \leq h \leq 8,\ -9 \leq k \leq 9,\ -24 \leq l \leq 24$
Reflections collected	32617
Independent reflections	1942 [R_{int} = 0.0521, R_{sigma} = 0.0159]
Data/restraints/parameters	1942/1/154
Goodness-of-fit on F^2	1.076
Final R indexes [I>=2σ (I)]	R_1 = 0.0288, wR_2 = 0.0762
Final R indexes [all data]	R_1 = 0.0319, wR_2 = 0.0785
Largest diff. peak/hole / e Å^{-3}	0.45/-0.37

Table 10.12) Fractional Atomic Coordinates ($\times 10^4$) and Equivalent Isotropic Displacement Parameters ($Å^2 \times 10^3$) for BIRM-6

Atom	X	Y	Z	U(eq)
C1	2887(2)	7215(2)	5656.8(9)	12.8(3)
H1A	2269.99	6370.47	5309.04	15
H1B	2442.64	8390.98	5497.72	15
C2	5181(3)	7107(3)	5715.6(9)	16.4(4)
H2A	5794.73	7846.16	6101.67	20
H2B	5602.84	5894.38	5824.22	20
C3	5970(3)	7676(2)	5065.1(9)	15.8(4)
P1	2023.3(6)	6765.1(6)	6471.1(2)	9.59(13)
Mg1	4174.4(8)	7653.1(7)	8069.0(3)	10.38(15)
O1	3247.1(17)	7944.1(15)	7022.1(6)	11.9(3)
O2	2338.5(17)	4817.3(16)	6654.2(6)	12.5(3)
O3	-247.5(17)	7276.0(16)	6347.9(6)	12.7(3)
O4	4875.0(18)	7973.4(19)	4507.0(7)	20.2(3)
O5	7953.3(18)	7824.6(19)	5128.3(7)	20.1(3)
H5	8520(40)	7670(30)	5548(10)	30
O6	6691.0(19)	9258.4(18)	8063.7(7)	16.0(3)
H6A	7320(40)	9400(30)	7774(14)	24
H6B	6340(30)	10350(30)	8210(12)	24
O7	5505(2)	6938.8(19)	9071.5(7)	18.6(3)
H7A	6710(40)	7020(30)	9218(14)	28
H7B	4870(40)	6900(30)	9368(14)	28
O8	1537.1(18)	6388.9(18)	8231.0(7)	15.1(3)
H8A	1510(30)	5310(40)	8192(12)	23
H8B	980(40)	6650(30)	8568(14)	23
O9	5421.0(18)	5175.8(17)	7777.0(7)	12.9(3)
H9A	4570(40)	4890(30)	7441(13)	19
H9B	5470(30)	4380(30)	8062(13)	19

Table 10.13) Anisotropic Displacement Parameters ($Å^2 \times 10^3$) for BIRM-6

Atom	U11	U22	U33	U23	U13	U12
C1	11.7(8)	18.8(8)	8.3(8)	0.5(6)	2.7(6)	0.1(6)
C2	13.1(8)	26.0(9)	10.9(8)	2.1(7)	4.0(6)	1.3(7)
C3	12.8(8)	22.5(9)	12.6(8)	-0.4(7)	3.6(6)	-0.2(7)
Mg1	10.4(3)	13.1(3)	8.0(3)	0.1(2)	2.6(2)	-0.1(2)
P1	9.2(2)	12.5(2)	7.6(2)	0.50(15)	2.88(15)	-0.06(14)
O1	13.5(5)	13.4(6)	8.8(6)	0.0(4)	1.9(4)	-0.1(5)
O2	12.8(5)	12.2(6)	12.9(6)	0.2(5)	3.6(4)	-0.3(4)
O3	10.0(5)	16.6(6)	11.8(6)	0.6(5)	2.6(4)	1.2(4)
O4	14.3(6)	34.9(8)	11.6(6)	2.8(5)	2.8(5)	0.0(5)
O5	11.5(6)	38.0(8)	11.0(6)	3.2(6)	2.7(5)	-0.1(5)
O6	14.0(6)	18.9(7)	16.9(6)	-2.5(5)	8.1(5)	-2.3(5)
O7	15.3(6)	31.2(8)	9.6(6)	1.0(5)	2.5(5)	1.8(5)
O8	17.4(6)	13.8(6)	16.3(6)	-2.8(5)	9.0(5)	-1.5(5)
O9	12.2(6)	15.2(6)	11.6(6)	1.4(5)	2.5(5)	0.5(5)

BIRM-7

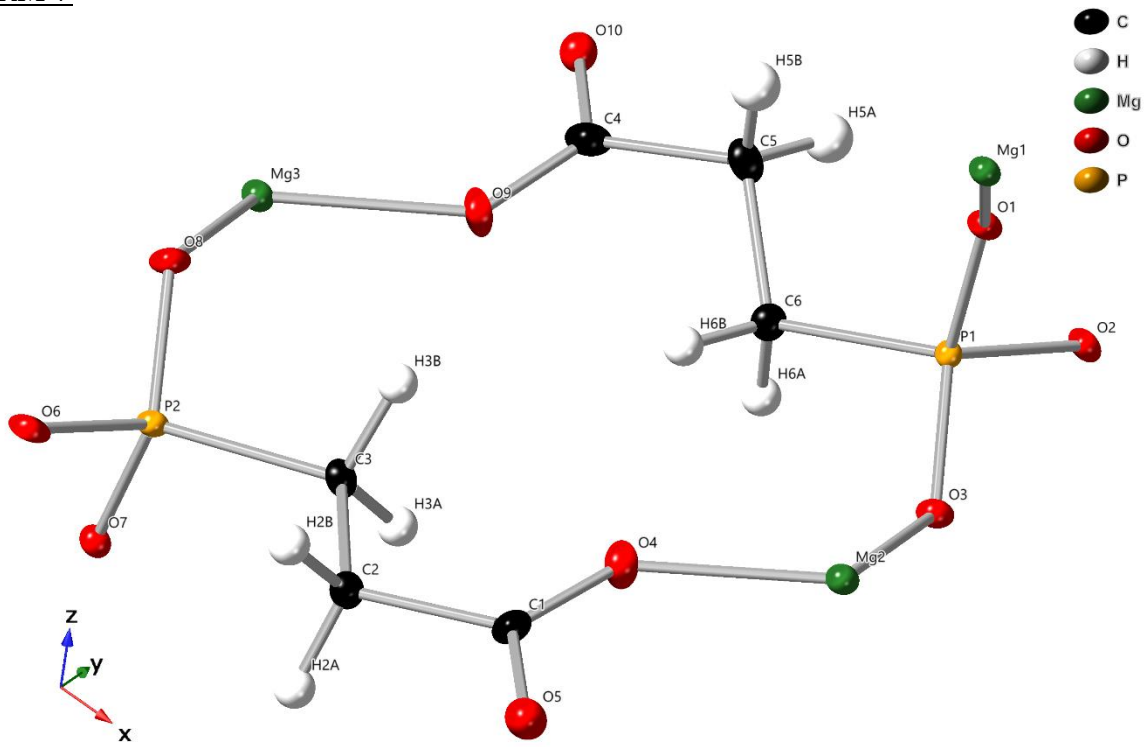

Figure 10.5) Asymmetric unit of BIRM-7. Ellipsoids drawn to 50% probability levels.

Table 10.14) Crystal data and structure refinement for BIRM-7

Identification code	BIRM-7
Empirical formula	$C_6H_8Mg_3O_{10}P_2$
Formula weight	374.99
Temperature/K	100.15
Crystal system	monoclinic
Space group	*P*21
a/Å	8.1016(3)
b/Å	9.0014(3)
c/Å	9.0443(4)
α/°	90
β/°	107.744(4)
γ/°	90
Volume/Å^3	628.19(4)
Z	2
ρcalc g/cm^{-3}	1.983
μ/mm^{-1}	5.150
F(000)	380.0
Radiation	CuKα (λ = 1.54184)
2Θ range for data collection/°	10.27 to 145.636
Index ranges	$-10 \leq h \leq 9,\ -11 \leq k \leq 11,\ -10 \leq l \leq 10$
Reflections collected	10071
Independent reflections	2456 [R_{int} = 0.0263, R_{sigma} = 0.0194]
Data/restraints/parameters	2456/2/191
Goodness-of-fit on F^2	1.078
Final R indexes [I>=2σ (I)]	R_1 = 0.0478, wR_2 = 0.1234
Final R indexes [all data]	R_1 = 0.0487, wR_2 = 0.1244
Largest diff. peak/hole / e Å^{-3}	1.77/-0.70
Flack parameter	0.18(6)

Table 10.15) Fractional Atomic Coordinates ($\times 10^4$) and Equivalent Isotropic Displacement Parameters ($Å^2 \times 10^3$) for BIRM-7

Atom	X	Y	Z	U(eq)
C1	6636(7)	1824(7)	1911(7)	9.3(12)
C2	4669(7)	1644(7)	1270(7)	11.4(12)
H2A	4358.27	1365.95	159.56	14
H2B	4303.1	822.61	1827.81	14
C3	3683(7)	3053(8)	1428(7)	10.9(12)
H3A	4046.35	3859.51	850.53	13
H3B	4043.01	3341.79	2536.33	13
C4	3491(7)	8106(8)	3195(7)	11.3(12)
C5	5430(7)	8097(8)	4048(7)	16.3(14)
H5A	5860.2	9133.27	4178.78	20
H5B	5626.65	7666.91	5094.85	20
C6	6450(7)	7220(7)	3203(6)	11.2(12)
H6A	6267.98	7672.6	2167.86	13
H6B	5978.78	6197.72	3038.55	13
Mg1	9889(2)	5015(3)	7459(2)	7.1(4)
Mg2	9576(2)	3731(2)	3401(2)	7.5(4)
Mg3	522(2)	6283(2)	1569(2)	7.8(5)
O1	9129(5)	6719(5)	5889(4)	7.5(8)
O2	9581(5)	8658(5)	4212(4)	8.2(8)
O3	9448(5)	5960(5)	3270(5)	9.2(9)
O4	7209(5)	3085(6)	2461(5)	13.9(10)
O5	7537(5)	716(5)	1815(5)	12.2(9)
O6	676(5)	1378(5)	853(4)	10.7(9)
O7	710(5)	3297(5)	-971(5)	8.9(9)
O8	697(5)	4078(5)	1723(5)	8.9(9)
O9	2901(5)	6909(6)	2503(5)	14.4(10)
O10	2638(5)	9236(5)	3261(5)	11.7(9)
P1	8733.9(16)	7114.6(16)	4170.6(15)	6.6(4)
P2	1363.4(16)	2940.8(16)	757.0(15)	6.9(4)

Table 10.16) Anisotropic Displacement Parameters ($Å^2 \times 10^3$) for BIRM-7

Atom	U11	U22	U33	U23	U13	U12
C1	11(3)	6(3)	12(3)	3(2)	6(2)	2(2)
C2	8(2)	9(3)	16(3)	-4(2)	3(2)	2(2)
C3	6(2)	14(3)	10(3)	-2(2)	-1.6(19)	2(2)
C4	16(3)	11(3)	8(3)	2(2)	4(2)	4(2)
C5	13(3)	17(4)	17(3)	-7(2)	2(2)	-3(2)
C6	8(2)	14(3)	12(3)	-1(2)	1.8(19)	2(2)
Mg1	9.1(7)	5.4(7)	6.5(7)	-0.1(5)	2.0(5)	0.0(6)
Mg2	8.5(9)	6.4(10)	7.3(9)	0.5(8)	1.9(7)	1.6(7)
Mg3	9.4(9)	5.6(11)	8.1(10)	-0.2(8)	2.2(7)	0.0(7)
O1	9.0(17)	6(2)	6.7(19)	-0.3(15)	1.3(13)	2.4(15)
O2	12.2(18)	4.3(17)	7.6(19)	-0.7(16)	2.0(15)	-1.8(15)
O3	12.6(18)	7(2)	8.6(19)	-0.8(17)	4.7(15)	0.3(16)
O4	10.5(19)	9(3)	21(2)	-2.2(18)	3.1(16)	-1.1(17)
O5	13.0(18)	8(2)	14(2)	0.4(18)	2.7(15)	3.0(17)
O6	14.1(19)	13(2)	4.4(19)	-1.4(17)	1.8(15)	1.7(17)
O7	9.6(17)	9(2)	8(2)	-1.1(15)	2.1(14)	-1.6(15)
O8	13.9(19)	6(2)	8.4(19)	1.0(16)	6.6(15)	1.7(16)
O9	10.9(19)	9(3)	21(2)	-5.7(18)	1.8(16)	-4.1(17)
O10	10.0(18)	12(2)	13(2)	-0.1(19)	2.4(15)	1.2(17)
P1	6.7(6)	7.3(8)	5.9(7)	-0.1(5)	2.0(5)	-1.2(5)
P2	7.9(6)	5.9(8)	7.0(7)	-0.9(6)	2.4(5)	1.8(5)

BIRM-8

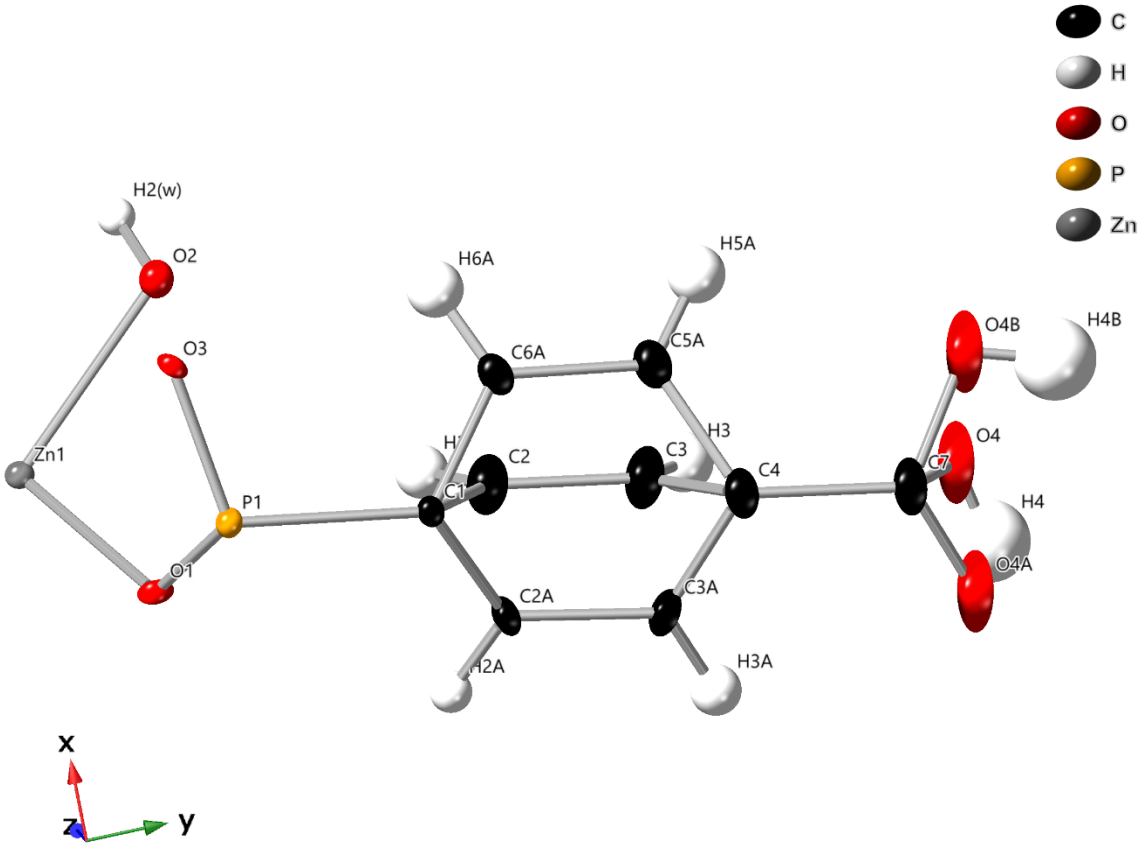

Figure 10.6) Asymmetric unit of BIRM-8. Ellipsoids drawn to 50% probability levels

Table 10.17) Crystal data and structure refinement for BIRM-8

Identification code	BIRM-8
Empirical formula	$C_7H_7O_6PZn$
Formula weight	283.47
Temperature/K	100.00(10)
Crystal system	orthorhombic
Space group	*Pnnm*
a/Å	4.7698(3)
b/Å	38.0812(15)
c/Å	5.6235(4)
α/°	90
β/°	90
γ/°	90
Volume/Å^3	1021.45(11)
Z	4
ρcalc g/cm^{-3}	1.843
μ/mm^{-1}	4.945
F(000)	568.0
Crystal size/mm	0.356 × 0.07 × 0.023
Radiation	Cu Kα (λ = 1.54184)
2Θ range for data collection/°	9.29 to 145.752
Index ranges	$-3 \leq h \leq 5,\ -46 \leq k \leq 47,\ -6 \leq l \leq 6$
Reflections collected	8921
Independent reflections	1107 [R_{int} = 0.0485, R_{sigma} = 0.0256]
Data/restraints/parameters	1107/40/125
Goodness-of-fit on F^2	1.231
Final R indexes [I>=2σ (I)]	R_1 = 0.0522, wR_2 = 0.1161
Final R indexes [all data]	R_1 = 0.0550, wR_2 = 0.1170
Largest diff. peak/hole / e Å^{-3}	0.91/-1.46

Table 10.18) Fractional Atomic Coordinates ($\times 10^4$) and Equivalent Isotropic Displacement Parameters ($Å^2 \times 10^3$) for BIRM-8

Atom	X	Y	Z	U(eq)
C(1)	7211(15)	3403.6(16)	5000	10.0(14)
C(2)	6980(20)	3581(2)	7136(19)	20(2)
H(2)	7144.96	3461.11	8568.01	24
C(3)	6480(30)	3944(2)	7130(20)	25(2)
H(3)	6277.41	4063.94	8556.58	30
C(2A)	4780(40)	3544(4)	5870(40)	12(4)
H(2A)	3452.36	3395.33	6548.16	15
C(2B)	9270(50)	3628(5)	5880(40)	22(5)
H(2B)	10959.68	3536.08	6417.75	27
C(3A)	4220(40)	3908(5)	5790(40)	19(5)
H(3A)	2489.77	3997.17	6249.59	22
C(3B)	8810(50)	3993(5)	5950(40)	23(4)
H(3B)	10140.68	4143.83	6603.23	28
C(4)	6297(18)	4123.1(18)	5000	21.6(17)
C(7)	5745(19)	4512.1(19)	5000	28.0(19)
O(1)	6319(7)	2774.4(7)	7184(6)	10.6(7)
O(2)	11424(11)	2963.8(12)	10000	12.0(10)
H(2B(w))	12460(100)	2920(20)	11190(40)	120(50)
O(3)	10925(10)	2876.6(11)	5000	9.7(9)
O(4)	5540(20)	4661.0(18)	7001(17)	38(2)
H(4)	3895.26	4706.39	7273.34	57
O(4A)	3420(40)	4624(3)	5590(30)	38(2)
O(4B)	7820(40)	4710(4)	5830(30)	38(2)
H(4B)	7304.5	4914.68	5904.87	57
P(1)	7811(4)	2936.9(4)	5000	7.5(4)
Zn(1)	8366(2)	2563.4(2)	10000	8.4(3)

Table 10.19) Anisotropic Displacement Parameters ($Å^2 \times 10^3$) for BIRM-8

Atom	U11	U22	U33	U23	U13	U12
C(1)	8(3)	6(3)	16(3)	0	0	0(2)
C(2)	30(6)	15(4)	16(5)	-2(4)	-1(5)	5(4)
C(3)	33(6)	13(4)	27(6)	-7(4)	-5(5)	8(4)
C(2A)	14(7)	5(6)	19(9)	-5(6)	0(7)	-1(6)
C(3A)	15(8)	10(7)	32(13)	-2(7)	2(8)	7(6)
C(4)	21(4)	9(3)	35(5)	0	0	1(3)
C(5A)	24(7)	10(6)	35(9)	-6(7)	-10(7)	-1(6)
C(6A)	16(8)	9(7)	41(13)	-2(8)	-3(9)	-2(6)
C(7)	27(5)	9(3)	48(5)	0	0	3(3)
O(1)	5.1(17)	11.9(14)	14.9(18)	2.0(13)	-1.7(14)	-0.4(12)
O(2)	12(3)	10(2)	14(2)	0	0	0.7(19)
O(3)	6.0(13)	6.6(18)	16(2)	0	0	-2.9(16)
O(4)	55(5)	11(2)	47(5)	-5(3)	-1(4)	10(3)
O(4A)	55(5)	11(2)	47(5)	-5(3)	-1(4)	10(3)
O(4B)	55(5)	11(2)	47(5)	-5(3)	-1(4)	10(3)
P(1)	7.5(8)	6.2(7)	8.7(8)	0	0	0.7(6)
Zn(1)	6.2(5)	7.3(4)	11.7(5)	0	0	0.1(3)

Table 10.20) Atomic Occupancies for BIRM-8

Atom	Occupancy	Atom	Occupancy	Atom	Occupancy
C(2)	0.5	H(2)	0.5	C(3)	0.5
H(3)	0.5	C(2A)	0.25	H(2A)	0.25
C(3A)	0.25	H(3A)	0.25	C(5A)	0.25
H(5A)	0.25	C(6A)	0.25	H(6A)	0.25
O(4)	0.5	H(4)	0.25	O(4A)	0.25
O(4B)	0.25	H(4B)	0.25		

BIRM-9

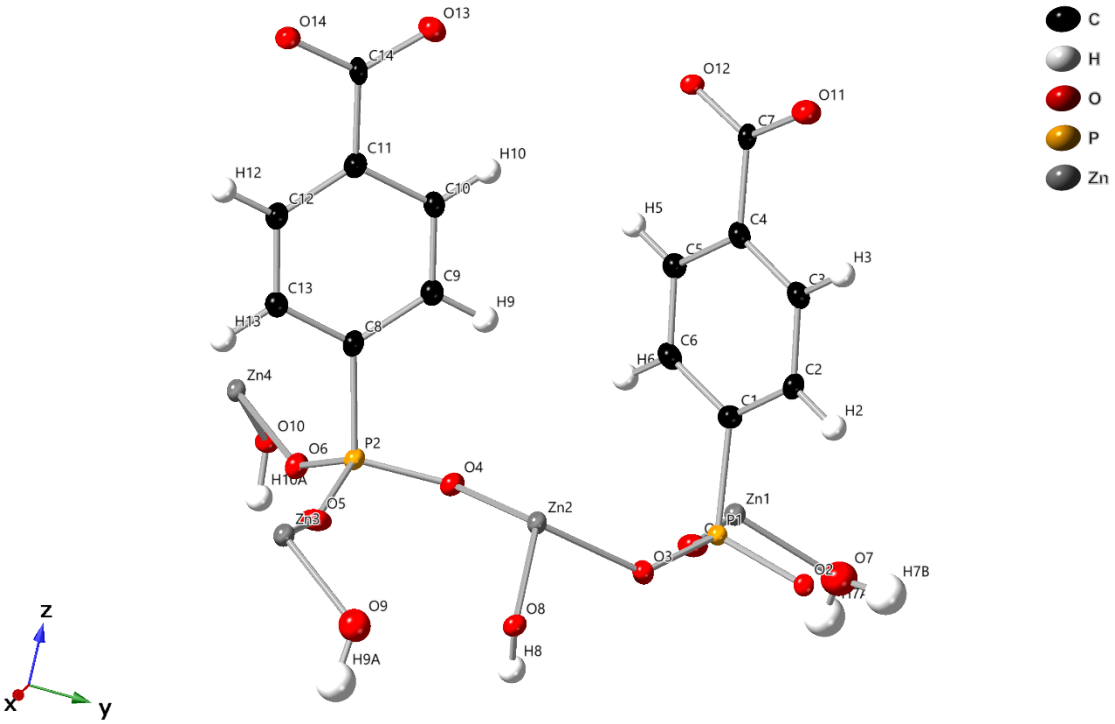

Figure 10.7) Asymmetric unit of BIRM-9. Ellipsoids drawn to 50% probability levels

Table 10.21) Crystal data and structure refinement for BIRM-9

Identification code	BIRM-9
Empirical formula	$C_{14}H_{13}O_{14}P_2Zn_4$
Formula weight	728.66
Temperature/K	100.01(10)
Crystal system	monoclinic
Space group	*P*21/*c*
a/Å	7.6382(2)
b/Å	10.8640(2)
c/Å	25.2711(6)
α/°	90
β/°	90.379(2)
γ/°	90
Volume/Å^3	2096.99(8)
Z	4
ρcalc g/cm^{-3}	2.308
μ/mm^{-1}	7.333
F(000)	1436.0
Crystal size/mm	0.1 × 0.06 × 0.01
Radiation	Cu Kα (λ = 1.54178)
2Θ range for data collection/°	6.996 to 133.164
Index ranges	$-9 \leq h \leq 9, -12 \leq k \leq 12, -30 \leq l \leq 30$
Reflections collected	4294
Independent reflections	4294 [R_{int} = 0.4246, R_{sigma} = 0.0222]
Data/restraints/parameters	4294/328/326
Goodness-of-fit on F^2	1.127
Final R indexes [I>=2σ (I)]	R_1 = 0.0441, wR_2 = 0.1301
Final R indexes [all data]	R_1 = 0.0468, wR_2 = 0.1319
Largest diff. peak/hole / e Å^{-3}	1.04/-0.85

Table 10.22) Fractional Atomic Coordinates (×10^4) and Equivalent Isotropic Displacement Parameters (Å^2×10^3) for BIRM-9

Atom	X	Y	Z	U(eq)
C1	1151(8)	7515(7)	6582(3)	13.6(12)
C2	1896(8)	8366(6)	6928(3)	13.1(11)
H2	2399.52	9101.58	6793.95	16
C3	1905(8)	8143(7)	7474(2)	13.3(12)
H3	2400.94	8730.72	7709.06	16
C4	1198(8)	7072(6)	7669(3)	12.7(11)
C5	481(8)	6202(6)	7322(3)	12.8(11)
H5	3.71	5458.45	7456.04	15
C6	466(8)	6427(6)	6782(3)	13.8(11)
H6	-15.81	5832.59	6547.33	17

C7	1125(8)	6854(6)	8255(2)	10.9(11)
C8	3583(8)	2468(6)	6592(3)	11.9(11)
C9	2934(8)	3298(6)	6968(3)	13.9(10)
H9	2376.84	4032.71	6852.41	17
C10	3092(8)	3064(7)	7502(2)	13.3(10)
H10	2653.8	3633.38	7753.72	16
C11	3914(8)	1966(6)	7671(3)	11.5(10)
C12	4561(8)	1143(6)	7297(2)	13.0(11)
H12	5119.34	405.95	7409.72	16
C13	4391(8)	1400(6)	6762(2)	13.8(11)
H13	4834.97	834.66	6509.57	17
C14	4130(7)	1735(6)	8249(2)	11.7(11)
O1	-475(6)	7226(4)	5628.6(19)	15.8(10)
O2	1514(6)	9095(4)	5745.5(17)	15.0(9)
O3	2777(5)	7027(4)	5660.7(17)	12.4(9)
O4	2643(5)	4145(4)	5851.1(17)	12.4(8)
O5	5091(6)	2698(5)	5618.0(19)	17.2(10)
O6	2061(6)	1911(4)	5652.5(17)	13.9(9)
O7	-4147(7)	8880(6)	5373(2)	27.9(12)
H7A	-4680(120)	8850(80)	5080(20)	42
H7B	-3820(140)	9620(30)	5400(40)	42
O8	6073(6)	5848(4)	5408.5(18)	12.3(9)
H8	5580(110)	5930(80)	5090(30)	19
O9	8942(7)	4008(5)	5381(2)	25.5(12)
H9A	9780(90)	4190(70)	5590(30)	38
H9B	8460(110)	4690(40)	5320(40)	38
O10	-1721(6)	983(4)	5430.0(17)	12.6(9)
H10A	-1790(120)	1050(70)	5091(10)	19
O11	1790(6)	7655(4)	8551.2(19)	15.7(10)
O12	420(6)	5860(4)	8412.1(17)	14.9(10)
O13	3512(6)	2527(5)	8563.5(19)	16.5(10)
O14	4935(6)	767(4)	8392.5(17)	15.4(10)
P1	1217.7(19)	7731.4(15)	5872.9(6)	9.5(3)
P2	3330.5(19)	2823.1(15)	5894.0(6)	9.7(3)
Zn1	-2954.9(10)	7406.7(8)	5676.3(4)	10.6(2)
Zn2	4096.8(10)	5587.8(7)	5885.4(3)	10.1(2)
Zn3	7596.0(11)	2615.5(8)	5685.4(3)	10.9(2)
Zn4	381.4(10)	653.6(7)	5857.3(3)	10.6(2)

Table 10.23) Anisotropic Displacement Parameters ($Å^2 \times 10^3$) for BIRM-9

Atom	U11	U22	U33	U23	U13	U12
C1	9(2)	17(3)	16(3)	2(2)	3(2)	4(2)
C2	10(2)	10(3)	19(3)	1(2)	2(2)	0(2)
C3	8(2)	15(3)	17(3)	-3(2)	1.8(19)	2(2)
C4	8(2)	12(3)	17(2)	-4(2)	1.1(18)	0(2)
C5	7(2)	13(3)	18(2)	-1(2)	3.9(18)	-4(2)
C6	8(2)	16(3)	17(2)	-4(2)	2.1(18)	-1(2)
C7	8(2)	7(3)	18(2)	-1(2)	0.9(19)	-1(2)
C8	9(2)	9(2)	18(2)	-0.6(19)	0.0(19)	-4(2)
C9	11(2)	13(2)	18(2)	0(2)	2.7(18)	1(2)
C10	9(2)	12(2)	19(2)	-0.5(19)	5.2(18)	1(2)
C11	6(2)	11(3)	18(2)	0(2)	1.4(18)	-5(2)
C12	8(2)	13(3)	18(2)	1(2)	-0.2(19)	3(2)
C13	12(2)	13(3)	17(2)	-1(2)	3(2)	-2(2)
C14	7(2)	10(3)	18(2)	-3(2)	1.7(19)	1(2)
O1	13(2)	21(3)	13(2)	1(2)	0.8(16)	-2.7(19)
O2	22(2)	10(2)	13(2)	0.5(18)	3.0(16)	3.7(18)
O3	8(2)	13(2)	15(2)	0.0(18)	4.3(16)	1.7(17)
O4	11.2(19)	12(2)	14(2)	1.2(18)	-0.8(15)	-3.8(17)
O5	14(2)	25(3)	14(2)	2(2)	4.1(18)	-0.5(19)
O6	15(2)	10(2)	16(2)	-0.8(18)	-2.5(16)	-3.9(18)
O8	12(2)	11(2)	14(2)	2.4(18)	2.2(16)	-1.3(18)
O10	12.3(19)	15(2)	11(2)	0.5(18)	-0.3(15)	0.7(19)
O11	11(2)	22(3)	14(2)	1.3(18)	-1.1(16)	1(2)
O12	19(2)	13(2)	13(2)	1.3(18)	4.0(16)	-2(2)
O13	15(2)	20(3)	14(2)	-2.1(19)	1.3(17)	3.2(19)
O14	20(2)	17(2)	10(2)	0.9(17)	-3.1(15)	3(2)
P1	7.7(7)	9.6(8)	11.2(7)	0.3(6)	1.6(5)	0.7(6)
P2	7.1(7)	9.5(8)	12.5(7)	1.1(6)	0.5(5)	-1.4(6)
Zn1	8.4(4)	10.6(4)	12.9(4)	-0.2(3)	1.1(3)	-1.0(3)
Zn2	7.9(4)	9.0(4)	13.3(4)	-0.4(3)	0.6(3)	-0.4(3)
Zn3	8.5(4)	10.4(5)	13.7(4)	0.5(3)	0.9(3)	-0.1(3)
Zn4	10.3(4)	8.3(4)	13.1(4)	-0.2(3)	1.1(3)	0.4(3)
O7	23(3)	33(3)	27(3)	3(2)	0(2)	1(2)
O9	24(3)	23(3)	29(3)	0(2)	-1(2)	5(2)

BIRM-10

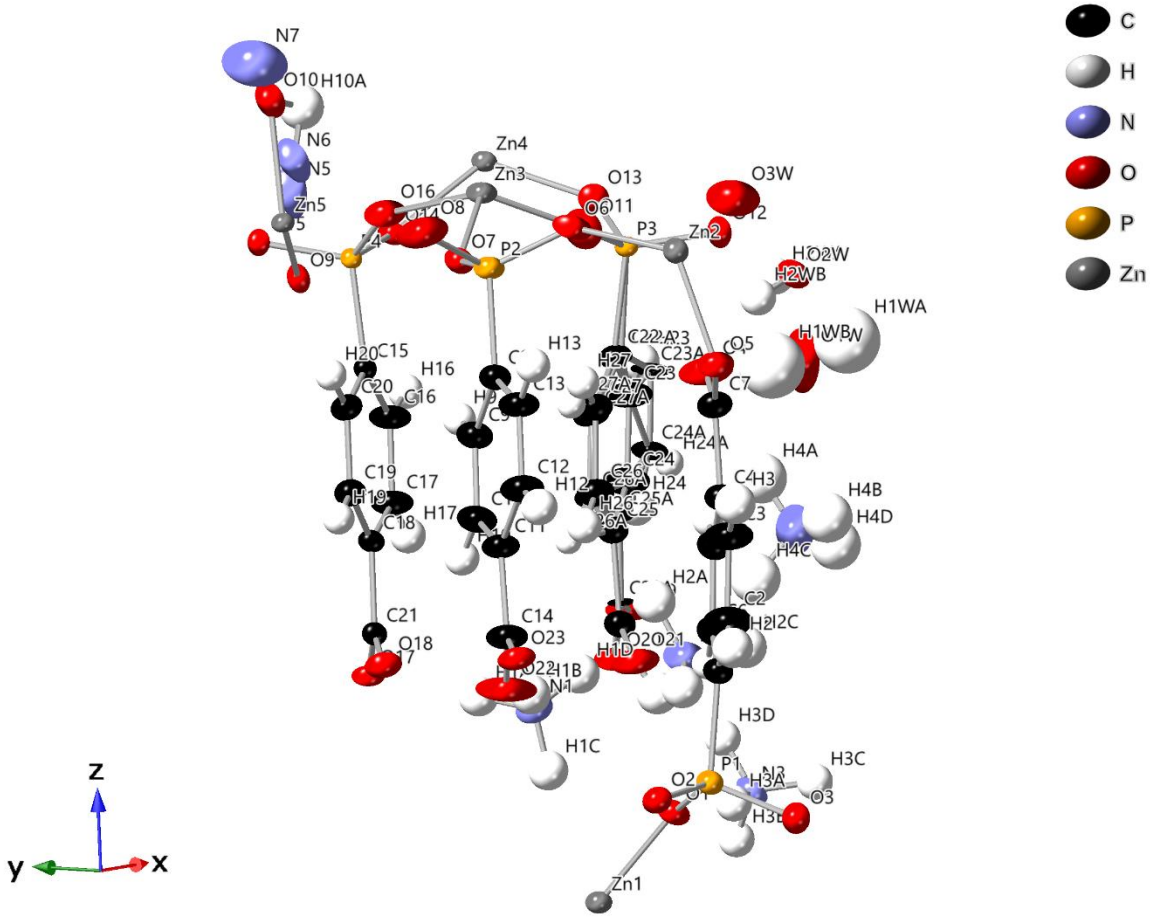

Figure 10.8) Asymmetric unit of BIRM-10. Ellipsoids drawn at 50% probability level. Note that the large asymmetric unit makes producing an image where each atom and its label is clearly visible impossible.

Table 10.24) Crystal data and structure refinement for BIRM-10

Identification code	BIRM-10
Empirical formula	$C_7H_{7.12}N_{0.9}O_{5.44}PZn_{1.08}$
Formula weight	292.56
Temperature/K	100(2)
Crystal system	monoclinic
Space group	*P*21/*c*
a/Å	10.41240(10)
b/Å	19.4412(2)
c/Å	19.8815(2)
α/°	90
β/°	92.2820(10)
γ/°	90
Volume/Å^3	4021.41(7)
Z	16
ρcalc g/cm^{-3}	1.933
μ/mm^{-1}	5.226
F(000)	2342.0
Crystal size/mm	0.123 × 0.074 × 0.036
Radiation	CuKα (λ = 1.54184)
2Θ range for data collection/°	8.498 to 146.38
Index ranges	$-12 \leq h \leq 12,\ -24 \leq k \leq 23,\ -20 \leq l \leq 24$
Reflections collected	53789
Independent reflections	7976 [R_{int} = 0.0330, R_{sigma} = 0.0196]
Data/restraints/parameters	7976/266/722
Goodness-of-fit on F^2	1.038
Final R indexes [I>=2σ (I)]	R_1 = 0.0285, wR_2 = 0.0660
Final R indexes [all data]	R_1 = 0.0326, wR_2 = 0.0682
Largest diff. peak/hole / e Å^{-3}	0.90/-0.73

Table 10.25) Fractional Atomic Coordinates (×10^4) and Equivalent Isotropic Displacement Parameters (Å^2×10^3) for BIRM-10

Atom	X	Y	Z	U(eq)
C1	1797(2)	4124.1(13)	6331.7(12)	21.5(5)
C2	1099(3)	3744.5(17)	6787.4(15)	37.4(7)
C3	1364(3)	3797.0(17)	7475.5(14)	38.0(7)
C4	2329(3)	4231.3(14)	7723.5(13)	24.7(5)
C5	3045(2)	4599.0(14)	7271.7(13)	24.4(5)
C6	2784(2)	4542.4(14)	6587.9(13)	23.3(5)
C7	2553(3)	4338.2(14)	8464.9(14)	28.8(6)
C8	470(2)	5768.0(13)	8729.2(13)	21.5(5)
C9	924(3)	6171.4(14)	8211.8(13)	25.4(5)

C10	541(3)	6037.1(15)	7549.4(14)	28.4(6)
C11	-288(2)	5491.5(15)	7396.5(13)	26.6(6)
C12	-726(3)	5082.6(15)	7911.3(14)	30.7(6)
C13	-361(3)	5220.2(14)	8574.5(13)	27.9(6)
C14	-653(3)	5324.8(17)	6680.0(14)	31.3(6)
C15	3512(2)	8244.7(12)	8524.8(12)	16.3(4)
C16	4467(2)	8375.8(16)	8072.5(13)	28.3(6)
C17	4220(3)	8295.2(16)	7386.6(13)	29.5(6)
C18	3027(2)	8067.9(12)	7145.1(12)	19.4(5)
C19	2089(2)	7904.7(14)	7597.2(13)	23.3(5)
C20	2327(2)	7999.1(14)	8280.0(13)	22.7(5)
C21	2755(2)	7970.1(13)	6403.7(12)	21.1(5)
C22	5961(5)	6642(4)	8574(3)	20.3(11)
C22A	6306(11)	6697(10)	8579(7)	13(3)
C23	6968(5)	6889(2)	8197(2)	34.5(10)
C23A	7525(10)	6867(6)	8376(4)	22(2)
C24	6861(5)	6900(3)	7494(2)	33.8(12)
C24A	7697(8)	6979(5)	7698(4)	19.0(19)
C25	5759(4)	6648(2)	7163(2)	24.5(8)
C25A	6665(9)	6919(7)	7230(5)	13(2)
C26	4740(3)	6418(2)	7533.4(17)	28.2(8)
C26A	5449(9)	6753(6)	7439(5)	17(2)
C27	4837(4)	6422(2)	8228.0(19)	26.0(8)
C27A	5294(9)	6643(6)	8117(4)	19(2)
C28	5674(3)	6582(2)	6399.4(18)	25.9(7)
C28A	6954(9)	7049(5)	6490(4)	15.2(17)
O1	2001.8(16)	4712.3(9)	5135.5(9)	21.6(4)
O2	-94.9(15)	4075.6(9)	5373.8(9)	21.6(4)
O3	1863.9(15)	3416.5(9)	5157.2(9)	22.5(4)
O4	3397(3)	4735.6(13)	8677.9(11)	46.6(6)
O5	1791.9(19)	4022.2(10)	8850.5(9)	30.0(4)
O6	1579(3)	5343.8(10)	9921.2(10)	44.2(6)
O7	1781.9(15)	6586.3(9)	9579.0(8)	19.4(3)
O8	-313.1(19)	6151.6(12)	9937.4(10)	40.4(8)
O9	278(4)	7655(3)	9460(3)	19.2(10)
O10	-901(6)	7421(3)	10997(5)	31.2(14)
O11	4770.9(19)	6452.3(13)	9690.8(12)	42.0(5)
O12	6839.1(17)	5852.7(9)	9586.9(10)	26.3(4)
O13	6852(2)	7124.9(9)	9804.8(10)	30.4(4)
O14	5198.9(15)	8551.0(10)	9531.6(8)	22.6(4)
O15	3044.8(16)	9099.2(9)	9542.9(9)	23.6(4)
O16	3227(2)	7871.8(10)	9828.7(9)	34.1(5)
O17	3443.8(18)	8315.1(10)	6006.3(8)	24.9(4)
O18	1890.6(18)	7563.4(10)	6211.8(9)	29.9(4)

O19	7930(8)	7343(4)	6360(4)	26.5(18)
O20	6346(2)	6921.4(12)	6058.6(10)	36.8(5)
O21	4906(3)	6149.1(17)	6150.9(13)	37.6(7)
O22	-75(2)	5573.8(15)	6208.9(10)	50.6(7)
O23	-1557.9(17)	4891.3(10)	6570.7(9)	27.9(4)
P1	1365.5(5)	4088.9(3)	5441.6(3)	17.40(12)
P2	928.7(6)	5959.8(3)	9592.8(3)	18.77(12)
P3	6122.5(5)	6531.7(3)	9472.0(3)	14.85(12)
P4	3763.9(5)	8438.4(3)	9406.3(3)	13.37(11)
Zn1	1492.0(3)	5317.1(2)	4394.6(2)	15.45(7)
Zn2	1786.6(3)	4380.2(2)	9765.6(2)	17.81(8)
Zn3	3310.0(3)	6912.3(2)	10040.7(2)	17.49(8)
Zn4	6458.2(3)	8071.9(2)	10081.4(2)	15.87(7)
Zn5	-1092.3(8)	7268.5(4)	10005.8(4)	12.50(17)
N1	2218(2)	6170.9(12)	5903.6(11)	29.0(5)
N2	4838(7)	5615(4)	6217(4)	32.5(16)
N3	5053(8)	5069(4)	5139(2)	24.3(14)
N4	6231(3)	4973(2)	7222(2)	46.8(9)
N5	-70(30)	7544(10)	10205(14)	84(8)
N6	-500(10)	7359(5)	10482(5)	53(3)
N7	-1340(20)	7395(12)	11317(10)	81(6)
O1W	6060(5)	4772(2)	8625(3)	81.8(18)
O2W	5586(7)	4637(4)	9366(4)	24.4(15)
O3W	5000	5000	10000	52(4)

Table 10.26) Hydrogen Atom Coordinates (Å×10^4) and Isotropic Displacement Parameters (Å^2×10^3) for BIRM-10

Atom	X	Y	Z	U(eq)
H2	434.13	3446.11	6624.77	45
H3	880.7	3533.77	7778.71	46
H5	3719.32	4891.39	7434.27	29
H6	3288.64	4794.48	6285.75	28
H9	1500(30)	6542(17)	8298(16)	30
H10	830(30)	6317(17)	7204(17)	34
H12	-1279.56	4705.63	7807.8	37
H13	-674.93	4942.42	8925.08	33
H16	5293.23	8521.5	8234.55	34
H17	4872.5	8396.08	7080.55	35
H19	1283.49	7727.95	7436.74	28
H20	1675.32	7895.29	8585.39	27
H23	7732.52	7051.64	8420.83	41
H23A	8225.11	6905.68	8694.76	26
H24	7542.62	7079.44	7243.14	41
H24A	8523.65	7098.42	7549.91	23
H26	3976.21	6256.65	7308.39	34
H26A	4741.57	6716.57	7124.75	20
H27	4127.13	6273.09	8476.19	31
H27A	4467.3	6525.79	8267.49	23
H1A	2095.27	6686.08	5986.51	44
H1B	1442.1	5906.58	6072.82	44
H1C	2295.17	6083.18	5398.61	44
H1D	3035.9	6006.39	6157.1	44
H1WA	6290(70)	4390(30)	8800(50)	123
H1WB	5252(12)	4770(40)	8630(50)	123
H2A	4634.58	5824.28	6673.43	49
H2B	5072.59	5998.48	5891.45	49
H2C	5593.76	5280.42	6278.06	49
H2D	4048.96	5355.07	6025.67	49
H2WA	6030(80)	4990(30)	9310(70)	37
H2WB	4850(50)	4730(50)	9210(70)	37
H3A	4120.31	4904.85	5090.07	36
H3B	5286	5334.59	4716.23	36
H3C	5650.01	4653.3	5201.48	36
H3D	5157.62	5385.33	5549.84	36
H10A	89.38	7482.67	10882.42	56
H4A	6250.57	5299	7627.4	70
H4B	5877.56	4504.91	7362.18	70
H4C	5650.68	5174.92	6843.99	70
H4D	7142.17	4913.41	7056.09	70

Table 10.27) Anisotropic Displacement Parameters ($Å^2 \times 10^3$) for BIRM-10

Atom	U11	U22	U33	U23	U13	U12
C1	18.9(11)	27.5(12)	18.2(12)	2.2(10)	1.8(9)	-0.6(9)
C2	41.2(16)	45.5(17)	25.7(15)	1.3(13)	3.3(12)	-24.6(14)
C3	47.6(17)	46.9(18)	19.8(14)	4.0(13)	6.8(12)	-22.4(14)
C4	27.9(13)	28.3(13)	18.2(12)	1.7(10)	2.6(10)	-0.7(10)
C5	20.3(11)	29.5(13)	23.2(13)	2.1(11)	-1.3(10)	-2.6(10)
C6	17.9(11)	30.2(13)	22.2(13)	5.1(10)	3.1(9)	-0.9(10)
C7	37.8(15)	29.5(14)	19.4(13)	0.3(11)	3.7(11)	-2.4(11)
C8	21.3(11)	24.7(12)	18.3(12)	0.0(10)	-1.1(9)	-5.0(9)
C9	25.8(12)	29.4(13)	20.8(13)	2.6(11)	-1.1(10)	-9.8(10)
C10	26.3(13)	39.5(15)	19.6(13)	5.9(11)	2.2(10)	-9.7(11)
C11	21.7(12)	41.4(15)	16.5(12)	-3.3(11)	-0.7(10)	-5.7(11)
C12	32.3(14)	38.8(15)	20.6(13)	-3.6(11)	-1.2(11)	-17.5(12)
C13	33.7(14)	32.4(14)	17.4(13)	0.6(11)	0.6(10)	-14.6(11)
C14	22.9(12)	53.7(18)	17.3(13)	-3.4(12)	-0.8(10)	-6.1(12)
C15	18.5(10)	16.1(10)	14.2(11)	0.4(9)	0.0(9)	2.4(8)
C16	22.0(12)	46.7(16)	16.2(12)	-0.3(11)	-0.6(10)	-12.2(11)
C17	25.6(13)	46.7(16)	16.3(12)	-0.2(12)	1.8(10)	-11.5(12)
C18	22.1(11)	21.4(11)	14.4(11)	-0.5(9)	-2.3(9)	2.3(9)
C19	17.1(11)	31.1(13)	21.5(13)	-4.4(10)	-3.0(9)	-1.9(10)
C20	17.9(11)	31.0(13)	19.5(12)	-3.2(10)	2.6(9)	-1.5(10)
C21	23.2(12)	23.3(12)	16.4(12)	-2.8(10)	-4.1(9)	6.3(9)
C22	20(2)	26(2)	15(2)	-1.9(16)	2.6(17)	-2(2)
C22A	12(5)	18(6)	9(5)	1(4)	-2(4)	3(5)
C23	28(2)	56(3)	19(2)	-4.6(19)	-1.0(19)	-17(2)
C23A	15(5)	44(6)	6(4)	-1(4)	-5(4)	-12(5)
C24	26(2)	55(3)	21(2)	1(3)	2.6(19)	-12(2)
C24A	9(4)	37(5)	11(4)	1(4)	-2(3)	-11(4)
C25	22.0(19)	30(2)	21(2)	-0.7(17)	0.3(15)	-0.1(16)
C25A	12(4)	21(5)	6(5)	0(5)	-3(3)	-3(4)
C26	22.8(17)	40(2)	21.8(17)	-5.5(15)	-2.6(14)	-5.9(16)
C26A	7(4)	32(6)	12(4)	-2(4)	1(3)	-2(4)
C27	22(2)	36(2)	19.9(18)	-1.9(16)	0.9(15)	-1.7(16)
C27A	9(4)	38(6)	10(4)	-2(4)	7(4)	-7(4)
C28	19.3(15)	36.7(19)	21.2(18)	-3.0(15)	-4.1(13)	3.4(14)
C28A	26(5)	18(4)	1(4)	1(3)	3(3)	0(4)
O1	19.8(8)	26.0(9)	18.6(8)	5.7(7)	-1.9(7)	-5.1(7)
O2	15.4(8)	29.3(9)	20.2(9)	-3.3(7)	1.4(6)	0.1(7)
O3	14.6(7)	25.1(9)	27.9(9)	-0.9(7)	1.6(7)	-0.2(6)
O4	64.4(15)	53.9(14)	21.7(10)	-6.4(10)	3.1(10)	-26.9(12)
O5	40.3(11)	33.4(10)	16.6(9)	3.3(8)	6.5(8)	-2.5(8)
O6	92.4(18)	18.4(9)	20.1(10)	1.2(8)	-18.3(11)	-0.3(10)
O7	16.7(7)	20.7(8)	20.3(8)	1.3(7)	-4.0(6)	-4.7(6)

O8	31.4(11)	63.1(15)	27.1(11)	-9.6(10)	8.3(8)	-24.2(10)
O9	15(2)	22(2)	22(3)	8(2)	7.9(19)	5.3(18)
O10	21(3)	33(3)	39(5)	2(3)	-9(3)	5(3)
O11	20.9(9)	64.1(15)	42.2(12)	13.0(11)	13.5(9)	9.1(9)
O12	24.4(9)	22.6(9)	31.1(10)	-7.0(8)	-10.6(7)	7.6(7)
O13	42.6(11)	21.7(9)	25.9(10)	-7.3(8)	-11.4(8)	2.2(8)
O14	13.7(7)	39.0(10)	15.0(8)	0.8(7)	-1.3(6)	6.5(7)
O15	21.5(8)	26.2(9)	22.5(9)	-7.0(7)	-7.2(7)	11.2(7)
O16	56.9(13)	27.7(10)	18.2(9)	3.9(8)	8.2(9)	-11.9(9)
O17	32.6(9)	30.2(9)	11.8(8)	-0.2(7)	-0.8(7)	0.7(8)
O18	30.8(10)	37.4(11)	21.0(9)	-8.8(8)	-5.6(8)	-3.5(8)
O19	24(4)	44(5)	11(3)	3(3)	2(3)	-27(3)
O20	46.1(12)	52.7(13)	12.0(9)	3.7(9)	6.2(9)	10.4(10)
O21	39.0(15)	56(2)	18.2(13)	-7.8(13)	2.1(11)	-16.2(14)
O22	35.6(11)	100(2)	16.2(10)	3.0(11)	0.5(9)	-27.6(12)
O23	24.5(9)	43.1(11)	15.9(9)	-7.6(8)	-0.8(7)	-3.6(8)
P1	14.4(3)	21.5(3)	16.3(3)	1.9(2)	1.0(2)	-1.9(2)
P2	23.2(3)	18.2(3)	14.7(3)	0.3(2)	-1.2(2)	-7.2(2)
P3	13.3(2)	19.3(3)	11.9(3)	-1.4(2)	-0.3(2)	1.8(2)
P4	13.5(2)	14.9(3)	11.7(3)	0.5(2)	0.0(2)	1.8(2)
Zn1	13.60(14)	18.52(15)	14.13(15)	-0.86(12)	-0.58(11)	-3.35(11)
Zn2	15.50(14)	18.71(15)	19.05(16)	-0.52(12)	-1.49(12)	-0.46(11)
Zn3	16.44(14)	23.46(16)	12.57(15)	0.97(12)	0.73(11)	-6.60(12)
Zn4	15.01(14)	19.50(15)	12.83(15)	-1.18(12)	-2.87(11)	-0.24(11)
Zn5	10.9(4)	15.8(4)	10.8(4)	-0.7(3)	0.8(3)	-1.1(3)
N1	30.9(12)	33.7(12)	22.9(11)	-2.1(10)	8.2(9)	-5.8(10)
O1W	67(3)	44(2)	131(5)	-38(3)	-53(3)	18(2)
N2	37(4)	33(4)	27(4)	6(3)	0(3)	-19(3)
O2W	24(3)	26(4)	23(4)	6(3)	-3(3)	-5(3)
N3	23(2)	31(4)	19(4)	11(3)	-3(4)	3(2)
N4	17.1(15)	54(2)	70(3)	1(2)	8.0(16)	0.7(14)
N5	110(20)	35(11)	100(20)	-24(10)	-47(15)	41(11)
N6	58(5)	34(4)	63(7)	-8(4)	-40(5)	12(3)
N7	72(14)	112(17)	58(12)	11(11)	4(10)	-22(12)
O3W	77(10)	42(7)	36(7)	8(6)	-1(7)	-27(7)

Table 10.28) Atomic Occupancies for BIRM-10

Atom	Occupancy	Atom	Occupancy	Atom	Occupancy
C22	0.75	C22A	0.25	C23	0.75
H23	0.75	C23A	0.25	H23A	0.25
C24	0.75	H24	0.75	C24A	0.25
H24A	0.25	C25	0.75	C25A	0.25
C26	0.75	H26	0.75	C26A	0.25
H26A	0.25	C27	0.75	H27	0.75
C27A	0.25	H27A	0.25	C28	0.75
C28A	0.25	O8	1.039(8)	O9	0.3333
O10	0.3333	O19	0.25	O21	0.75
Zn5	0.3333	O1W	0.6667	H1WA	0.6667
H1WB	0.6667	N2	0.3333	H2A	0.3333
H2B	0.3333	H2C	0.3333	H2D	0.3333
O2W	0.25	H2WA	0.25	H2WB	0.25
N3	0.5	H3A	0.5	H3B	0.5
H3C	0.5	H3D	0.5	N4	0.75
H10A	0.3333	H4A	0.75	H4B	0.75
H4C	0.75	H4D	0.75	N5	0.25
N6	0.5	N7	0.25	O3W	0.25

Indexing Details

Cadmium BIRM-1 Phase

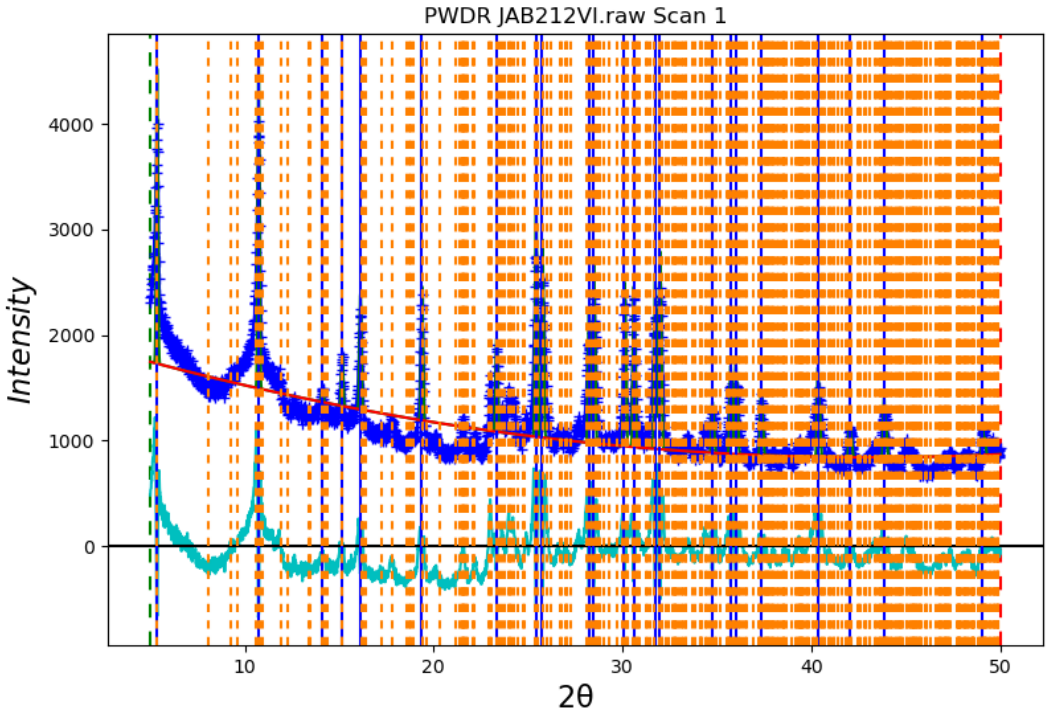

Figure 10.9) Diffraction pattern of the cadmium product (blue) used for indexing. Peak positions used are indicated by blue lines and calculated positions based of the indexed cell are shown by the dotted orange lines. The width of the peaks were not refined as it led to the positions refining away from the actual peaks. Thus the difference line (teal) looks very similar to the actual diffraction data

Table 10.29) List of peaks used for indexing the cadmium product

Peak	Position	Intensity
1	5.3558	13516.5
2	10.7285	15432.7
3	14.4024	579.1
4	15.1449	2574.2
5	16.1151	5820.4
6	19.3640	7005.6
7	23.3798	5125.8
8	25.4115	13053.5
9	25.7471	11255.1
10	28.2120	7689.4
11	28.4646	10618.9
12	30.0944	10002.6
13	30.5881	9815.3
14	31.7225	10531.5
15	31.9723	12259
16	34.7527	3239.8
17	35.7175	5697
18	35.9938	5824.2
19	37.3325	4155.4
20	40.3406	5961.1
21	42.0200	2311.5
22	43.8462	3979.1
23	49.0614	2259.3

Unsolved Magnesium Phase

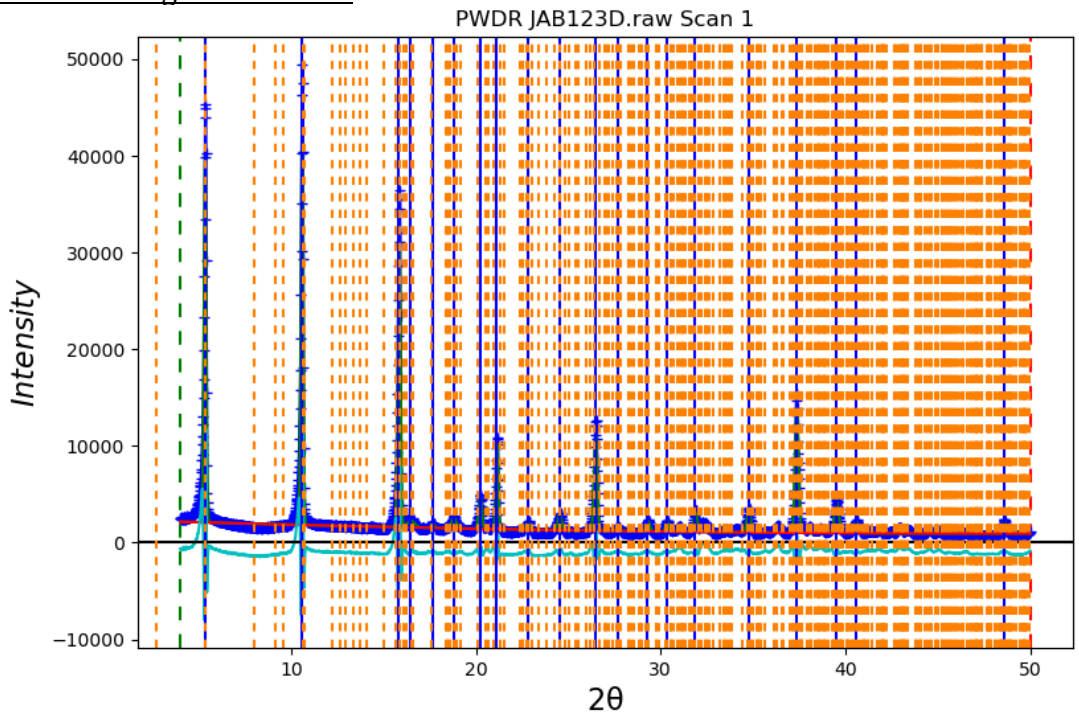

Figure 10.10) Diffraction pattern of the unknown magnesium-based phase (blue) used for indexing. Peak positions used are indicated by blue lines and calculated positions based of the indexed cell are shown by the dotted orange lines. The difference line is shown in teal.

Table 10.30) List of peaks used for indexing the unknown magnesium phase

Peak	Position	Intensity
1	5.3379	260393.6
2	10.5782	283292.8
3	15.8316	245390
4	16.4796	15312.5
5	17.6585	3880.5
6	18.8007	15210.4
7	20.2232	30595.3
8	21.1287	68622.4
9	22.8032	7452.1
10	24.5214	18778.5
11	26.4615	97121.4
12	27.6649	4144.8
13	29.2937	10849.3
14	30.3283	9905
15	31.8675	22980
16	34.7459	26202.2
17	37.3395	135749
18	39.5029	42240.8
19	40.5634	17440
20	48.5842	13519.4

PDF Data

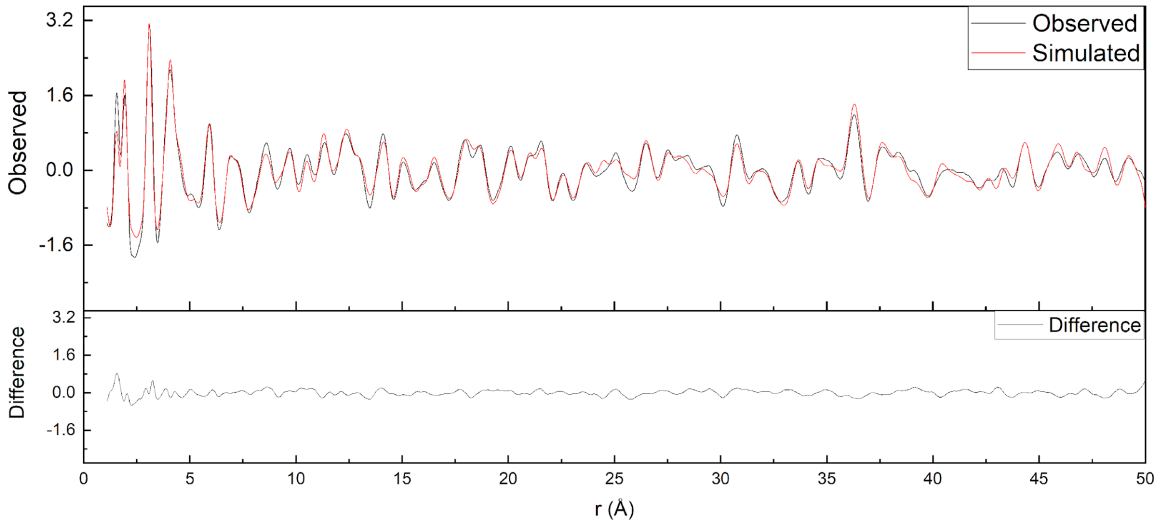

Figure 10.11) PDF fit of the data collected on BIRM-1 at 50 °C

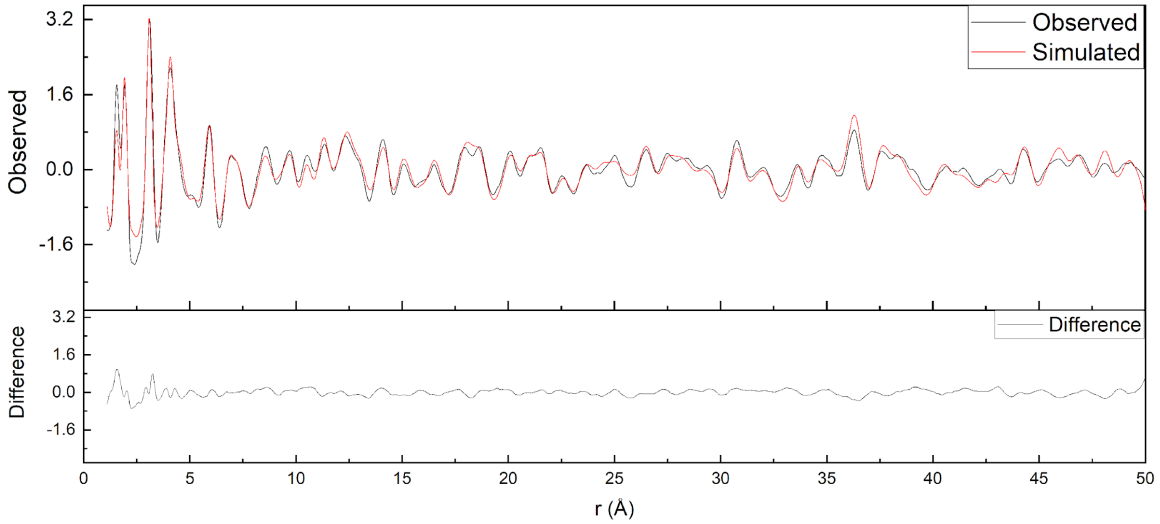

Figure 10.12) PDF fit of the data collected on BIRM-1 at 75 °C

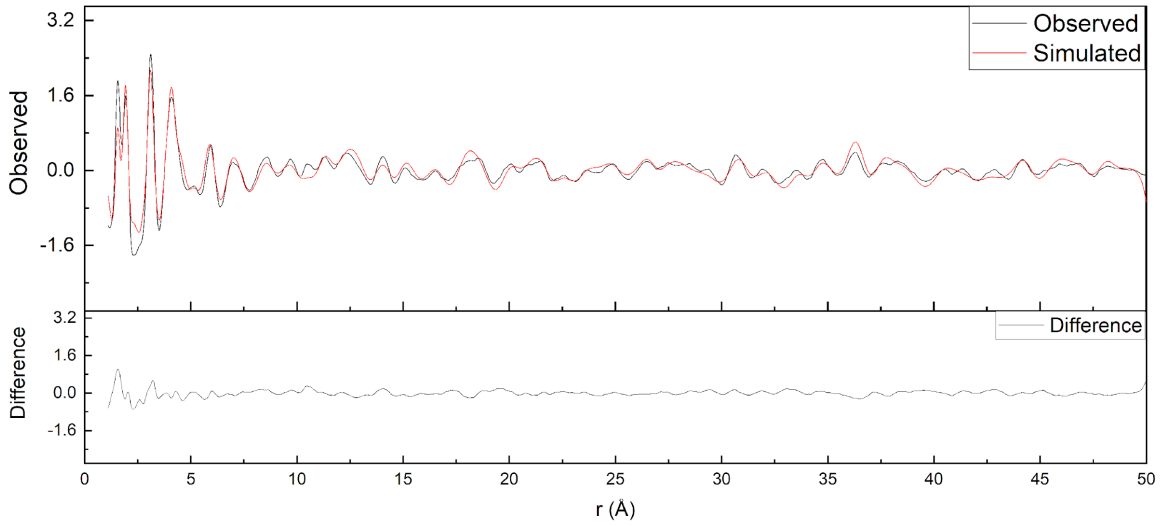

Figure 10.13) PDF fit of the data collected on BIRM-1 at 100 °C

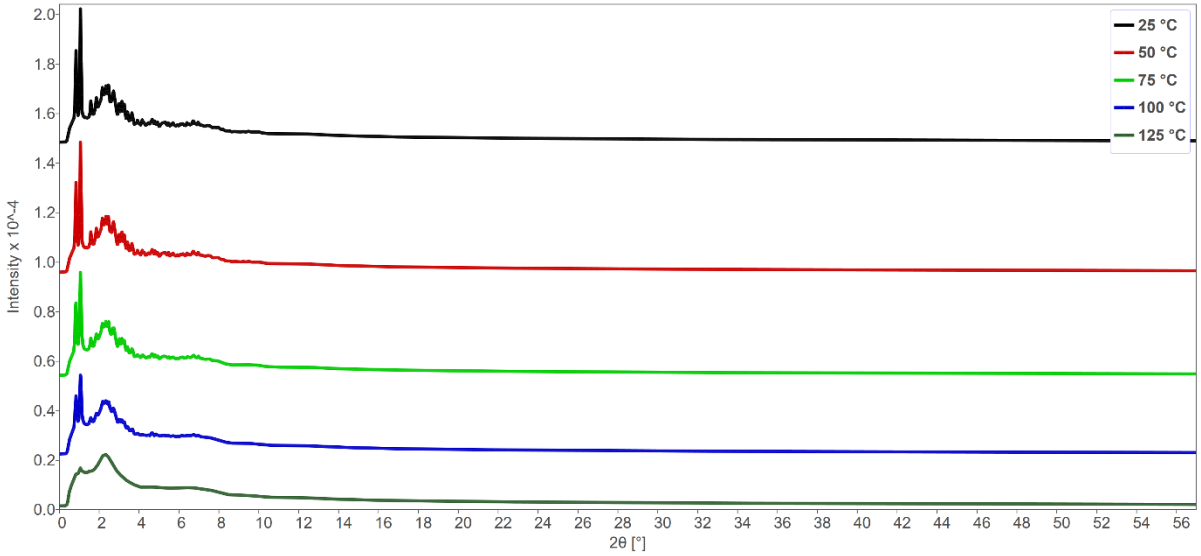

Figure 10.14) The Bragg data collected on BIRM-1 during in-situ dehydration of the material collected at Diamond Light Source I15-1